A New Texturing Technique for Silicon Solar Cells using Gas Phase Etching

By

Eleanor Caitlin Shaw

Thesis submitted for Degree of Doctor of Philosophy

Trinity Term 2022

Supervised by

Prof Peter R Wilshaw and Prof Ruy Sebastian Bonilla

University of Oxford

Department of Materials

A love letter to every young girl that dreams of pursuing science.

Acknowledgements

I would first like to thank EPSRC and Innovate UK for funding my doctorate. Thank you to Tetreon Technologies and Ian Sharp for the building and modifications of the texturing tool so I could undertake this project. I would also like to thank all the different groups that collaborated on this project for its success: Trina Solar, the Black-Si group at UNSW, and Warwick University. I would also like to thank everyone that aided in the Black Si experimental work at Oxford, including Dr Mohsen Goodzari, Samira Kelly, Rory Rose, and a special thank you to Dr Isabel Al-Dhahir for aiding in the HF work this project necessitated. Finally, I would like to thank the Materials Department for hosting me for 10 years and allowing me to academically flourish.

Firstly, I would like to thank my supervisor Prof Peter Wilshaw. You are one of the few people in my academic career that has actively intellectually challenged me. It has been wonderful to have someone so invested in my development to whom I can ask questions and I will get such an enthusiastic and lively response (of course with a whiteboard diagram). Over the last 6 years you have allowed me to hone my critical thinking skills and foster the confidence to argue my point. Although I think I will probably pause on every presentation slide for many years to come, with the expectation of a discussion before continuing. Secondly, I would like to thank my co-supervisor Prof Sebastian Bonilla. You have also intellectually pushed me, even when I would just like the answer you make me sit and think and I am eternally grateful for this skill. You have been incredibly kind and supportive, and I am endlessly thankful to have had you during trying times. You have also been wonderful at reading my thesis and helped me to craft a document I am proud of, thank you. In addition, I would like to thank the two post-docs that helped on the project. Thank you to Dr Mohzen Goodarzi who helped in the second half of the project, particularly with the experimental work, and thank you to Dr Matthew Wright who was a huge help in bouncing ideas off for my thesis structure, thinking about the big-picture ideas, and readily explaining concepts to me.

I could not have done any of this without the support of the team of the Semiconductors research group over the last 5 years: Katie, Gaby, David, Isabel, Shona, Avery, Donghao, Yifu, John, Xinya, and Erica. Not to mention the countless part II students who have brought their bright-eyed love to the lab for their first taste of academic research. You have all been wonderful with helping bounce ideas around and lightening the mood when experiments decide they do not want to work.

I also want to thank the Oxford Powerlifting Club as the club and its members that have given me so much joy in my DPhil. I particularly want to thank you for the time I spent as the women's captain, something which my younger self would never have dreamed of.

Lastly, I want to thank my family and friends. To Jen, my comrade in doctorate life, my ear in thesis writing, and a believer in chocolate bribery will make you write quicker, thank you. To Meg, your kind soul and bubbly personality has given me relief in tough times, it makes me so glad to have you as my sister. Denise, Martin; your love, support, and belief in me and my abilities is an endless ocean, not just during my time at Oxford but throughout my life. You are better than the best parents I could have ever asked for and I love you dearly. Ilia. Oh, Ilia. Never did I think that the boy that sat across from me at the fresher's welcome dinner would have become my husband-to-be. I am so lucky to have grown with you over the last 10 years, you have helped me become confident, spontaneous, and reminded me it is okay to say no and relax. You are my boulder, and I could not have undertaken this doctorate without your love, support, and smiles.

Abstract

Solar energy is vital to combatting climate change. However, not all incident photons can transmit into a typical solar cell for electricity generation, a portion of the photons are lost to front surface reflectance. By changing the front surface texture of typical solar cells from microscale to nanoscale, the solar cell front surface reflectance (at wavelengths of interest), can be reduced to almost 0%. Such a change would increase the number of photons available in the solar cell for electricity generation. Despite the excellent optical properties nano-textures can offer, all current industrially relevant nanoscale texturing methods have drawbacks that prevent them from gaining a significant market share. This thesis explores texturing in the gas-phase to overcome the drawbacks of other nanoscale texturing techniques, whilst still providing exceptional optical properties to improve solar cell efficiency.

Texturing Si in the gas-phase using ozone and hydrofluoric acid vapours at atmospheric pressure and low temperature was investigated. The premise of the texturing mechanism was to use the increased activity of ozone to oxidise the Si surface, at significantly lower temperatures than for O_2 oxidation, then etch the oxide away using HF vapour, causing an ultra-low reflectance surface texture to form. A texturing tool was designed, built, and refined to study gas-phase texturing in this project. With this new tool, texturing reproducibility and uniformity were found to be dependent upon the surface chemistry of the Si wafers. By intentionally changing the surface chemistry via a precursor containing colloidal silica and IPA, reproducible and uniform texturing could be performed on sample sizes up to full-sized industrial Si wafers, with an average reflectance as low as $1.8\% \pm 0.2\%$ in 2 mins texturing. The mechanism behind the precursor was attributed to the Na^+ counter-ions present in the colloidal silica and a full texturing mechanism was proposed for the first time, accounting for the different morphologies gas-phase texturing could produce. Upon implementing gas-phase textured Si into a solar cell for the first time, a median cell

efficiency of 17.24% was achieved, without any optimisation of the solar cell fabrication methods for the nano-texture.

1 Table of Contents

List of Figures

List of Tables

List of Acronyms

a-Si – amorphous Si
ALD – Atomic Layer Deposition
ARC – Anti-Reflection Coating
c-Si – crystalline Si
DWS – Diamond Wire Sawn
EDL – Electric Double Layer
EQE – External Quantum Efficiency
FEP – Field Effect Passivation
FF – Fill Factor
GaPTex – Gas Phase Texturing
LCOE – Levelised Cost of Electricity
LDSE – Laser Doped Selective Emitter
MACE – Metal Assisted Catalytic Etching
mc-Si – multicrystalline Si
mono-Si – monocrystalline Si
PECVD – Plasma Enhanced Chemical Vapour Deposition
PERC – Passivated Emitter Rear Cell
pFF – Pseudo Fill Factor
PSG – Phosphosilicate Glass
PV – Photovoltaics
RIE – Reactive Ion Etching
sc-Si – single crystal Si
SRH – Shockley-Read Hall
SRV – Surface Recombination Velocity
VdW – Van der Waals
WAR – Weighted Average Reflectance
XPS – X-ray Photoelectron Spectroscopy

List of Symbols

λ – Wavelength
η – Solar cell efficiency
I_0 – Carrier recombination current
I_{mp} – Current at the maximum power drawn of the solar cell
I_{sc} – Short circuit current
J_0 – Carrier recombination current
J_{sc} – Short circuit current
P_{mp} – Maximum power drawn from the solar cell
R_s – Series Resistance
R_{sh} – Sheet Resistance
R_{shunt} – Shunt Resistance
V_{mp} – Voltage at the maximum power drawn of the solar cell
V_{oc} – Open circuit voltage
τ – effective carrier lifetime

1 Introduction

1.1 Climate Change & Renewable Energy

In the 1800s humanity unlocked a new energy resource, fossil fuels. Figure 1.1 shows the rapid uptake in fossil fuel consumption as an energy resource since its first use in 1800. However, harvesting energy from fossil fuels had a deleterious effect. The gases released during fossil fuel energy production retain infrared radiation in the atmosphere. Such gases are known as greenhouse gases. The increased volumes of greenhouse gases released from burning fossil fuels enable the retention of infrared radiation, causing global temperatures to rise. Figure 1.2 shows the increase in global temperature since 1965, corresponding to the increased energy consumption of fossil fuels from 1965 onwards, as demonstrated in Figure 1.1. Changing the global temperature has dire consequences for both the planet and its inhabitants. With raised global temperature comes the increased frequency of droughts, wildfires, tropical cyclones, heavy precipitation, and sea levels rising, which has resulted in damage to ecosystems, settlements, infrastructure, loss of life and even species extinctions [1]. For humanity and all other ecosystems on the planet to survive, the increase in global temperature must be abated now. This requires the global absolute temperature to not exceed a 1.5 °C increase above average pre-industrial temperatures [1].

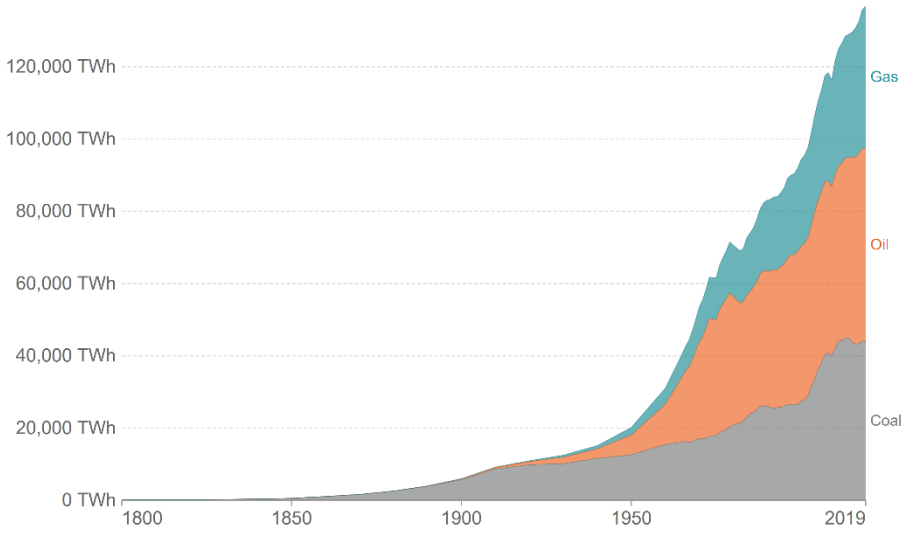

Figure 1.1 Global energy consumption of fossil fuels since 1800, using data from V. Smil [2]*, and BP* [3]*, graph produced by Our World in Data* [4]*.*

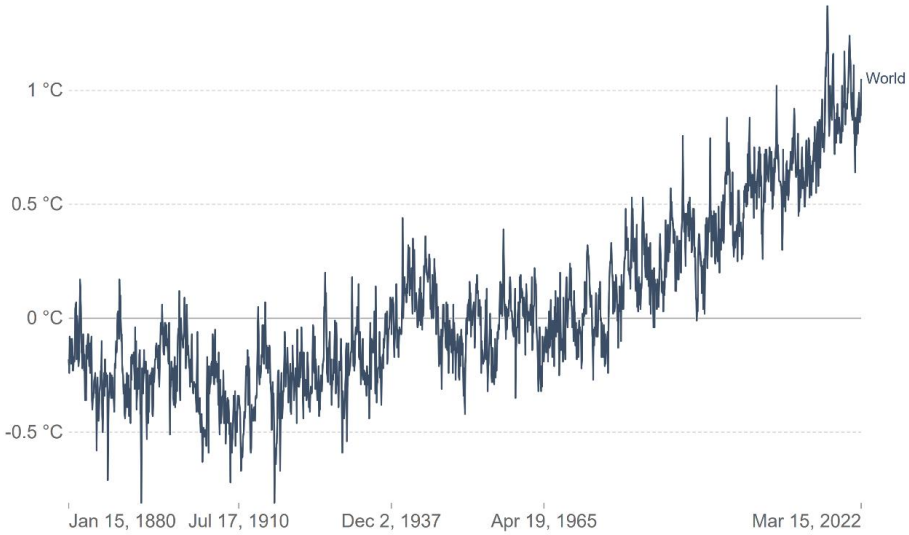

Figure 1.2 Monthly global temperature deviation from the mean temperature of 1951-1980, using data from the GISTEMP Team [5] *graph produced by Our World in Data* [6]*.*

To reduce fossil fuel consumption, the energy market must transition towards energy sources that produce little to no greenhouse gases during energy generation. Such energy production methods are known as renewable energy sources, where electricity is extracted from sources such as wind, solar, hydropower, or geothermal power. To become economically viable in replacing fossil fuels, renewable energy sources must achieve grid parity, which is defined as energy generation with an equal or lower levelized cost of electricity (LCOE) than current electricity sources. Figure 1.3 presents the LCOE for utility-scale renewable energy sources between 2010 and 2020 against the cost range of fossil

fuels [7]. All renewable technologies in 2020 in Figure 1.3 are equal to or cheaper than fossil fuels. Therefore, transitioning to renewable energy sources can be financially competitive while preventing global temperatures from rising further.

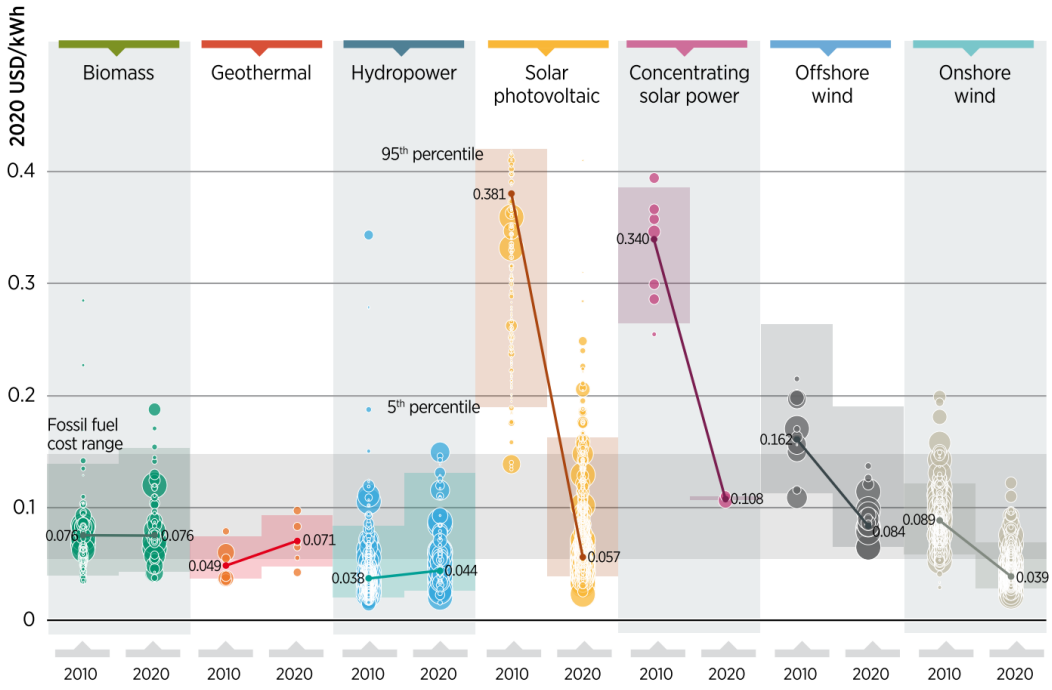

Figure 1.3 Levelized Cost of Electricity (LCOE) of renewable energy sources between 2010 and 2020 against fossil fuels. The fossil fuel cost range is shown by the horizontal grey band that spans across the seven renewable energy source graphs. Graph produced by IRENA [7].

1.2 Solar Power and Silicon Photovoltaics

Out of all renewables, solar photovoltaics (solar-PV) has made the most aggressive transition to becoming a feasible energy source that can replace fossil fuels. LCOE for solar-PV reduced by 0.324 USD/kWh in 10 years, from 0.381 USD/kWh to 0.057 USD/kWh, a reduction of 85% [7]. The second largest reduction outside of solar-PV came from wind of 0.078 USD/kWh, from 0.162 USD/kWh to 0.084 USD/kWh (a 48% reduction), and in the case of geothermal, and hydropower LCOE increased [7]. The sharp decrease in LCOE for solar-PV was caused by a virtuous cycle. The first event of the cycle was the use of solar panels to power the Vanguard I satellite in 1958 [8]. Solar panels continued to find their use for space-based applications and thus the demand for solar panels increased. The continued and increased demand for solar cells allowed manufacturers to refine production techniques, therefore allowing solar panel prices to decrease from the expensive panels

originally used for the Vanguard I. At lower prices, solar-PV became competitive in new markets. To meet market demand, solar-PV underwent price reductions and thus continued the cycle once again. Figure 1.4 presents the relationship between price reduction and increased production, where the trend line is known as the learning curve. The learning curve for solar-PV shows that as installations increased exponentially, solar module prices decreased exponentially. Between 1976 and 2021, when total installed capacity doubled, solar module prices dropped 24.1% [9], known as the 'learning rate'. However, the modern-day learning rate is even higher. Considering the start of mass production of solar-PV in 2006, the learning rate was 39.5% in 2021 [9]. This strong learning curve has led to solar-PV becoming a significant component of the energy transition [7], [10]. Figure 1.5 presents the energy mix required to deliver less than 1.5 °C global warming by 2050, where Solar-PV is predicted to provide approximately a third of energy generation with 14 TW of installed capacity, almost half of all renewable energy capacity in 2050 [7]. However, the International Technology Roadmap for solar-PV (ITRPV) has consistently predicted since 2018 this may become as large as 60 TW [9], [11]–[13].

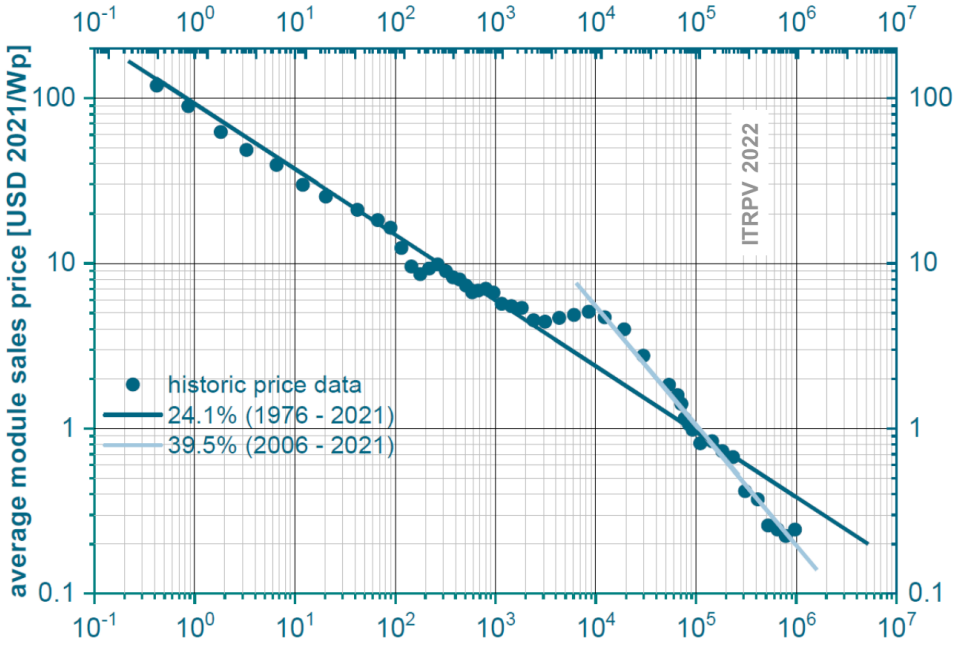

Figure 1.4 PV learning curve of average module price against the number of installations, graph produced by ITRPV [9]*. Average learning rates of 24.1% are presented for 1976 – 2021, and 39.5% for 2006 – 2021.*

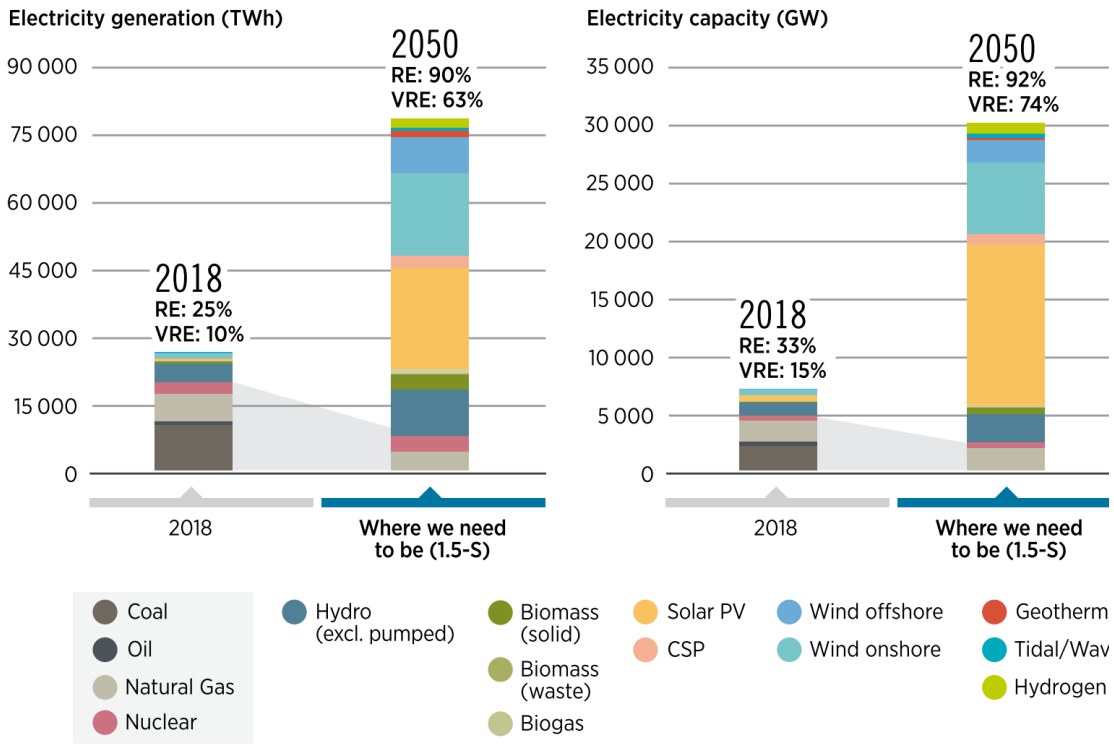

Figure 1.5 The composition and evolution of the energy market from 2018 to achieve no more than 1.5 °C global warming by 2050, demonstrating solar-PV will be a significant portion of the market to prevent irreversible global warming. RE stands for renewable energy, and VRE stands for variable renewable energy sources such as wind and solar. Graph produced by IRENA [7].

Solar-PV provides additional benefits beyond clean energy production. Firstly, solar-PV employs the most people out of any renewable energy source, with almost 4 million jobs in 2018 [10], [14] and another 15.1 million by 2050 [10]. Secondly, not only is solar-PV socio-economically supportive but it also bolsters ecosystems. The shading from solar panels has been shown to support declining pollinator species by extending local flowering seasons [15]. Finally, solar-PV, and renewables in general, increase the quality of health and reduce loss of life by minimising air pollution [16]–[18].

While solar-PV provides many benefits, there are also drawbacks. To achieve the installation goal of 2050, the electricity requirement for PV manufacture is of the order of 360 – 380 kWh/kg, resulting in 16.4 – 58.8 Gt of CO_2 emissions by 2050 [19]. This is one of the greatest environmental impacts from the production of any renewable energy source. However, it is still considerably less than using non-renewable sources. For large-scale production, it was estimated that solar-PV generated approximately 19 times fewer emissions with global warming potential than fossil fuels [20]. Considering the 2050 target

of 60 TW of solar-PV installed, the production of solar-PV, instead of fossil fuel energy sources, would save 15 – 17% of the global carbon budget for 2050, equivalent to 71 – 89 Gt CO_2 [21]. In addition, solar-PV emission production can be reduced further as the PV production emission intensity varies on the energy source used by the country it was manufactured in. Total emissions to produce the dominant Si solar cell technology on the solar-PV market, using coal as the predominant energy source, such as is commonly practised in China, is 360 – 680 kg CO_2/Si wafer [21]. Countries that have established hydropower as a significant energy source have demonstrated emission intensity can be reduced to levels of the order of 246 – 304 kg CO_2/Si wafer [21]. Furthermore, environmental impact can be additionally minimised by methods such as using more efficient solar cells, using less Si per cell, reducing the Si lost during wafer cutting, and using non-traditional Si-purification methods that emit less CO_2 [19]. While the emission of greenhouse gases during solar-PV production is undesirable, it is a dramatic reduction in comparison to the emissions produced from fossil fuel sources and has the potential to be reduced further.

The secondary concern regarding TW production of solar PV is the disposal of panels at the end of their life. By 2050, cumulative solar PV panel waste is predicted to reach 60 - 78 million tons [22], where the lack of well-defined regulations around solar PV disposal and the current costly recycling processes result in the majority of solar-PV being disposed of via landfill [23]–[26]. Landfilled solar-PV has been shown to be damaging to water, soil, and air as toxic substances leach into the surrounding environment as well as the atmosphere [23], [27]. To prevent solar-PV from causing environmental damage after use, further research must be performed so that informed regulations can be made regarding safe panel disposal. M. Lunardi et al. [28] noted that the majority of published research on recycling solar-PV focussed on laboratory-scale techniques, which resulted in high-energy, costly recycling processes. But when studies considered recycling at the industrial scale, lower energy consumption was achieved, causing a smaller environmental impact and at cheaper cost. While research has previously been limited on the recycling of solar-PV, the

rapid scaling of solar-PV to TW production has prompted an increase in research so that contributions to global warming are minimised or avoided whilst meeting the 2050 solar-PV deployment targets [21], [23], [24], [28], [29].

For solar-PV to continue following the learning curve and maintain its competitive status as an energy source, the cost per watt must continue to decrease. This can be achieved by two methods. Firstly, manufacturing costs can continue to reduce, making each cell cheaper for the same power output. Secondly, cell efficiency can be increased, elevating power output for the same manufacturing cost [9]. Thus, continuing research into solar-PV is vital to aid in the fight against climate change.

1.3 Silicon Solar Cells

Solar-PV is dominated by crystalline silicon (c-Si) solar cells, accounting for 95% of the solar-PV market. Within the c-Si market share, the passivated emitter and rear cell (PERC) has a market majority with an ~85% share [9], [30]. The operating principles and efficiency losses in PERCs are discussed next.

1.3.1 Operating Principles

Solar cells generate electricity by the Photovoltaic effect, where photons from incident sunlight are converted into electricity. Semiconductors are uniquely placed to convert photons of sunlight into electricity due to their electronic structure; valence and conduction bands are separated in energy with a band gap in between, caused by energy states that electrons cannot occupy. In the case of Si, this bandgap can be traversed by carriers when photons of energy >1.12 eV are absorbed into the bulk. An absorbed photon causes an electron to be promoted from the valance band to the conduction band, also generating a hole in the valence band. This mobile electron-hole pair can then be extracted into an external circuit to generate electrical energy.

Si is well placed for electron-hole generation from sunlight. Figure 1.6 showcases solar radiation on the Earth's surface as a function of photon wavelength, known as the AM1.5G spectrum. All photons with wavelengths less than 1100 nm (equivalent to 1.12 eV) can

induce electron-hole generation in Si, which is most of the solar spectrum that reaches the Earth's surface. Thus, Si is an ideal material to fabricate solar cells from.

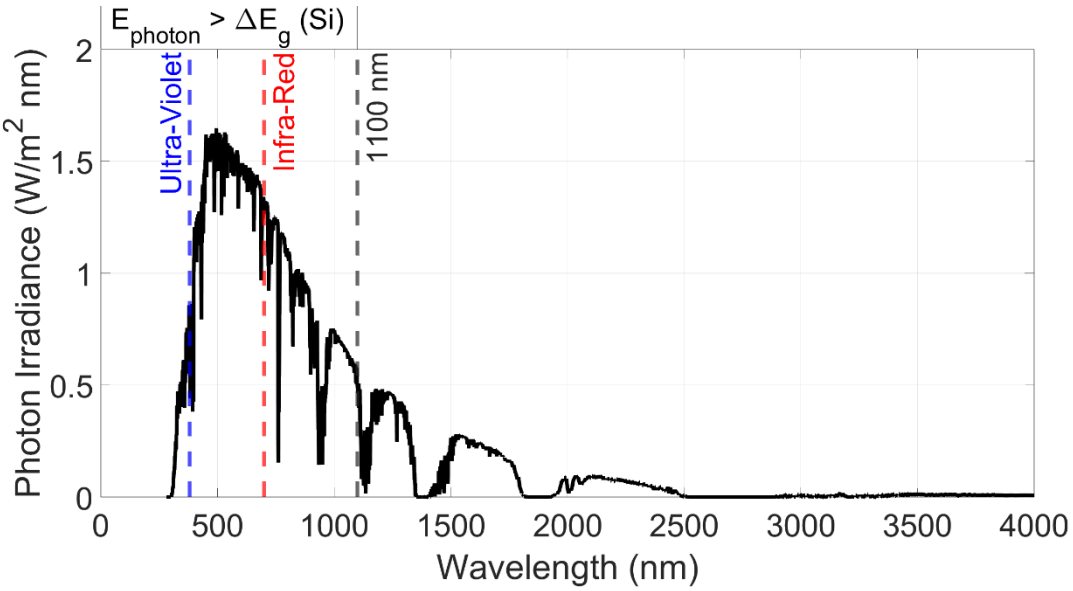

Figure 1.6 Global spectrum of photon irradiance on the Earth's surface as a function of photon wavelength, using data from C. Honsberg et al. [17]. Troughs in the spectrum are attributed to the absorption of species in Earth's atmosphere such as O_3, H_2O, O_2, and C.

To extract the generated carriers into an external electrical circuit they must remain separated. In a PERC this is achieved by a p-n junction. Figure 1.7 presents the architecture of a PERC. The cell base consists of p-type Si, and an n-type emitter layer is formed on top, where minority carriers are electrons in the base, and holes in the emitter. The p-n junction causes the valence and conduction bands to bend, inducing a local electric field that sweeps minority carriers across the junction to the opposite side. Once across the junction, minority carriers become majority carriers and any loss of charge is reduced in each layer because of the limiting number of minority carriers available. Mobile carriers are then extracted by their respective contacts.

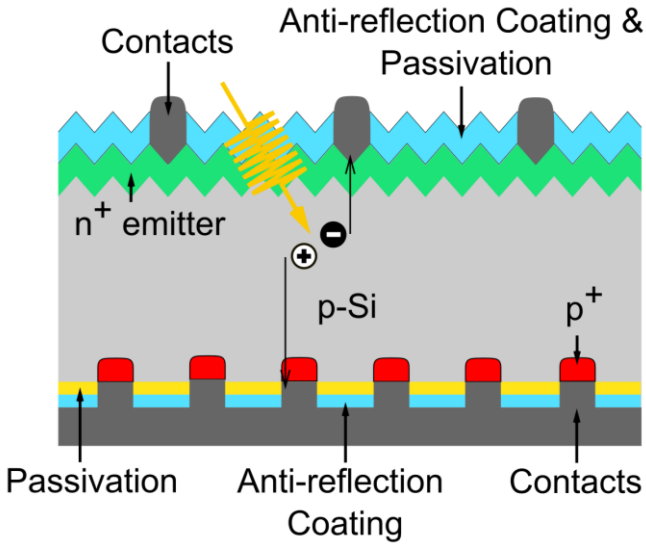

Figure 1.7 Schematic of PERC architecture. Electricity generation is depicted by a photon in yellow entering the cell, generating an electron-hole pair (the electron is black with a '-' sign and the hole white with a '+' sign), and separation of the pair for harvest at their respective contacts. Different cell components are coloured differently to distinguish them from one another: the contacts are dark grey, the anti-reflection coating (ARC) blue, the front-side n^+ emitter green, the p-type Si base grey, the rear-side passivation yellow, and the rear-side p^+ doping next to the contacts is red.

Several metrics are used to measure the quality of solar cells. Carrier recombination current (J_0) measures the flow of carriers recombining per unit area. Short circuit current density (J_{sc}) is the maximum current density, and thus the maximum number of carriers that can be generated from the solar cell. It is predominately affected by optical properties. Open circuit voltage (V_{oc}) is the maximum voltage that can be drawn from the cell and is dependent on J_0, thus is a measure of carrier recombination and material quality. Efficiency (η) is the ratio of a cell's output power to the input power from the sun and is dependent on J_{sc}, V_{oc}, and fill factor (FF). FF is the ratio of the power drawn from the solar cell to the maximum possible power the cell can generate. Equation (1.1) describes FF, where P_{mp} is the maximum power from the cell, V_{mp} and I_{mp} are the voltage and current respectively at the maximum power point, V_{oc} is open circuit voltage, and I_{sc} is the short circuit current.

$$FF = \frac{P_{MP}}{V_{OC} \times I_{SC}} = \frac{V_{MP} \times I_{MP}}{V_{OC} \times I_{SC}} \qquad (1.1)$$

Fill factor (FF) is comprised of pseudo-fill factor (pFF), series resistance (R_s), and shunt resistance (R_{shunt}). R_s describes the losses in FF caused by the resistance carriers experience when traversing the intended route through the solar cell for extraction into the

external circuit, such as the resistance encountered at the metallic contacts. R_s is aimed to be minimised, ideally zero, to maximise FF and thus cell efficiency. R_{shunt} describes losses due to low resistance paths that carriers were not intended to take by the design of the solar cell, and therefore do not get extracted into the external circuit. Thus, R_{shunt} is aimed to be maximised, ideally infinity, to limit carriers to paths that result in extraction from the solar cell. R_{shunt} is typically very large in industrial cells, thus FF is typically considered to comprise of R_s and pFF. pFF is FF without the effect of resistive losses (R_s and R_{shunt}) and therefore represents the upper limit of FF for a solar cell. This limit is governed by recombination, as pFF has been empirically shown to depend upon V_{oc}, which in turn is dependent on the recombination current (I_0) [31]. Figure 1.8 shows a typical IV curve, where the values used to calculate FF in equation (1.1) are marked, as well as the effect of R_s and R_{shunt} losses on the IV curve.

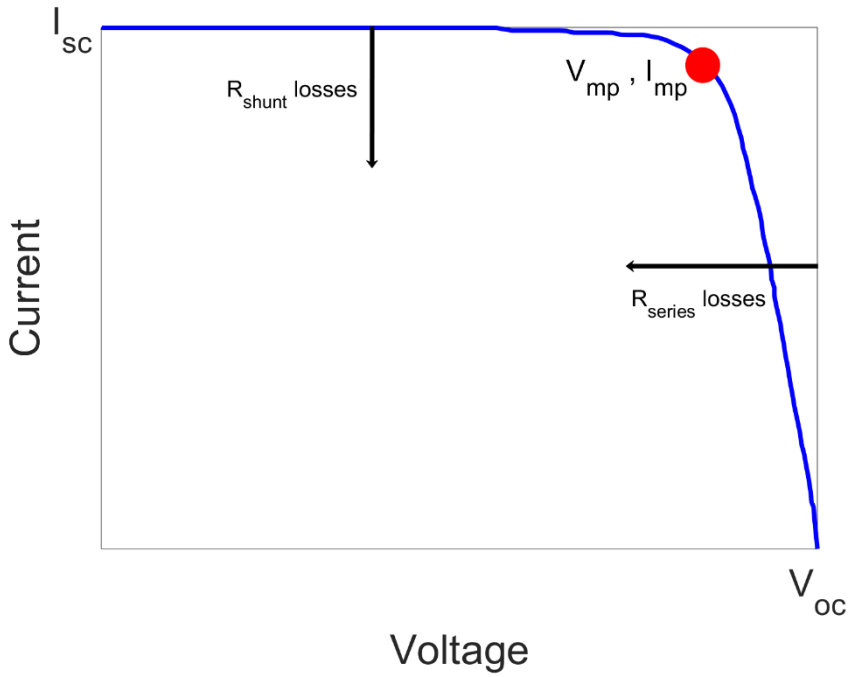

Figure 1.8 An IV curve for a solar cell, demonstrating the point that is used in FF calculations as well as how losses due to shunt and series resistance effect the IV curve. Data obtained from pv-education.org [32].

Table 1.1 shows a summary of typical parameters for a 180 µm thick, p-type, monocrystalline-Si (mono-Si) PERC manufactured by Longi [33].

Table 1.1 Solar cell parameters of a typical PERC manufactured by Longi [33].

J_{sc} (mA/cm^2)	V_{oc} (mV)	η (%)	FF (%)
40.28	687	22.50	80.89

1.3.2 Efficiency Losses

1.3.2.1 Reflection

Before light can enter the bulk of a material, it must first interact with the sharp discontinuity of the surface interface. The light interaction at an interface has the same nature as within the material bulk, where light is scattered in all directions upon interacting with the media. For the example of a uniform medium in a vacuum, there are only molecules on one side of the interface. This lack of molecules prevents the backwardly scattered wave produced at the medium surface from being destroyed by destructive interference [34]. This backwardly scattered, uncancelled wave is known as reflection. When the medium is not in a vacuum, some cancellation of the backwardly scattered wave can occur, but it is incomplete due to the change in the molecular arrangement between the two sides of the interface. The uniformity of reflected light is dependent on the shape of the interface. For flat interfaces, the reflected waves propergate in one direction, known as specular reflection. However, if the surface is rough then the waves will be reflected in many directions, causing diffuse reflection. Figure 1.9 depicts specular and diffuse reflectance.

a)

b)

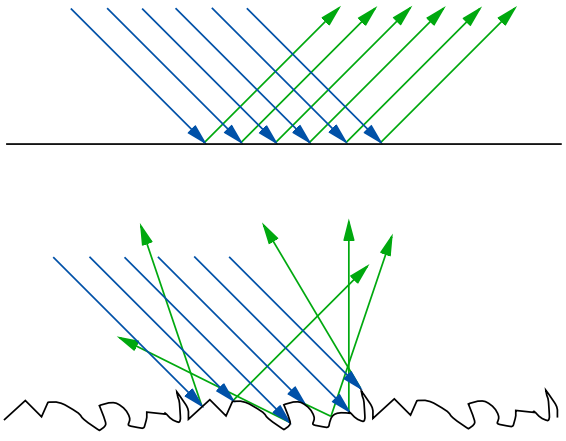

Figure 1.9 a) specular reflection b) diffuse reflection.

Figure 1.10 shows the reflection of a flat Si surface as a function of incident light wavelength. Two distinct peaks are present, one at 280 nm (4.5 eV) and another at 360 nm (3.4 eV), known as E_1 and E_2 respectively [31]. A typical explanation for peaks in reflectance

spectra would be low absorption. A common example of this phenomenon is plants having a low absorption of green light, thus resulting in a high reflectance at such wavelengths and therefore appearing green. However, Si is strongly absorbing short wavelengths. Figure 1.11 demonstrates the absorption coefficient of Si is greater than 10^6 cm^{-1} for wavelengths less than 350 nm, thereafter the absorption coefficient continually decreases with increasing wavelength [31]. The large absorption coefficient at shorter wavelengths is caused by the photons possessing sufficient energy to facilitate both direct and indirect transitions between the bands, as opposed to only the indirect transitions at longer wavelengths. The transition rate between bands for direct absorption is much larger than indirect transitions [35], resulting in high absorption at short wavelengths. The origin of the E_1 and E_2 peaks appearing in both the reflectance and absorption spectra is caused by critical points in energy-momentum (E-k) space [31]. A critical point is defined as a point in E-k space where the gradient of the valence and conduction band is the same [31]. When the two bands have the same gradient, and are approximately parallel to one another, it allows carriers to undergo direct transitions at a single photon energy but for multiple k values. Thus, the number of transitions between the energy bands at critical points increases, in turn increasing absorption at such points [35]. In Si, there is a large number of critical points where the transition between the bands is 3.4 eV and 4.5 eV, the energy of peak E_1 and E_2 peak respectively [31]. Whilst this explains the peaks in the absorption spectra it is perhaps counterintuitive for the peaks that appear at the corresponding energies in the reflectance spectra. As there is an increase in the different types of transitions that can occur at the critical point energies E_1 and E_2, the density of states is also very large [31]. As such, the number of carriers at that energy per unit volume becomes so great that all optical processes increase in magnitude, both absorption and reflectance, thus the peaks E_1 and E_2 appear in both the reflectance and absorption spectra.

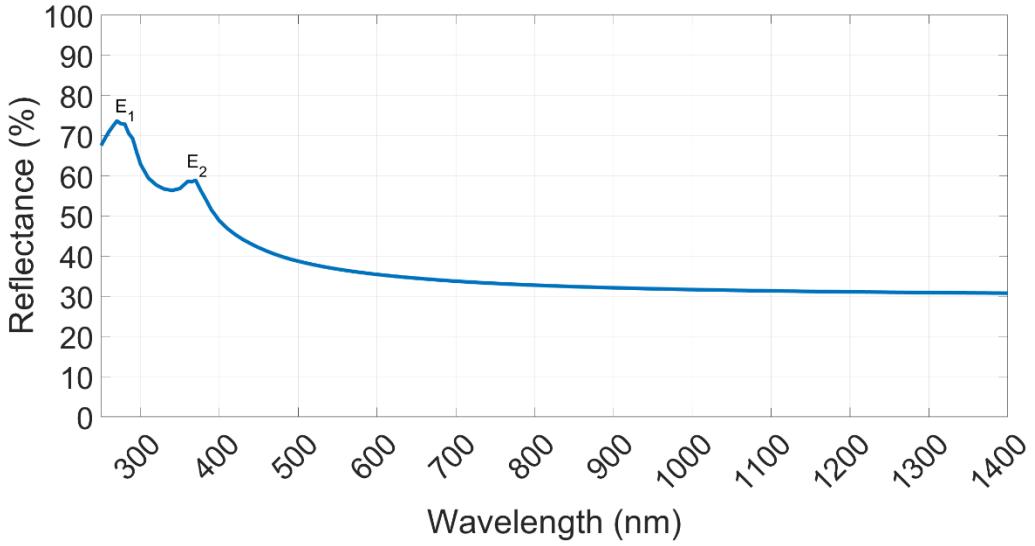

Figure 1.10 Reflectance spectrum of planar Si as a function of incident photon wavelength, using data from OPAL 2 [36].

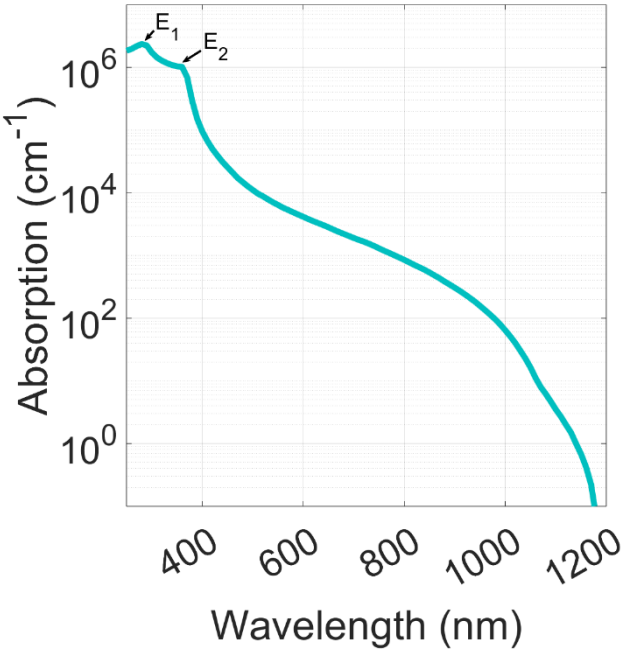

Figure 1.11 Absorption of Si as a function of incident photon wavelength. The peaks E_1 and E_2 are marked at 280 nm (3.4 eV) and 350 nm (4.5 eV) respectively. Data sourced from M Green [31].

The weighted average reflectance (WAR) of a planar Si surface between 280 nm – 1100 nm, using the photon irradiance of the AM1.5G spectrum, is 37%. Therefore, a bare Si surface immediately loses 37% of incident photons for carrier generation due to front surface reflectance. With regards to a solar cell's performance, increased surface reflectance negatively impacts both the External Quantum Efficiency (EQE) and J_{sc}. EQE is the ratio of the number of photons that contribute to carrier generation against the total

number of incident photons. As reflectance increases, the number of photons contributing to carrier generation decreases, lowering EQE. This also impacts J_{sc}, as the number of charge carriers that can be extracted is reduced. In turn, cell efficiency is reduced due to its dependency on J_{sc}.

1.3.2.2 Absorption

Transmitting light into the cell does not guarantee it will contribute to carrier generation. Photon absorption as a function of travelled distance is described by the Lambert-Beer Law:

$$I(x) = I(0)e^{-\alpha x} \quad (1.2)$$

here $I(x)$ is the light intensity at wafer depth x, $I(0)$ is the intensity of the light at the surface of the wafer, α is the absorption coefficient and describes light attenuation in Si as a function of light wavelength. Figure 1.12a) presents light absorption through 200 µm of Si for several different wavelengths of light. Current industrial wafer thickness is 160 – 170 µm [9], thus wavelengths up to 900 nm have the potential to be completely totally absorbed within the thickness of the cell for carrier generation. However, absorption at longer wavelengths dramatically reduces, as the photon energy is only sufficient to facilitate indirect transitions of the bandgap, thus resulting in a decrease in absorption coefficient as shown in Figure 1.11. Less than 10% of light at 1100 nm can absorb into a Si wafer, meaning even if all incident light was transmitted into the cell, not all of it would be absorbed in the cell for carrier generation. Furthermore, cell thickness is predicted to decrease further in the next 10 years to 145 – 125 µm [9], thus total absorption, and therefore total carrier generation, would reduce further.

Another important factor for photon absorption is location. Carriers generated more than one diffusion length away from the p-n junction cannot be harvested to the contacts. Figure 1.12b) shows that photons at shorter wavelengths can be absorbed at depths where the subsequently generated carriers would have a high probability of being collected at contacts. Figure 1.12b) also shows that very few photons at longer wavelengths can be absorbed at

depths for successful carrier collection. Thus, even if light is absorbed into the cell, it may not necessarily contribute to carriers that can be extracted from the cell.

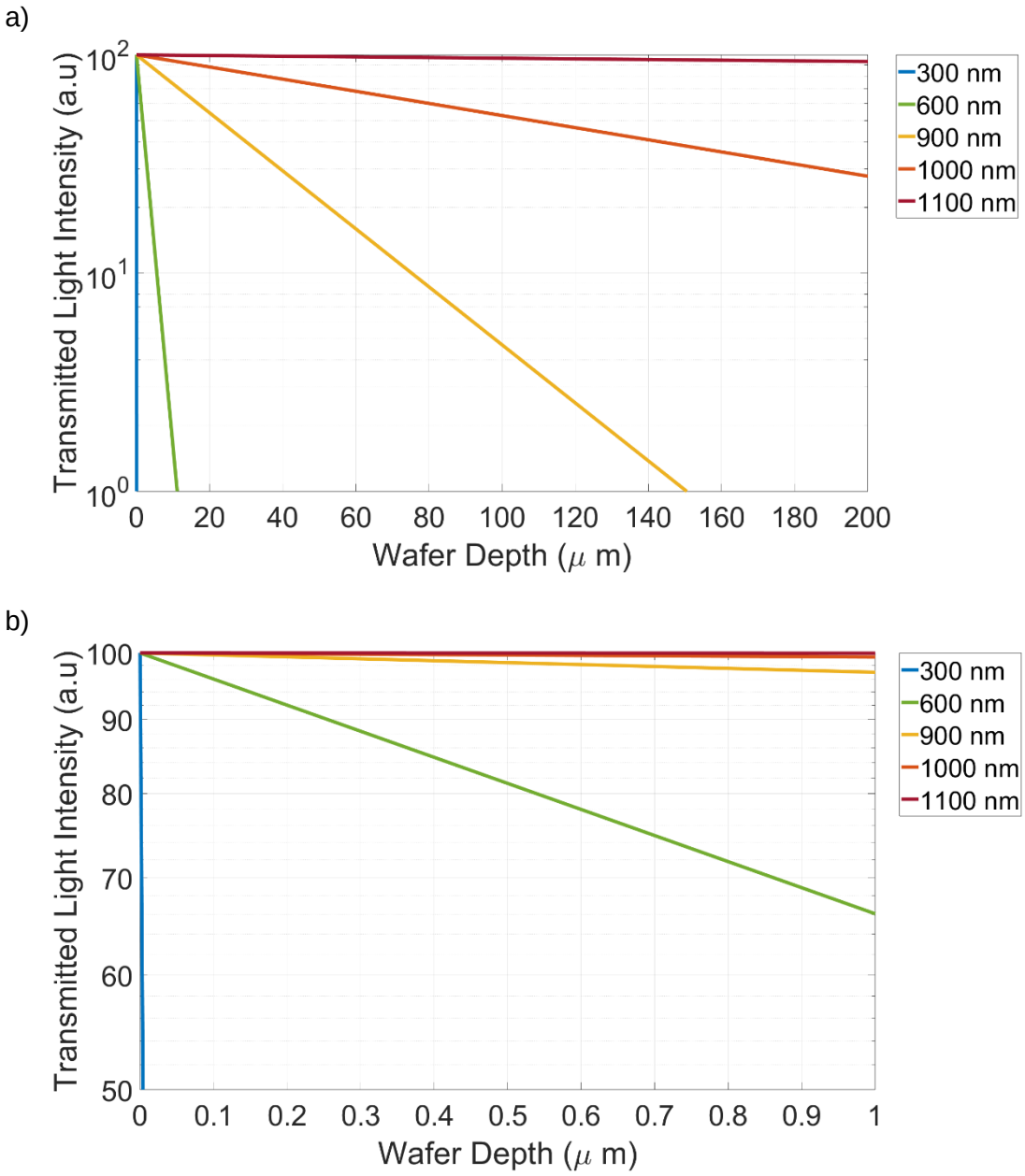

Figure 1.12 Light absorption in Si for different wavelengths as a function of Si thickness a) in 200 µm b) in 1 µm. All x-axes are linear, and all y-axes are logarithmic. Data sourced from M. Green [31].

The variation in photon absorption as a function of wavelength affects a solar cell's EQE and J_{sc} performance. At long wavelengths, EQE is reduced, as absorption within the cell thickness is less probable and fewer carriers are generated. J_{sc} and cell efficiency are also reduced by the reduction in carrier generation. Figure 1.13 presents a typical EQE curve suffering from non-optimised optics. Increased surface reflectance causes EQE losses across the whole wavelength spectrum. Reduced absorption of photons at long

wavelengths causes a corresponding drop in EQE. Lastly, the reduction in EQE at short wavelengths is caused by carrier recombination at the front surface.

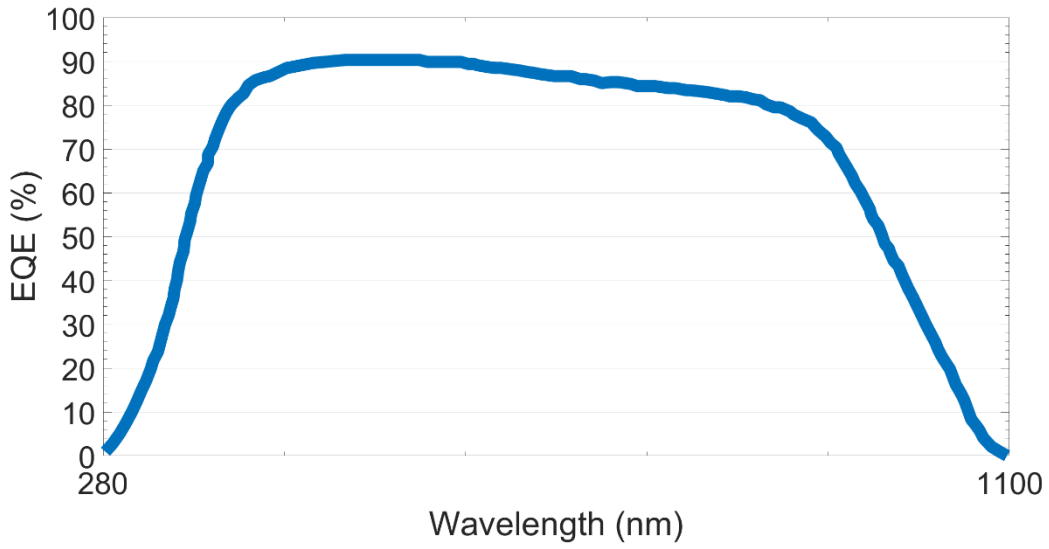

Figure 1.13 EQE of a solar cell suffering from non-optimal optical properties.

1.3.2.3 Recombination

Recombination is the process in which an electron transitions from the conduction band to the valence band, occupying a hole in the valence band, and annihilating both mobile carriers. If carriers do not remain separated, they will attempt to reduce their energy state by recombining. The average time taken for a minority carrier to recombine is termed the minority carrier lifetime, τ. The total minority carrier lifetime can be split into components from the surface and bulk:

$$\frac{1}{\tau_{eff}} = \frac{1}{\tau_{surface}} + \frac{1}{\tau_{bulk}} \qquad (1.3)$$

where $\tau_{surface}$ and τ_{bulk} are the minority carrier lifetimes for the surface and bulk respectively. Within the bulk, three recombination mechanisms affect carrier lifetime: radiative, Shockley-Read-Hall (SRH), and Auger. The effects of the three mechanisms' on τ_{bulk} are additive, leading to a sum of the inverse lifetime components:

$$\frac{1}{\tau_{bulk}} = \frac{1}{\tau_{radiative}} + \frac{1}{\tau_{SHR}} + \frac{1}{\tau_{auger}} \qquad (1.4)$$

The three mechanisms are presented in Figure 1.14.

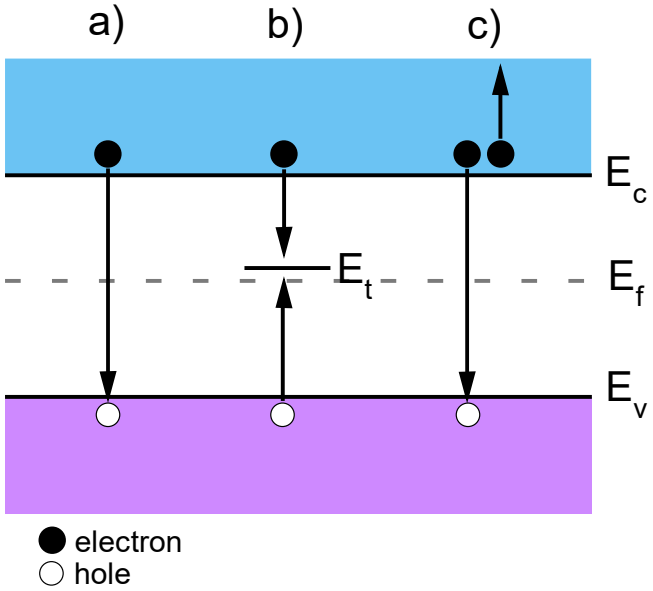

Figure 1.14 The three recombination mechanisms present in bulk semiconductors a) radiative b) SRH c) Auger.

Radiative recombination is the direct transition of an electron from the conduction band into the valence band, releasing the excess energy as a photon. Mathematically it is described as [37]:

$$\tau_{radiative} = \frac{1}{B\,\Delta n\,[n_0 + p_0 + \Delta n]} \qquad (1.5)$$

where B is the probability of recombination, n_0 and p_0 are the electron and hole carrier concentrations in Si respectively, Δn is the excess carrier concentration generated by incident photons, where total carrier number, n, is defined as:

$$n = \Delta n + n_0 \qquad (1.6)$$

In the case of Si, B = 10^{-15} cm^3s^{-1} [31], [38], which is low compared to other semiconductors, such as GaAs where B is 10^{-8} to10^{-10} cm^3s^{-1} [38]. This is caused by the indirect bandgap of Si, where a phonon is needed to mediate the transition between bands. Therefore, radiative recombination in Si is typically negligible.

In Auger recombination, three carriers are involved. The excess energy released from two carriers recombining is passed to another carrier instead of being released as a photon. This third carrier is pushed to a higher energy state within its energy band and relaxes in

energy over time via phonon emission [31], [39]. This process applies to both holes and electrons thus net Auger recombination (R_{auger}) is dependent on the sum of n^2p and p^2n:

$$R_{auger} = C_p(p^2n - pn_i{}^2) + C_n(n^2p - nn_i{}^2) \quad (1.7)$$

here C_p and C_n are the Auger coefficients for hole-hole-electron and electron-electron-hole processes, and n_i is the intrinsic carrier concentration at thermal equilibrium. Depending on if the material is n or p-type, one of the two terms in R_{auger} will dominate. In p-type, the first term becomes the most influential, while in n-type the second term dominates [31], [39]. Finally, as Auger recombination requires three carriers it only dominates net recombination at high doping levels [31], [39].

Opposed to the intrinsic processes of radiative and Auger recombination, SRH recombination occurs by defects such as impurities, vacancies, and crystallographic defects, creating energy levels within the bandgap. Electrons from the conduction band and holes from the valence band can relax into such defect levels, annihilating one another. Carrier lifetime due to SRH recombination can be statistically described [40], [41] using:

$$\tau_{SRH} = \frac{\tau_{n0}(p_0 + p_1 + \Delta n) + \tau_{p0}(n_0 + n_1 + \Delta n)}{p_0 + p_1 + \Delta n} \quad (1.8)$$

$$p_1 = N_v exp\left[\frac{-(E_D - E_V)}{kT}\right] \quad (1.9)$$

$$n_1 = N_c exp\left[\frac{-(E_C - E_D)}{kT}\right] \quad (1.10)$$

$$\tau_{n0} = \frac{1}{N_t \sigma_n v_{th}} \quad (1.11)$$

$$\tau_{p0} = \frac{1}{N_t \sigma_p v_{th}} \quad (1.12)$$

here τ_{n0} and τ_{p0} are capture time constants for electrons and holes respectively, p_1 and n_1 are hole and electron carrier trap densities respectively, N_v and N_c are the effective density

of states for the valence and conduction bands respectively, E_V, E_c and E_D are the energy of the valence band, conduction band and defect level respectively, k the Boltzmann constant, T temperature, N_t impurity concentration, σ_n and σ_p the capture cross section for electrons and holes respectively, and v_{th} the thermal carrier velocity. From the above equations, the amount of SRH recombination depends upon defect concentration, the probability a majority carrier occupies a defect state, and the probability a minority carrier can transition to the defect state occupied by the majority carrier. The efficacy of SRH recombination in the bulk of Si is affected by impurity type and concentration, dislocation density, grain boundary type and density, and the decoration of dislocations or grain boundaries with impurities [31], [42]–[46].

The surface of Si represents a large SRH defect where many energy states are generated in the bandgap due to the unsatisfied lattice bonds [31]. A unique parameter is given to categorise the effectiveness of SRH recombination at the surface, termed surface recombination velocity (SRV):

$$S_0 = \frac{R_{surface}}{\Delta p} \qquad (1.13)$$

where S_0 is SRV in cm/s, $R_{surface}$ is surface recombination rate in cm^2/s. It is desirable to minimise S_0, indicating few carriers recombine at the surface.

All recombination processes are deleterious to solar cell performance as they lower V_{oc} and subsequently reduce cell efficiency. V_{oc} is inversely proportional to the dark saturation current I_0, which is a measure of recombination, as shown by the equation for V_{oc}:

$$V_{oc} = \frac{nkT}{q} ln\left(\frac{I_L}{I_0} + 1\right) \qquad (1.14)$$

where n is the ideality factor and is a measure of how closely a device follows the ideal diode equation and changes according to which recombination mechanism dominants in the device (typically it is 1), k is the Boltzmann constant, T is temperature, q is the electron

charge, I_L is the illumination current. Thus, when I_0 increases, due to increased recombination, V_{oc} decreases and consequently efficiency is lowered due to its proportionality to V_{oc}.

1.4 Optical Loss Mitigation

1.4.1 Anti-Reflection Coatings

The PERC structure employs several techniques to mitigate the optical losses described in section 1.3.2. One technique to minimise front surface reflectance is an anti-reflection coating (ARC). As described in section 1.3.2.1, incident light can either reflect or transmit at the air/Si surface boundary. Figure 1.15 shows that by applying a coating to the surface, additional interactions occur between the incident light and the front surface. By tailoring the ARC thickness, the two reflected waves in air can be made to be λ/2 out of phase with one another to cause destructive interference and eliminate front surface reflectance.

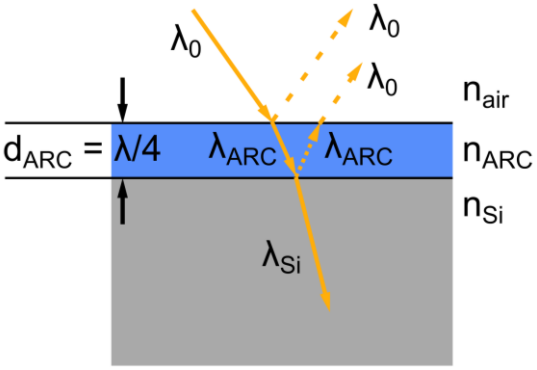

Figure 1.15 Reflectance reduction mechanism using an ARC atop Si, where dARC is λ/4 to enable destructive interference, causing all incident light to be transmitted into Si.

To cause destructive interference, the ARC thickness, d_{ARC}, must be equal to λ/4, as the wave must travel in and out of the ARC:

$$d_{ARC} = \frac{\lambda_{ARC}}{4} \qquad (1.15)$$

Where d_{ARC} is ARC thickness and λ_{ARC} is the wavelength of the light exiting the ARC. However, it is more useful to describe d_{ARC} in terms of the wavelength prior to entering the coating (λ_0):

$$d_{ARC} = \frac{\lambda_0}{4n_{ARC}} \quad (1.16)$$

Where n_{ARC} is the refractive index of the ARC. To determine the value of n_{ARC} for minimal reflectance, the amplitude of the two exiting waves must be equal for destructive interference to occur. Using this constraint and the Fresnel equations for the amplitude of reflectance at normal incidence [47], n_{ARC} can be defined by n_{air} and n_{Si}:

$$\frac{n_{ARC} - n_{air}}{n_{ARC} + n_{air}} = \frac{n_{Si} - n_{ARC}}{n_{Si} + n_{ARC}} \quad (1.17)$$

Simplifying to:

$$n_{ARC} = \sqrt{n_{air} n_{Si}} \quad (1.18)$$

Thus:

$$d_{ARC} = \frac{\lambda_0}{4\sqrt{n_{air} n_{Si}}} \quad (1.19)$$

As is apparent from the above equations, ARCs can only be tuned to minimise reflectance at one wavelength. For solar cells, this is typically localised around 600 nm as this is where photon density is greatest in the AM1.5G spectrum. Taking into consideration that solar cells are encapsulated in glass, n_{air} should be replaced by n_{glass} at 1.4 in equations (1.17) - (1.19), making n_{ARC} = 2.33 and d_{ARC} = 68 nm. SiN_x:H is commonly used for ARCs as the refractive index can be tuned between 1.8 and 3.0 at λ = 633 nm by altering the gas ratios when using plasma-enhanced chemical vapour deposition (PECVD) [48]–[50]. Figure 1.16 shows the reflectance reduction achieved by a SiN_x:H ARC on planar Si versus planar bare-Si, where the WAR reduces from 36.7% to 12.8% with an ARC.

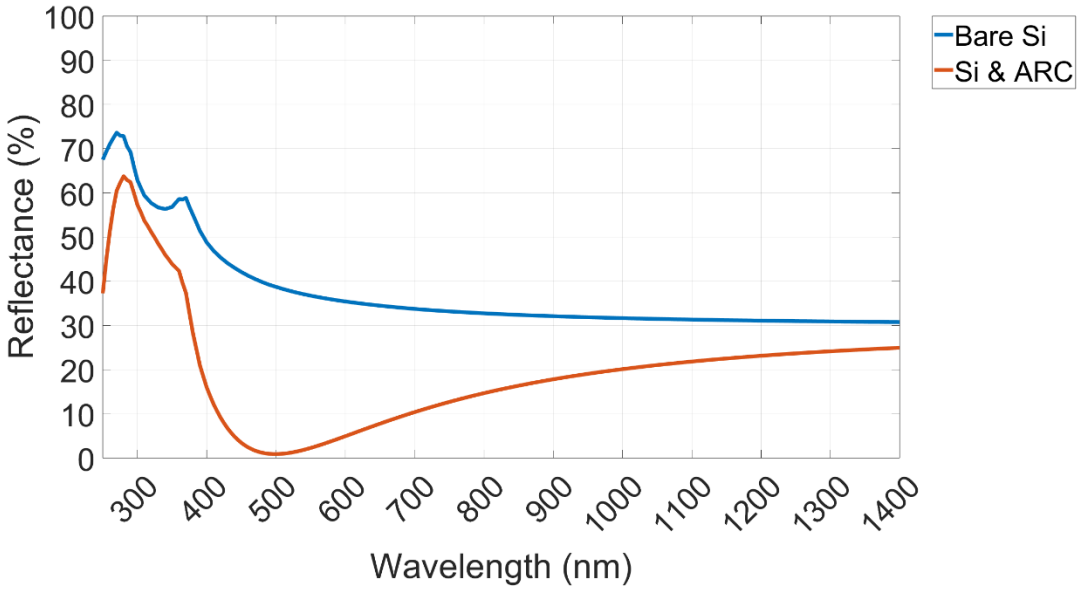

Figure 1.16 Reflection of planar Si with and without an ARC. Data sourced from OPAL 2 [36].

1.4.2 Surface Texture

A second method to reduce front surface reflectance is to roughen the surface, known as texturing. Figure 1.17 shows that texturing can cause the light to interact with Si more than once, increasing the number of transmission events into the Si. Mono-Si PERC employs texturing to great effect, using a texture of microscale random upright pyramids to lower reflectance to 10.6% on bare-Si (without an ARC) [36]. The full mono-Si PERC architecture combines this front surface texture with an ARC, as shown in Figure 1.7, reducing reflectance to < 1% at 600 nm and achieving a WAR of 2.0% between 400 nm – 1100 nm [36]. Figure 1.18 presents the reflection reduction caused by pyramidal texturing and the further reductions achieved when combining texturing with a SiN_x:H ARC.

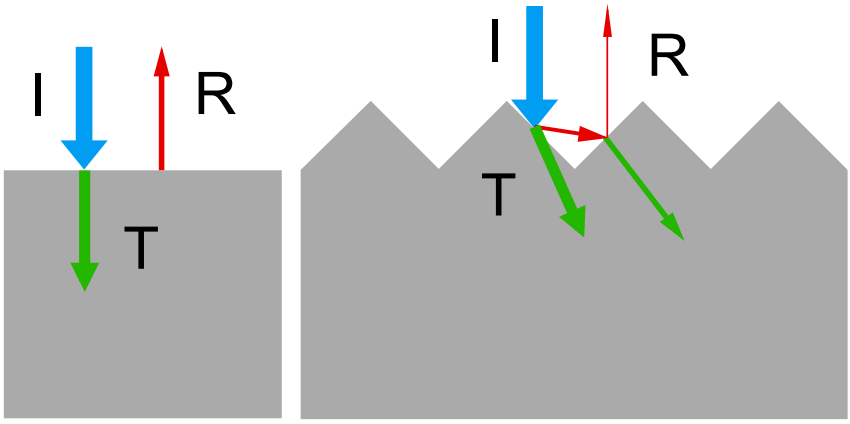

Figure 1.17 Reflection of a planar surface and a v-grooved surface.

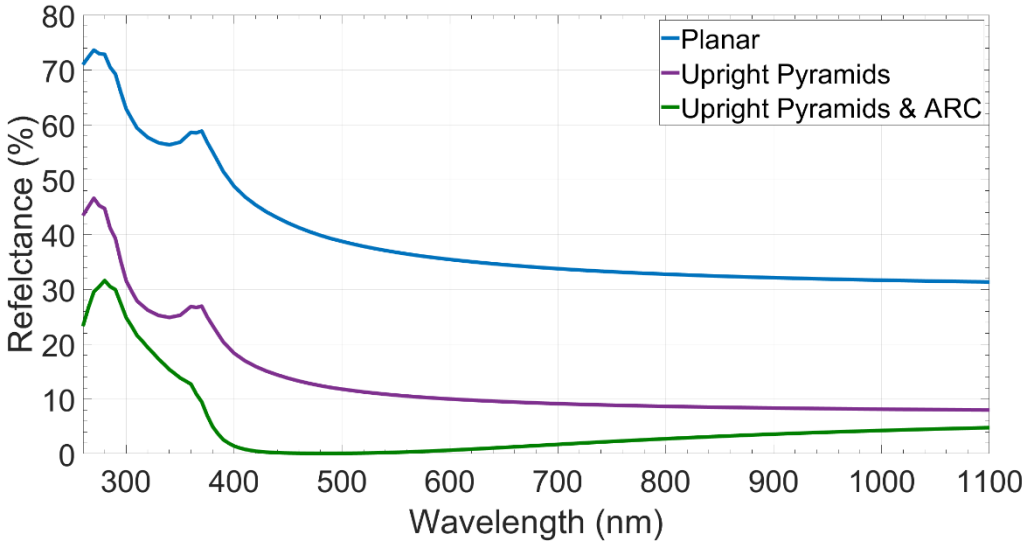

Figure 1.18 Reflectance spectra of planar Si, Si textured with upright pyramids, and Si textured with upright pyramids with a SiN_x:H ARC on top. Data sourced from OPAL 2 [36].

Even with the combination of a pyramidal texture and an ARC, the largest loss to J_{sc} in a PERC still comes from the front surface reflection. Y. Zhang et al. [51] simulated an upright pyramidal front surface texture (texture size of 5 µm) PERC without any optical losses and the resulting J_{sc} was 46.92 mA/cm^2. Yet a typical industrial PERC, with 22.2% cell efficiency, had a measured J_{sc} of 40.31 mA/cm^2 [51]. Analysing the losses to J_{sc} showed the four greatest loss mechanisms were optical, where front surface reflection was the largest source causing a reduction of 2.81 mA/cm^2 to J_{sc}, approximately a factor of three greater than the next loss source [51]. Therefore, even though a front surface texture of microscale pyramids and an ARC provides a substantial improvement to J_{sc} (via front surface reflection reduction), the front surface reflection must be minimised further to achieve the greatest gain to J_{sc}. Y. Zhang et al. [51] suggested alternative ARC schemes as well as different texture morphologies to lower front surface reflectance and increase light trapping (see section 1.4.3) for improved J_{sc}.

Nanoscale textures overcome the limitations of microscale textures, offering broadband reflectance reduction for the entirety of the solar spectrum useful to solar cells. The reflectance reduction mechanism for nanoscale textures uses a texture feature size that is smaller than the wavelength of light but extends for a depth of several hundred nanometres [36], [37]. Such structures are no longer treated as sharp interfaces but instead are

considered as diffuse layers transitioning from the density of air to bulk-Si [36], [37]. Reflection occurs throughout the depth of the texture, as it is no longer a sharp interface, where each reflection has a different phase depending on the depth it was reflected at. When the total texture depth is ≥ $\lambda_0/2$, all phases are present in the reflected waves. Thus, when considering the summation of the reflected waves from the texture layer, destructive interference is facilitated, causing the nett reflectance of the texture layer to fall to zero for $\lambda \leq \lambda_0$ [36], [37].

Figure 1.19 demonstrates the dependency of nanotexture depth on reflectance reduction as a function of the incident wavelength. Figure 1.19a) demonstrates reflectance reduction in a thick texture layer for both short and long light wavelengths. The thickness of the texture layer is great enough that all the different phases are present, thus destructive interference is facilitated between waves within the texture layer. Therefore, for the deeper texture, no reflected waves emerge from the texture layer into the air. Figure 1.19b) illustrates the reflectance reduction of a shallower nanotexture for short and long light wavelengths. At short wavelengths, the texture depth is sufficient that both scattering events that cause destructive interference occur in the texture layer, thus no net reflected wave exits the texture layer into the air. However, for longer wavelengths, the scattering event that would have caused the two waves to be out of phase for destructive interference now occurs within the bulk region of the Si, where no reflected wave is produced. Thus, destructive interference is not caused for the longer wavelength wave for a shallower nanotexture. The longer wavelength reflected wave exits the Si into the air, increasing the reflectance of the Si surface at longer wavelengths. Therefore, maximising the total texture depth of nanotextures is crucial to reducing reflectance.

a)

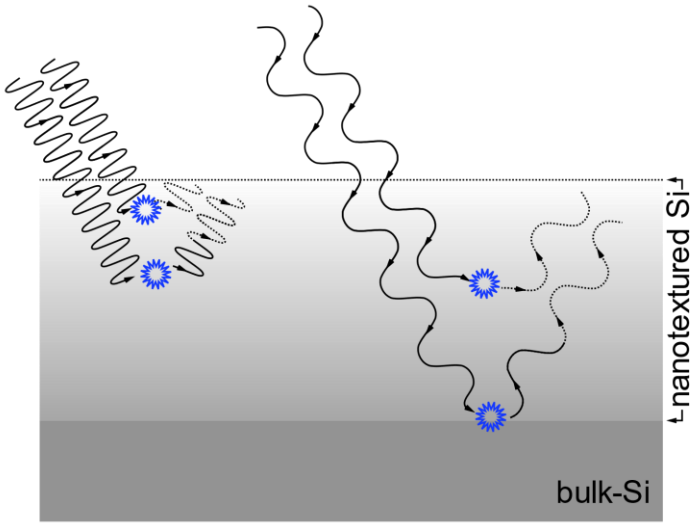

b)

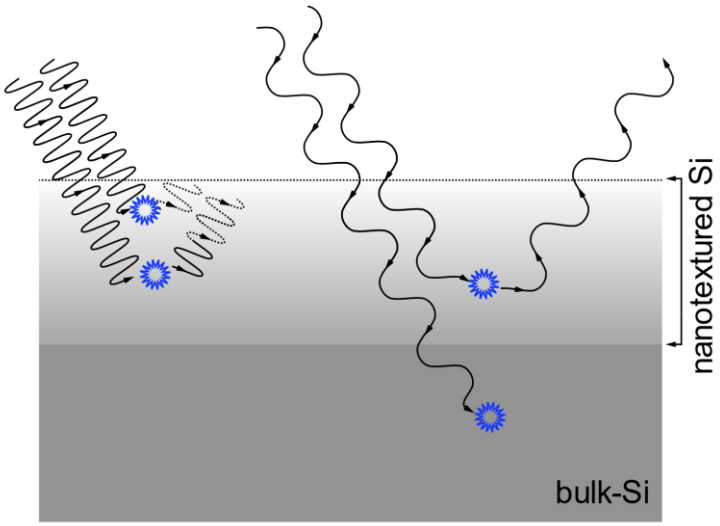

Figure 1.19 Reflection reduction by nanotextures for a) deep textures b) shallow textures. Deep textures can reduce reflectance for a wide range of wavelengths, thus no reflected waves exit the nanotextured Si layer. For shallower textures, reflected waves at longer wavelengths can escape, due to the waves that would have caused destructive interference being absorbed in the bulk-Si. Scattering events are denoted by blue stars. Waves that are λ/2 out of phase and undergo destructive interference are dashed.

Si nanotextures that achieve ultra-low reflectance undergo a colour change from silver to black and thus are termed “black Si” (B-Si). Figure 1.20 shows how bare B-Si suppresses reflectance across the entire range of useful wavelengths for solar cells, against microscale upright pyramids with an ARC which are only optimised for a single wavelength. Due to its broadband reflectance minimisation, B-Si can overcome the limitations of microscale textures and increase J_{sc} and cell efficiency beyond what is currently possible for solar cells such as PERC. Hence, B-Si is an extremely attractive solution for the necessary cell

efficiency improvements to increase the deployment of solar energy and tackle climate change.

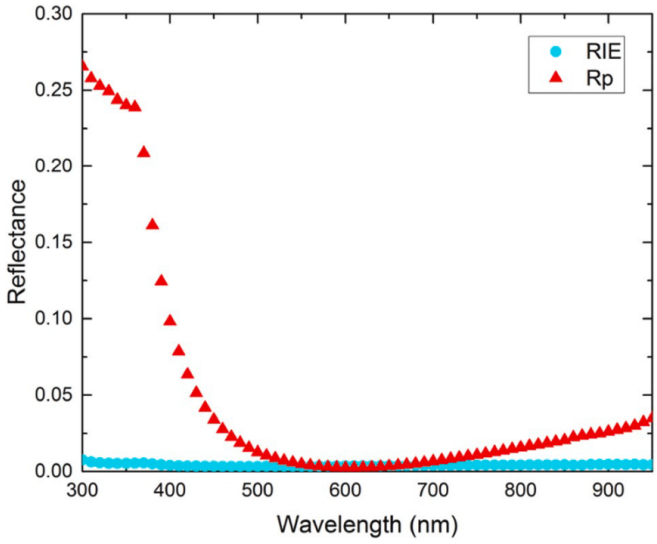

Figure 1.20 An example of nanotextures' superior optical properties over micro-textures. 'Rp' are micro-scale, randomly arrayed upright pyramids, with a SiN_x:H ARC. 'RIE' are nanoscale cones, with no further optical optimisation. Figure reproduced from T.H. Fung et al. [52].

1.4.3 Light Trapping

Section 1.3.2.2 demonstrated that not all incident light transmitted into the cell is absorbed in the cell, nor is it all absorbed in a region of high collection probability. To increase absorption, whilst continuing the trend of wafer thinning (for reduced bulk recombination and lower manufacturing costs [9], [11], [31]), the distance a photon travels through the cell must be increased. This is termed light trapping. Light trapping is caused by total internal reflection. Si is denser than air, thus when a photon interacts with the Si/air interface, from the Si side, the photon only has a limited number of angles from which it can escape the Si, otherwise it is reflected into the Si. These limited angles are defined as the 'exit cone' and on average for Si is 14.5° on either side of the normal. Figure 1.21 presents the trapping effect of the exit cone for light already within the Si.

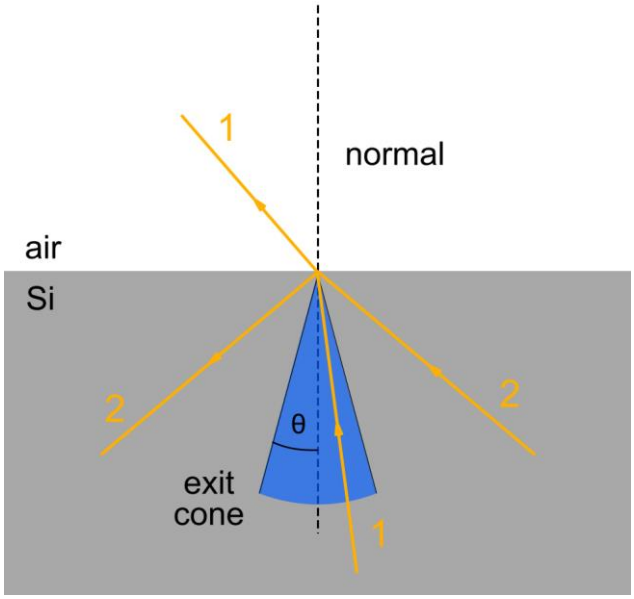

Figure 1.21 The exit cone for Si to air. Light ray 1 can escape Si, as its angle to the normal is within the cone, whilst light ray 2 is reflected into Si as its angle is larger than the cone.

There are two types of light trapping schemes; Lambertian, and geometrical, both are presented in Figure 1.22. Lambertian scattering causes light to be scattered uniformly in every direction, regardless of the incident angle and can increase light path length by approximately a factor of 50 in Si [31], [53]. Geometrical scattering prioritises keeping the more intense incident light close to the normal, away from the exit cone, over the less intense light at oblique angles [31], [53]. Geometrical scattering is caused by surface texture; thus, its efficacy will vary depending on the relative angle of the surface to the incident light [31]. For example, random upright pyramids will cause ~40% of light to undergo 5 passages or more before exiting the Si [31]. Geometric light trapping via total internal reflection is not limited to Si surface texture. E. Yablonovitch [54] demonstrated the encapsulation layer also provides light trapping, further reducing surface reflectance by 20%.

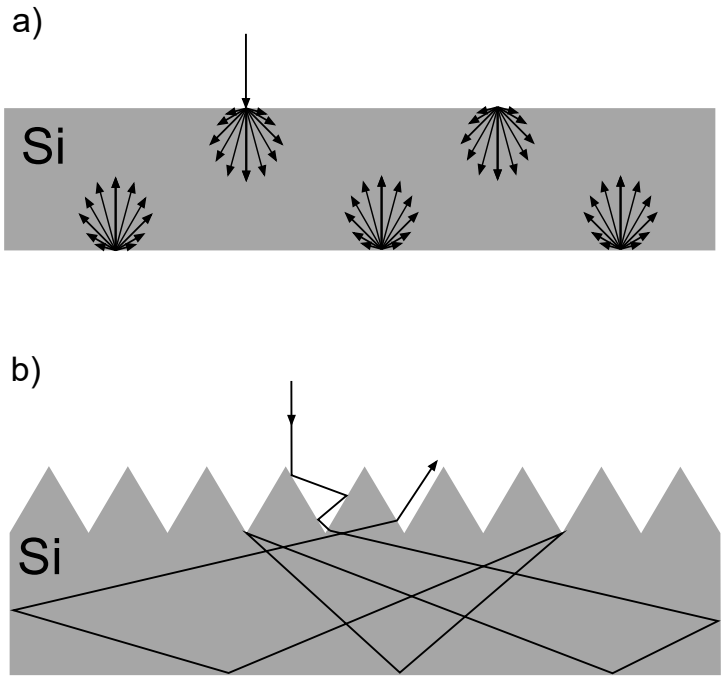

Figure 1.22 a) Lambertian scattering b) geometrical scattering.

Light trapping efficacy has also been demonstrated with texture size. T. Scheul et al. [55] found that nano-wire textures scattered a greater proportion of transmitted light to larger angles in Si than micron-sized pyramids [55], [56]. By scattering to larger angles, a greater number of photons are trapped in nanotextures for absorption than in microtextures, as more photons are kept away from the escape cone. Furthermore, it was found that the broad-angle scattering for nanotextures occurred for the whole solar spectrum, the effect was not localised to a single wavelength, such as for an ARC [55]. When encapsulated, nanotextures also improved the light trapping between the encapsulant and glass interface of the solar cell. In a stack of Si/ethylene vinyl acetate (EVA)/glass, microscale upright pyramidal textures were found to cause 14.5% of the light hitting the EVA/glass interface, from the Si side, to undergo total internal reflection and reflect back into the Si [55], [56]. In contrast, when the Si had a texture of nanoscale wires, this increased to up to 40% of all light at the EVA/glass undergoing total internal reflection and returning to the Si [55]. This increase was caused by nanotextures scattering a greater number of photons to oblique angles, thus when the photons interacted with the EVA/glass interface they were outside the escape cone and reflected back into the Si [55]. The resulting photocurrent gain from B-Si textures light trapping was measured at 0.45% compared to 0.21% for microscale

textures [55]. Therefore, the improved light trapping effect of nanotextures, combined with the broadband reflection reduction, provides an avenue for superior optical and electrical properties for solar cells.

Lastly, path length can also be increased with the use of rear reflectors. Instead of allowing light the option to escape through the back of the Si wafer, a rear reflector is used to reflect light off the back surface of the solar cell into the wafer. Reflectors consist of the rear passivation layer and the Al back contact and can reflect above 95% of incident light near the normal [31]. Figure 1.23 presents the optical path length enhancement of texturing, encapsulation, and a rear reflector combined.

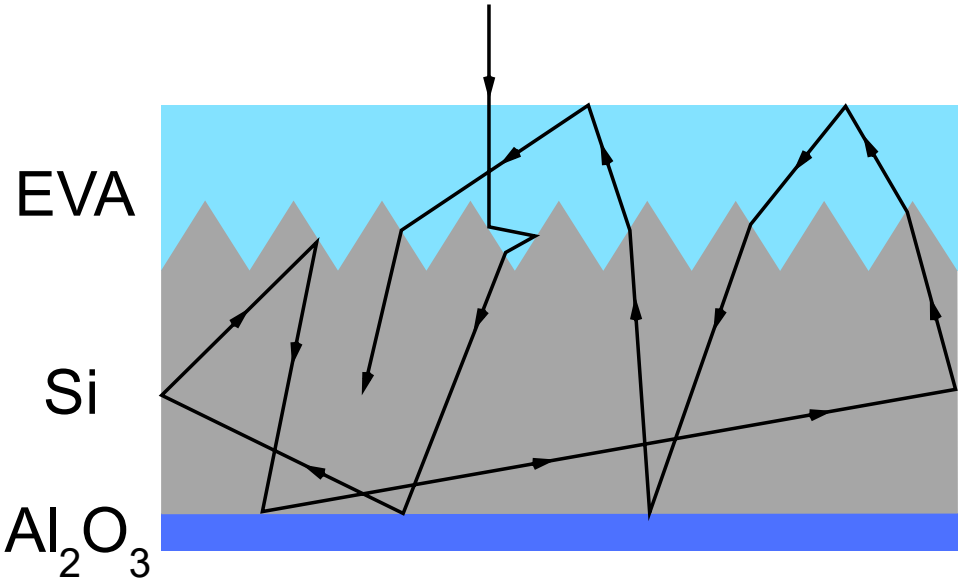

Figure 1.23 Demonstration of reflection reduction typically used in solar cells including a textured front surface, EVA encapsulation layer, and an Al_2O_3 rear reflector.

1.5 Solar Cell Manufacturing

The stages of PERC manufacturing are presented in Figure 1.24, where highlighted steps are discussed in detail.

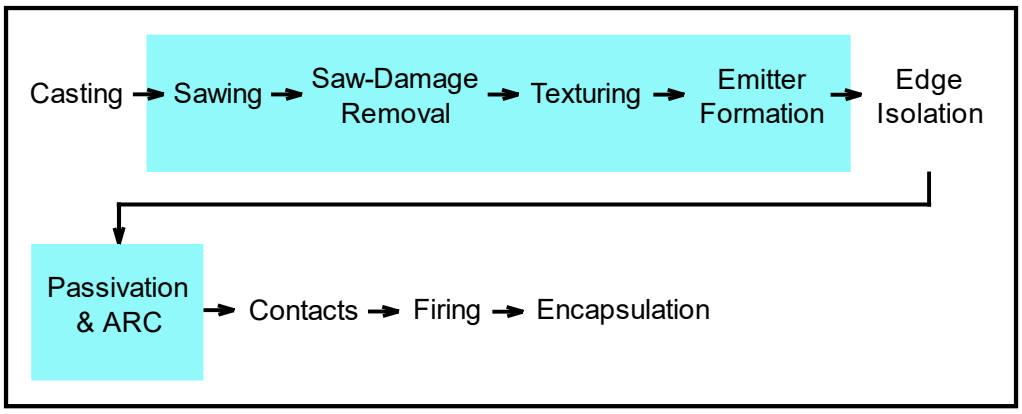

Figure 1.24 Manufacturing stages of a PERC. The highlighted stages are discussed in detail.

1.5.1 Wafer Sawing, Saw-Damage Removal & Texturing

Cutting Si ingot into bricks and then wafers uses a water-cooled diamond wire saw (DWS). Surfaces produced have wire striations with occasional pits and the damage layer is a total of 5 µm [57], [58]. Additionally, the pressure from the DWS on the Si surface is sufficient to produce amorphous-Si (a-Si) in regions across the surface, demonstrated in Figure 1.25 as well as confirmation via Raman spectroscopy [59]–[61].

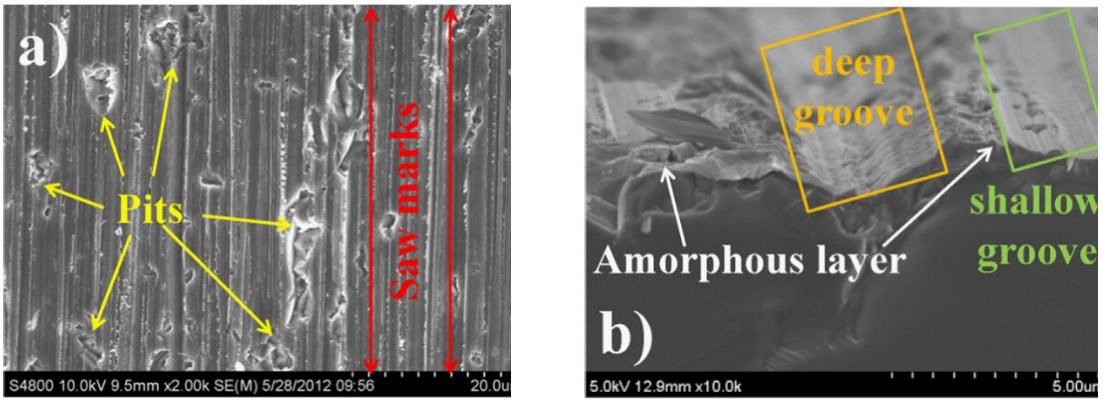

Figure 1.25 a) top-down SEM view of a DWS surface b) a cross-sectional view of a DWS surface demonstrating the a-Si layer and grooves. Figure reproduced from K. Chen et al. [58].

The surface damage from sawing must be removed to minimise its deleterious recombination effects. Mono-Si wafers are etched using solutions of NaOH or KOH at 30 – 40 wt% in deionised water at 70 – 80 °C, removing 2 – 4 µm/min, to induce semi-isotropic etching [62]–[66]. Multicrystalline-Si (mc-Si) wafers are etched using acidic mixtures of $HF/HNO_3/H_2O$ at 6 – 10 °C to maintain etching rates as the process is exothermic [67], [68]. Etching to texture the front surface is performed after saw-damage removal, section 1.6 discusses texturing in detail.

1.5.2 Emitter Formation

To create the p-n junction, the surface of p-type Si is doped n-type with phosphorous from a liquid source of $POCl_3$ [69]. N_2 is bubbled through $POCl_3$, and along with O_2 is transported into a diffusion furnace, forming a phosphosilicate-glass (PSG) on the wafers' surface at 800 °C – 900 °C [69], [70]. The PSG is the source of phosphorous atoms for doping and on further heating are driven into the wafer surface [69], [70]. After driving-in the phosphorous, the PSG is removed using dilute hydrofluoric acid (HF). Finally, surface etching is required to remove the excessively high concentration of phosphorous at the surface of the wafer, known as the dead layer. The dead layer is deleterious to device performance as phosphorous atoms that exceed the solid solubility form electrically inactive precipitates, facilitating SRH recombination [12], [71]–[73].

An alternative to homogenous emitters is selective emitters. Selective emitters consist of a uniform surface of lighter doping than a typical emitter, but under the metal contacts doping is increased. This heavily doped region decreases contact resistivity and recombination at the metal-silicon interface. The lightly doped area maximises light absorption with low recombination, resulting in gains in J_{sc}, V_{oc}, and efficiency over traditional front surface diffusions [74]–[77].

1.5.3 Surface Passivation & Anti-reflection Coatings

After the p-n junction is formed, front surface recombination is addressed. The surface is coated with layers of dielectric material to satisfy the dangling bonds at the Si-surface, thus reducing the number of states in the bandgap for carriers to recombine at. This is termed chemical passivation. Charge from the dielectric layer can also minimise recombination by reducing the concentration of minority carriers at the surface thus inhibiting SRH recombination as it requires both types of carriers. This mechanism is termed field effect passivation (FEP).

SiN_x:H is the most common dielectric for Si surface passivation. It acts as a chemically passivating layer to the front surface whilst also introducing positive charge to repel positive

carriers away from the surface. Furthermore, upon firing, it releases hydrogen to passivate bulk defects and acts as an effective ARC due to its tunable refractive index [78]–[80]. Industrially, SiN_x:H films are applied using PECVD due to their high through-put and low processing temperatures [78]–[80]. Reaction gases of silane, ammonia, and nitrogen are excited into a plasma state using radio frequency coils at 350 °C – 400 °C to create the SiN_x:H layer [78], [79]. Layer thickness, refractive index, and hydrogen content are optimised by gas flow and temperature to achieve the best balance of optical and electrical properties [79].

Rear surface passivation requires an alternative to SiN_x:H, as the positive charge attracts minority carriers for recombination at the p-type rear [81]. PECVD AlO_x provides effective rear surface passivation with its high density of negative fixed charge to repel electrons (minority carriers) away from the rear surface [82]–[86]. Atomic layer deposition (ALD) of AlO_x is effective at 6 nm thickness, yielding an increase of 0.4 – 0.8% absolute for PERC while becoming more common industrially [9], [87]–[91]. SiN_x is added atop AlO_x for increased rear side reflection to improve long-wavelength absorption [86], [92].

1.6 Texturing Silicon

1.6.1 Microscale Texturing

1.6.1.1 Alkaline Etching

Texturing to reduce reflectance for solar cells was first realised with alkaline etchants in 1974 [93]. 48 years later, alkaline etchants remain the dominant industrial texturing technique for mono-Si [33]. The texture generated from alkaline etchants is caused by the preferential etching of Si(100) over Si(111). Each surface atom of the Si(100) has two unsatisfied (dangling) bonds and two bonds to Si atoms in the lattice, while Si(111) has one unsatisfied bond and three bonds to Si atoms in the lattice [94], [95]. Therefore, the energy required to etch Si(100) is less than Si(111), as only two Si-Si bonds need to be broken to remove the atom from the surface for Si(100) while three must be broken for Si(111) [94],

[95]. This variation in etch rates combined with the diamond-cubic structure of Si results in a pyramidal texture, as shown in Figure 1.26.

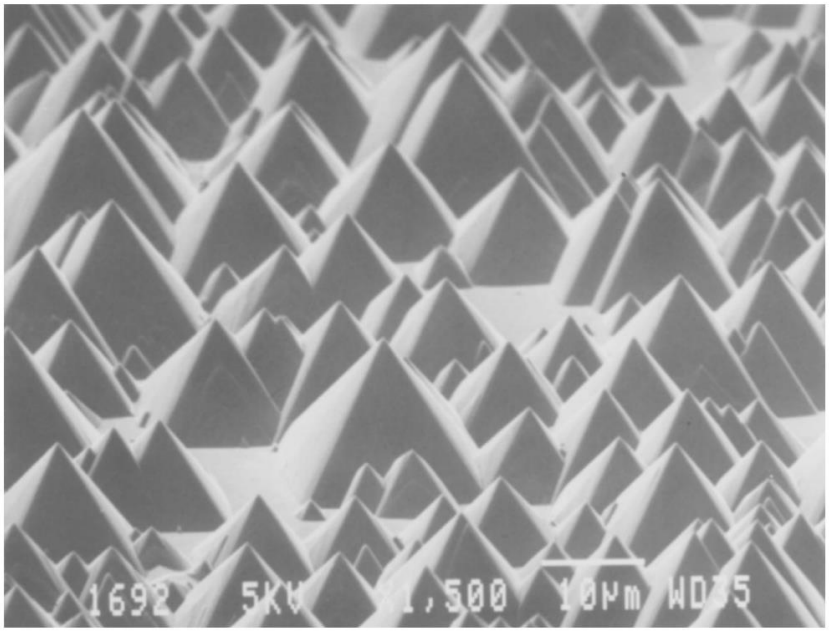

Figure 1.26 The random upright pyramidal texture on mono-Si, figure reproduced from E. Vazsonyi et al. [64].

The mechanism to remove Si atoms from the surface with alkaline etchants uses OH^- ions and H_2O in four steps. Firstly, two OH^- ions bond to the two unsatisfied bonds of the Si atom on the (100) [95]. The second and third steps occur effectively simultaneously, where the $Si(OH)_2$ breaks away from the Si surface and bonds with another two OH^- ions to form $Si(OH)_4$ [66], [95]. The electrons generated from this reaction go on to react with water molecules, creating further OH^- ions and H_2 [95]. The total reaction is defined as:

$$Si + 2OH^- + 2H_2O \rightarrow SiO_2(OH)_2{}^{2-} + 2H_2 \qquad (1.20)$$

The typical industrial alkaline species used are NaOH or KOH, where micro-pyramids form under 1 - 4 wt% KOH or NaOH at 80 °C and typical industrial etch times are ~7 mins [65], [96]–[100]. WAR of bare surface pyramids achieves 10.6 – 15.0% [65], [96]–[100]. IPA is commonly added to alkaline etching to increase the wettability between the etching solution and the Si surface, thus mitigating the masking effect of the H_2 bubbles produced from the reaction [63], [64], [97], [101], [102]. IPA also ensures high texturing coverages by increasing the nucleation of new pyramids; thus 100% texturing coverage can be reached

in a shorter processing span [64], [65]. To balance the benefits of IPA whilst maintaining etch anisotropy, Si. Vazsonyi et al. [64] recommended IPA be kept at 3 vol%.

Reflection reduction with alkaline textures is achieved with multiple photon-surface interactions. The characteristic angle between the pyramid base and one of the four walls is 54.7 °, ensuring all light is double-bounced, 25.6% is triple-bounced and 6.1% is quadruple-bounced [36]. However, due to the continued etching of the formed texture throughout texturing, square-based pyramids are not truly made, in practise hillocks with a 50 – 52° characteristic angle and an octagonal base form [103]. The probability of multiple bounce conditions thus slightly reduces from 16.5 – 19.1% for triple bounce and 2.7 – 3.4% for a quadruple bounce. As such, microscale random upright pyramids can achieve a reflectance of ~10% on bare-Si [36]. Overall, alkaline texturing is the industry standard for mass production of mono-Si solar cells, achieving ~ 22 – 23% industrial cell efficiency across the different cell geometries used [9], [33].

1.6.1.2 Acidic Etching

Alkaline textured mc-Si was less successful at reducing reflection than mono-Si. Figure 1.27 presents alkaline textured mc-Si, where the multiple grain orientations at the Si surface cause irregular pyramids to form. These irregular pyramids yield lower reflectance than those formed on Si(100), where the texture, and thus reflectance, of some planes was indistinguishable from a polished Si surface [104]. Therefore, isotropic texturing is required for mc-Si.

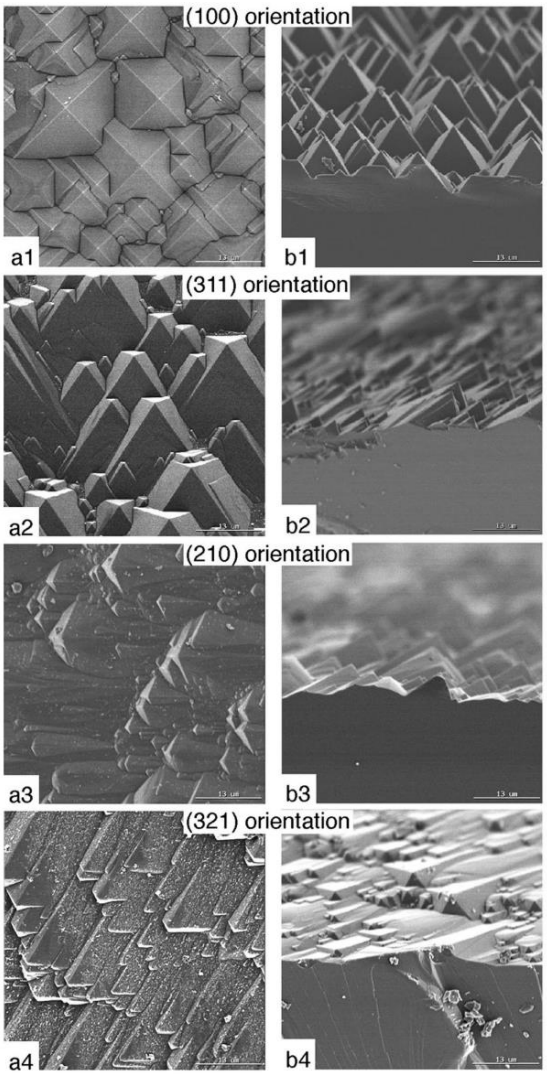

Figure 1.27 Alkaline etching of various crystal planes of Si, producing various morphologies. Figure reproduced from J. Hylton et al. [104].

Texturing of mc-Si is achieved with acidic, isotropic etchants. Etching occurs by an electrochemical process where Si oxidation occurs under cathodic conditions and subsequent oxide etching under anodic conditions [105]. When there is an imbalance between these two processes, etch pits form [105]. The most common acidic etching system is $HNO_3/HF/H_2O$. Etching is initiated by HNO_3 oxidation by hole injection into the valence band of Si, weakening the Si-Si bond [105], [106]. More commonly, this process is undertaken by the HNO_2 intermediate under steady state etching, as it has a greater oxidation potential than HNO_3 [107]. HNO_2 provides a further benefit as oxidation does not become diffusion limited at the surface due to the autocatalytic generation of HNO_2, where one molecule of HNO_2 and one molecule of HNO_3 generates four molecules of HNO_2 [107].

Oxide-etching occurs by Si-F bond formation via a F^- providing an electron to the Si. This addition polarises the other Si-Si bonds, initiating further Si-Si bond breaking until $SiHF_3$ is formed [108]. The full etching process is demonstrated in Figure 1.28. The resulting morphology is an inverted hemispherical cap [109]–[111].

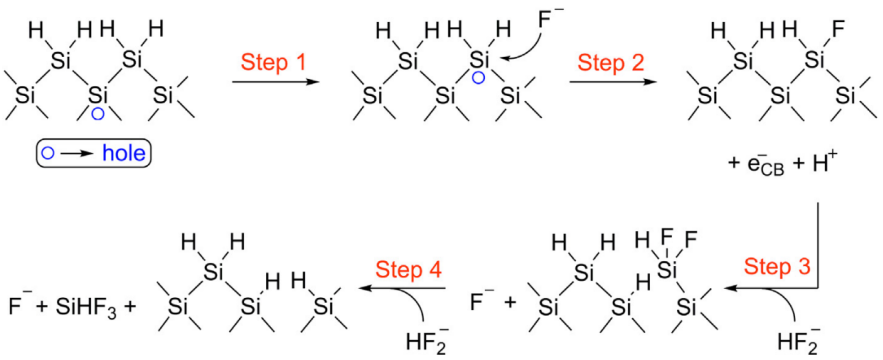

Figure 1.28 Schematic of acidic etching of Si, reproduced from K. P. Sreejith et al. [112].

Acidic etching produces a range in surface reflectance as, unlike alkaline texturing, the morphology of the texture is not maintained throughout texturing. Parameters that effect the texture morphology include the starting surface, the ratio of the etching mixture, and etching time. Considering the starting surface first, defects need to be present to create an imbalance between cathodic and anodic sites across the surface for texture to arise. This results in the textured surface having a 'memory' of the starting surface where planar starting surfaces produce smooth textures whilst rough starting surfaces will produce rough textures. Typically this works in the favour of manufacturing as texturing can be directly initiated from the saw-damaged surface [109]–[111]. With regards to the etch ratio, HF-rich environments create effective textures but etch rates become uncontrollable with rates such as 50 µm/min, whilst HNO_3-rich environments create smooth surfaces but have controllable etch rates [113]. For etch time, a balance must be struck to ensure the surface is completely textured against preventing etch structures from becoming too large and resulting in a higher reflectance [111], [114]. Cheng et al. [114] varied $HF:HNO_3:H_2O$ in four different ratios of 2.5:1:2.5, 7:1:2.5, 15:1:2.5, 36:1:2.5 for etch durations 25 s, 30 s, 60 s, 120 s at room temperature. The best balance was found to be 15:1:2.5 for 60 s, resulting in a bare surface reflectance of 21.4%. Additives have been used to increase etch rates whilst

maintaining optimal texture with varying degrees of success [113], [115]. The addition of H_2SO_4 to $HNO_3/HF/H_2O$ enabled surface reflectance to reduce to 19.3%.

While standard wet chemical etchants currently dominate the texturing market for Si solar cells [12], the microscale textures they produce do not provide the optimal optics for solar cells. The lowest reflectance achieved with microscale textures on bare-Si is 10.6% [36]. With the addition of an ARC, the reflectance of microscale textures can be made effectively 0% for a single wavelength and the WAR is 2.0% across the wavelengths of interest [36]. As reflectance is not minimised for all wavelengths of use to solar cells, photons that could contribute to carrier generation are being lost at the front surface, preventing maximum cell efficiency from being achieved. Alternatives to microscale texturing must be sought out to achieve maximum cell efficiency.

1.6.2 Nanoscale Texturing

1.6.2.1 Metal Assisted Chemical Etching

Metal Assisted Chemical Etching (MACE) catalyses acidic etching with metals to produce nanostructures. Metallic nanoparticles are distributed across the Si surface before being subjected to the previously described acidic wet etchant. Etching local to the particles is catalysed, causing particles to sink into the Si surface [108], [116], [117]. Figure 1.29 presents a schematic of this etching process.

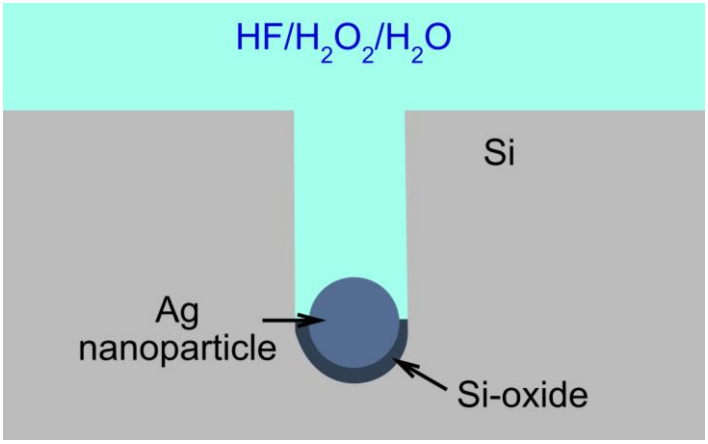

Figure 1.29 An Ag nanoparticle facilitating hole injection to oxidise local Si and catalyse etching surrounding the particle. The particles etch channels into the Si where the particles to sink to the bottom of the channels.

The catalytic effect of MACE occurs in the oxidation phase of texturing [116]–[120]. Instead of HNO_3, H_2O_2 is used as the species for Si oxidation, as it has a larger oxidation potential of +1.76 eV (the oxidation potential of HNO_3 is +0.94 eV), thus H_2O_2 enables faster oxidation rates than HNO_3 [116], [121]. However, HNO_3 can make Si oxidation an autocatalytic reaction, through the generation of nitric intermediates and no such effect occurs when H_2O_2 is the oxidant. Instead, the metal nanoparticles take on the catalytic role by reducing H_2O_2:

$$H_2O_2 + 2H^+ \rightarrow 2H_2O + 2h^+ \qquad (1.21)$$

The holes generated from this reduction diffuse through the metal and are injected into the local Si, causing it to oxidise. As in the previously described acidic etching, this oxide is then etched away by the HF.

Only specific metals facilitate catalytic oxidation. Ag, Au, and Pt are the three metals traditionally used for MACE as the reduction potentials of these metals are below the valence band of Si in HF solutions, promoting hole injection [108], [116]. Ag is the most used metal for MACE to minimise costs [108], [122]. Metal deposition of the nanoparticles can occur by a variety of methods. Thermal evaporation, sputtering, and electron-beam evaporation have been used but the most common method is electroless deposition as it is the most cost-effective [108], [116]. For the example of Ag, particles are generated by submerging wafers in a solution of $AgNO_3$/HF to generate Ag nanoparticles and then a H_2O_2/HF solution for etching. Lastly, as metals can facilitate recombination [31], the particles are removed to prevent them from becoming incorporated into the solar cell upon further processing. Several methods have been used to remove metal particles, including a solution of Iodine and potassium iodide [122], [123], an RCA 2 clean (Radio Corporation of America clean consisting of water, H_2O_2, and HCl) [124], but the most commonly used method is a dip in HNO_3 at room temperature for 10 - 60 mins [125]–[131]. After removal from the Si surface, the metals have the potential to be recovered from the waste metallic-nitrate solution [132]. This not only reduces cost MACE, as the metal can be reused for further MACE processing, but also reduces the strain PV manufacture has on natural

resources, particularly for species such as Ag [20], [21], [25], [28], [29]. Whilst recovering Ag from MACE textures has not been directly demonstrated (likely due to the only recent interest of material recycling to aid multi-TW production of solar-PV, see section 1.2), G. Zante et al. [133] examined recovering Ag from solar cell contacts using copper(II) chloride and were able to successfully recover 95 wt% of Ag.

MACE can produce ultra-low reflectance structures for the entire wavelength spectrum used by solar cells. Needle-like structures with a radius of 60 nm and a height greater than 750 nm have shown <1% reflectance across the visible spectrum [134]–[137]. While MACE can achieve textures that yield <1% reflectance, for solar cell applications MACE has been more commonly shown to yield structures with < 5% surface reflectance [138]–[142]. Figure 1.30 presents the needle-like morphology to achieve sub-5% reflectance.

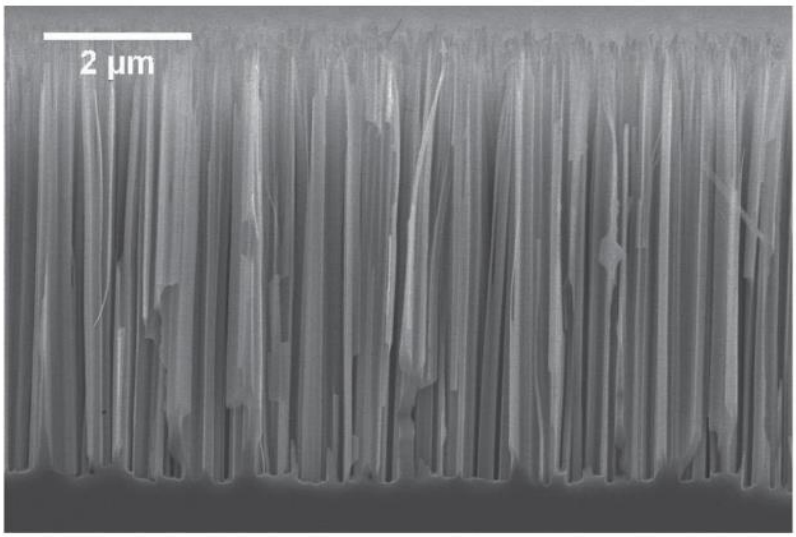

Figure 1.30 Nanowire morphology produced by Ag-MACE; figure reproduced from M. Otto et al. [134].

However, when passivating such textures with PECVD SiN_x:H, coating conformality is poor and bare-Si surfaces remain [122], [143]. Cells made with these poorly passivated nanoscale textures yield worse electrical properties than micro-textured cells [122], [143]. To combat the poor coating conformality of the passivation layer, additional processing steps have been added after MACE to increase texture feature size, thus enabling full coating conformality when passivating with SiN_x:H PECVD [124], [125], [144]–[146]. Yet by introducing additional processing steps to increase the texture feature-size, ultra-low reflectance can no longer be achieved. After processing the nano-textures with pore-

opening etchants surface reflectance increased to 12 – 17% [124], [125], [144]–[146]. Such reflectance is comparable to microscale pyramids with alkaline etching, thus the benefits nanotexturing can offer to solar cell performance are not realised when feature size is increased to accommodate SiN_x:H PECVD passivation.

There is an alternative to compromising on the excellent optics MACE textures can offer and that is to passivate with an alternative technique. ALD has demonstrated surface passivation layers of the order of single nanometres on Si [87], [88], [90], [91], [147]–[149]. ALD Al_2O_3 passivation layers < 20 nm thick have demonstrated complete effective coating conformality on MACE nanostructures, enabling ultra-low reflectance to be maintained without compromising the electrical properties [88], [91], [140], [150].

In recent years, MACE has been combined with microscale textures, creating what is known as a hybrid texture [151]–[155]. A nano-texture's total texture depth dictates how effectively reflectance is reduced, where shorter textures cannot reduce reflectance at longer wavelengths. By applying a short nano-texture atop a micro-texture, the reflectance reduction properties of both structures combine, thus depressing reflectance across the entire wavelength spectrum. T. Rahman et al. [152] demonstrated reflectance could be less than 2% across 400 – 1000 nm wavelengths when nanowires were formed atop upright random pyramids from alkaline etching. Figure 1.31 shows the superior optical performance of the hybrid structure in comparison to both pyramids or nanowires and Figure 1.32 presents all three morphologies. Additionally, the authors demonstrated this unique structure could be passivated with ALD and could yield effective lifetimes three times greater than passivated microscale pyramids. Therefore, both optical and electrical benefits can be realised for solar cells when combining textures of different scales.

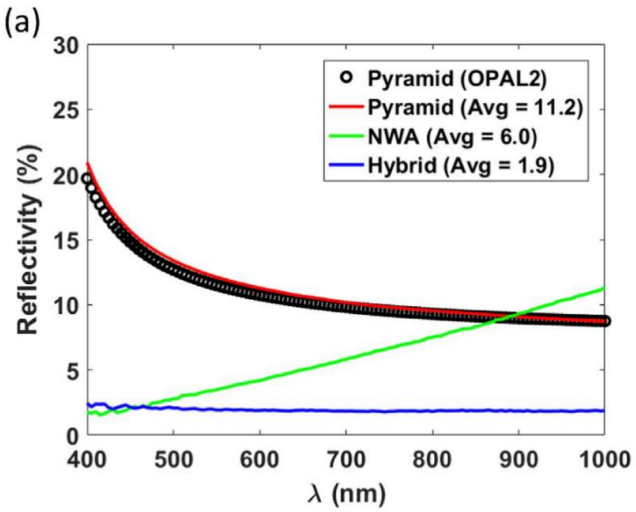

Figure 1.31 Reflectance of pyramidal texture from OPAL 2 software model, pyramids the authors etched themselves, nanowires, and the hybrid texture of nanowires atop pyramids. Graph produced by T. Rahman et al [152].

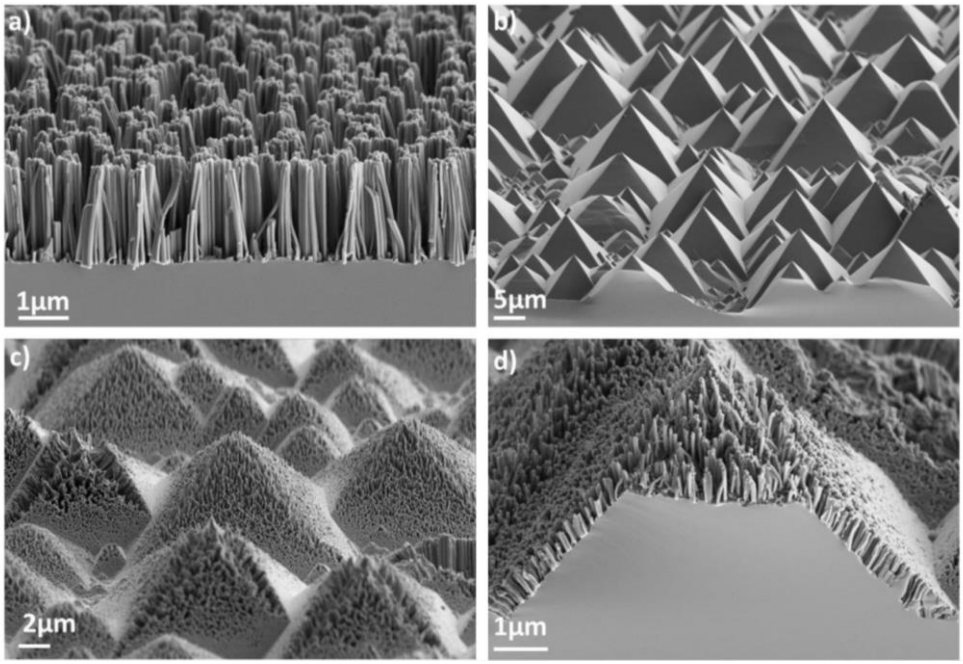

Figure 1.32 Morphology of a) nanowires b) upright random pyramids c) the hybrid texture d) the hybrid texture in cross-section passivated with ALD Al_2O_3. Figure reproduced from T. Rahman et al. [152].

While Ag-MACE has demonstrated excellent optics to improve cell efficiency, increasing the use of Ag in solar cell production is problematic. For solar cells to achieve the necessary multi-TW production target to significantly impact climate change, Ag consumption in solar cell production must reduce by a factor of 7 [29]. As this estimate was made for alkaline textured cells, introducing additional Ag to cell manufacturing by Ag-MACE would require even greater reductions in Ag consumption for other aspects of cell

manufacturing. Therefore, it is desirable to avoid adding Ag to cell production, with the introduction of techniques such as Ag-MACE. An alternative to using Ag in MACE, is Cu-MACE. However, while Cu-MACE has gained research interest, it has been unable to replace Ag-MACE as Cu-MACE requires additional processing steps and processing time to meet the optical benefits of Ag-MACE [156]–[163]. Thus, MACE still must overcome the challenge of developing a fabrication method that can provide improvements in solar cell efficiency, beyond a traditional microscale texture, and support the multi-TW production of solar cells.

1.6.2.2 Reactive Ion Etching

An alternative to wet etching is dry reactive ion etching (RIE). A Si-reactive ion plasma is generated and accelerated towards the Si surface and upon contact etches the Si, forming volatile products. Figure 1.33 presents the typical set-up of RIE of Si. A radio frequency (RF) generator is used to set-up a sufficiently strong electric field to cause ionization of the source gases in a low-pressure environment [164]. This is achieved by releasing the source gases between two electrodes, typically powered with a 13.56 MHz signal. SF_6/O_2 or $SF_6/O_2/Cl_2$ gases are primarily used for Si etching as they can provide etch rates of the order of µm/min with their dissociation into F^-, F-radical (F*) and SF_5^+ where the ionised F species etch Si forming the volatile SiF_4 [164], [165]. The Si-reactive species are accelerated towards the Si surface situated on the lower electrode for etching.

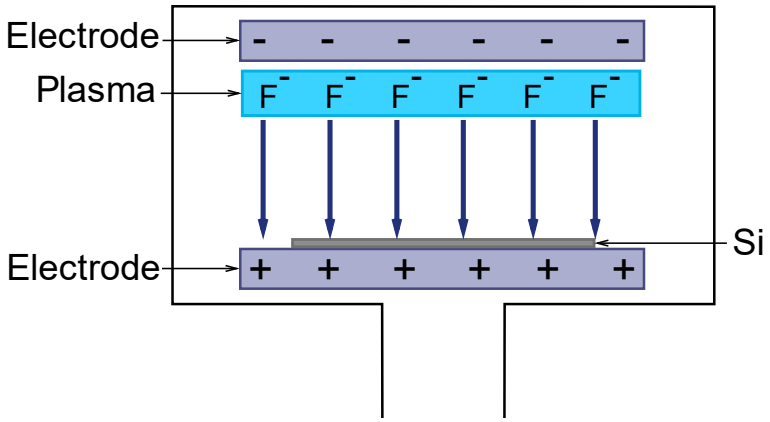

Figure 1.33 Schematic of a RIE chamber texturing Si with F radicals.

Whilst SF_6 is used for etching Si, O_2 is vital to creating texture. O-radicals from the plasma generate a silicon-oxyfluoride layer on the wafer surface, which is slower to etch than Si thus acting as an etch mask [164]–[166]. The removal of the surface oxide is non-uniform, forming perforations in the oxide layer [165]. With further etching, the oxide layer is more readily destroyed on horizontal surfaces where ion bombardment is greatest, thus resulting in needle-like structures [166]. Different morphologies can be generated depending on gas ratio, chamber pressure, sample temperature, and plasma power, producing needle-like, cone, pyramid-like, and inverted pyramid structures [166], [167]. Figure 1.34 presents the needle-like, cone, upright pyramidal, and inverted pyramidal textures formed by RIE. RIE is also able to produce ultra-low reflectance structures and create b-Si, where sub-1% reflectance was measured on 1 µm high bare-Si needles by T. Fung et al. [52].

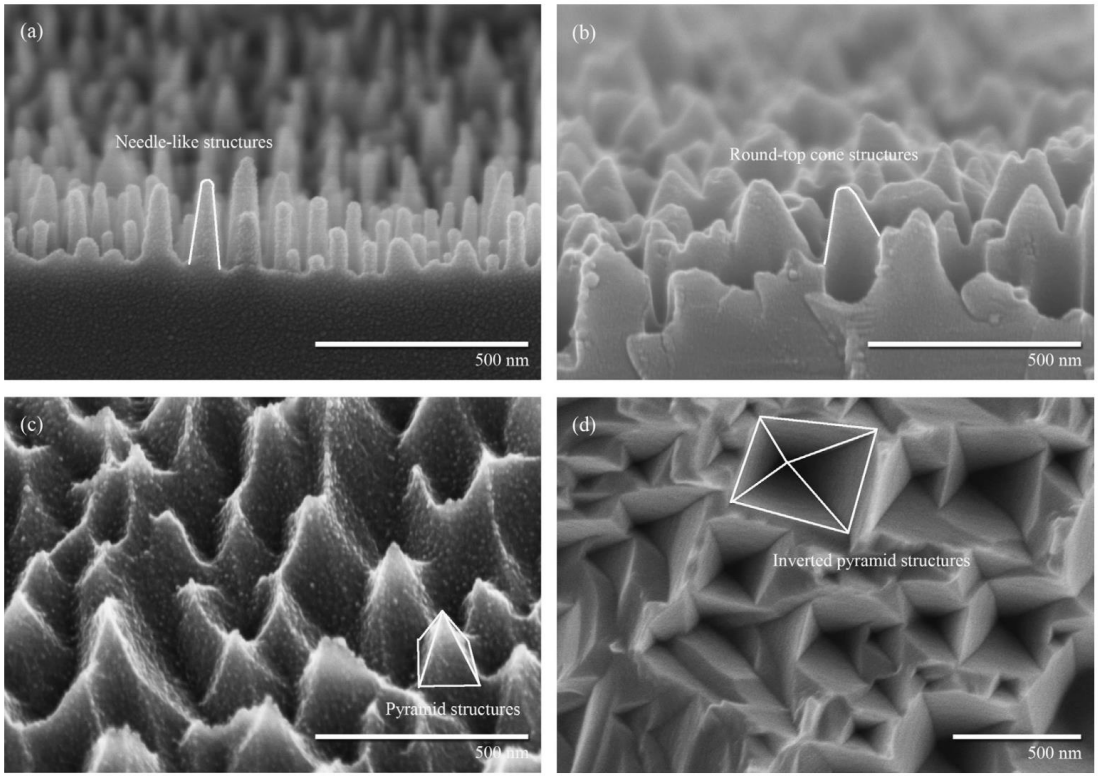

Figure 1.34 Different morphologies RIE can produce. Figure reproduced from K. M. Park et al. [167].

However, texturing DWS surfaces to produce nano-textures with RIE has necessitated the use of Cl_2 [168], [169]. Whilst nanotextures were successfully produced and cell properties improved [137], [141], [168]–[170], Cl_2 is a toxic gas and therefore a barrier to

RIE being integrated successfully into industry. Furthermore, RIE uses costly equipment, thus the market share of RIE was predicted to grow to no more than 2% by 2030 for mc-Si [12].

1.6.2.3 Plasma-less Dry Etching

To avoid the expensive equipment used in RIE, texturing Si with gases has been investigated. Several species have been used to texture Si in the gas-phase for solar cell applications, including ClF_3 [171], F_2 [172]–[175], HF/H_2O_2 with Ag particles [176], but the most well-studied system is for HF/HNO_3 [177]–[180]. The typical set-up for the latter involves holding the Si wafer over a heated bath of HF/HNO_3, where the vapours from the acid solution can contact the Si surface for etching. Yet, the proposed etching mechanism was not entirely in the vapour phase [181]. Whilst the reactants were emitted from the liquid source in a vapour, etching only occurred on the Si surface when a liquid film condensed on the wafer surface, creating typical acidic wet etching conditions. The surface reflectance achieved by HF/HNO_3 vapour etching is between 5 – 20% [177]–[180], [182]. Perhaps the most viable balance between texture properties and texture processing conditions was demonstrated by B. Mohamed et al. [180], where a single-step etching process achieved a surface reflectance of 8% in 8 mins. However, the reflectance and processing time are approximately equal to those exhibited by microscale alkaline texturing, thus no benefit is achieved by HF/HNO_3 vapour etching by either improving solar cell performance or reducing manufacturing processing time.

The second gas-phase etching system that presented industrial promise for nanotexturing Si was F_2 vapour etching by B. Kafle et al. [172]–[174]. F_2 gas was pre-heated to form Si-reactive F-atoms before exposure to Si wafers for etching. The tool designed was intended for in-line use, whereby wafers are rolled along a heated belt, into the etching tool where they are surrounded by a N_2 gas curtain thus creating a safe environment to exposure the F_2 etching gas to the wafers. Figure 1.35 presents the variety of morphologies F_2 vapour texturing can produce, where the lowest reflectance structures were found as

processing temperature decreased and F_2 concentration in the reaction gas increased [172]. The lowest surface reflectance achieved with F_2 vapour etching was < 2% [172]. No explicit comment was given on texturing processing time, only the belt speed was given (2 – 8 mm/s) and the length of the belt was not stated. Thus, a direct comparison for processing time to assess the industrial feasibility of F_2 vapour etching cannot be made at this time.

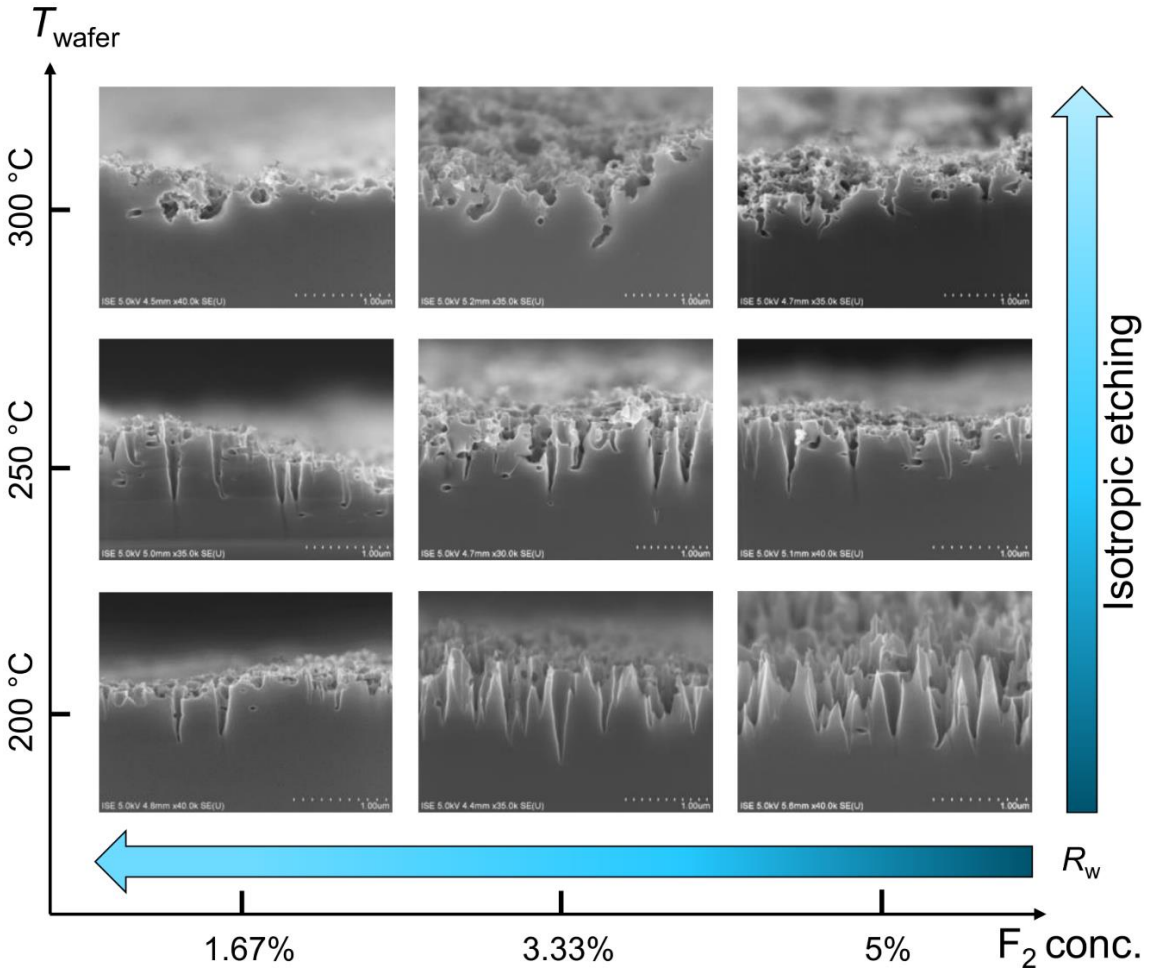

Figure 1.35 The morphologies produced by F_2 vapour etching when processing time and F_2 concentration in the reaction gas are varied. Figure produced by B. Kafle et al. [172].

1.6.2.4 HF/O_3 Gas-Phase Texturing

Gas-phase texturing using gaseous HF/O_3 (GaPTex) was investigated by the Semiconductor group at The University of Oxford [183]. Etching was analogous to acidic wet etching, where O_3 was used to oxidise the Si surface and HF-vapour to etch the oxide away. Figure 1.36 presents the experimental set-up that was used within the work. O_3 produced from a GM-1 Primozone generator was passed over a heated HF-reservoir of 40 wt% liquid HF. The combined vapour of HF/O_3 was directed into the heated reaction

chamber, over the wafer surface. Gas flow rates could be varied between 1 and 5 L/min into the reaction chamber and the temperature of the water bath housing both the HF-reservoir and the reaction chamber could be varied between 40 °C and 80 °C. The pick-up of HF vapour was improved upon from passing the O_3 vapour across the HF reservoir surface by using a 'bubbler-coil' design. A perforated coil was inserted into a HF-resistant container filled with HF, forcing the O_3 to bubble through the liquid HF rather than pass over the liquid surface.

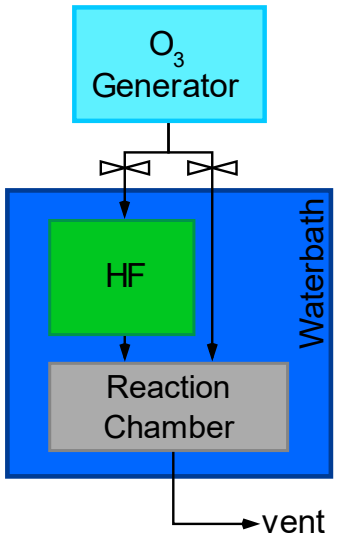

Figure 1.36 The experimental set-up schematic for HF/O_3 texturing [183]*, where O_3 was passed through a HF reservoir to a reaction chamber to texture Si.*

The most influential operating parameter affecting GaPTex morphology and subsequent optical properties was the ratio of HF/O_3. Figure 1.37 presents the change in morphology between etching in a HF-rich environment to an O_3-rich environment, where textures made from HF-rich environments yielded lower surface reflectance. The lowest WAR achieved on DWS mc-Si was measured at 11.7% after 30 mins of etching.

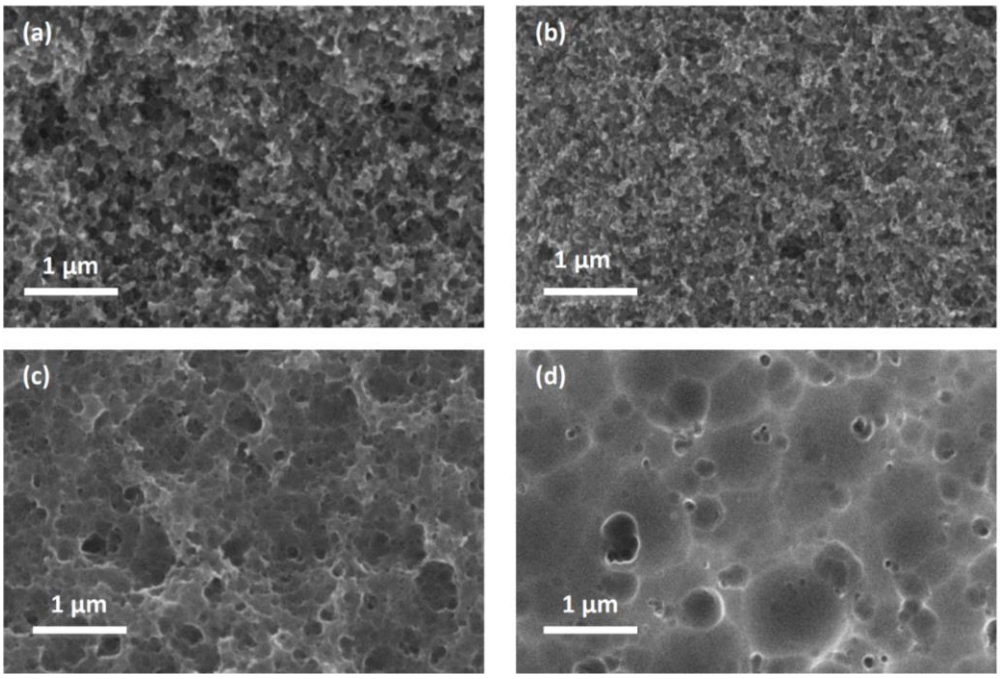

Figure 1.37 HF/O_3 texture morphology as a function of average reaction gas composition from HF-rich (a) through to O_3-rich (d).

The project suffered several limitations. Firstly, regardless of the water-bath temperature, the incoming gas to the reaction chamber was 35 °C, therefore no effect on temperature was truly studied. Secondly, texturing uniformity was poor, Figure 1.38 presents the typical texturing non-uniformity produced across the wafer surface. Thirdly, the etching time of 30 mins was too great for the process to be industrially desirable. For GaPTex to become a desirable and competitive industrial process further investigations must focus on reducing processing time, increasing texturing uniformity, demonstrating compatibility with standard manufacturing techniques, and further optimisation of optical properties.

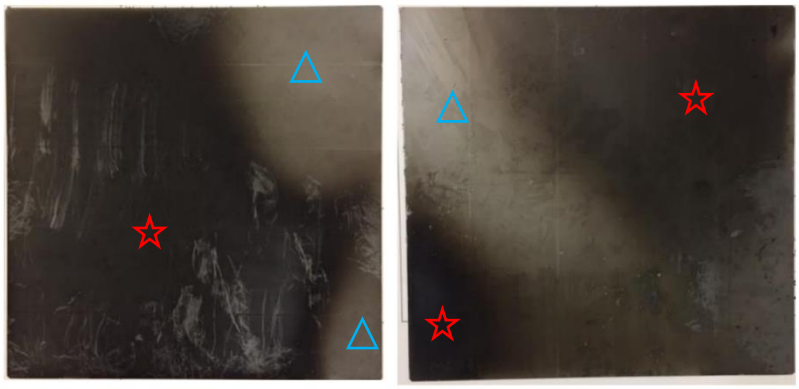

Figure 1.38 Two 156 mm × 156 mm wafers textured with the same texturing conditions, demonstrating the lack of uniformity across a wafer surface and between wafers. Blue triangles indicate local regions of low reflectance whilst red starts indicate local regions of high reflectance.

1.7 Thesis Aims

Nanotextured Si can provide superior optical properties for Si solar cells, enabling the full solar spectrum to be used for carrier generation. However, each nanotexturing technique has a limitation preventing industrial up-take. MACE primarily used Ag, which is undesirable to add to solar cell production, as current solar cells must already minimise Ag content to achieve multi-TW production. RIE uses costly equipment and toxic species for texturing. Etching in the gas-phase is a potential new alternative to mitigate the weaknesses of prior methods, by using simple cost-effective equipment and processing under atmospheric pressure at low sample temperatures. However, current gas-phase texturing techniques either have excessively long processing times or are a two-step process with wet chemicals to create optimal solar cell properties.

The aim of this thesis is to develop HF/O_3 gas-phase texturing (GaPTex) to mitigate the current drawbacks of other gas-phase texturing techniques whilst realising the benefits of gas-phase texturing over wet etching techniques. To achieve this, a texturing tool was designed and manufactured to enable gas-phase texturing to be studied in detail. The texturing mechanism was further investigated as well as the variety of morphologies that could be produced. Finally, the performance of the texture in a solar cell was assessed for the first time.

1.8 Thesis Structure

The materials and experimental methods used in this thesis are presented in Chapter 2. The design, manufacture, and refinement of the GaPTex equipment are presented in Chapter 3. The initial results using the new GaPTex tool are demonstrated in Chapter 4. The texturing process optimisation to achieve reproducible, ultra-low reflectance B-Si is presented in Chapter 5. Chapter 6 investigates the significance of surface chemistry on the texturing reaction. Chapter 7 explores the different morphologies GaPTex can generate and contains the proposal of the full texturing mechanism for GaPTex. The implementation of

GaPTex Si into a PERC is presented in Chapter 8. Chapter 9 describes the thesis conclusions and suggested future work for GaPTex.

2 Materials and Methods

2.1 Materials

2.1.1 Substrates

Table 2.1 presents a summary of the characteristics of the Si substrates used in this project, including the reference name given to each substrate used throughout the thesis. All material used in the project was diamond wire sawn. For the substrate Ox 1, the type and source are unknown as it was sourced from the Si 'remnants' store in the Semiconductors lab.

Table 2.1 Summary of Si substrates used within this thesis.

Reference	Type	Crystallinity	Surface Texture	Resistivity (Ω.cm)	Source
Longi	P-type	Multi	SD	1-3	Longi
Ox 1	Unknown	Mono	Flat, polished	Unknown	Unknown
Trina 1	P-type	Mono	SDE	1-3	Trina
Trina 2	P-type	Mono	SD	1-3	Trina
Ox 2	N-type	Mono	Flat *	1	Fraunhofer ISE
UNSW	P-type	Mono	SDE	1-3	UNSW
UNSW Control	P-type	Mono	Upright pyramids	1-3	UNSW

** 100 nm thermally grown oxide*

SD = Saw-damage present

SDE = Saw-damage etched/removed

2.1.2 Precursors

A precursor containing colloidal silica and IPA coated on the Si substrates surface was found to strongly influence the gas-phase texturing (GaPTex) process. Analytical reagent grade IPA of > 99.8% purity was used, and the range of colloidal silicas used in this work is presented in Table 2.2. The full investigation of the precursor application methods and their effect on texturing is presented in Chapter 5. In Chapter 5, it is demonstrated that the precursor stability is crucial to achieving ultra-low reflectance surfaces and texturing reproducibility. 96 wt% sulphuric acid (H_2SO_4) was used to stabilise the precursor, which was added individually to the colloidal silica and IPA, in separate containers, until pH 2 was

achieved. Each container was manually agitated, before adding the desired amount of colloidal silica into the IPA. The range of dilutions investigated was from 1:10 to 1:2000 of colloidal silica to IPA respectively. pH was monitored using the Hanna Instruments HI-98100 Checker Plus pH Tester. Agitation later became automatic with a PTFE coated magnetic stirrer atop a stirrer hotplate, set to 1000 RPM, to improve ease of preparation for the operator, this change was found to have no significant change to texturing.

The effect of the stabilising counter-ion within the colloidal silica of the precursor was of particular interest to GaPTex. Na^+ stabilised, and ammonium (NH_4) stabilised colloidal silicas were both investigated, the details of which are presented in Table 2.2. In Chapter 7, Li, Na, K, or Cs were added to the NH_4-stabilised colloidal silica (AS-40) to investigate the effect different alkali metals had on texturing. To add the alkali metal to the precursor, a hydroxide solution of the desired alkali metal was made. It was assumed that NaOH was the only contribution to cause the colloidal silica pH to deviate from neutral in the Col-K (NC) colloidal silica. To mimic the final alkali metal concentration of 0.0033 M the Col-K (NC) colloidal silica had, an alkali hydroxide solution of 0.037 M was used during precursor preparation. After making the hydroxide solution, H_2SO_4 was added to the hydroxide solution until pH 2 was reached (thus maintaining the stabilisation pH of the precursor). The same volume of the hydroxide solution with H_2SO_4 as the colloidal silica was then added to the prepared precursor base of colloidal silica, IPA, and H_2SO_4, completing the preparation.

Table 2.2 The colloidal silicas tested in the Precursor.

Name	Nanoparticle Diameter (nm)	Si Content (wt%)	Counter-Ion	pH	Source
Col-K NC	70-90	20	Na	9-11	Kemet
TM-40	22	40	Na	9	Ludox
AS-40	22	40	NH_4	9.2	Ludox

2.2 HF/O_3 Texturing Tool

The design and refinements of a new HF/O_3 GaPTex tool, overcoming the issues of that used in M. Cohen's work [183], are presented in Chapter 3.

2.3 Wet Chemical Processing

Table 2.3 presents the details of the substrate cleaning methods used in Chapter 4. To maintain sample cleanliness during RCA cleaning (Radio Corporation of America cleaning), dedicated beakers and tweezers were cleaned with RCA solutions prior to cleaning specimens.

Table 2.3 The five different cleaning processes used in chapter 4.

Cleaning Medium	**Temperature**	**Duration**	**Agitation**	**Post Cleaning**	**Drying**
Acetone	Room Temperature	10 mins	Ultrasonic bath	Acetone rinse	Air
Acetone IPA rinse	Room Temperature Room Temperature	10 mins seconds	Ultrasonic bath Rinsing	Acetone rinse IPA rinse	Air
IPA	Room Temperature	10 mins	Ultrasonic bath	IPA rinse	Air
De-ionised water	Room Temperature	10 mins	Ultrasonic bath	De-ionised water rinse	Pressurised-air gun
RCA 1: H_2O_2 30 wt% 60 ml, NH_3 40 wt% 60 ml, de-ionised water 360 ml **De-ionised water rinse** **RCA 2**: H_2O_2 30 wt% 60 ml, HCl 36 wt% 60ml, de-ionised water 360 ml **De-ionised water rinse** **HF dip**	**RCA 1**: 70 ºC – 80 ºC **De-ionised water rinse**: room temperature **RCA 2**: 70 ºC – 80 ºC **De-ionised water rinse**: room temperature **HF dip**: room temperature	**RCA 1**: 6 mins once solution begins to bubble **De-ionised water rinse**: 6 mins **RCA 2**: 6 mins once solution begins to bubble **De-ionised water rinse**: 6 mins **HF dip**: 1 min	**RCA1**: from evolving bubbles **De-ionised water rinse**: water source **RCA 2**: from evolving bubbles **De-ionised water rinse**: water source **HF dip**: none	None	Pressurised-air gun

2.4 Solar Cell Fabrication Methods

2.4.1 Emitter Formation

Phosphorous emitters were formed with a liquid $POCl_3$ source using the Tempress TS81004 Tube Furnace by the in-house team in the Solar Industrial Research Foundation (SIRF) at the University of New South Wales (UNSW). An optimised emitter recipe for upright random pyramids PERC and LDSE (Laser Doped Selective Emitter) cell architectures was used on GaPTex wafers as well as pyramidally textured wafers, where the latter were control specimens. Exact conditions for emitter formation are not reported due to IP restrictions at UNSW. However, typical sheet resistance (R_{sh}) produced on upright random pyramids for PERCs was quoted at 80-90 Ω/□ and for LDSE 115-125 Ω/□.

2.4.2 Surface Passivation

Surface passivation was performed by the in-house team at SIRF using the Roth & Rau MAiA XS Plasma Enhanced Chemical Vapour Deposition (PECVD) system at UNSW SIRF. SiN_x:H was used as both surface passivation and an ARC. Whilst exact operating conditions are confidential by SIRF, it was stated that the recipe was optimised for random upright pyramids. SiN_x:H thickness was quoted at 70 nm and a refractive index of 2.00.

2.5 Characterisation Methods

2.5.1 Optical

2.5.1.1 Spectrophotometry

Surface reflectance was measured using an Ocean Optics Flame-S-XTR1-ES spectrophotometer, DH-2000-BAL light source, and ISP-50-8-R-T integrating sphere. Figure 2.1 schematically shows the set-up for reflectance measurements including a detailed view of the spectrophotometer.

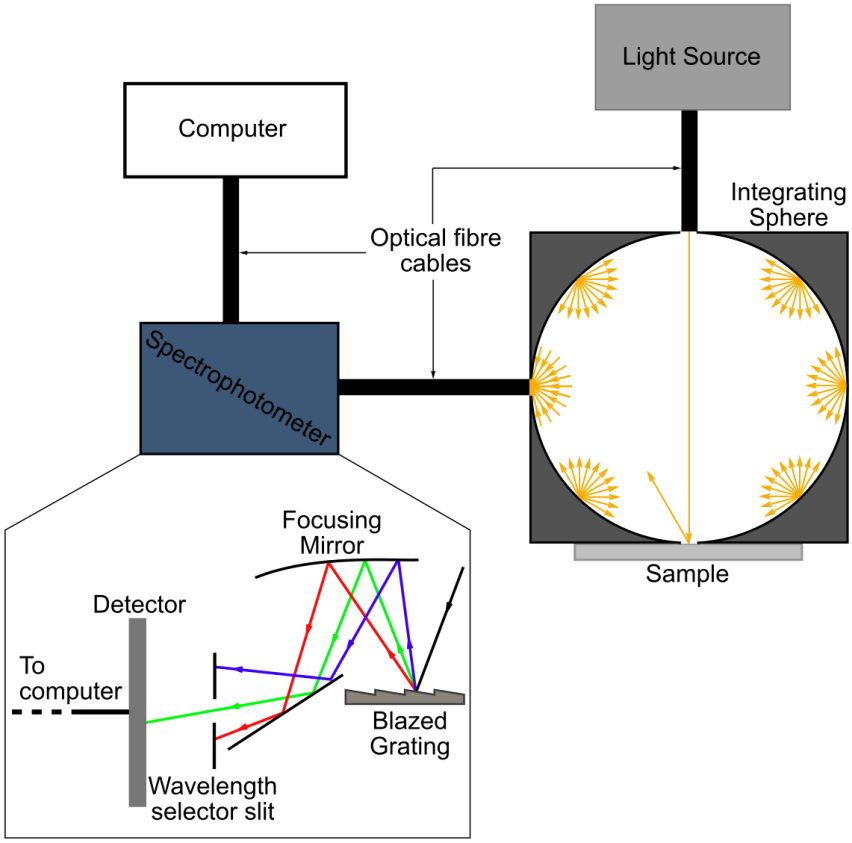

Figure 2.1 Schematic of the light source, integrating sphere, and spectrophotometer for reflectance measurements. A detailed view of the inside of the spectrophotometer is included.

The light source consisted of a deuterium bulb emitting 210 - 370 nm light, and a tungsten-halogen bulb emitting 320 – 1100 nm; mimicking the relative wavelengths used for carrier generation in solar cells by sunlight. Light is directed along an optical fibre cable to an integrating sphere, where it hits the sample perpendicularly. Any reflected radiation from the sample is uniformly scattered by the integrating sphere's Lambertian reflector interior. Light is collected in the exit port, 90 º from the sample, and is directed along an optical cable into the spectrophotometer. Within the spectrophotometer, light is separated into its wavelength components by a blaze-grating. The blaze-grating also aids wavelength selection as it localises the amount of power to a specific diffraction order, effectively creating one diffracted beam per wavelength. Individual wavelengths are subsequently selected using a slit and directed onto the photodiode detector, converting the light to an electrical signal for display.

Before measuring samples, the system was calibrated in the OceanView software. First, to improve the signal-to-noise ratio of measurements, the signal strength of the light reaching the detector was increased until 85% saturation of the detector occurred. This was achieved by increasing the integration time per measurement. The signal-to-noise ratio was additionally improved across the whole spectrum by using a boxcar averaging method. The second step of calibration was to define 100% and 0% reflectance. A reflectance measurement using a spectralon standard defined 100% reflectance, as spectralon has effectively 100% reflectance from 300 nm – 2000 nm [184]. The 0% reflectance was defined by repeating the measurement but with the shutter to the light source closed. Another standard of 4% was also available for reflectance measurements, which allowed for an improved signal-to-noise ratio at 4% reflectance and lower. In this work, the spectralon standard was used, as the main body of this work focussed on the development of GaPTex where reflectance commonly exceeded 4%. In future GaPTex research, the 4% standard should be taken into consideration for low-reflectance studies, as this project has successfully demonstrated ultra-low reflectance reproducibly, but must be used in tandem with the 100% standard to prevent inaccurate results.

After calibration, sample reflectance measurements were performed. Five areas were measured per square sample at: (0.25, 0.25), (0.25, 0.75), (0.50, 0.50), (0.75, 0.25), (0.75, 0.75), where (0, 0) was defined as one corner of the square the specimen, and (1, 1) was the corner diagonally opposite. If specimens were irregularly shaped, measurements were taken to avoid overlap between measurement areas whilst creating an even distribution of measurement points. The spectrophotometer and software were set to acquire measurements with a ~0.5 nm wavelength bin. Each measured point on the sample was an average of five measurements in the OceanView software. The five averaged points measured per sample were then used to calculate the mean reflectance of the sample. The standard deviation of these five measurements was used to describe the variation in reflectance uniformity of a sample. Weighted average reflectance (WAR) was used to generate a single value of reflectance for a sample. Equation (2.1) shows the calculation

used where reflectance measurements (R) at a given wavelength for 400 nm ≤ λ ≤ 1000 nm were weighted against the respective photon density in the AM1.5G spectra.

$$WAR = \frac{\sum_{i=\lambda_0}^{i=\lambda_n} R(i) \times AM1.5G(i)}{\sum_{i=\lambda_0}^{i=\lambda_n} AM1.5G(i)} \quad (2.1)$$

An area of potential systematic error was the decay of light within the integrating sphere. Defining light decay uses radiance, which is the variation of radiant flux as a function of interaction area and angle. Equation (2.2) describes radiance, L, for a diffuse sphere as a function of incident radiant flux, Φ_i, sphere reflectance, ρ, the total projected angle from the surface, π, the area of the sphere, A_s, and the fraction of sphere area lost to input and output ports, f [184]:

$$L = \frac{\Phi_i}{\pi A_s} \frac{\rho}{1 - \rho(1 - f)} \quad (2.2)$$

Radiance increases as port fraction, f, decreases causing less light to be lost to open ports, and as sphere reflectance, ρ, increases allowing less light to be lost to the material coating the inside of the sphere. Therefore, spheres with high-ρ internal coating and low f allow the greatest collection of light at the output port, post-sample interaction. Spectralon coated the inside of the ISP-50-8-R-T integrating sphere, due to it having effectively 100% reflectance 300 nm – 2000 nm [184]. The port fraction of the integrating sphere was 2.56%, which is below the recommended 5% and thus within acceptable limits [184].

The noise in reflectance measurements increased for wavelengths < 400 nm and > 1000 nm, demonstrated by the rapid changes in reflectance of more than 1% on adjacent wavelength measurements. For λ < 400 nm, signal-to-noise became poorer due to a reduction in light intensity from the light source of approximately one order of magnitude. Below 230 nm, another drop of approximately two orders of magnitude occurs, further increasing noise in the measurement. Noise at infrared wavelengths was caused by the reduced quantum efficiency of the Si detector (as the absorption coefficient of Si decreases), and as the efficiency of the blaze grating to separate wavelengths reduced. Reflectance

measurements were performed between 400 nm and 1000 nm to reduce effects from noise whilst balancing the range of relevant wavelengths for solar cell operation.

In addition to the noise inherent to the spectrophotometer, an error was introduced to reflectance measurements by the set-up between the sample, sample holder, and integrating sphere. Figure 2.2 shows the reflectance spectra of an as-sawn, untextured Si wafer, where four peaks foreign to the Si reflectance spectra occur between 450 nm and 600 nm. These peaks are attributed to stray light interfering with the reflectance measurement caused by an imperfect seal between the sample holder, sample, and integrating sphere. The reflectance measurements of Chapters 4 – 7 contain these additional peaks. Later in the project, the set-up of the sample during measurements was changed. The integrating sphere was inverted (with the measurement port facing upwards), the sample was placed on top, over the measurement port, and a weight was used to improve the seal between the sample and the integrating sphere. This change to the measurement set-up removed the additional peaks from the reflectance spectra. The majority of the reflectance spectra in Chapter 7 do not contain the additional peaks of Figure 2.2.

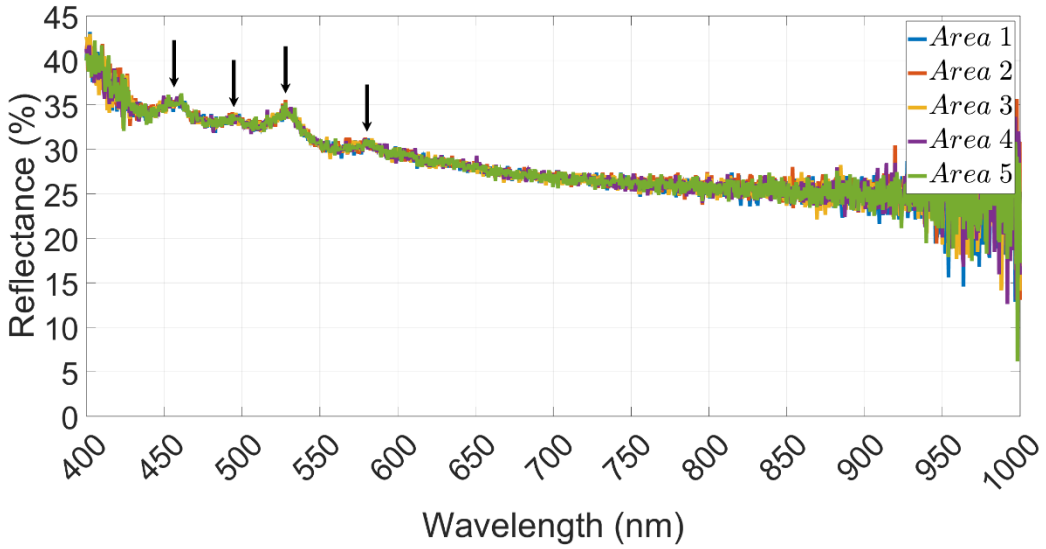

Figure 2.2 A reflectance spectra of bare mc-Si where stray light introduced additional peaks, non-native to the Si reflectance spectra.

2.5.1.2 Ellipsometer

Oxide thickness measurements were performed using a Film Sense FS1 ellipsometer. For a 2 nm thick native oxide on Si, accuracy is reported as 0.013 nm and the precision 0.00035 nm [185]. The refractive index used was for a native SiO_2, at 1.75 [186].

2.5.2 Physical

2.5.2.1 Scanning Electron Microscopy

To analyse texture morphology, a Carl Zeiss Merlin scanning electron microscopy (SEM) was used to resolve nanoscale features. This SEM used a field emission gun as an electron source, subsequent condenser lenses refocussed the electron beam (e-beam) throughout the SEM column, and objective lenses focussed the e-beam before sample interaction [187]. Resultant EM radiation from the surface was collected by a variety of detectors for image creation. Figure 2.3 shows the schematic of a typical SEM set-up.

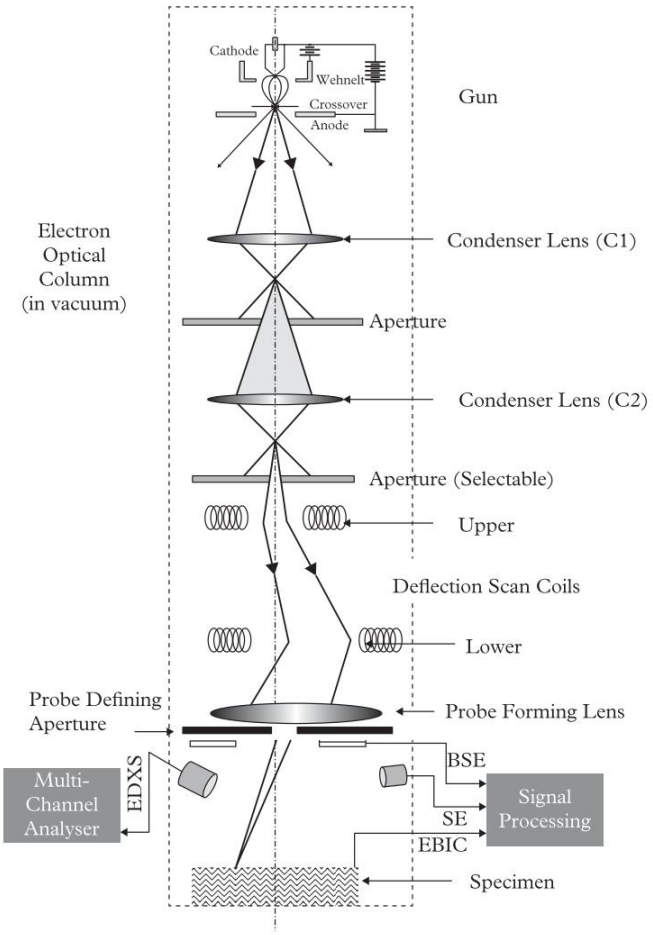

Figure 2.3 Schematic of a SEM, reproduced from K. M. Krishnan [187].

For analysis of surface topography, the secondary electron (SE) mode was used. The e-beam was inelastically scattered by the sample surface, re-emitting lower energy SE < 50 eV, where only SEs in the top 5-50 nm could escape the sample surface for collection [187][188]. An InLens detector was used for SE collection, due to its higher collection efficiency of SEs produced from direct e-beam-sample interaction (known as SE1) [187][189], over traditional Everhart-Thornley detectors.

The feature size of textures generated was of the order of tens nm, therefore SEM operating conditions were optimised to achieve the highest image resolution possible. The highest image resolution is achieved by focussing electrons into a smaller area, known as reducing the electron beam spot size. However, by reducing spot size for high-resolution images, image brightness also lowers due to a drop in probe current. No image will be able to form if there is not sufficient current. K Krishnan [187] demonstrated the SE spot size from a field emission electron source is approximately invariant up to ~100 pA, but at a higher current, spot size increases. Therefore, the probe current used in this project was kept at 100-101 pA to achieve the highest resolution possible whilst still producing a sufficiently bright image.

Accelerating voltage has also been shown to affect image resolution and image brightness. The highest resolution is achieved by maximising accelerating voltage as it reduces spot size; however, SE yield varies with accelerating voltage [187]. Initially, more SEs are generated by increasing the accelerating voltage, producing bright, high-resolution images. However, as accelerating voltage increases further, SEs are generated deeper within the sample, thus lowering the resultant image brightness as fewer SE escape the sample surface to the detector [187]. To balance image brightness and resolution, the accelerating voltage in the project was initially set at 5 kV and later optimised to 3 kV for improved image quality.

The working distance was optimised for resolution over depth of field, as nanostructures imaged were < 1 µm deep, which is well within the range of a SEMs depth of field [187]. The working distance was initially set at 5 mm and later optimised to 3 mm to increase

image resolution by a smaller spot size. In-Lens detectors are less sensitive to variation in working distance than Everhart-Thornley detectors [189], thus the short working distance did not negatively affect image quality.

2.5.2.1.1 Total Texture Depth & Etch-Pit Diameter Measurements

SEM micrographs were used to define the GaPTex total texture depth and etch-pit diameter. Samples were cleaved with a diamond-tipped pen and then hand mounted onto a Ted Pellar 90° pin stub to examine the cross-section using electrodag 1415 paste. An exact 90° view of the surface in cross-section was not possible due to the hand-mounting of the samples. After SEM imaging, ImageJ software was used to analyse the total texture depth and etch-pit diameter by hand. Total texture depth was defined from where the bulk-Si ends to the top of the generated texture on the cleaved interface. Figure 2.4a) demonstrates a total texture depth measurement on a SEM micrograph. Etch-pit diameter measurements were also performed on SEM micrographs. Figure 2.4b) presents the process of measuring etch-pits, where 10 measurements were taken per cross-section image at ×150k magnification in ImageJ software and used to calculate the mean and standard deviation of etch-pit diameter. Etch-pits included in the measurements were circular in cross-section so that only one measurement was needed per etch-pit. The precision associated with hand-measuring etch-pit diameter in ImageJ was ±1 nm. Total texture depth and etch-pit diameter measurements were semi-quantitative, as they were subject to the operator defining the top and bottom of the texture depth as well as which etch-pits to include for diameter measurements. However, all specimens were subject to the same measurement criteria and were performed by the same operator, thus the error is systematic, and comparisons can be drawn between samples.

a)

b)

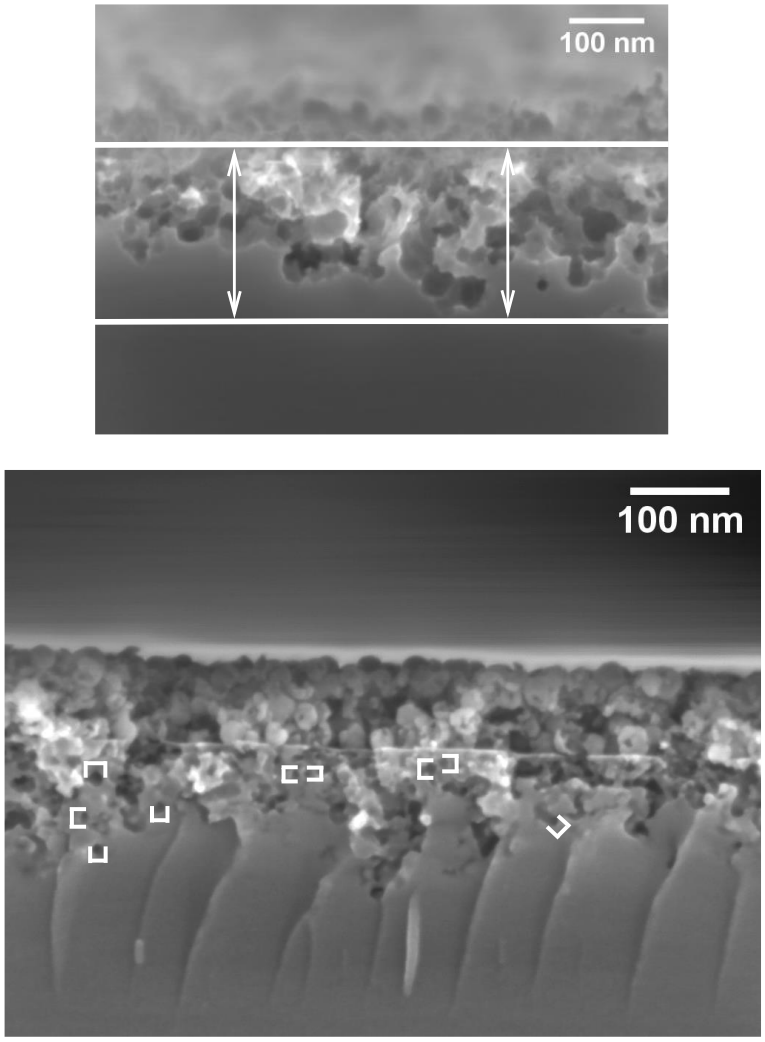

Figure 2.4 a) an example of a total texture depth measurement, measured from the end of the bulk-Si to the top of the texture at the cleaved plane b) an example of the etch pits included for the etch-pit diameter measurements, where individual and circular etch-pits were included for measurements while large, irregular etch pits that appeared to be formed by several etch-pits joining were discounted.

2.5.3 Chemical

2.5.3.1 X-Ray Photoelectron Spectroscopy

To determine the surface composition, X-ray Photoelectron Spectroscopy (XPS) was performed by the Oxford Materials Characterisation Service, using a Thermo Scientific K-alpha XPS. XPS is a surface-specific analysis technique, the Thermo Scientific K-alpha used was quoted to analyse the first 2 – 8 monolayers of the surface of the specimen. Figure 2.5 presents a schematic of a typical Thermo Scientific XPS set-up for surface composition measurements. The X-ray source was Al K-α, yielding 1486.6 eV with a line width resolution of 0.85 eV [190]. X-rays were passed through a quartz monochromator

before sample interaction to improve the measurement signal-to-noise ratio [191]. Chemical accuracy was quoted to 0.1 atomic% and the measured energy range from samples was 100 eV – 4000 eV. The atomic% of each element on the surface was calculated using the primary photoelectron peaks for each element. Four areas were measured per sample to calculate the mean and standard deviation of each element present.

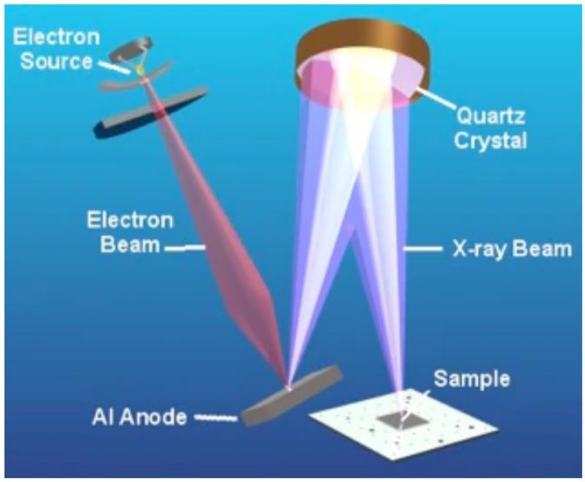

Figure 2.5 Schematic of XPS measurements, figure reproduced from ThermoFisher Scientific [191].

2.5.4 Electrical

2.5.4.1 Minority Carrier Lifetime

I performed effective minority carrier lifetime (τ_{eff}) measurements using the Sinton Instruments WCT-120 lifetime tester with the Quantum Qflash X5d-R flash lamp. A set-up of the lifetime tester used is presented in Figure 2.6, including the flash lamp, illuminating flash, sample, and the inductive coil contained within the sample stage. Samples were placed on the stage and illuminated with red light to generate carriers throughout the entire thickness of the sample. An inductive coil is situated beneath the sample in the stage to monitor sample conductivity as the flash decays to determine τ_{eff}.

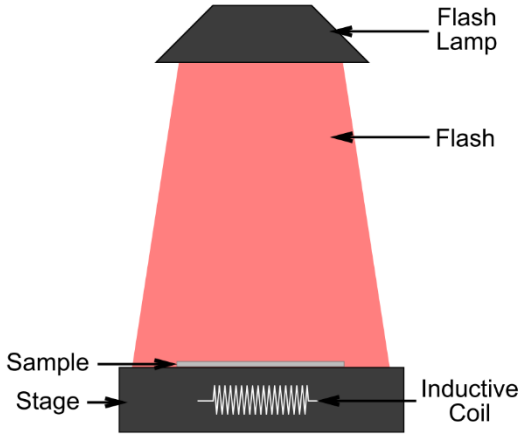

Figure 2.6 Set-up of WCT-120 Lifetime Tester with Quantum Qflash X5d-R flash lamp for effective lifetime measurements.

Three modes are used for measuring τ_{eff} : transient, quasi-steady-state, and generalised. Transient is used for high τ_{eff} samples (> 200 µs), where a short pulse of light is emitted, and subsequent carrier density decay is monitored over time. Equation (2.3) describes Transient lifetime where Δn is excess minority carrier density and $\frac{d(n)}{d(t)}$ is rate of carrier decay with time [192].

$$\tau_{eff} = -\frac{\Delta n}{\frac{d(n)}{d(t)}} \qquad (2.3)$$

Quasi-Steady-State mode is used for low τ_{eff} samples (< 100 µs), where it is assumed that the change in flash intensity causes generated carriers to be effectively in a steady-state [192], [193]. Equation (2.4) describes Quasi-Steady-State τ_{eff}, where $G(t)$ is the carrier generation rate as a function of time.

$$\tau_{eff} = \frac{\Delta n}{G(t)} \qquad (2.4)$$

Generalised mode bridges Transient and Quasi-Steady-State measurement modes for increased accuracy, as both are limiting cases when either $G(t)$= 0 or $\frac{d(n)}{d(t)}$ = 0 respectively [193], [194]. Equation (2.5) describes Generalised mode τ_{eff}. Generalised mode was used to measure τ_{eff} in this work.

$$\tau_{eff} = \frac{\Delta n}{G(t) - \frac{d(n)}{d(t)}} \quad (2.5)$$

2.5.4.2 Sheet Resistance

I used a SunLab Sherescan sheet resistance scanner at SIRF UNSW to calculate R_{sh} of samples. Measurements were performed after emitter formation to infer how heavy or light emitter doping was. 100 measurement points were made in a 10 × 10 grid across the wafer surface to produce the mean, standard deviation, median of a sample, and a spatially resolved map of the wafer surface of high or low R_{sh} areas. Measurement accuracy was quoted as 0.5% of the measured value [195].

2.5.4.3 Current-Voltage

I used a LOANA solar cell analysis system by PV Tools to measure the I-V characteristics of solar cells in SIRF at UNSW. Measurements included J_{sc}, V_{oc}, FF, internal quantum efficiency (IQE), EQE, and η. Illumination was varied up to 1 sun and the output I-V characteristics were recorded. Equations (2.6)-(2.9) present how FF, η, EQE, and IQE can be calculated from IV measurements, but LOANA automatically calculated values upon measuring the solar cell.

$$FF = \frac{P_{MP}}{V_{OC} I_{SC}} = \frac{V_{MP} I_{MP}}{V_{OC} I_{SC}} \quad (2.6)$$

$$\eta = \frac{P_{max}}{P_{input}} = \frac{V_{oc} J_{sc} FF}{P_{input}} \quad (2.7)$$

$$EQE = \frac{generated\ electrons/second}{incident\ photons/second} = \frac{J_{ph}}{qA\phi} \quad (2.8)$$

$$IQE = \frac{generated\ electrons/second}{absorbed\ photons/second} = \frac{EQE}{1 - R - T} \quad (2.9)$$

For FF: V_{MP} is cell voltage at maximum power output, I_{MP} is cell current at maximum power output, and P_{MP} is cell maximum power output. For η: P_{input} is power input into the solar cell. For EQE: J_{ph} is the photocurrent generated by the cell, q is the electron charge, A is

the area of the solar cell, and ϕ is the photon incidence on the solar cell (photons per unit area per unit second). For IQE: R is cell reflectance, and T is cell transmission.

3 Development of the HF/O_3 Texturing Tool

Within Chapter 1, the initial investigation of texturing in the gas phase with HF/O_3 was reviewed and it was determined that the equipment imposed limitations on the investigation. Thus, to further investigate HF/O_3 GaPTex, the first stage of this project was to design a new texturing tool.

3.1 Tool Design

3.1.1 Limitations of Prior Tool

M. Cohen's GaPTex tool design successfully demonstrated:

- Si could be textured by HF/O_3 in the gas phase.
- Reflectance reduction from texturing was competitive with other industrial techniques, achieving 12% on DWS mc-Si surfaces.
- The technique was industrially applicable as it was able to texture full-sized industrial Si-wafers.

However, this initial design suffered several drawbacks:

- Regardless of the modifications to the incoming gas to the texturing chamber, texturing uniformity was poor across the wafer surface. Uniformity across an entire 156 mm × 156 mm wafer was not demonstrated.
- The sample temperature and the HF-reservoir temperature were not independent parameters.
- The maximum incoming reaction gas temperature to the reaction chamber was limited to 35 ºC, regardless of the heating provided by the water-bath up to 80 ºC.
- The heating of the sample was slow due to thick PTFE reaction chamber walls and a subsequent air gap between the chamber walls and the sample. Thus heating the sample to the highest operating temperature would take several hours, slowing overall experimental productivity.
- The sample temperature could not be verified with the reaction chamber design.

- The sample handling to insert and remove wafers was difficult for the operator.
- Condensation formed during experiments on the inside of the sample holder, making sample handling difficult due to the necessary safety aspects required when working with HF.
- Whilst GaPTex was demonstrated in some areas of full-sized industrial wafers, this set-up was limited to processing only industrially sized wafers, becoming very material-intensive since only such large samples could be placed in the chamber.

It was clear that while the tool used successfully demonstrated GaPTex, a re-design of the tool was required for further research.

3.1.2 New Tool Design

As well as mitigating the tool drawbacks in section 3.1.1, several other features were noted as desirable additions to the new tool design:

- Increasing the sample temperature range beyond that of the water-bath, ideally to at least 200 ºC, depending on the operating temperatures of the HF/O_3 resistant materials required.
- Maximising the extraction of HF-vapour from the reservoir, possibly by decreasing the bubble size in the HF-reservoir further, or by increasing the number of HF-reservoirs.
- Improving the quantitative aspect of the tool with the addition of flow meters to verify the output from the O_3 generator and a thermocouple to determine the sample processing temperature.
- Improving the ease of use for operators.
- Minimising the chemical reservoir and sample heating time.
- Increasing the number of chemical reservoir lines with the possibility of using other chemical species in texturing, such as water, or HCl.
- Possibly use illumination such as UV in texturing, as UV has been shown to increase Si oxidation rates when using O_3 to temperatures as low as room temperature [196].

With the aid of Tetreon Technologies, a design to accommodate the desirable qualities listed above, as well as mitigating the tool drawbacks in section 3.1.1, was created. Figure 3.1 presents the initial tool design schematic as well as a picture of the new tool installed in the Semiconductor laboratory.

a)

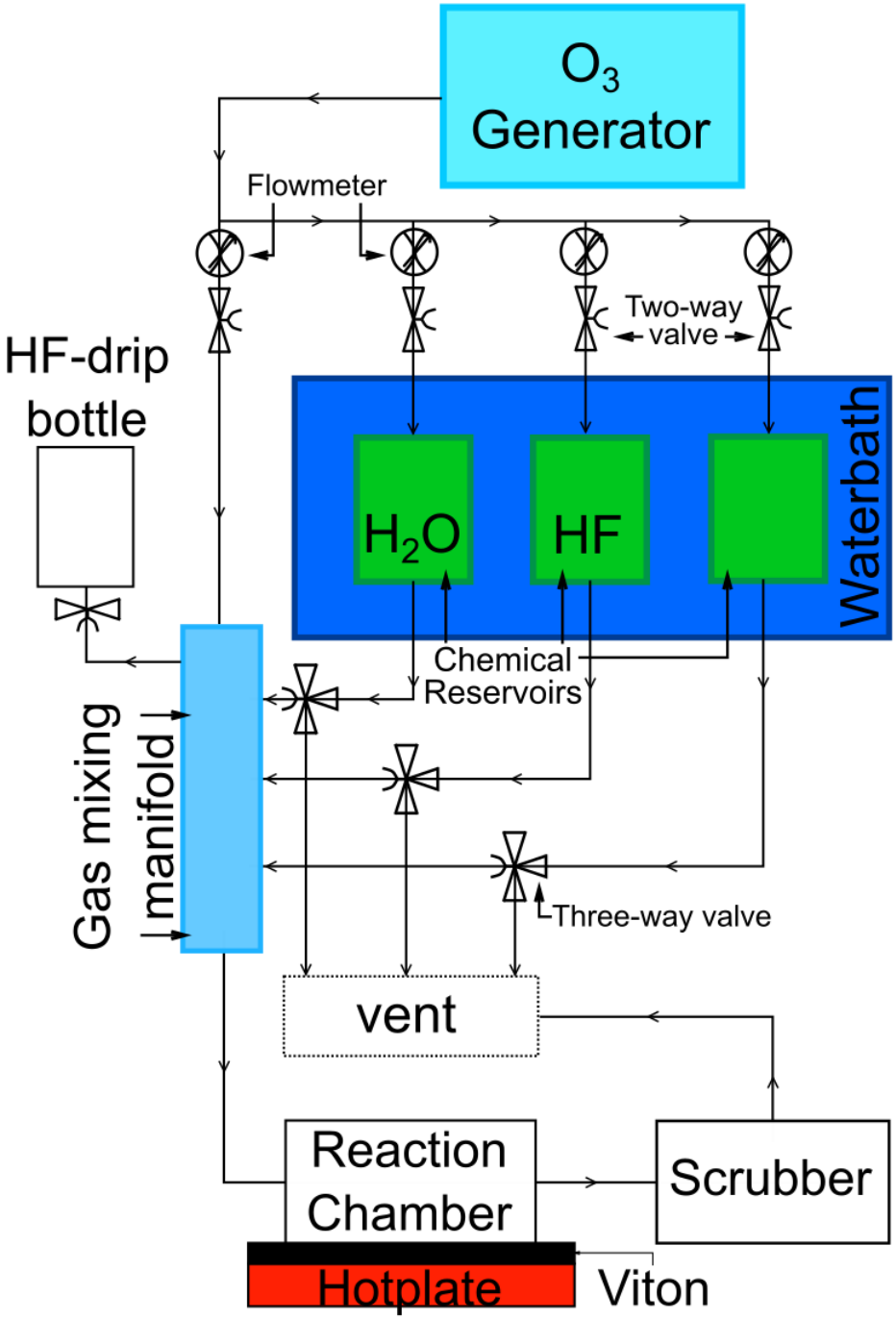

b)

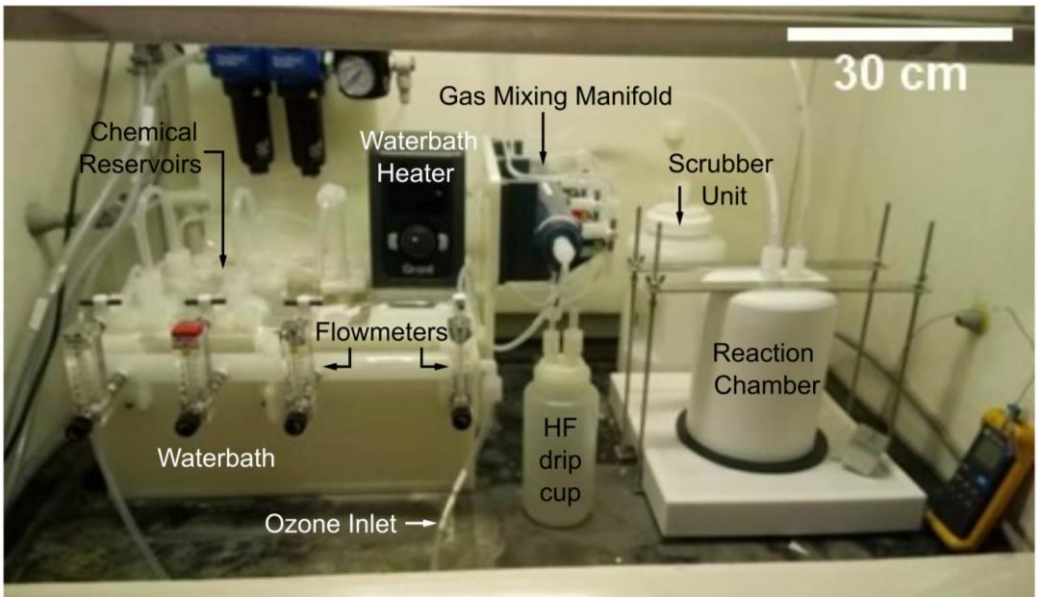

Figure 3.1 a) Design schematic of the new HF/O_3 GaPTex tool b) the newly designed tool installed in the fume-cupboard at the Semiconductor laboratories. The ozone generator is beneath the fume-hood and the source gases are to the left of the fume-cupboard.

O_3 was generated by the same Primozone GM-1 Ozone Generator as used in the prior work. The generatsor was moved out of the fume-cupboard into a ventilated cabinet, creating more space for equipment that necessitated the fume-cupboard. The source gases for the O_3 generator were changed to include industrial-grade N_2, as Primozone recommended a mixture of ~94% O_2 with the remainder being N_2 for generator longevity. Figure 3.2 presents the schematic of the two source gases and the flowmeters used to achieve the correct source gas ratio for the O_3 generator.

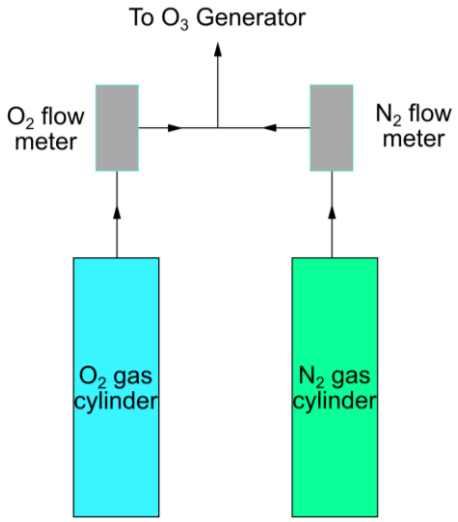

Figure 3.2 Source gases of O_2 and N_2 for the O_3 generator, connected to flow meters to make the appropriate gas ratio for the O_3 generator.

After generation, O_3 was routed into the fume-cupboard where it could either interact with chemical species in a heated water-bath or by-pass directly to the reaction chamber. A Grant TC120 Heated Circulator was used to heat the water-bath and the chemical reservoirs housed within it. The accuracy of the water-bath heater was checked using a thermometer in four locations across the water-bath and was found to be accurate within ± 0.5 ºC of the digital display of the heater. Three different chemical reservoir lines were installed within the water-bath: a de-ionised water line, a 40 wt% HF line, and the third line was left empty for future chemical investigations. Flow meters were attached before each chemical line, including the O_3 by-pass, to verify the gas flow from the O_3 generator. Within each chemical line, the number of reservoirs was increased to maximise the HF-vapour content in the reaction gas from the prior GaPTex tool. Determining the increase in the number of reservoirs was performed by using humidity measurements with a ATP AHTD-625 High Accuracy Thermo-Hygrometer. De-ionised water reservoirs were used as HF and water have similar thermal properties, thus humidity results with water would accurately describe the results with HF whilst ensuring operator safety. Measurements were performed at room temperature (22 ºC) to determine a lower bound for evaporation and the fume-hood extraction was turned off to better mimic the operating conditions of a contained system of gas contained within the gas lines. The baseline humidity in the fume-hood was measured at 48.1% ± 0.2% and the humidity directly exiting the de-ionised water reservoir was 73.3% ± 2.2%. To further increase humidity, and thus the total HF evaporation into the reaction gas, the number of chemical reservoirs per line was increased to two. Three reservoirs were discussed, but due to the confines of space within the water-bath this was not deemed necessary at the time. In addition to increasing the number of chemical reservoirs, the bubbler-coil used within each reservoir was changed to incorporate a greater quantity of HF-vapour into the reaction gas. A porous PTFE diffuser from Ozone Solutions provided a pore diameter of 20 µm, decreasing bubble size from the bubbler-coil where perforation diameter was < 2 mm. The maximum flow rate quoted for the porous diffuser

was 20 L/min, maximum operating pressure of 7.0 bar, and maximum temperature of 100 ºC.

All gas lines exiting the chemical reservoirs, as well as the ozone by-pass line, met in the gas mixing manifold. A HF-drip bottle was installed beneath the mixing manifold to drain any HF condensation. After the gas mixing manifold, the reaction gas was directed into the PTFE reaction chamber for texturing. The reaction chamber was separated from the water-bath in the new design, enabling separate temperature control. The reaction chamber was a 5000 ml PTFE cylindrical container with one open end pressed against a gasket to ensure a secure seal to contain reaction gases. The reaction chamber was clamped to a PTFE hotplate using two clamps, with a Viton gasket between the chamber and the hotplate to contain gases. A thin sheet of PTFE was placed between the hotplate and the Viton gasket to maintain sample heating whilst protecting the surface of the hotplate. The gas outlet from the reaction chamber was attached to a scrubber unit before venting out the back of the fume-cupboard.

3.1.3 Safety

During the tool re-design, maintaining operator safety was taken into consideration at each design stage, including material choice, operating temperatures, and overall design.

For HF/O_3 resistance the materials selected were: PFA for the gas lines, PTFE for the reaction chamber, Viton for the gasket, PTFE for the sheet between the hotplate and sample, PTFE for the water-bath, and HDPE for the chemical reservoir bottles. All equipment used for replacing HF in the chemical reservoirs or changing out the reservoirs themselves was also HF-resistant.

To prevent material degradation, the operating temperature range of the chosen HF/O_3 resistant materials was taken into consideration to define tool operation limits. HF reservoirs were kept at ≤ 80 °C, as the maximum continuous service temperature of Fisher-Scientific's thick-walled HDPE bottles was quoted at 120 °C. The hotplate operating temperature was primarily dominated by the Viton gasket, as it was in direct contact with the plate, but the

reaction chamber was also taken into consideration as it sat close to the hotplate surface, atop the gasket. Viton can act as a seal indefinitely up to 204 °C; however, it has been shown to provide high sealing performance up to 255 °C [197] and was tested at 250 ºC for 70 hours with no significant degradation [198]. It has also been quoted to provide an excellent seal for more than 48 hours at 315 °C [199] and a maximum service temperature of 350 ºC [200]. PTFE's upper limit operating temperature is 260 °C [201]–[203]. To balance the interest in investigating a wider range of sample texturing temperatures against the necessary safety requirements, the maximum hotplate operating temperature was set to 250 ºC to maintain a seal between the hotplate and reaction chamber and maintain structural integrity of the reaction chamber.

Not only was the new tool design used to broaden operating parameters and mitigate prior operating issues, but it was also designed to further minimise the risk of working with hazardous substances. All chemical reservoirs were housed in a PTFE water bath, thus any compromises to the reservoirs were contained in a HF-resistance container and were diluted in the water. All gas-line connectors were a push-and-screw fit, enabling a secure connection between different locations of the texturing tool. The prior tool directly vented exhaust gases out the back of the fume-cupboard, without prior neutralisation. From discussions with the Departmental Safety Officers, it was recommended a scrubber unit be installed to neutralise HF before venting out the back of the fume-cupboard. However, vent lines were also installed after the chemical reservoirs directly out the back of the fume-hood for emergency use in case of an overpressure in the system, as this was the single region where overpressure could be generated by improper operator use. Additionally, the Viton gasket was visually inspected at the start of each experimental session and was swapped out if any visual degradation has occurred or if it had been in use for one month. Alongside inherent design features to minimise risk, I wrote a standard operating procedure (SOP) for users detailing typical operating conditions, an operating checklist, a starting-up procedure of the equipment, a shutting-down procedure of the equipment, a detailed procedure for changing the HF in the reservoirs, emergency procedures regarding HF spills of small

volumes (< 100 ml) and large volumes (> 100 ml), emergency procedures of O_3 leaks. Lastly, a series of documentation alongside the SOP was generated with the aid of the Departmental Safety Officers. I wrote COSHH for O_3, and HF, and an equipment risk assessment for the entire GaPTex tool. In the case of changing the HF in the reservoirs, a HF buddy was required in the lab throughout the procedure and was briefed on the procedure thoroughly before undertaking the work. All documentation was discussed with the Departmental Safety Officer and signed off before the equipment became operational, with a copy stored outside the lab for operators to use.

3.2 Tool Development

3.2.1 Initial Tool Performance

Before texturing with the new tool, it was determined if the new design features mitigated the issues from the prior tool. Firstly, the maintenance of reaction gas temperature between the chemical reservoirs and the reaction chamber was verified. To determine the upper-temperature limit the reaction gas could be heated to, the water-bath heater was set to the maximum operating temperature of 80 °C. The temperature at the exit port of the de-ionised water reservoir and at the exit of the gas inlet line to the reaction chamber was monitored using a thermocouple. At the exit of the gas inlet to the reaction chamber, the vapour temperature was 20.0 °C. Thus, the new tool design did not meet the requirement of maintaining reaction gas temperature between the chemical reservoirs and the reaction chamber.

The second new feature of the upgraded tool was to make the sample temperature independent from the chemical reservoirs and heat samples to temperatures beyond those used in the prior tool. By removing the reaction chamber from the water-bath and housing it atop a hotplate, sample temperature could be independently controlled from the chemical reservoirs and increased beyond the water-bath heater limit. Furthermore, the sample temperature could be verified by using an independent thermocouple from the hotplate display. Therefore, the requirement of sample temperature being independent of the

chemical reservoirs, increasing temperature beyond 80 °C and verifying sample temperature was met.

The third feature evaluated was the use of a porous PTFE diffuser tubing for bubbling O_3 through the chemical reservoirs, to increase HF content in the reaction gas. An upper limit operating pressure was quoted for the porous tubing but no lower limit, thus before using the porous tubing in the HF-reservoirs the minimum operating pressure was determined to prevent any overpressure occurring in the tool. The lower bound of operating pressure of the porous diffuser was tested by submerging the tubing in a beaker of water and passing compressed air through. A flow meter was added before the porous tubing to determine what flow rates could be achieved to the corresponding pressure. The pressure of the compressed air was set in 0.5 bar increments from 0.5 bar to 6.0 bar. Figure 3.3 depicts the relation between pressure and flow rate. Within the operating pressure range of the O_3 generator of 2.0 – 3.0 bar, the maximum flow rate measured was limited to 1.0 L/min or was unable to flow. Therefore, while the porous diffuser tubing had the potential to increase the content of HF vapour in the reaction gas, there was a safety concern of generating overpressure in the system and compromising structural integrity.

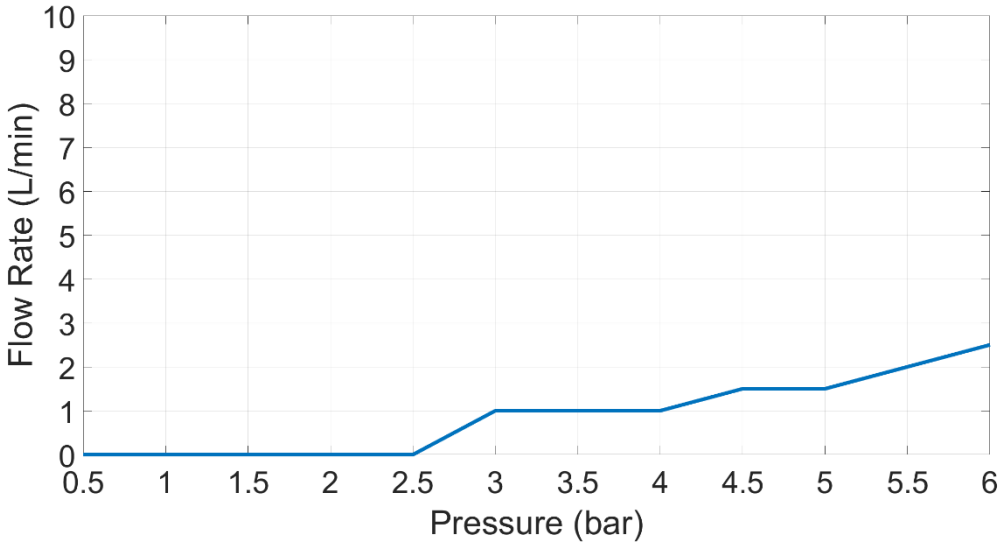

Figure 3.3 Range of flow rates the porous tubing produced as a function of incoming gas pressure.

Sample handling and the ability to test a variety of sample sizes was met with the new design. Samples were laid flat atop the hotplate, without the need of a holder, allowing

sample sizes less than full wafers to be tested. Furthermore, as samples were laid flat and temperature control was independent of the chemical reservoirs, if any condensation formed on the surface, it could be evaporated by increasing hotplate temperature post-processing before handling samples.

Lastly, an unforeseen issue occurred with the new design. HF condensation from gas lines spat onto the sample surface, causing large surface texturing non-uniformities. Figure 3.4 shows the non-uniformity of textured Si from HF spat onto the Si. The surface remained high reflectance where HF landed and was localised to beneath the gas inlet, whilst regions farther away were able to successfully texture.

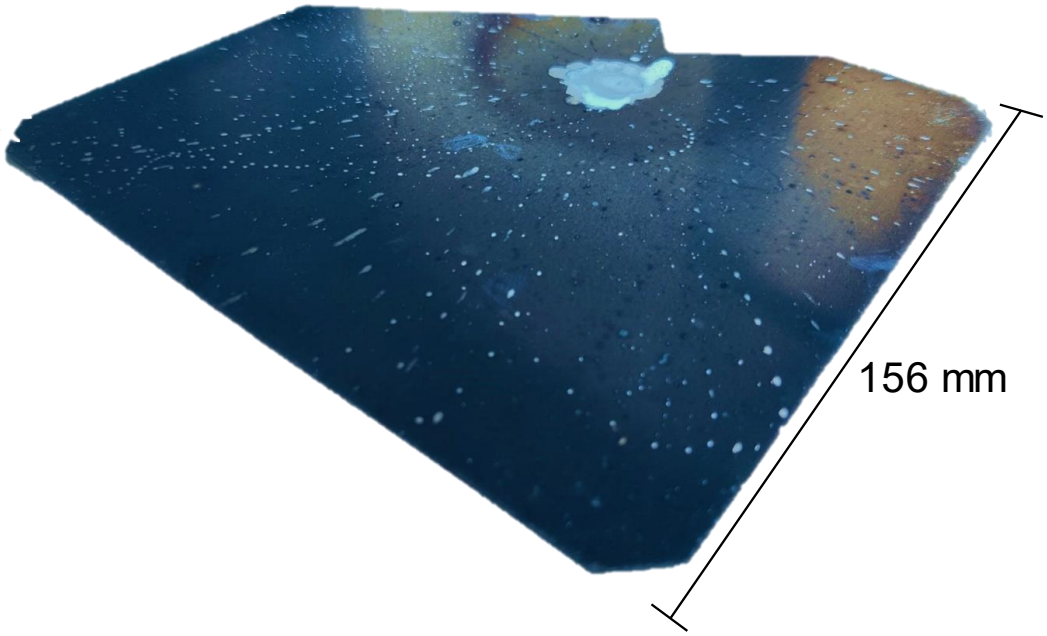

Figure 3.4 Camera image of a textured sample with HF spat onto the surface from the gas inlet during texturing.

3.2.2 Tool Optimisation

The tool design was optimised to mitigate or minimise the issues described in section 3.2.1. Table 3.1 presents a summary of the new GaPTex tool design features, if they successfully overcame the prior issues, or the new desired operating features, and if any further optimisation was required to make the tool operate as desired. Figure 3.5 and Figure 3.6 present the final, optimised tool used in the rest of this work. To maintain the reaction

gas temperature between the chemical reservoirs and the reaction chamber, the gas lines between the two points were shortened and insulated using the Thermawrap foil wrap insulation. Figure 3.6a) presents the new, insulated, floating rig between the two points. Gas temperature at the gas inlet to the reaction chamber was remeasured using the same method as described in section 3.2.1 and was found to be 55.6 °C ± 0.6 °C on average across 10 minutes. Whilst gas temperature was not completely maintained between the two points, it was improved from the prior tool and the first design iteration of the new tool.

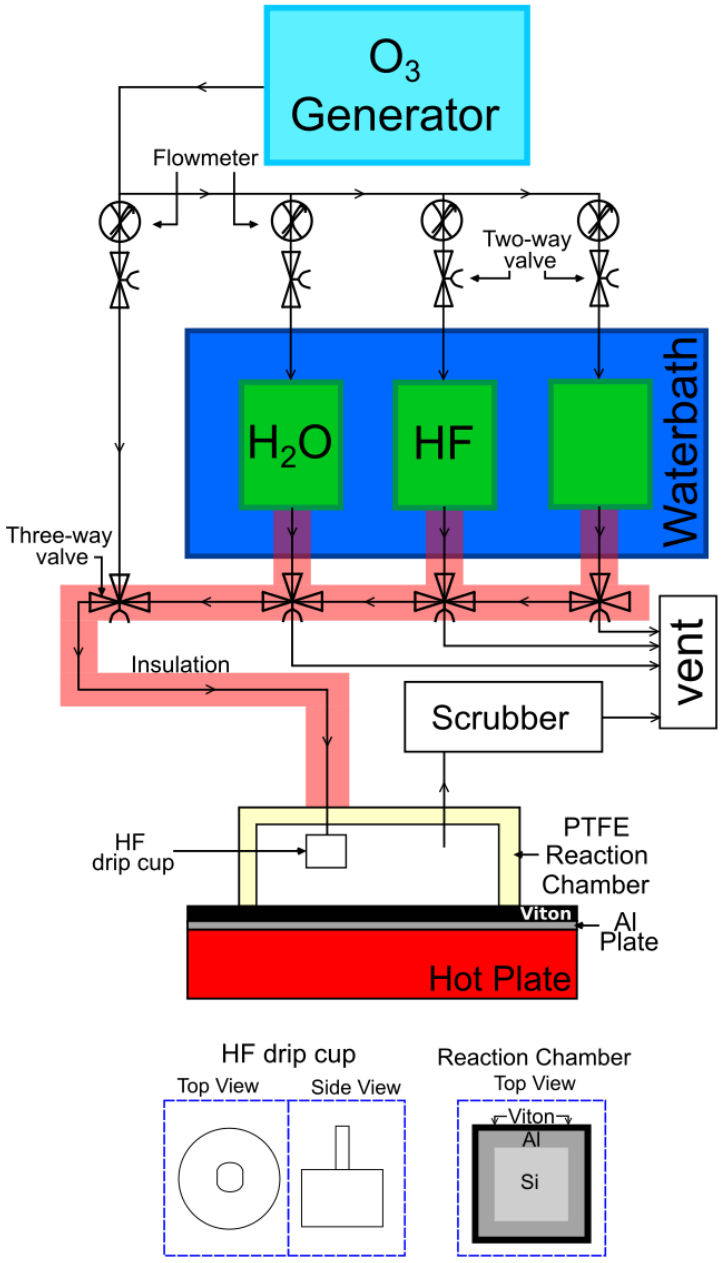

Figure 3.5 Schematic of the optimised HF/O_3 texturing tool, including insulated and shorted gas lines to the reaction chamber and a HF-drip cup.

a)

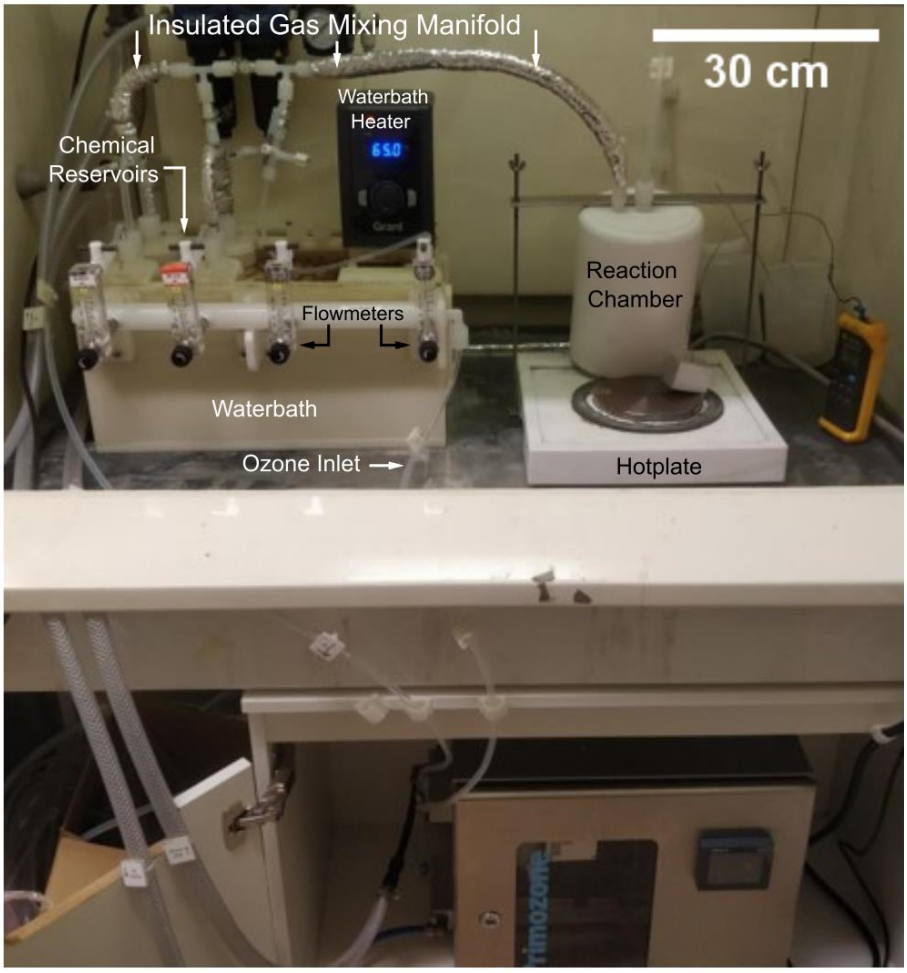

b)

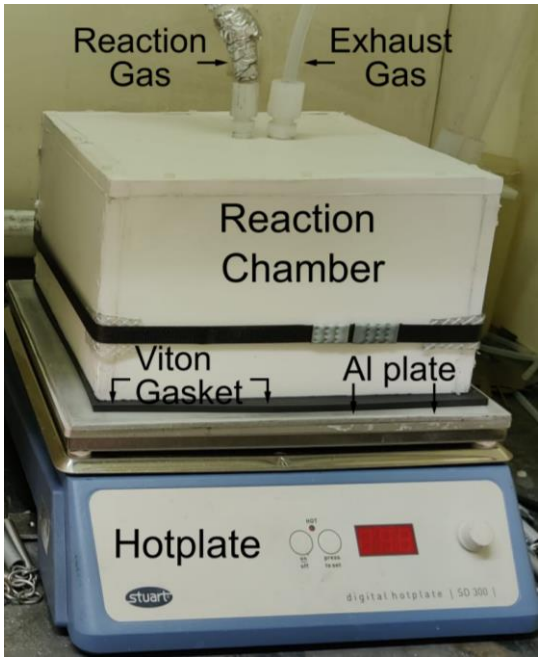

Figure 3.6 a) The upgraded texturing tool including the shortened, insulated, floating gas manifold b) the upgraded reaction chamber to texture full-sized industrial Si-wafers atop the hotplate protected by the Al-plate.

To mitigate the concerns of using the porous diffuser tubing in the chemical reservoirs, the prior bubbler-coil was tested using the set-up described in section 3.2.1. The resulting relationship between inlet gas pressure and flow rate is presented in Figure 3.7. There are no safety concerns when using the bubbler-coil, as in the operating pressure range of 2.0 – 3.0 bar, flow rates of 5.5 – 6.5 L/min were achieved. Thus, the bubbler-coil was used in the chemical reservoirs instead of the porous tubing to mitigate the safety concerns of causing an overpressure in the tool. To imitate the porous diffuser further, the number of perforations was increased in the bubbler-coil.

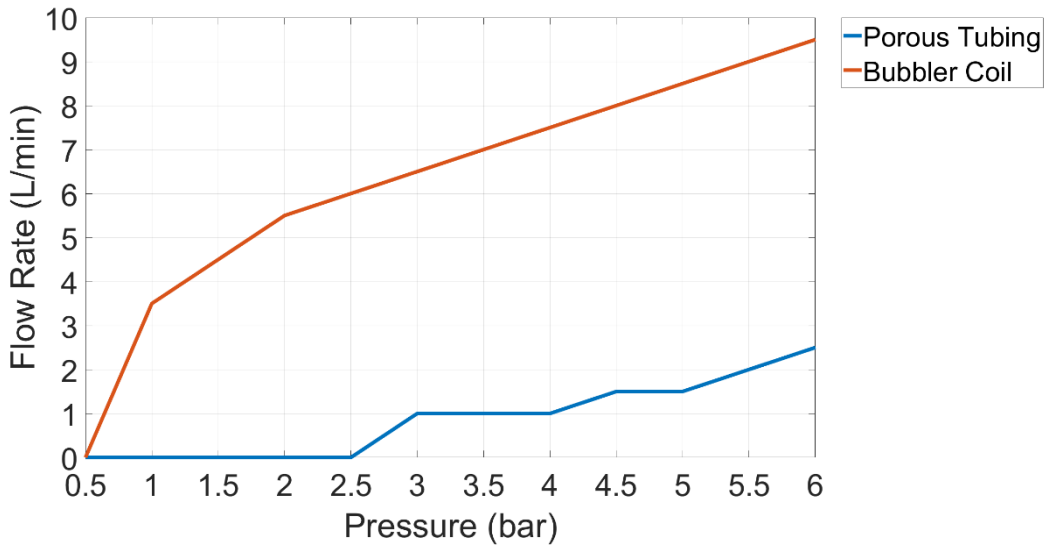

Figure 3.7 Flow rate as a function of inlet gas pressure for both the porous tubing and the bubbler coil.

To avoid HF dripping onto the sample surface and causing texturing non-uniformities, a detachable HF drip-cup was fitted to the end of the reaction chamber gas inlet pipe. The cup was made from PTFE to resist the reaction gases. The stem of the drip-cup was non-circular in cross-section to balance griping against the inlet tube alongside emitting reaction gas into the reaction chamber. The drip-cup was emptied every three experiments to avoid any collected droplets of liquid being flung onto the sample surface beneath. Figure 3.8 presents the drip-cup.

Figure 3.8 HF drip-cup to catch any condensation from the gas inlet, preventing it from hitting the Si surface.

Lastly, the reaction chamber was changed to allow texturing of full 156 mm × 156 mm wafers. An Al-plate was added atop the hotplate to protect the hotplate surface and improve thermal conductivity between the sample and the hotplate surface over the previously used PTFE sheet. Figure 3.6b) presents the new reaction chamber atop the Al-plate and hotplate.

Table 3.1 A summary of the design requirements, initial design changes to meet them, the success of the design changes, and any subsequent modifications if the initial design implementations did not meet the design requirements.

Tool Operating Feature	Initial Design Implementation	Operating Requirement Met	Design Modification	Operating Requirement Met
Increase the reaction gas temperature beyond 35 ºC	New design and layout of the texturing tool.	No – the new layout of the texturing tool limited reaction gas temperature to 20 ºC	Gas mixing manifold removed, floating gas mixing manifold installed, all chemical lines thermally insulated.	Yes – reaction gas temperature range was increased up to 55.6 °C ± 0.6 °C.
Remove the dependency between the sample temperature and chemical reservoirs temperature	Sample chamber was removed from the water-bath and placed atop a dedicated hotplate.	Yes		
Increasing the sample temperature to at least 200 ºC	Sample chamber was removed from the water-bath and placed atop a dedicated hotplate.	Yes		
Maximising the extraction of HF-vapour from the reservoir	Number of chemical reservoirs per chemical line increased to 2.	Yes		
	Micro-Porous diffuser inside the chemical reservoirs to increase the	No – pressure required to operate the micro-porous	Revert back to prior bubbler-coil design with increased	Yes

	contact area between the incoming gas and the liquid chemical.	diffuser tubing was beyond that in the GaPTex tool.	perforations to maximise gas-liquid contact.	
Improving the quantitative aspect of the tool	Flow meters installed to verify flow after O_3 generator and before each chemical line.	Yes		
	Thermocouple used to verify hotplate temperature and thus sample temperature	Yes		
Improving ease of use for operators	Sample chamber removed from the water-bath and reaction chamber changed to a clamp mechanism	Yes		
Reducing heating time for Samples	Sample placed atop an Al-plate in contact with a hotplate.	Yes		
Processing a range of sample sizes	Samples no longer housed in a one-size slot-holder but laid flat atop a hotplate.	Yes		
Increase the number of chemical reservoir lines for alternative chemicals to be used	Three different chemical reservoir lines installed, one for water, one for HF, and an un-designated one.	Yes		
-	-	HF condensation spitting onto sample surface causing texturing non-uniformities.	Detachable HF drip-cup fitted to the end of the inlet pipe in the reaction chamber to allow gas in but catch droplets.	Yes

3.3 Chapter Summary

A new HF/O_3 GaPTex tool has been presented in this chapter. Issues from the prior tool were reviewed as well as additional desirable capabilities. A new tool design was created, implemented, and optimised to balance the desired improvements against the necessary safety measures. The next chapter will present the texturing results using this new tool.

4 Si Surface Chemistry and Gas-Phase Texturing

This chapter presents the first findings using the new GaPTex tool, with a focus on how the surface chemistry of the Si substrates relates to the texturing efficacy, uniformity, and reproducibility.

4.1 Texturing Uniformity and Reproducibility

Whilst the new GaPTex tool has the same concept of texturing Si as the prior tool (passing an HF-O_3 gas mixture across a Si surface), it was unclear if the same nominal operating parameters would produce the same texturing results. Therefore, the texturing recipe that produced the lowest reflectance for DWS-Si on the old tool was repeated on the new tool. The texturing recipe is presented in Table 4.1. Three 4 cm × 4 cm specimens were used to determine the reproducibility of the texturing recipe on the new GaPTex tool. The samples were cut from Longi substrates using the MicroAce3 dicer machine from LoadPoint. The water residue on the specimen surfaces from the dicer was removed with tissue paper and no further treatment was given to samples before texturing. Figure 4.1 presents the camera images of textured samples and Figure 4.2 presents the WAR of each sample with their corresponding standard deviation as the error bars. The WAR value for texturing with the prior tool in Figure 4.2 is taken from M. Cohen's thesis [183].

Table 4.1 Operating parameters of the optimal texturing recipe for DWS-Si from the prior tool.

Operating Parameter (units)	**Values**
Processing Time (min)	20
Ozone Concentration (wt%)	20
Gas Flow Rate (L/min)	3
HF Reservoir Temperature (ºC)	50
Sample Temperature (ºC)	50

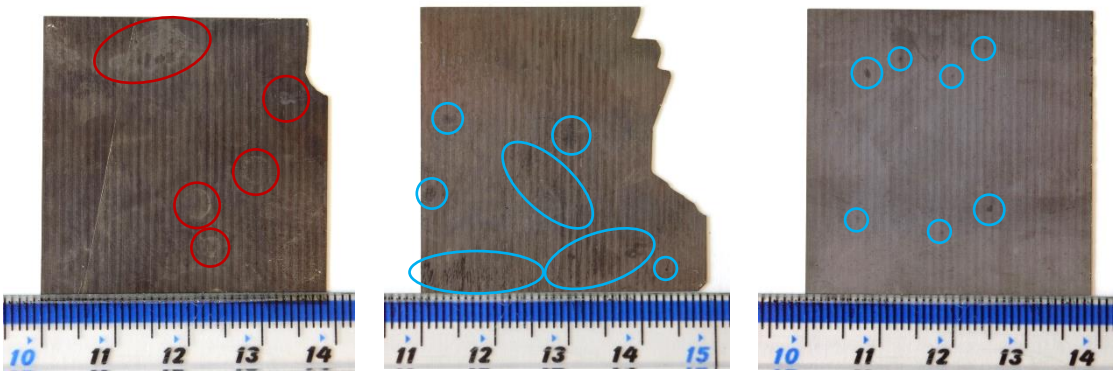

Figure 4.1 Visual appearance of the three Si specimens after GaPTex, using the recipe in Table 4.1. Blue circles indicate regions of lower reflectance to the local area. Red circles contain regions with higher reflectance. The vertical lines on each sample are the striations from the wire-sawing process.

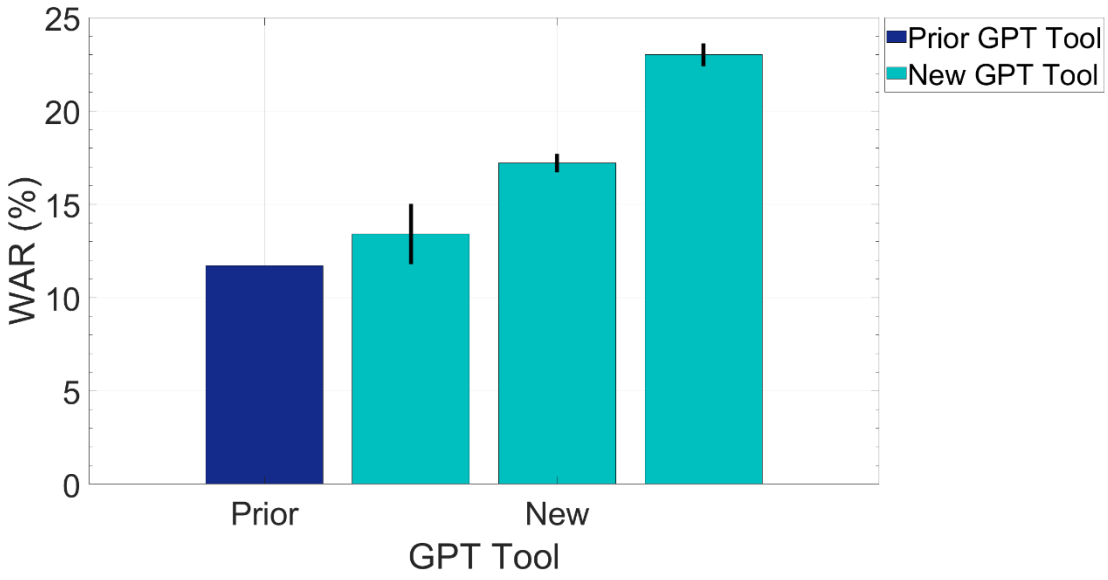

Figure 4.2 The WAR of samples textured either using the GaPTex tool from prior work or the new GaPTex tool.

Figure 4.2 shows that the surface reflectance from texturing with the old GaPTex tool could not be reproduced on the new GaPTex tool. The WAR achieved in prior work when using the texturing recipe in Table 4.1 was 11.7%. However, the WAR measurement from prior work was not performed on the optical measurement set-up used in this project. The WAR measurement was instead indirectly performed using a Filmetrics 500 light source, an Edinburgh Instruments 2-inch diameter integrating sphere, a Thorlabs SM05PD1A silicon photodiode, and an ammeter. Light was directed from the Filmetrics light source, along an optical cable into the integrating sphere where the incoming light hit the sample at normal incidence. Post-sample interaction, light was collected at the output port of the

integrating sphere and converted to a current via the Si photodiode, which was then quantified by the ammeter. Current was converted to WAR by establishing a relationship between the two parameters. WAR measurements of four samples were performed at UNSW, the current of these four samples was then measured in the prior optical set-up. WAR versus current was plotted for these samples and the resulting graph was used to convert further current measurements in the project to WAR measurements. Whilst this method allowed optical measurements to be performed within the scope of the previous project, ultimately it was an indirect measurement of surface reflectance and thus the precision was less than the direct optical measurements performed in this project. Therefore, whilst the WAR of 11.7% was quoted for the best result in the prior project, there will be an error associated with this, unfortunately this was not discussed further in the prior work and thus cannot be quantified. When the texturing recipe from Table 4.1 was performed with the new GaPTex tool, WAR was measured at 13.4% ± 1.5% up to 23.0% ± 0.5% for the three specimens. A change in WAR between the two projects by a specific factor would not be unexpected, as the texturing tool and optical measurement set-up changed between projects. However, what is unexpected is that the WAR of the three samples textured in the new tool varies when the same texturing tool and optical measurement technique was used for all three specimens. The broad variation in WAR demonstrated in the new GaPTex tool shows a lack of texturing reproducibility between samples in the current work.

Figure 4.1 presents the lack of texturing uniformity across the sample surfaces and between samples. Dark spots and varying shades of grey are circled on each sample's surface in Figure 4.1, demonstrating the lack of visual uniformity. In addition, the pattern of the dark spots appears random and is not reproduced between samples, thus demonstrating a lack of texturing reproducibility between samples for the same texturing recipe. M. Cohen does not present the uniformity of the sample that achieved 11.7% WAR with this recipe, thus a comparison cannot be made concerning uniformity between the old and new GaPTex tools.

The source of the lack of reproducibility and uniformity is unclear. The change in reflectance is not by a specific value, or a specific factor, which would have indicated a constant change between prior and current work. In addition, the texturing pattern of dark spots on the sample surfaces is not the same pattern on each sample surface, also indicating an uncontrolled variable occurring between experiments. One could suggest that the texturing tool is the source of the unaccounted parameter. However, the new GaPTex tool was evaluated in Chapter 3 and its operation was deemed reproducible. Yet there is one parameter that was not analysed in prior work and thus far has not been analysed in this work: the specimens. The Longi substrates used are the same substrates used in prior work, where difficulties were encountered with texturing reproducibility and uniformity. In the prior work, wafers were taken from the wafer storage box and with no cleaning were inserted into the GaPTex tool for texturing. In this work, specimen processing entailed dicing samples using the MicroAce3 dicer, removing residual water from the dicing process with tissue from the sample surface and then texturing the sample. In both cases, specimens did not undergo any cleaning before texturing. Therefore, any contamination from the manufacturer or the dicing machine was present on the surface during texturing. Specifically considering the MicroAce3 dicer as a source of contamination, samples were diced using a blade that was not cleaned between specimens and is used by multiple users and research groups. Contaminants from the cutting blade would be transferred across the entirety of the sample surface in a non-uniform distribution, as the water used to cool the cutting blade also covers the samples. As changes in chemistry can affect the texturing mechanism, the uncontrolled contamination from the dicer and the manufacturer could account for the lack of texturing uniformity presented in Figure 4.1 and the lack of reproducibility shown in Figure 4.2. Therefore, to achieve uniform and reproducible texturing, sample surface chemistry must be investigated further.

4.2 Texturing dependence on Si surface chemistry

4.2.1 Sample cleaning

The effect of Si surface chemistry on texturing was investigated by varying wafer cutting methods and introducing sample cleaning. Figure 4.3 presents the processing sequence of the six sets of samples used, each of which contains three samples. All sets were prepared by scribing Longi substrates with a diamond-tipped pen to cleave samples from a wafer, thus avoiding contamination from the MicroAce3 dicer. The first sample set investigated the effect of contamination from the wafer manufacturer and therefore underwent no further processing after scribing with the diamond-tipped pen. The remaining five sample sets each underwent a different cleaning route to determine if texturing reproducibility and uniformity could be improved, including acetone, acetone followed by an isopropyl alcohol (IPA) rinse, IPA, de-ionised water, or RCA1 followed by RCA2 with a subsequent HF dip. The cleaning processing methods are presented in Chapter **2**. After cleaning, all samples underwent the texturing recipe presented in Table 4.1. Figure 4.4 presents the WAR for all samples, including the specimens from section 4.1 for samples prepared using the MicroAce3 dicer and without further cleaning. All camera images of the samples post-texturing are presented in Appendix I and a selection of camera images is shown in Figure 4.5.

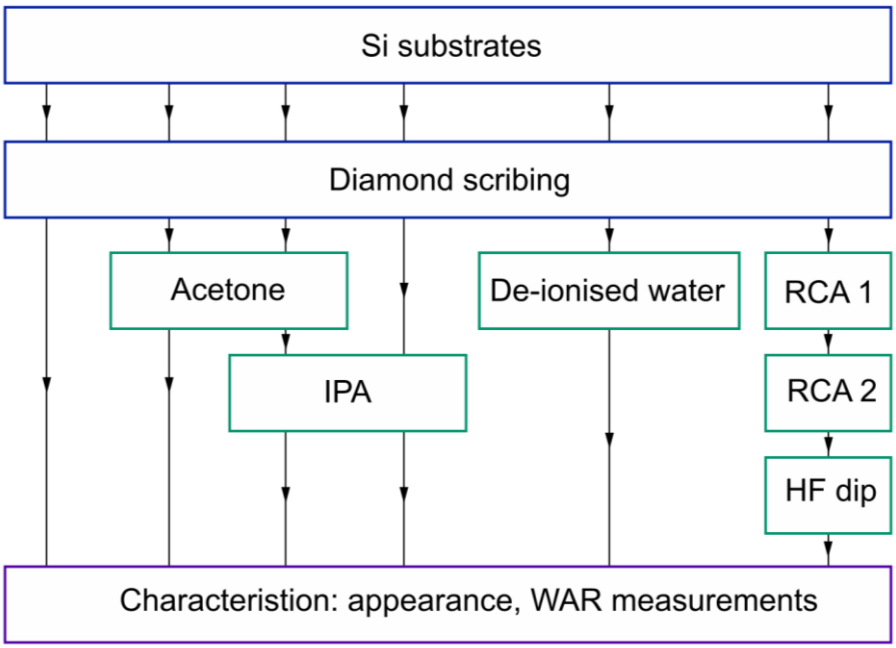

Figure 4.3 The flowchart of the different cleaning methods investigated.

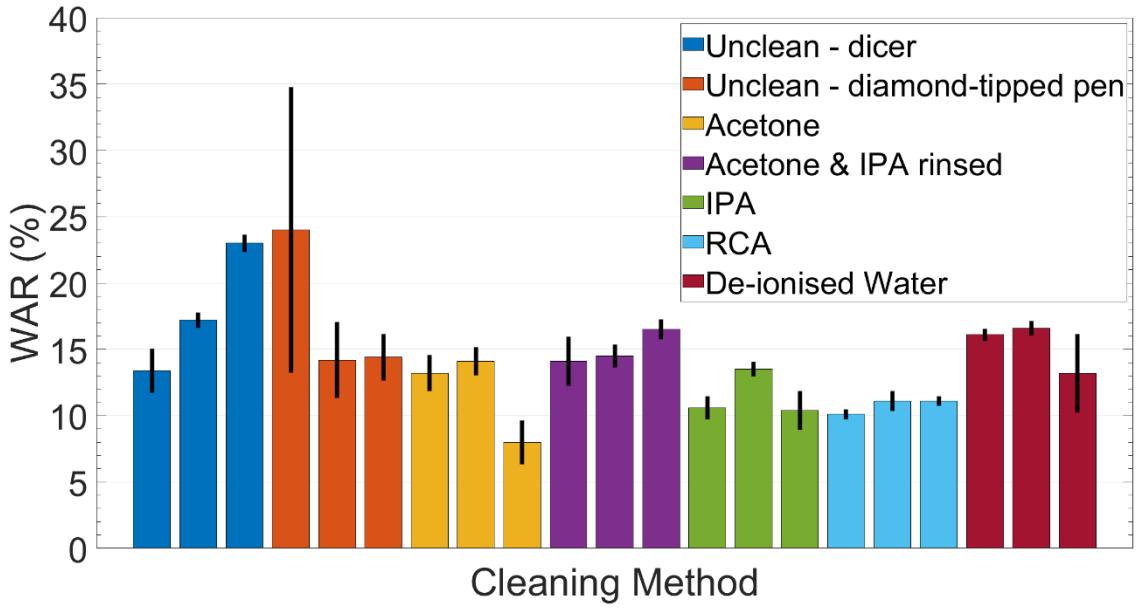

Figure 4.4 WAR for each of the five cleaning routes tested before texturing and the two processing routes where no cleaning was performed before texturing.

Figure 4.5 Camera images of samples that underwent different cleaning routes before texturing with the recipe in Table 4.1.

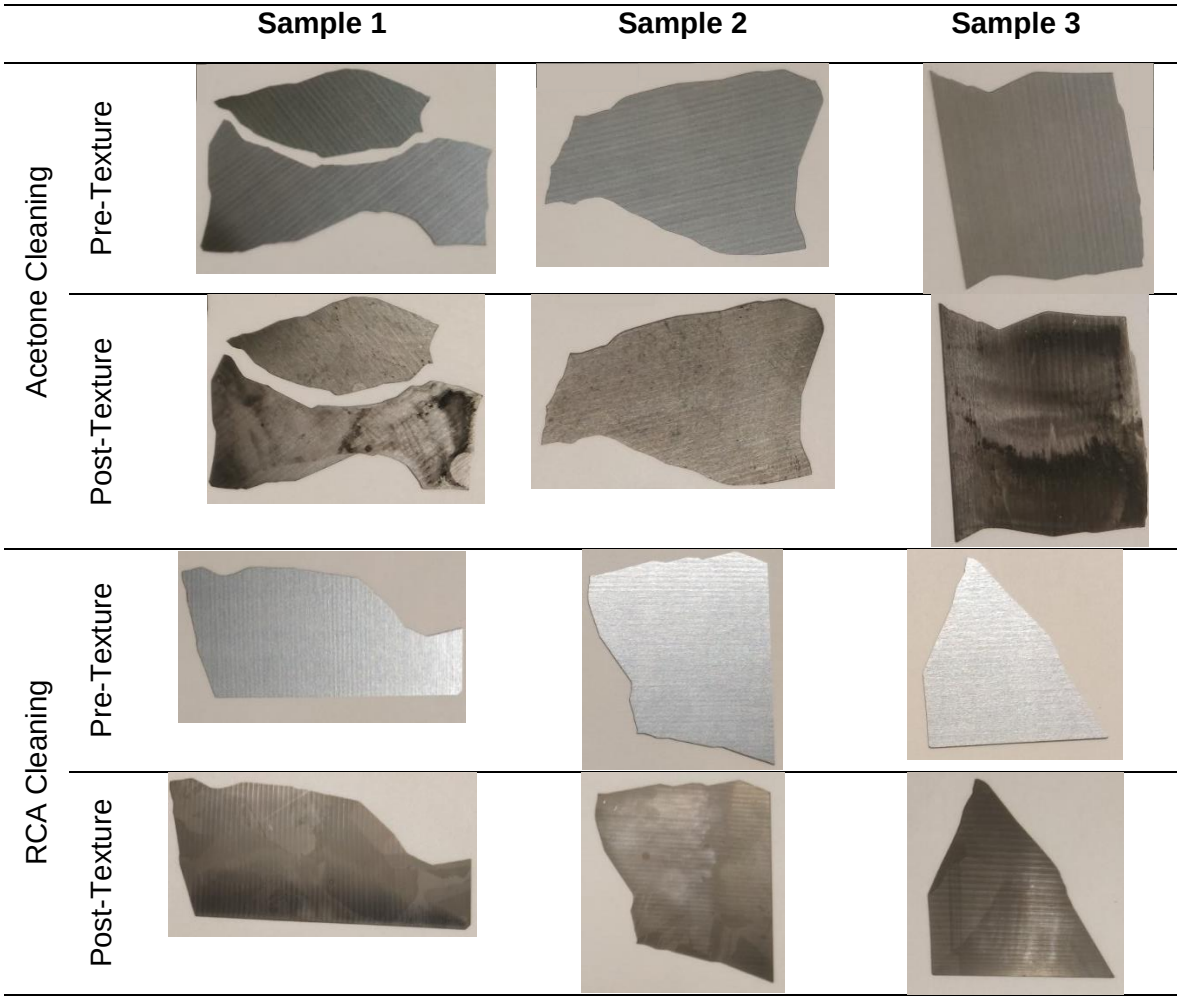

Cleaning improved texturing reproducibility and uniformity. Both sets of uncleaned samples had the greatest lack of reproducibility, where the WAR in Figure 4.4 ranged from 13.4% ± 1.5% to 23% ± 0.5% for the dicer cut samples and 14.2% ± 2.7% to 24% ± 10.6% for the diamond-tipped pen cut samples. The most reproducible WAR results came from samples that were RCA cleaned before texturing, where WAR varied by 1.0% between samples, the smallest variation in WAR for any group. RCA cleaning was the most rigorous cleaning performed thus the surface of the RCA cleaned samples were the least likely to have any contamination present and the most likely to have uniform surface chemistry. Figure 4.5 shows the RCA samples' appearance after texturing. From visual inspection, the random pattern of dark spots that occurred without cleaning in Figure 4.1 does not occur for the RCA samples, indicating an improvement in texturing uniformity and reproducibility. In comparison, the appearance of the acetone-cleaned samples in Figure 4.5 shows strong

variations in colour from silver to black on individual sample surfaces and between the samples. This lack of reproducibility is corroborated by the WAR results in Figure 4.4 for acetone-cleaned samples, which range from 8.0% ± 1.5% to 14.1% ± 0.9%. Nevertheless, all the cleaning routes performed improved texturing uniformity and reproducibility in comparison to when no cleaning was performed before texturing.

The blackest samples were not the cleanest samples. Acetone cleaning produced the darkest sample out of any processing route at 8.0% ± 1.5%. Yet, these low reflectance samples suffered a lack of uniformity and reproducibility as previously discussed. Acetone is known to be an effective cleaner for organic contaminants, yet it is difficult to remove from the surface, even when rinsing with further acetone. Therefore, the samples cleaned only with acetone likely had contamination remaining on the sample surface, which was simply redistributed across the surface during cleaning in an uncontrolled manner, causing the variations in texturing uniformity and reproducibility.

4.2.2 Surface chemistry

To confirm the presence of surface contamination, sample surface chemistry was analysed using X-ray photoelectron spectroscopy (XPS). The Oxford Materials Characterisation Service performed both the XPS measurements and the subsequent analysis to generate the surface chemical composition. The samples evaluated were Longi substrates, cut either using a diamond-tipped pen or the MicroAce3 dicer, and neither underwent any subsequent cleaning. The mean and standard deviation of the different elements on the sample surface for the sample cut with the dicer is presented in Figure 4.6, and for the sample cut with the diamond-tipped pen in Figure 4.7. The XPS spectra are presented in Appendix I.

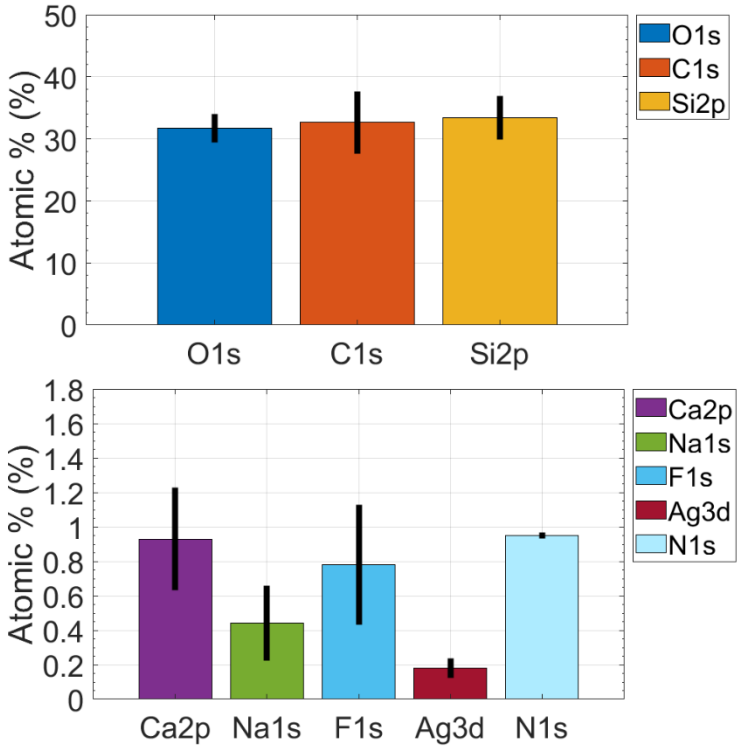

Figure 4.6 The surface atomic composition of an uncleaned Si wafer, cut with the MicroAce3 dicer.

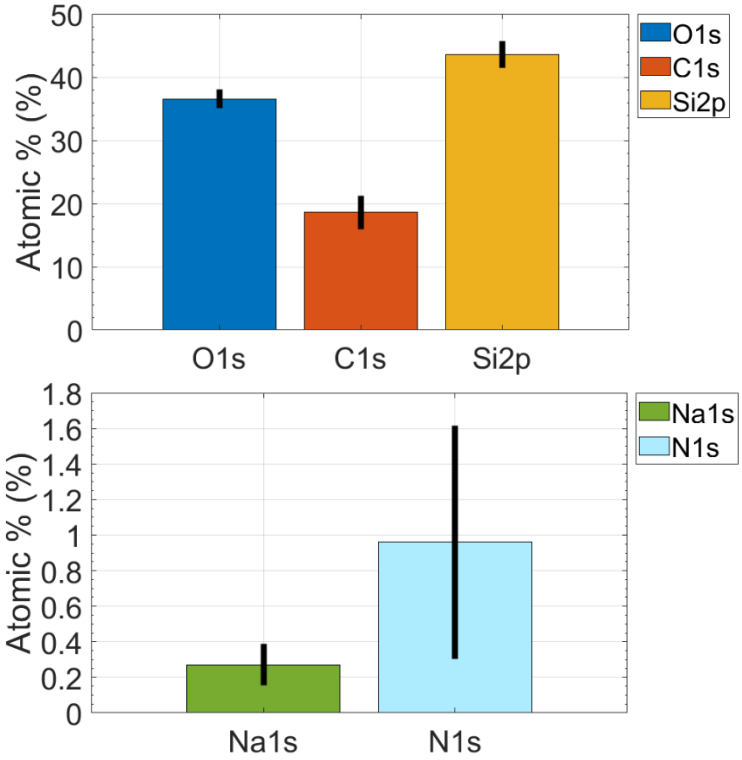

Figure 4.7 The surface atomic composition of an uncleaned Si wafer, cut with a diamond-tipped pen.

Expected and unexpected chemical species were found on both sample surfaces. From Figure 4.6 and Figure 4.7, the expected chemical species found were: Si, O - from a native surface oxide [204]–[206], C, N, Na, and Ca as they are accepted contamination sources

[207]–[213], likely from handling wafers outside a Cleanroom environment. The unexpected chemical species for the diced sample in Figure 4.6 included F, and Ag. These species are attributed to the dicing blade being shared between research groups to cut a variety of materials. The increase in the number of contaminants for the diced sample compared to the diamond-pen cut sample is likely caused by two factors. Firstly, the cooling fluid used during dicing was not rinsed off the sample surfaces but was patted with tissue paper, leaving residue behind on the surface. Secondly, the dicer machine is not intensively cleaned between users, allowing different chemical species to be transferred between samples.

4.2.3 Discussion

The reproducibility and uniformity issues surrounding GaPTex can be accounted for by the condition of the substrate surfaces. The XPS results in Figure 4.7 have demonstrated that the surfaces of the samples from the prior project would have had surface contamination of Na present during texturing, as no cleaning was performed to substrates before texturing. As this contamination was unintentional (potentially from the manufacturer and transportation), it would have been non-uniformly distributed across a sample surface and between samples. The subsequent texturing of such samples led to a lack of texturing uniformity and reproducibility. When samples were cleaned in this work, both texture uniformity and reproducibility improved, as demonstrated by the images of sample appearance in Figure 4.5 and the WAR of cleaned samples in Figure 4.4. These improvements to uniformity and reproducibility indicate consistently controlled texturing variables between texturing experiments, thus the uncontrolled variable for prior work and uncleaned samples in this work was the substrate surfaces.

Additionally, the condition of the substrate surfaces appears to change GaPTex efficacy. The blackest sample was produced by ‘cleaning’ with acetone. As previously discussed, acetone leaves a residue behind on the surface, thus it does not truly remove contamination from the surface. It is possible that the acetone re-arranged chemical species and physical

debris across the surface into a more favourable distribution for texturing, thus yielding the lowest WAR with GaPTex thus far of 8.0% ± 1.5%. However, this process was not controlled, as cleaning with acetone also yielded a WAR of 14.1% ± 0.9% on another substrate. Therefore, it would be beneficial to GaPTex for the conditions of the substrate surface to be controlled.

4.3 Summary

In this chapter, the importance of the Si surface chemistry to texturing was demonstrated. Uncleaned surfaces led to poor texturing uniformity and reproducibility, which accounted for the issues faced during the prior GaPTex project. XPS results confirmed the presence of contamination species for the uncleaned specimens used in prior work and this work. However, the lowest reflectance sample was achieved during acetone cleaning, attributed to the potential redistribution of surface contamination on the sample surface; thus, indicating that contamination may be beneficial to increasing texturing efficacy. The next chapter will investigate a controlled introduction of a chemical species to the wafer surface with the aim of aiding texturing efficiency, uniformity, and reproducibility.

5 Development of a Precursor for Gas-Phase Texturing

In the previous chapter, surface impurities were found to facilitate texturing. However, as impurities were not distributed in a controlled manner, the resulting texture was non-uniform and lacked texturing reproducibility between samples. In this chapter, chemical species are deliberately introduced to the surface in a controlled manner to facilitate GaPTex and promote texturing uniformity and reproducibility.

5.1 Utilising Chemical Species for Gas-Phase Texturing

To mimic the beneficial effect that an uncontrolled sample surfaces had on WAR in Chapter 4, a chemical species could be intentionally introduced to the sample surface to aid texturing. For this species to aid GaPTex, the nature of how the uncontrolled surfaces promoted GaPTex needs to be mimicked. One method that texturing may have been aided by was increasing the number of physical reaction sites for texturing to occur, such as increased surface roughness [108], [214], [215], pinholes in an oxide layer, or atomic steps on the surface [172], [216]. Therefore, the intentionally added chemical species would ideally create roughness variations at the micro-scale. However, to achieve uniform texturing at the macro-scale, the deposited chemical species would need to be in a macroscopic uniform distribution on the surface. Nanoparticles can fulfil these both micro and macro-scale requirements. A distribution of individual nanoparticles would provide non-uniformity at the nanoscale, causing variations in the surface profile by particle height. Furthermore, nanoparticles can be uniformly suspended in a liquid phase to create a colloid, enabling uniform, reproducible, macro-scale texturing upon application to the surface. Colloidal silica meets both requirements and provides additional benefits. Final device performance would not be compromised, as the particles would either be etched away by the HF gas during texturing or by the necessary cleaning performed before emitter formation. Lastly, colloidal silica suspensions are cheap, non-toxic, and readily available.

The Kemet Col-K (NC) colloidal silica was initially chosen to apply to the surface before texturing. It has a nominal particle size of 90 nm in diameter, but a size distribution was confirmed by the manufacturer in the range 70 nm – 90 nm.

5.1.1 Nanoparticle Density Calculation

Using neat Col-K (NC) colloidal silica atop the Si surface prevented the reaction gases from reaching the substrate, thus texturing could not occur. Therefore, the colloidal silica had to be diluted to allow reaction gases to reach the surface. Yet the dilution of the colloidal silica needed to allow for a sufficiently dense array of nanoparticles on the surface to nucleate many texturing sites for fast surface texturing. An initial estimate of a 1 µm separation between particle centres was used, producing, a particle density of 1 particle/µm^2 or 10^8 particles/cm^2 across the surface. The density of the silica particles in the colloidal silica was given in g/cm^3, which therefore needed to be converted to particles/cm^2 to understand the dilution needed to achieve 10^8 particles/cm^2 on the Si surface. To convert mass to number of particles, the mass/cm^3 of the silica particles in the colloidal silica was divided the mass of one silica particle:

$$m_{particle} = V_{particle} \times \rho_{particle} \quad (5.1)$$

$$m_{particle} = \left[\frac{4}{3}\pi(45 \times 10^{-7} cm)^3\right] \times 2.65\ g/cm^3 \quad (5.2)$$

$$m_{particle} = 3.82 \times 10^{-16} cm^3\ \times 2.65\ g/cm^3 \quad (5.3)$$

$$m_{particle} = 1.01\ \times 10^{-15} g \quad (5.4)$$

$$colloidal\ silica\ particles/cm^3 = \frac{colloidal\ silica\ g/cm^3}{m_{particle}} \quad (5.5)$$

$$colloidal\ silica\ particles/cm^3 = \frac{1.2\ g/cm^3}{1.01\ \times 10^{-15} g} \quad (5.6)$$

$$colloidal\ silica\ particles/cm^3 = 1.19 \times 10^{15}\ particles/cm^3 \quad (5.7)$$

Here $m_{particle}$ is the mass of a silica particle, $V_{particle}$ is the volume of a single silica particle, $\rho_{particle}$ is the density of silicon dioxide. The silica particle diameter was taken to be 90 nm,

the density of silicon dioxide 2.65 g/cm^3, and the silica density in the colloid was quoted at 1.2 g/cm^3.

The next stage of the calculation entailed converting the colloidal silica from particles/cm^3 to particles/cm^2 of the desired surface density of particles on the Si surface,. While the surface density of the particles on the Si is particles/cm^2, the particles themselves are three dimensional. Thus, to make a comparison between the two densities for dilution, the desired particle density on the Si surface needed to be converted from particles/cm^2 to particles/cm^3. Continuing the 1 µm separation between particles, the desired particles density is converted to 10^{12} particles/cm^3. Dilution was calculated by the ratio of the particles/cm^3 between the colloidal silica and the desired surface density:

$$dilution = \frac{colloidal\ silica\ particles/cm^3}{desired\ particles/cm^3} \quad (5.8)$$

$$dilution = \frac{1.19 \times 10^{15}\ particles/cm^3}{10^{12}\ particles/cm^3} \quad (5.9)$$

$$dilution = 1190 \quad (5.10)$$

The colloidal silica must be diluted by 1190 to achieve the desired particle separation of 1 µm on the Si substrate surface. IPA was chosen as the solvent to dilute the colloidal silica, as it benefits from shorter drying times and lower surface tension, thus reducing particle movement during drying, over aqueous-based solvents [217]. This solution of colloidal silica and IPA is termed the precursor.

5.2 Precursor Application Methods

Several application methods were investigated to provide a uniform, reproducible distribution of the precursor across the substrate surfaces, thus enabling uniform and reproducible texturing. Detailed results are presented in section 5.2.2 for the most successful application method, spraying the precursor onto substrate surfaces.

5.2.1 Surveying Application methods

A proof of concept for the hypothesis that a precursor of colloidal silica and IPA aided texturing was performed by painting the precursor onto the Si surface before texturing. An Ox 1 wafer was used to eliminate any other contributing physical factors to texturing. Three dilutions of the colloidal silica close to a dilution of 1190 were tested: 1:500, 1:1000 and 1:2000 of Col-K (NC) colloidal silica to IPA respectively. These precursors were made by adding 1 ml of colloidal silica with 9 ml of IPA, thoroughly shaking for 30 seconds, before adding 1 ml of this solution to 49 ml, 99ml, or 199 ml of IPA for the three dilutions to be tested. The precursors were each shaken again for 30 seconds before applying them onto the Si surface with a Winsor and Newton Series 7 real sable-hair brush, size 0.8mm. Two controls were used. Bare Si, to determine if texturing would occur without reactive sites present from the precursor or surface damage. Secondly, a droplet of IPA to separate the effects of IPA and the colloidal silica in the precursor. After the three precursors and IPA had dried on the surface, the sample was textured using the parameters given in Table 5.1. Figure 5.1 presents the post-textured surface.

Table 5.1 The texturing conditions for determining if the precursor improved texturing efficacy.

Operating Parameter (unit)	**Value**
HF Temperature (°C)	80
Sample Temperature (°C)	215
Ozone Concentration (wt%)	20
Flow Rate (L/min)	1
Processing Time (min)	10

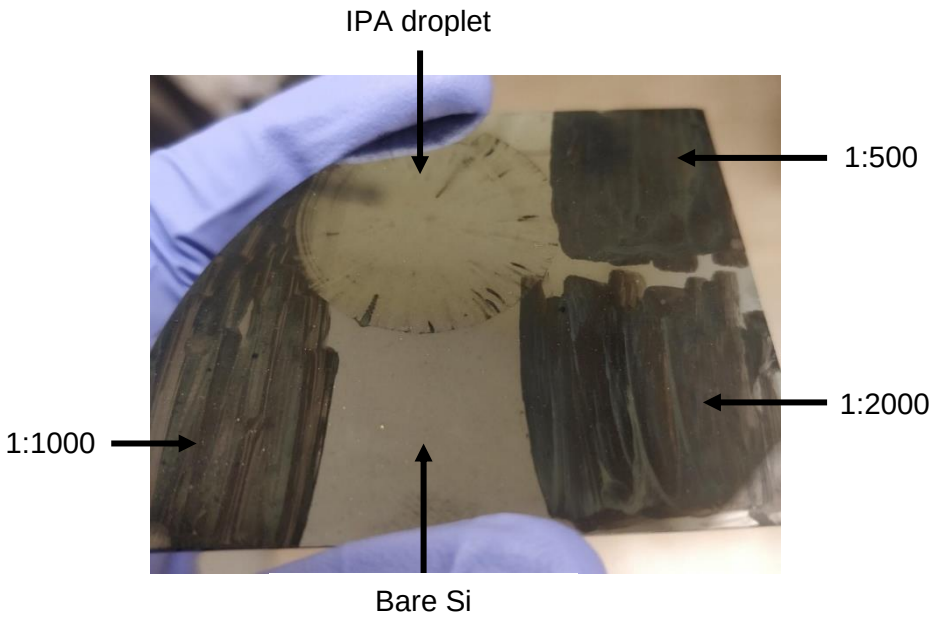

Figure 5.1 A post-texturing image of Si painted with 1:500, 1:1000, or 1:2000 diluted precursor, a droplet of IPA or a bare Si surface.

Figure 5.1 illustrates texturing occurring in the three regions where the precursors were applied. When no reactive sites were present on the surface, no texturing visibly occurred, as shown by the lack of texturing on the control area of the flat bare Si. Minor texturing occurred for the IPA control, radiating from the centre of where the droplet was deposited. The slight texturing was attributed to the trace impurities and plasticizers leaching into the IPA from the squeezy bottle in the lab. By eliminating IPA as a significant source of texturing, the improved texturing efficacy when using a precursor was attributed to colloidal silica.

Whilst painting the precursor showcased its success in aiding texturing, surface uniformity was poor. Figure 5.1 shows that the brush strokes from the precursor application are visible in all three precursor regions after texturing. To improve uniformity, samples were dipped in the precursor. The material used was changed from Ox 1 wafers to Longi wafers, as texturing had been established to be caused by the precursor, and not any other surface non-uniformities. Specimens were diced using the MicroAce3 dicer machine from LoadPoint and rinsed with IPA to remove contamination. Precursor dilutions included 1:250, 1:500, 1:2000, and 1:4000 to further test the effect of colloidal silica dilution on texturing. Precursors were made in the same manner as for painting. The precursors were manually shaken for 30 seconds after their preparation, before dipping specimens in with tweezers.

One sample was tested per precursor dilution. Specimens were left to air dry before texturing using the parameters in Table 5.1. Camera images of the textured surfaces are shown in Figure 5.2 and the corresponding reflectance in Figure 5.3. Sample illumination for camera images was varied between daylight and illumination with a white-bulb lamp to best showcase sample surface uniformity for each case.

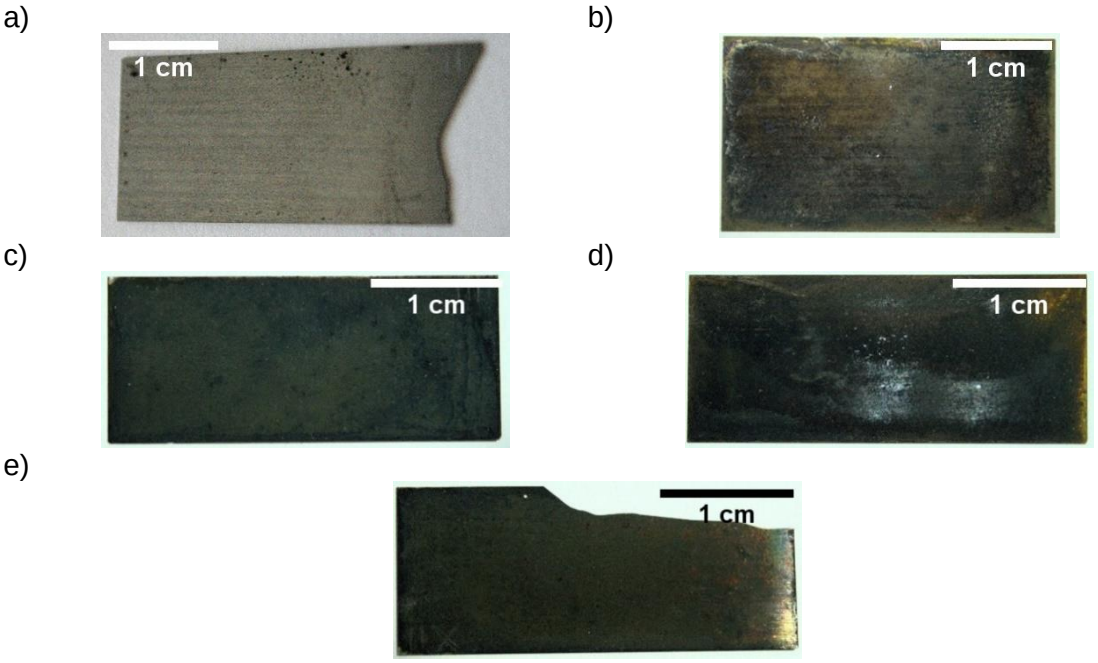

Figure 5.2 Post-texturing appearance of samples dipped into the precursor with dilutions a) IPA control b) 1:250 c) 1:500 d) 1:2000 e) 1:4000.

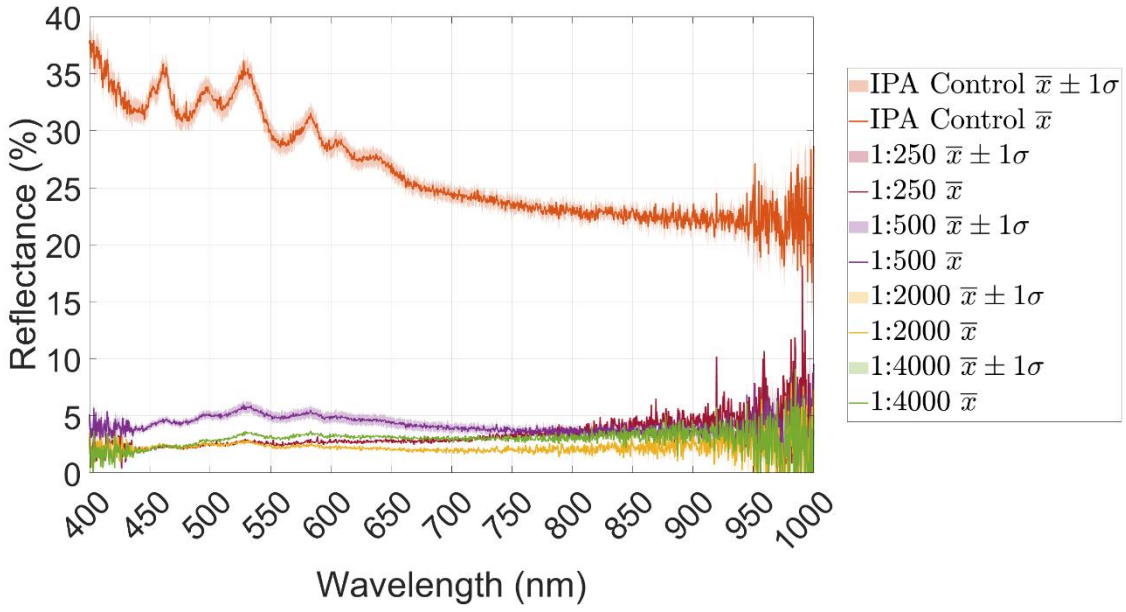

Figure 5.3 The post-texturing surface reflectance as a function of wavelength for samples dipped into the precursors.

Dipping samples into their precursor improved the texturing uniformity from painting the precursor on the surface. No brush stroke lines were observed in Figure 5.2 for any sample, nor was any standard deviation for reflectance greater than ± 0.5% in Figure 5.3. The WAR achieved when sample were treated with a precursor dilution of 1:250 to 1:4000 was 3.1% ± 0.5%, 4.2% ± 0.5%, 2.2% ± 0.3%, and 2.9% ± 0.4% respectively – the four lowest WARs achieved thus far by GaPTex. Figure 5.2 also shows variation in the texturing uniformity as the colour of sample surfaces treated with a precursor mottled from green to dark grey and brown to dark grey. Whilst this variation in texture uniformity was not evident in the standard deviations in reflectance, dipping was still deemed an unsuitable application technique on the grounds of uniformity.

Spin-coating was tested for precursor application due to its ability to apply uniform sub-micron films [218]–[220]. Samples were cleaved from Trina 1 wafers with a diamond-tipped pen, rinsed with IPA, and dried with compressed air. The precursor concentration range was expanded to include more concentrated precursors, as not all the deposited material would remain on the surface during spinning, unlike prior application methods. Precursor dilutions included: 1:10, 1:50, 1:100, 1:250, 1:500, and 1:2000 as well as neat colloidal silica, referred to as the ‘Neat’ precursor. The spin coater used was the Laurell WS-650MZ-23NPPB. The spinning programme used is shown in Table 5.2. 3 ml of each precursor was deposited onto the centre of each specimen surface in program step 1 with a pipette. The texturing recipe used is shown in Table 5.1. Camera images of the post-textured surface are presented in Figure 5.4. Reflectance as a function of wavelength for precursor dilutions is shown in Figure 5.5.

Table 5.2 Spin Coater programme used to deposit The Precursor.

Program Step	Spinner Velocity (RPM)	Time (s)
1	500	5
2	500	1.5
3	2000	1.5
4	3000	30

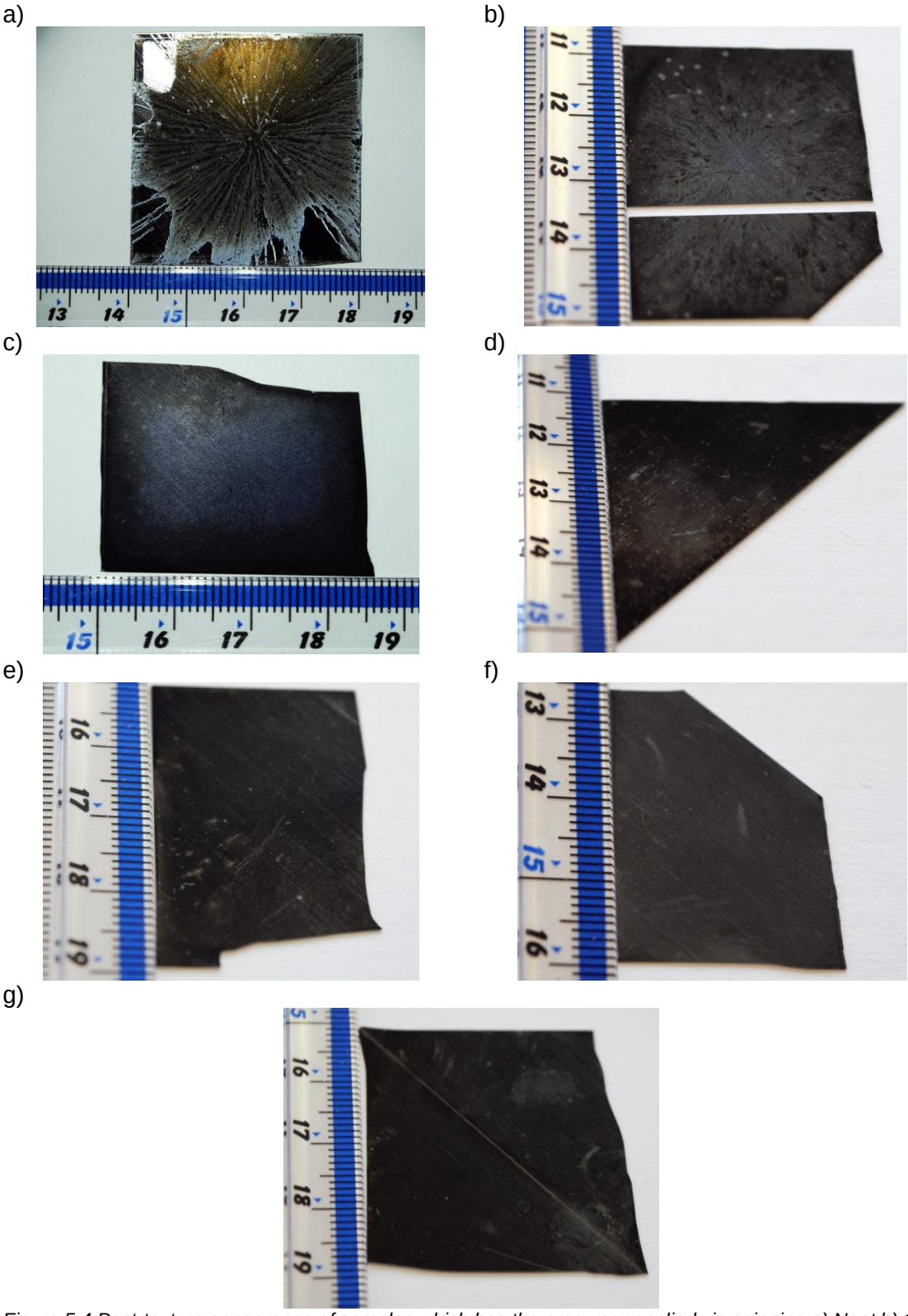

Figure 5.4 Post-texture appearance of samples which has the precursor applied via spinning a) Neat b) 1:10 c) 1:50 d) 1:100 e) 1:250 f) 1:500 g) 1:2000.

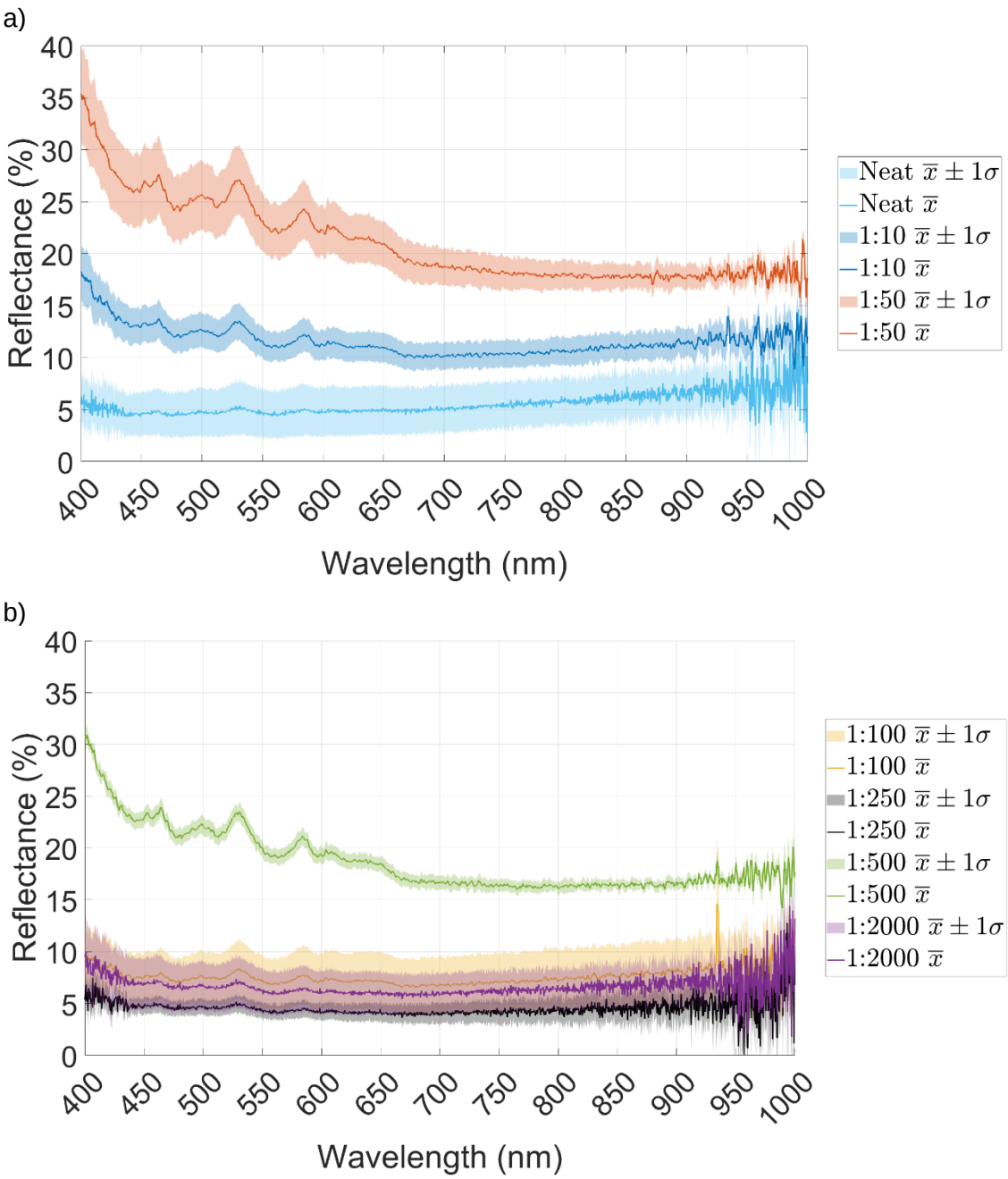

Figure 5.5 Surface reflectance for samples with the precursor spun onto the surface for the precursor dilutions a) 'Neat', 1:10, and 1:50 b) 1:100, 1:250, 1:500, and 1:2000.

Texturing uniformity worsened for all spin-coated samples compared to dipping. Figure 5.4 shows streaks radiating from the precursor deposition site at the sample centre for 'Neat' and 1:10 samples. Figure 5.4 also shows lines and dots of higher reflectivity material appear on the surface for samples with precursor dilutions 1:100 to 1:2000. Figure 5.5 corroborates the lack of texturing uniformity with broader standard deviations in reflectance than for prior application techniques, from ± 0.7% for 1:500 to ± 2.8% for 1:100. Furthermore, WAR increased to over 5% for all specimens, except the 1:250 precursor dilution at 4.6% ± 1.2%.

Thus, spinning was also concluded to be an unsuitable application method, both in terms of texturing uniformity and reflectance.

5.2.2 Spraying

An alternative method to produce uniform distributions of solid particles is spray-drying [221]–[223]. A spray nozzle is used to atomize suspensions, solutions, emulsions, or dispersions into a fine mist. This mist is then propelled towards a surface, creating a solid coating whilst the liquid phase evaporates. To attempt to improve the uniformity of the precursor application, the Series 176 ViscoMist, Nozzle body configuration 4 from Lechler Inc. was used for spraying the precursor onto specimen surfaces. The nozzle used four inlet ports: piston, atomizing air, liquid, and fan. The liquid port supplied the desired liquid medium, the precursor. The piston port housed the shut-off valve, allowing the liquid to pass through from the line to the nozzle tip when 40 psi (2.7 bar) was achieved. The atomizing-air port emitted compressed air to atomize the precursor into a mist on contact. Spray droplet size was controlled by varying the pressure of the atomizing port. The fan port changed the spray pattern from a cone to a flattened sheet and was not used in this work. Push fittings were attached to all four ports, creating water and air-tight seals around the pipes that either carried compressed air (taken directly from the pressurized air supplied to the laboratory) for the piston and atomizer lines, or the precursor for the media line. One pipe was used per precursor dilution. The nozzle was mounted at the top of a pyrex box with a door, of dimensions 20 cm × 20 cm × 50 cm, allowing 156 mm × 156 mm wafers to be sprayed. A Graseby 3400 Anaesthesia Syringe Pump supplied the precursor to the nozzle at a constant infusion rate, from 0.1 ml/hr to 400 ml/hr in 0.1 ml increments. The precursor was housed in a BD Plastipak 20 ml syringe, located in the syringe pump. A schematic of the spraying unit is presented in Figure 5.6.

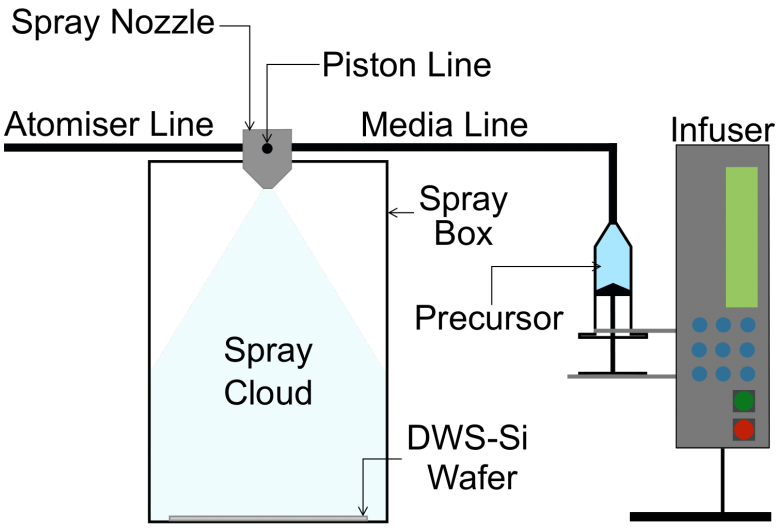

Figure 5.6 Schematic of the initial set-up for spraying the precursor onto sample surfaces.

A full-sized, 156 mm × 156 mm, Trina 1 wafer was rinsed with IPA, dried with compressed air, and then sprayed with the precursor using conditions presented in Table 5.3. Sample spray time was initiated once the spray cloud reached a maximum density observed by the eye. After the allotted spray time, the sample was left in the spray box until the surface appeared completely dry at ~20 minutes. The specimen was subsequently textured with conditions presented in Table 5.4. The resulting post-texture appearance and reflectance as a function of wavelength are shown in Figure 5.7.

Table 5.3 Spraying conditions that were used to deposit the precursor by spraying.

Precursor Spraying Parameter	**Value**
Precursor Concentration	1:2000
Infusion Rate (ml/hr)	400
Atomising Pressure (bar)	1.4
Sample Spray Time (s)	20

Table 5.4 Texturing conditions used for the sample with the precursor sprayed on.

Operating Parameter	**Value**
Processing Time (min)	20
HF Temperature (°C)	80
Flow Rate (L/min)	1
Sample Temperature	215
Ozone Concentration (wt%)	20

a)

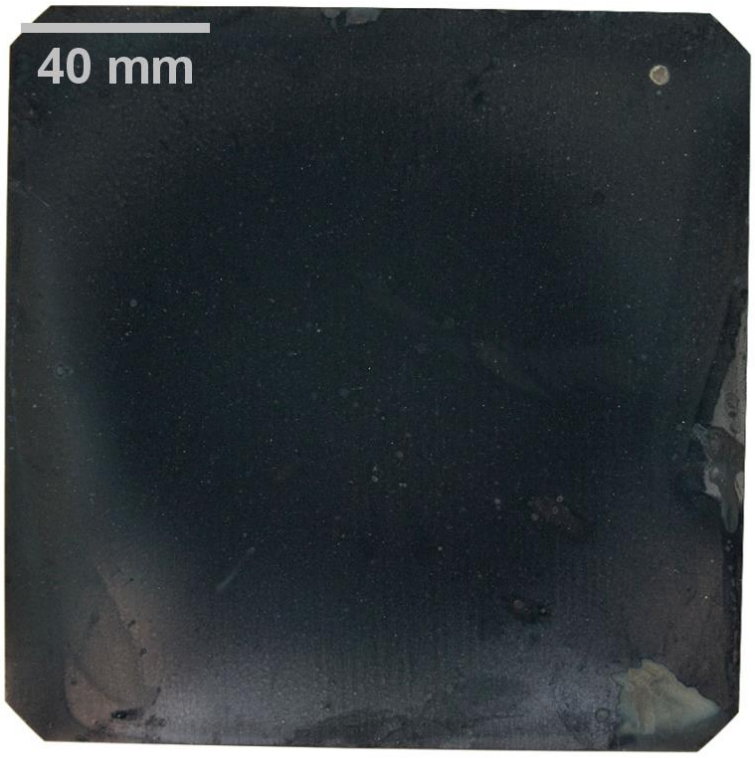

b)

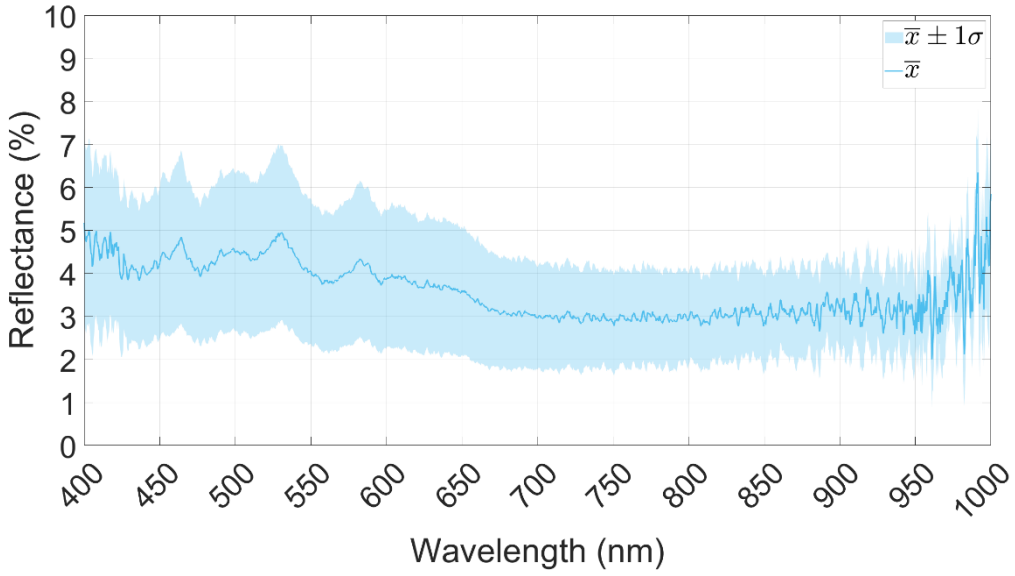

Figure 5.7a) Post-texture appearance of the first wafer with the precursor deposited via spraying b) surface reflectance of the first wafer where the precursor was deposited via spraying.

By spraying the precursor onto the surface, the lowest reflectance was achieved thus far. A WAR of 3.7% ± 1.5% was measured from the reflectance data in Figure 5.7b). This low reflectance was corroborated by the sample's visual appearance presented in Figure 5.7a), which varied from dark grey at the edges, darkening to black at the sample centre. The variation in texturing uniformity is over a greater area than for the samples used in

section 5.2.1, thus spraying can be considered to improve texturing uniformity. However, GaPTex is intended to be used on full-sized industrial wafers in the final application of a solar cell; therefore, texturing uniformity must be further optimised for whole wafers.

To eliminate the variation in reflectance from the centre to the edges of the wafer, the spraying set-up was further optimised. Spray deposition uniformity is dependent on the variation in spray velocity across the sample surface, and therefore the separation distance between the nozzle and the sample [224]. Thus, the darker circle of material at the wafer centre was attributed to a greater spray velocity in the middle than the edges of the wafer, indicating the separation distance between the nozzle and the wafer was too short. To homogenise the spray velocity across the sample surface, the distance between the nozzle and the sample was increased. The sprayer nozzle was mounted in a taller spray box of dimensions 20 cm × 20 cm × 70 cm, increasing the separation distance by 20 cm. However, upon spraying with the increased box height, the atomized IPA from the precursor evaporated before reaching the sample surface at the bottom of the box, no longer guaranteeing a uniform application of particles. Evaporation was minimised by installing an IPA reservoir on the atomising line, before the nozzle. Additional upgrades to the spraying unit included the installation of an aluminium plate shutter above the wafer. The shutter concealed the wafer until the spray cloud achieved uniform density, whereby the shutter was opened to reveal the wafer to the spray and closed to re-conceal it after the specific allotted time. When moving the Al-plate, care was taken to move it to the edge of the box, but not remove it to ensure the spray cloud was contained in the box. The upgraded schematic of the spraying unit and an image of the spray unit are shown in Figure 5.8. Texturing was re-attempted using a Trina 1 wafer, the same material as for the initial spray unit, the texturing parameters from Table 5.4 and the precursor spraying parameters from Table 5.5. Figure 5.9 presents the sample’s post-texture appearance and reflectance.

a)

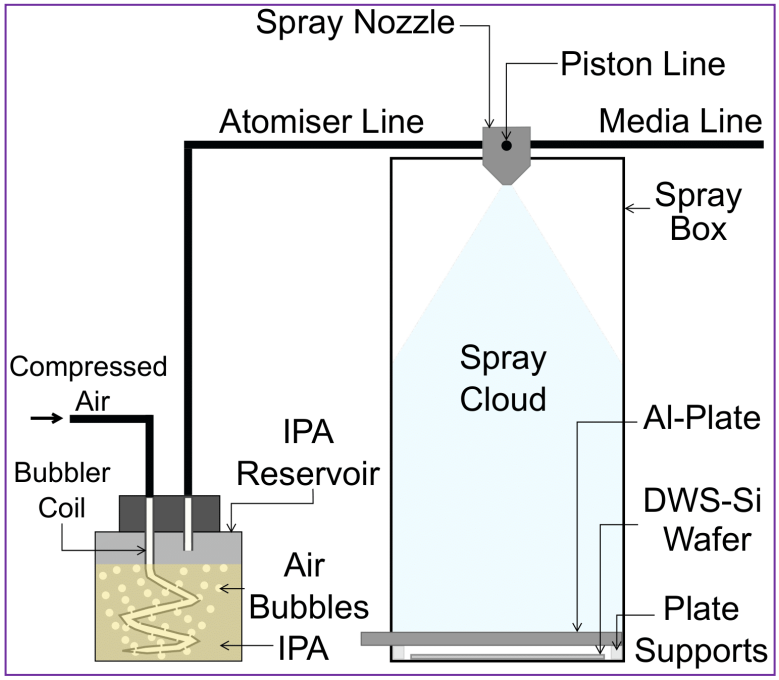

b)

Figure 5.8a) A schematic of the optimised spray unit, including increased box height, IPA reservoir in the atomiser line, and the Al-plate to conceal and reveal wafers to the spray cloud b) a camera image of the optimised spray unit.

Table 5.5 Spraying conditions used with the optimised spray unit.

Precursor Spraying Parameter	Value
Precursor Concentration	1:200
Infusion Rate (ml/hr)	400
Atomising Pressure (bar)	1.4
Sample Spray Time (s)	45

a)

b)

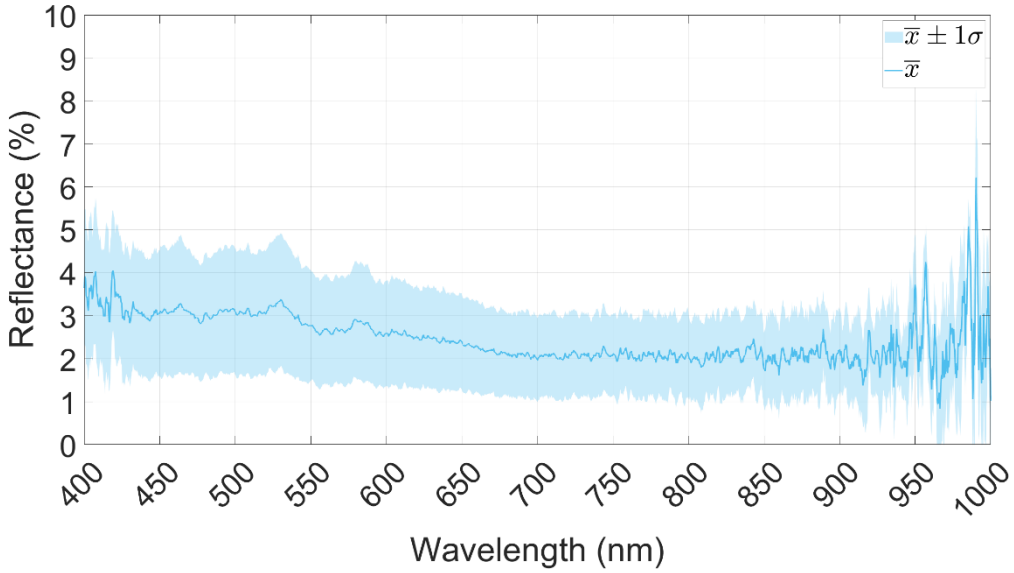

Figure 5.9 a) the post-texture appearance of the wafer sprayed in the optimised spray unit b) the reflectance of the wafer sprayed in the optimised spray unit.

Texturing uniformity was improved by the upgraded spraying unit. Figure 5.9a) shows the circle of lower reflectance material at the wafer centre was no longer visible and the reflectance standard deviation in Figure 5.9b) reduced to ± 1.2% from ± 1.5%. Figure 5.9 additionally demonstrated a reduction in WAR, from 3.7% ± 1.5%, when spraying with the un-optimised spraying unit, to 2.5% ± 1.2% with the newly optimised spray unit. Spraying was concluded to be the best precursor application method as it provided low reflectance, good surface uniformity, and a suitably uniform black surface to the naked eye.

Optical optimisation was attempted but halted due to variations in reproducibility in subsequent texturing runs, as described below. Further details on the cause of the lack of texturing reproducibility are discussed in section 5.3. Table 5.6 presents the operating parameters and spraying conditions of three sequentially textured wafers. Figure 5.10 presents the post-texture appearance, and Figure 5.11 shows the respective surface reflectance as a function of wavelength.

Table 5.6 Spraying conditions and texturing conditions of three sequentially textured wafers.

Operating Parameter (unit)	**Value**
Processing Time (min)	20
HF Temperature (°C)	80
Flow Rate (L/min)	1
Sample Temperature	215
Ozone Concentration (wt%)	20
Precursor Spraying Parameter	1
Precursor Concentration	1:200
Infusion Rate (ml/hr)	400
Atomising Pressure (bar)	1.4
Sample Spray Time (s)	45

a)

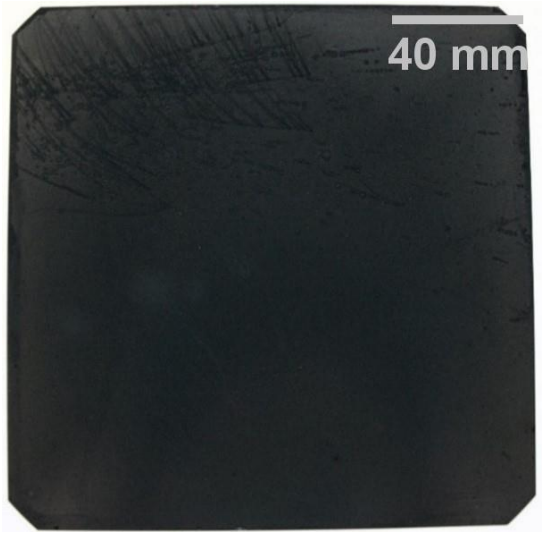

b)

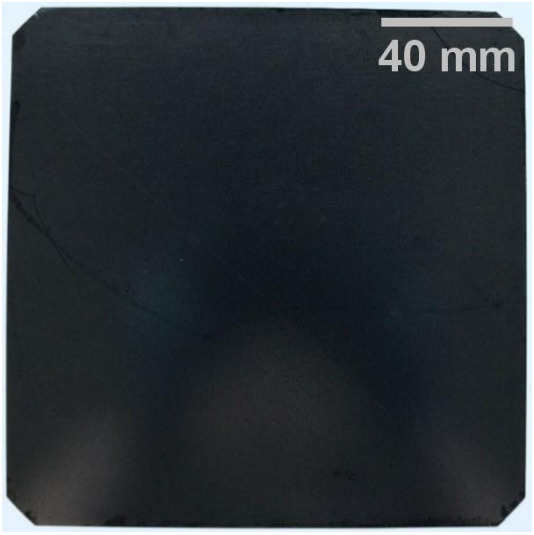

c)

Figure 5.10 Post-texture appearance of three sequentially textured wafers that lost reproducibility.

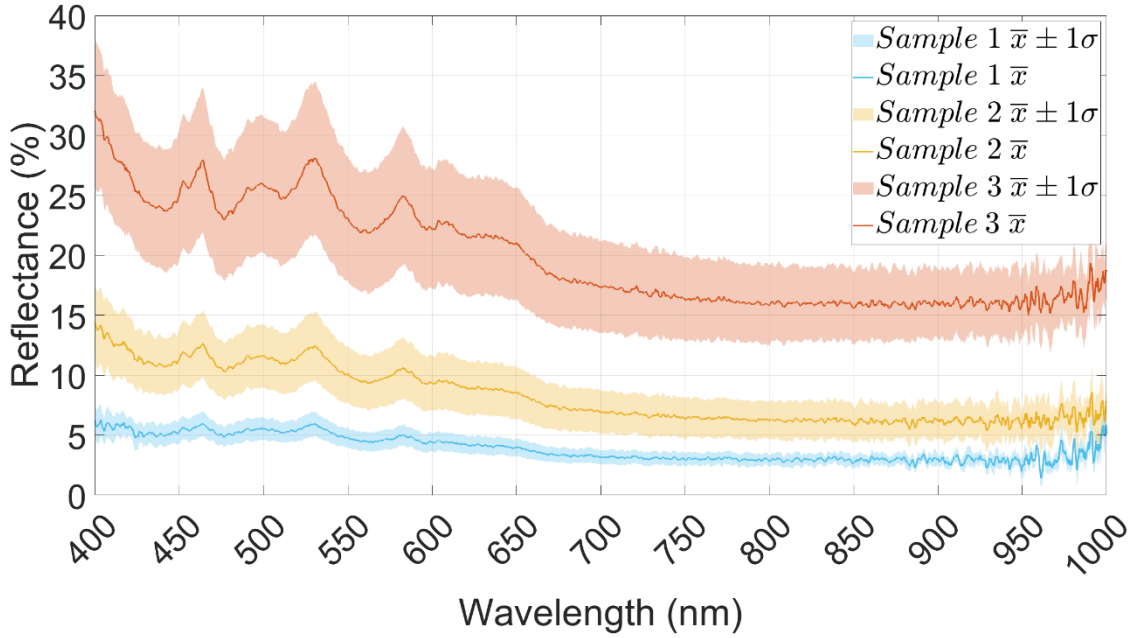

Figure 5.11 Reflectance of 3 sequentially textured wafers that lost reproducibility.

Surface reflectance increased with each sequential GaPTex run, as shown by the progressive lightening in colour from samples 1 to 3 in Figure 5.10a) to c). Figure 5.11 quantifies the lightening of colour shown in Figure 5.10, where reflectance progressively increased with each sample. Additionally, sample uniformity also became poorer with each sequential sample, from ± 0.8% for sample 1 to ± 4.5% for sample 3. As the texturing kit and the spraying unit were deemed to be fully functional, the precursor was investigated to determine if it could account for variations between experiments. Within the precursor, the colloidal silica settled out from the IPA, but thus far had been resolved by manually re-dispersing it before applying the precursor to the sample surface, creating macroscopic identical conditions between runs. However, if the precursor were to settle within the 2 minutes and 45 seconds needed to complete the entire spraying process (2 minutes to generate a uniform spray cloud and 45 seconds to expose the wafer to the spray cloud), the wafer would receive a non-uniform application of the precursor, creating non-uniformity between wafers on otherwise identical texturing runs.

The settling behaviour of the colloidal silica was examined to determine if the precursor became unstable and settled within 3 minutes. A freshly prepared precursor dilution of 1:200 (the dilution used to spray samples thus far) was made by depositing 1 ml of colloidal

silica in 200 ml of IPA and manually shaking for 30 seconds before dispensing 10 ml into a vial. Vials of the precursor were imaged immediately after precursor preparation, within 3 minutes of preparation, and 1 hour after preparation, and are presented in Figure 5.12.

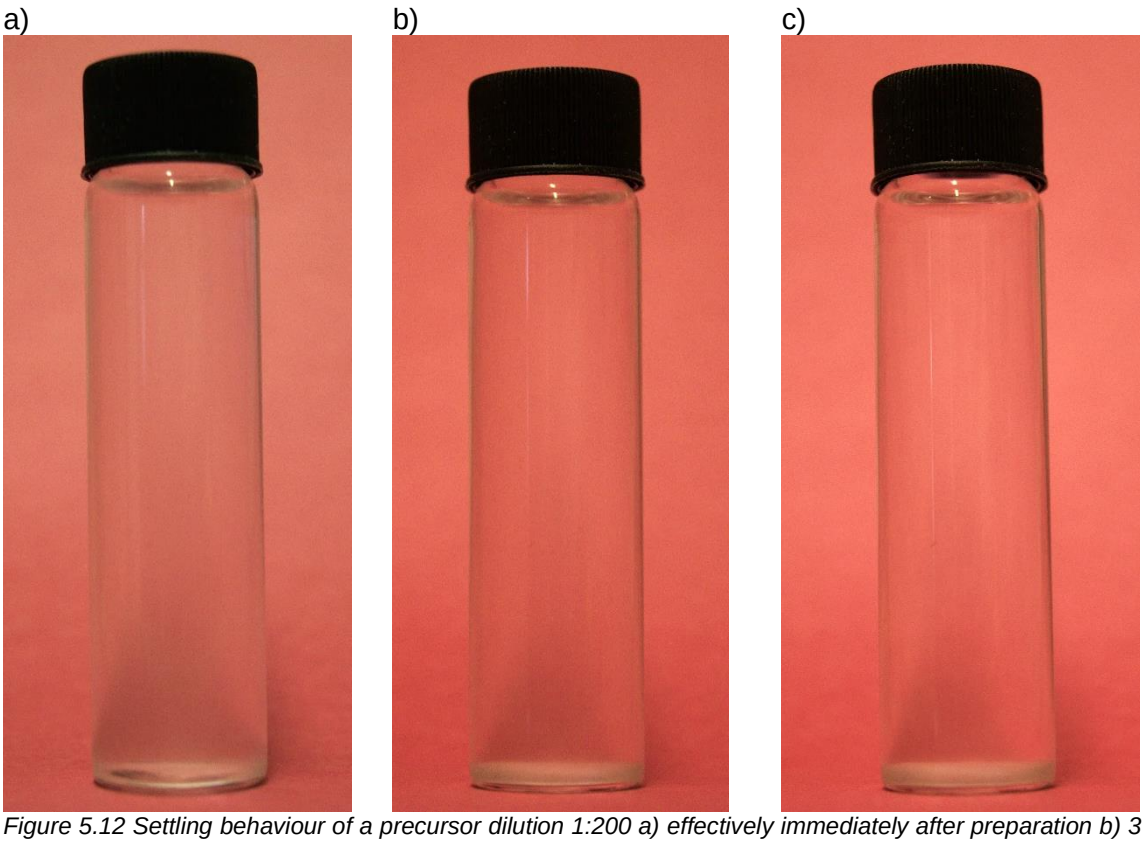

Figure 5.12 Settling behaviour of a precursor dilution 1:200 a) effectively immediately after preparation b) 3 mins after c) 1 hour after.

Figure 5.12 shows that the colloidal silica settled within 3 minutes of preparation, as demonstrated by the white layer at the bottom of the vial in b). This rapid settling behaviour indicates wafers did not receive an identical application of the precursor with each spray, and thus the cause of reproducibility is likely due to instability in the precursor. Furthermore, spraying is particularly susceptible to reproducibility issues with an unstable precursor. Firstly, the spraying deposition rate is the slowest out of all tested application methods, thus can experience the greatest amount of settling and consequentially non-uniformity between applications. Secondly, the syringe containing the precursor for deposition is mounted upside-down, as shown in Figure 5.8b), allowing particles to settle in the body of the syringe. Therefore, as spraying progresses, fewer particles are transported to the spray chamber,

making each application non-uniform. To create an entirely reproducible texturing process, the solution parameters that could generate a stable colloid suspension were investigated.

5.3 Precursor Stability

5.3.1 Colloidal Stability Theory

Colloidal stability is determined by the ratio of particle intermolecular forces. Colloidal particles attract one another via Van der Waals (VdW) forces, ultimately causing sedimentation in a colloidal suspension. Particles can remain in suspension by introducing repulsive forces between particles, such as electrostatic repulsion. Figure 5.13 illustrates where the repulsive component between particles stems from; ions of the opposite charge to the particle's surface, termed counter-ions, surround each particle in an Electric Double Layer (EDL). The EDL consists of two layers. The first is known as the Stern layer, where counter-ions form an immobile layer around the particle due to their strong attraction to the charge at the particle's surface. These counter-ions undergo no chemical bonding with the surface of the particles but are simply attracted to the surface by electrostatic forces. The second layer is termed the Diffuse Layer and contains counter-ions that are still attracted to the particle surface but are also being repulsed by the counter-ions in the Stern layer. The ions in the Diffuse Layer are mobile and can be exchanged with ions of the same charge as the particle moves through the solution.

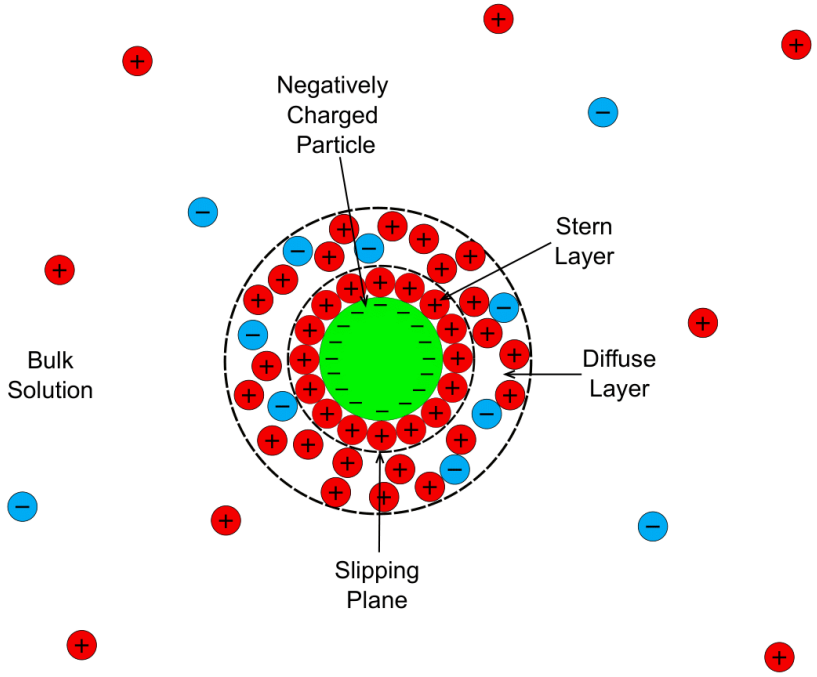

Figure 5.13 A particle in a solution, stabilised with an EDL. Immobile, positively charged counter-ions surround the negative charge of the particle's surface, whilst the outer layer ions are diffuse and can change with particle motion.

A colloid's stability is determined by the interaction between particle EDLs, which has been modelled by Derjaguin, Landau, Verwey and Overbeek (DLVO) [225], [226]. Figure 5.14 shows a particle's net potential energy as a function of particle separation, modelled by DLVO theory. It should be noted for the net potential energy curve, at very short distances Born repulsion occurs as particles cannot occupy the same physical space. Two approaching particles will initially attract as separation distance shortens, reaching the secondary minimum caused by VdW forces having a longer physical range. At the secondary minimum flocculation occurs, where particles are loosely bound together in a 'floc' but no chemical bonds form between particles. Particles are easily re-dispersed due to the shallow nature of the energy well. If particles are not redispersed and continue to attract, the two diffuse layers will overlap thereby increasing the repulsive term of the particles' net energy, resulting in a potential energy barrier being generated between particles. This barrier is the cause of colloidal stability as it prevents chemical bonding between particles (agglomeration) and ultimately settling. If the barrier is of sufficient height, particles will remain separate, and the colloid is stable. However, as barrier height reduces

more particles will have sufficient kinetic energy to overcome it, thus falling in energy to the primary minimum where irreversible agglomeration occurs.

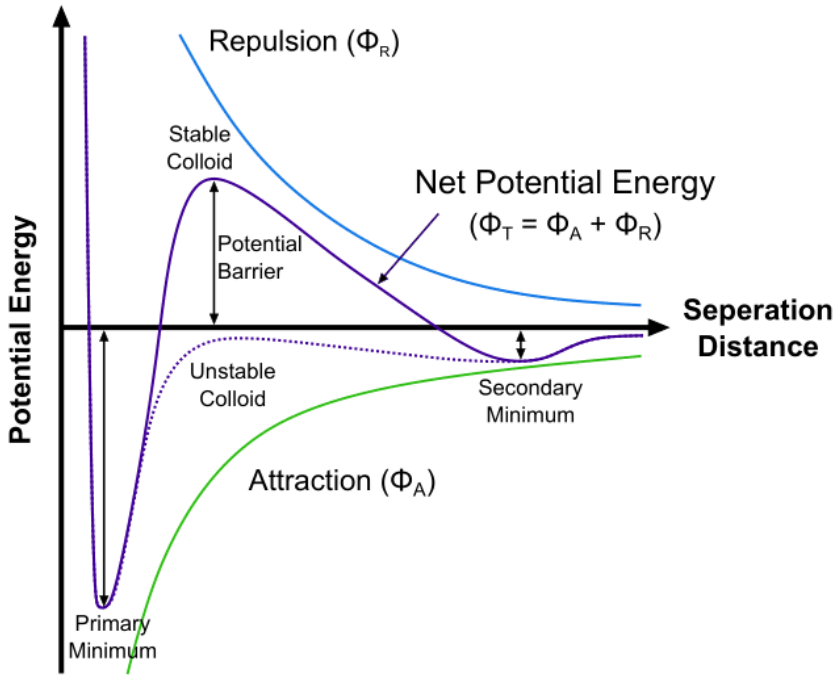

Figure 5.14 DLVO theory of the stability of two particles interacting as a function of particle separation distance. Individual repulsion and attraction curves are shown as well as the net potential energy for particles. Solid lines indicate the curves for a stable colloid, whilst dotted lines indicate an unstable colloid.

The potential barrier height, and thus colloid stability, is affected by the thickness of the two particles' interacting diffuse layers. The boundary of the diffuse layer marks where the particle's surface charge is neutralised, and therefore its thickness will change according to counter-ion valency and concentration [227], [228]. For weak solutions, the diffuse layer is large, whereas concentrated solutions cause the EDL to become compact. Figure 5.15 illustrates the effect of weak and concentrated solutions on particle stability. In weak solutions, the separation distance is relatively large when diffuse layers overlap, such that VdW forces are overcome by the repulsive potential barrier. However, when either counter-ion concentration or valency increases, the diffuse layer shrinks. Diffuse layers do not overlap until shorter separation distances, at which point the VdW term is much more massive than the repulsive component and dominates particles' net potential energy. Particles are swept into the primary energy minimum, creating an unstable colloidal suspension. Therefore, a balance of counter-ion concentration and valency must be struck

to create a stable colloidal suspension, as both too little and too great a number of counter-ions can cause particle agglomeration and a separated solution.

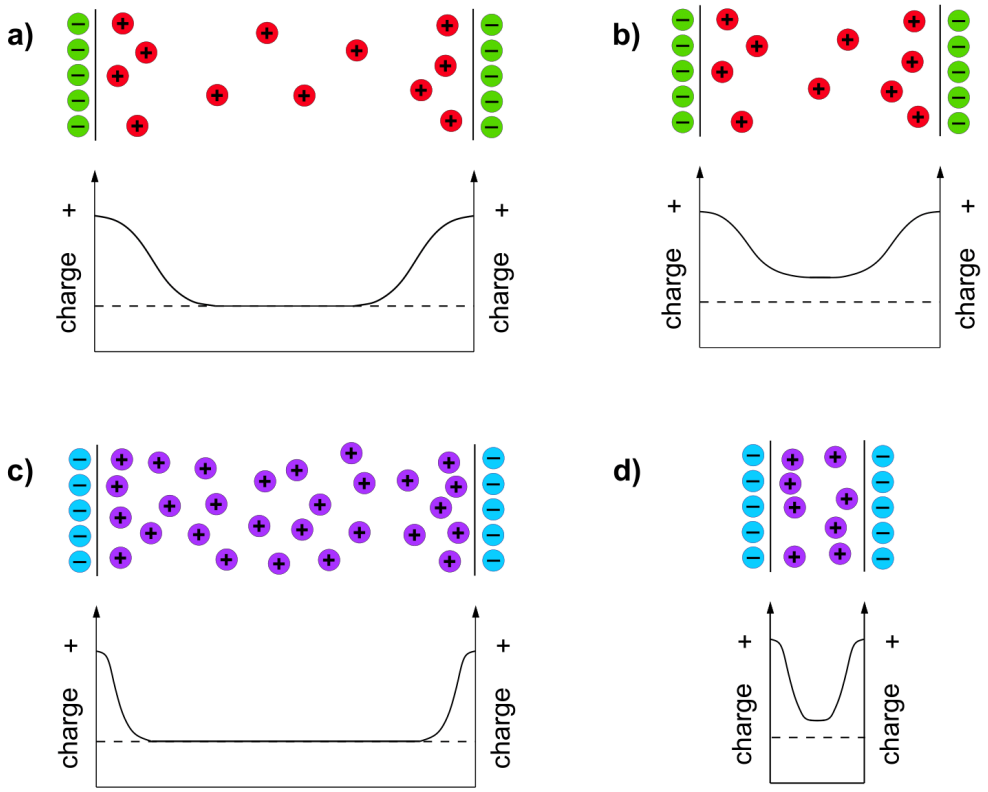

Figure 5.15 The effect of counter-ion concentration in the bulk solution on colloidal stability a) represents the diffuse layers for weak solutions and the corresponding thick diffuse layers at large separation distances b) shows the overlap between diffuse layers when particles in weak solutions approach one another c) shows the effect of concentrated bulk solutions on diffuse layers, shrinking them d) shows when particles approach one another in concentrated solutions, the particles reach very short separation distances before the diffuse layers overlap.

5.3.2 Colloidal Silica Stability

Colloidal silica's stability as a function of counter-ion concentration has been determined using DLVO theory [229]. Figure 5.16 presents the gelation time of colloidal silica for pH 0 – 14, where long gelation times indicate high stability. Agglomeration rapidly occurs at neutral pH where there is a lack of counter-ions to form an EDL around particles; siloxane bonds form between particles. Considering the case of the precursor instability, pH was measured using a Hanna Instruments HI-98100 Checker Plus pH Tester. pH was measured as neutral, indicating there was an insufficient concentration of counter-ions to stabilise the colloidal silica, causing particles to undergo irreversible agglomeration.

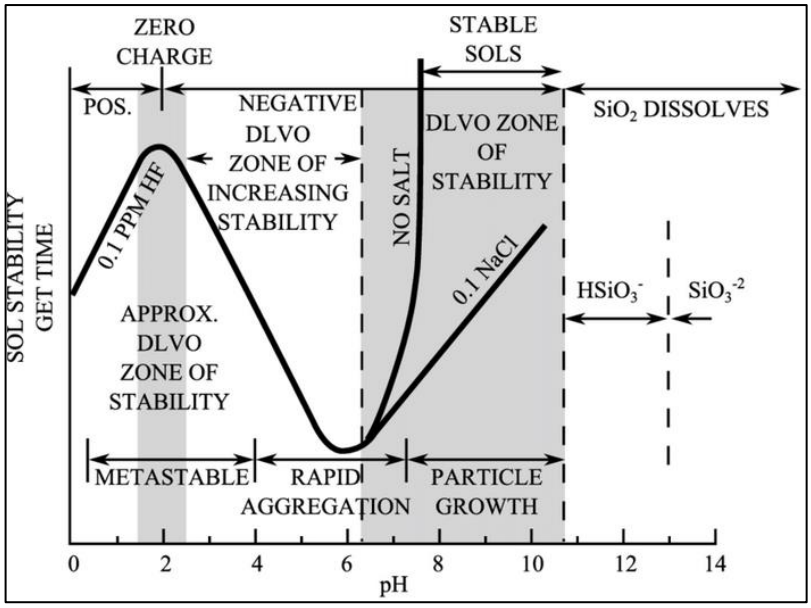

Figure 5.16 Stability of colloidal silica in aqueous solutions as a function of pH, reproduced from W. D. Kingery [229].

From Figure 5.16, two pH regions of colloidal stability exist for silica. True stability occurs at pHs 8-11, where gelation time is effectively infinite when no salts are added. The common counter-ions used for alkaline stability are NaOH or NH_4OH, where Na^+ or NH_4^+ respectively are the counter-ions in the EDL. Yet, DLVO theory does not successfully predict all colloidal silica's stability behaviour [230]. The secondary region of stability for colloidal silica is located at pH 2 [231]–[233], contrasting DLVO theory where zero repulsive charge is predicted. Instead, stability is proposed to occur by polysilicic acid forming on the particle surface in a 'hairy layer' [231]–[234], demonstrated schematically in Figure 5.17.

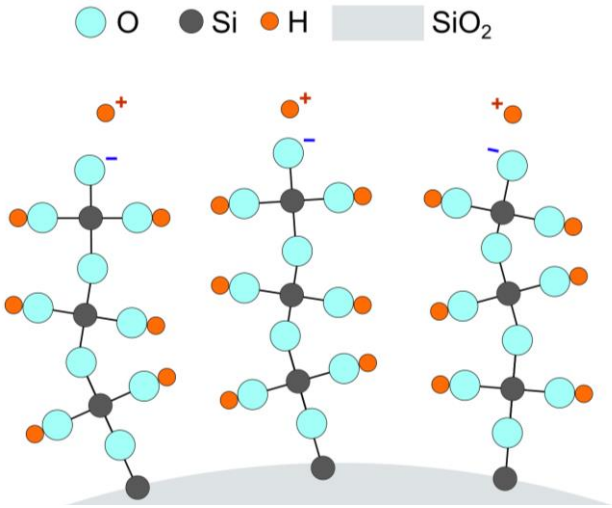

Figure 5.17 Schematic of how colloidal silica can be stabilised in acidic pHs with the formation of flexible chains of polysilicic acid from the surface.

5.3.3 Stable Precursor for Reproducible Gas-Phase Texturing

To determine the stability range of the precursor, the precursor pH was adjusted and the resulting settling behaviour was monitored. Precursors with pH 2, 5, 7, and 9 were made with solutions of NaOH, for the alkaline precursor, or H_2SO_4 for acidic precursors. The pH of the colloidal silica and the IPA were individually adjusted dropwise and once the desired pH was reached for each component, they were vigorously stirred for 5 seconds, before making a 1:200 dilution, as previously described in section 5.2.1. The precursor at pH 7 needed no adjustment from alkaline or acidic species and is the precursor that has been used thus far in GaPTex. All precursors were manually shaken for 30 seconds and then as quickly as possible imaged. Figure 5.18 presents the pH-adjusted precursors effectively immediately after preparation, after 3 mins, and after 1 hour.

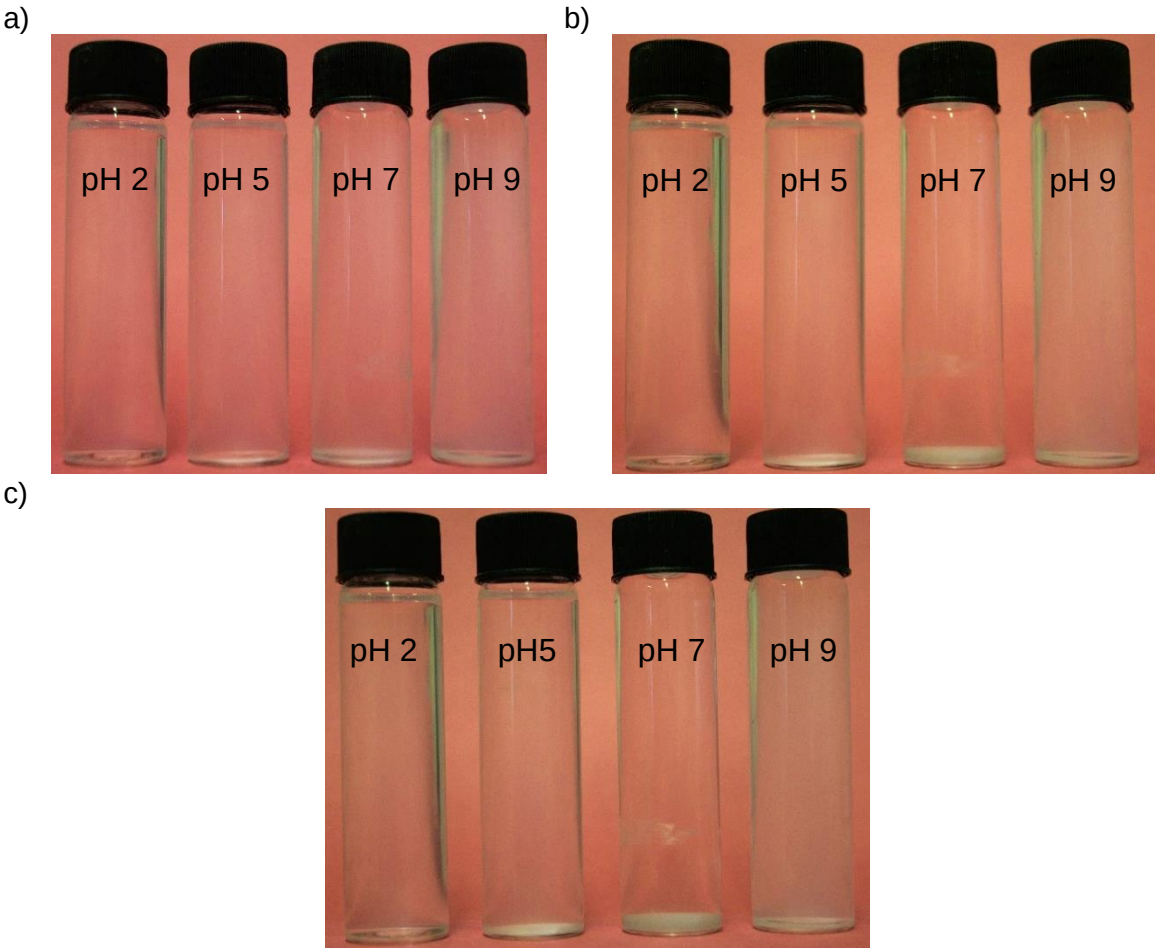

Figure 5.18 pH range of colloidal silica suspensions after a) 0 mins b) 3 mins c) 1-hour settling. From left to right within each image: pH 2, pH 5, pH 7, pH 9.

Figure 5.18 shows the successful stabilisation of the precursor at pH 2, where no settling was observed in the vial between the three imaging times. Settling occurred for all other precursor pHs. The greatest amount of settling occurred for the precursor used in texturing work thus far, pH 7, followed by precursor at pH 5 and 9.

The variation in settling behaviour across pH is accounted for by the EDL thickness changing with dilution and pH. Figure 5.19 shows a stabilised colloidal silica particle in the alkaline environment of undiluted colloidal silica. Na^+ counter-ions surround the silica particle in the EDL, which is sufficiently thick to cause particle stability and thus agglomeration cannot occur. By adding a small volume of the colloidal silica to the IPA, the concentration of Na^+ counter-ions dilute, resulting in a thickness reduction of the EDL, specifically the diffuse layer. In addition, the concentration of OH^- ions dilute, causing the pH to change from alkaline to neutral. Figure 5.20 demonstrates the new environment of the colloidal silica particles with the dilution in IPA to pH 7; the diffuse layer thickness is reduced in comparison to the stabilised silica nanoparticles in Figure 5.19 and fewer OH^- ions are present in the bulk solution. The diffuse layer is responsible for the potential barrier height to maintain particle separation and colloid stability, as discussed in section 5.3.1. Therefore, when the thickness of the diffuse layer is reduced, the potential barrier height also reduces, allowing particles to fall into the primary minima and undergo agglomeration and settling. An insufficiently thick diffuse layer accounts for all the settling behaviour observed in Figure 5.18.

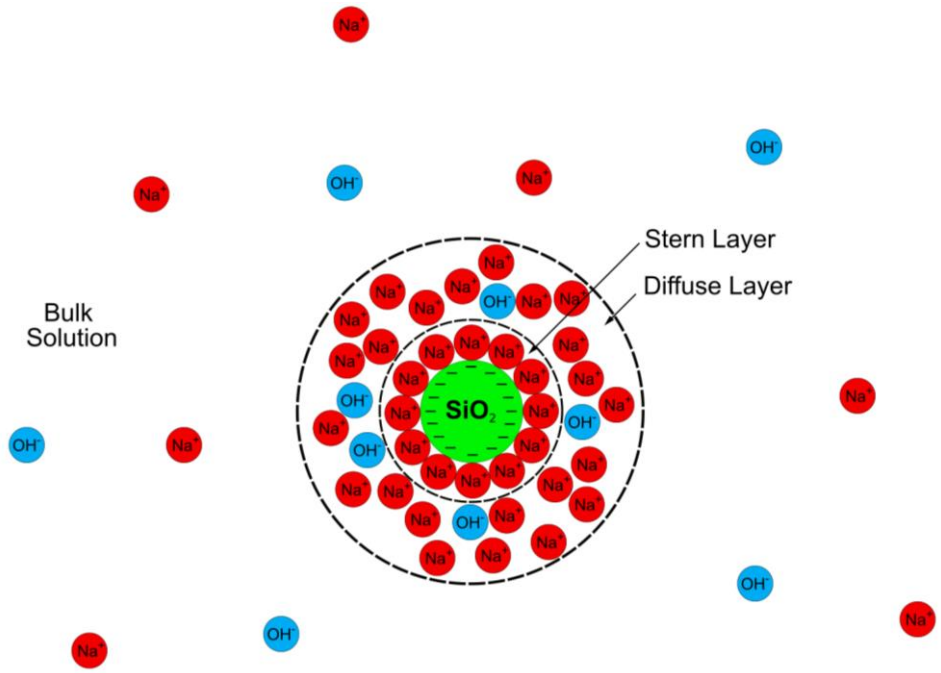

Figure 5.19 Schematic of the alkaline stabilisation the silica particles have in the Col-K NC colloidal silica, including the silica particle, the stern layer surrounding the particle, the diffuse layer surround the stern layer, and the bulk solution.

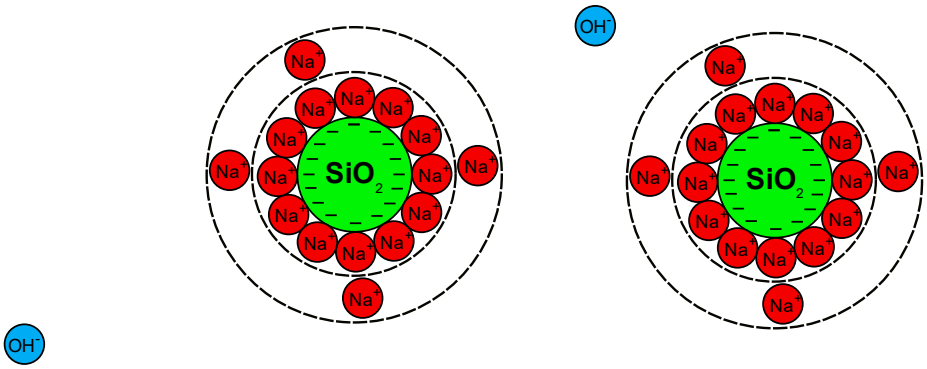

Figure 5.20 Schematic of the dilution of colloidal silica particles in IPA to pH 7. Fewer OH^- ions are in solution in comparison to in un-diluted colloidal silica, thus the pH is no longer alkaline. The concentration of Na^+ ions is also diluted with adding colloidal to IPA, resulting in the thinning of the diffuse layer, causing particle separation to decrease.

Upon adding sulphuric acid to the colloidal silica and the IPA, the precursor became stable. Figure 5.21 shows how the surface of the silica particles may have been stabilised with the addition of sulphuric acid. Na^+ counter-ions likely remain close to the silica surface in the IPA due to the strong attraction experienced between counter-ions in the stern layer and the particle surface. The addition of acid increases the diffuse layer thickness to result in particle stability, as observed in Figure 5.18 at pH 2. In the areas where there is a lack of Na^+ counter-ions, 'hairy legs' of poly-silicic acid form, using Si from the surface of the

particle to form the hydrated chain extending from the surface. The length of the poly-silicic acts is a repulsive force barrier, extending from the surface of the Si for 1- 3 nm, increasing the thickness of the EDL to enable particle repulsion in the acidic environment [231]–[233]. Any OH^- ions from the alkaline environment of the colloidal silica likely react with the H_3O^+ ions from the sulphuric acid to form water molecules. G. Vigil et al. [232] formed the chains of poly-silicic acid by exposing the silica to humid air, indicating water molecules aid in the formation of the 'hairy legs' at the particle surface. Thus, the formation of water molecules from the interaction between the OH^- and H_3O^+ ions have the potential to be aiding the particle stabilisation. Hence the stabilisation observed at pH 2 in Figure 5.18 is a mixture of Na^+ counter-ions and flexible chains of polysilicic acid extending from the silica particle surface.

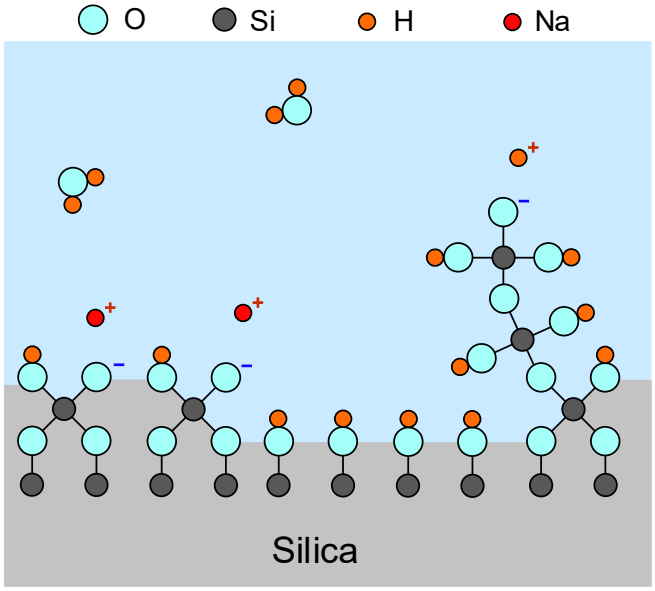

Figure 5.21 Schematic of a portion of a colloidal silica surface in an acid-stabilising environment.

Texturing reproducibility was retested using the stable precursor at pH 2. Three wafers were textured using the spraying conditions and texturing recipe from Sample 3 in Table 5.6. Figure 5.22, Figure 5.23, and Figure 5.24 present the images of the wafers post-texturing, the reflectance as a function of wavelength, and the microstructure respectively.

a)

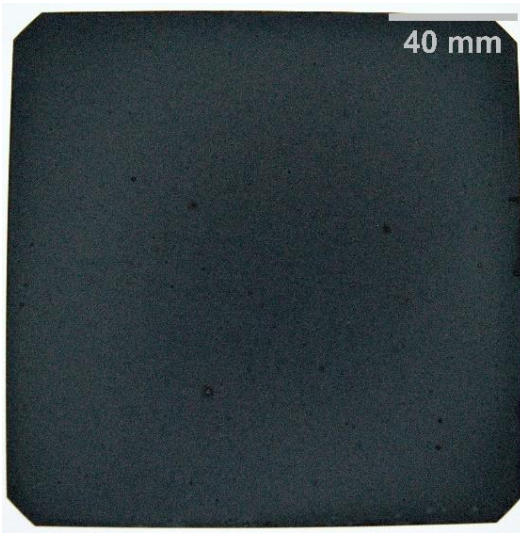

b)

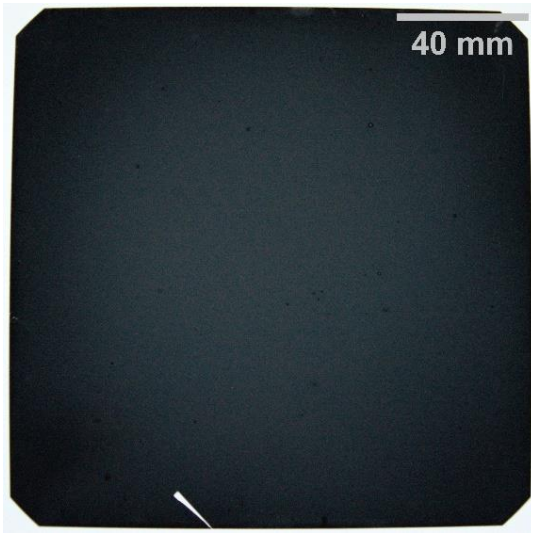

c)

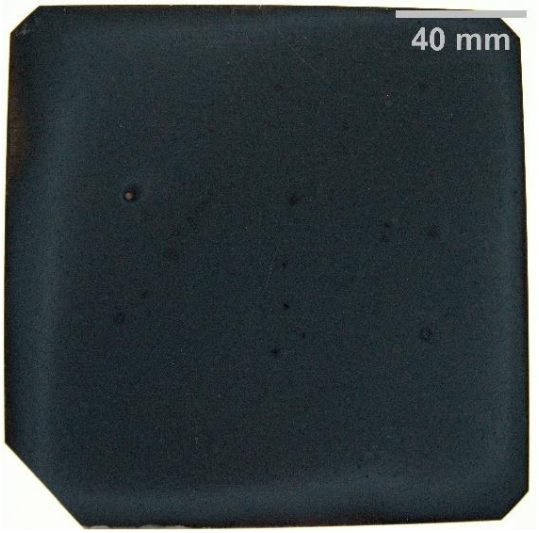

Figure 5.22 The post-texture appearance of three sequentially textured samples using the acid stabilised precursor.

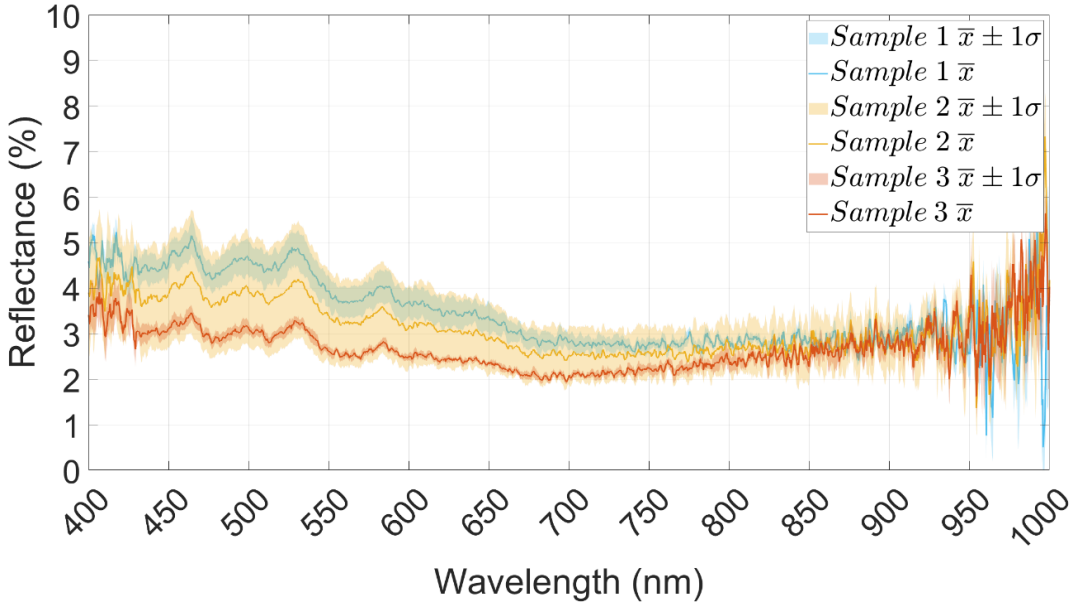

Figure 5.23 Reflectance of three samples textured using the acidic stabilised precursor.

When using the stabilised precursor, samples textured uniformly, and texturing reproducibility was recovered. Figure 5.23 shows the reflectance of the three samples is within 1% of one another, yielding WARs of 3.5% ± 0.3%, 3.2% ± 0.8%, and 2.7% ± 0.2% for samples 1-3 respectively. The standard deviation of the reflectance spectra in Figure 5.23 presents the improvement in texturing uniformity, where all reflectance standard deviations were < 1%. Figure 5.22 corroborates the improvements to texturing uniformity where only minor imperfections of a small number of darker spots, likely from HF droplets being flung from the drip-cup, were visually observed on the sample surfaces. Overall, uniformity was deemed acceptable both visually as well as being within a standard deviation variation for the reflectance of ± 1.0%. With the stabilisation of the precursor, the spraying application method has achieved the lowest reflectance, best uniformity, and reproducibility out of any precursor application method for GaPTex.

With a reproducible process demonstrated, texture morphology was examined using SEM. Figure 5.24 presents the microstructure in a plan view and a cross-sectional view of typical texture areas. At low magnification in plan-view, the surface appears to be effectively uniform as well as completely textured, except for seven islands of untextured material, as circled in Figure 5.24a), equating to less than 0.1% of the total image area. At increased magnification in Figure 5.24b), the texture is revealed to be unique in morphology from the nanoscale texture morphologies presented in Chapter 1 with a nanoscale fibrous structure. In a cross-sectional view, individual etch-pits can be seen next to the bulk Si. Their morphology appears cylindrical with an approximately circular cross-section that does not appear to change along the depth of the etch pit, as marked in Figure 5.24c). Moving away from the bulk Si, etch pits increase in number, overlapping one another to create a delicate, nanoscale texture at the surface, where surface features are the order of 10s nm, as shown in both Figure 5.24b) and c). Figure 5.24b) also shows the total texture depth varying across the surface, as shown by the corresponding variation in brightness of the texture features. Using Figure 5.24c), the total texture depth is approximately 250 nm thick.

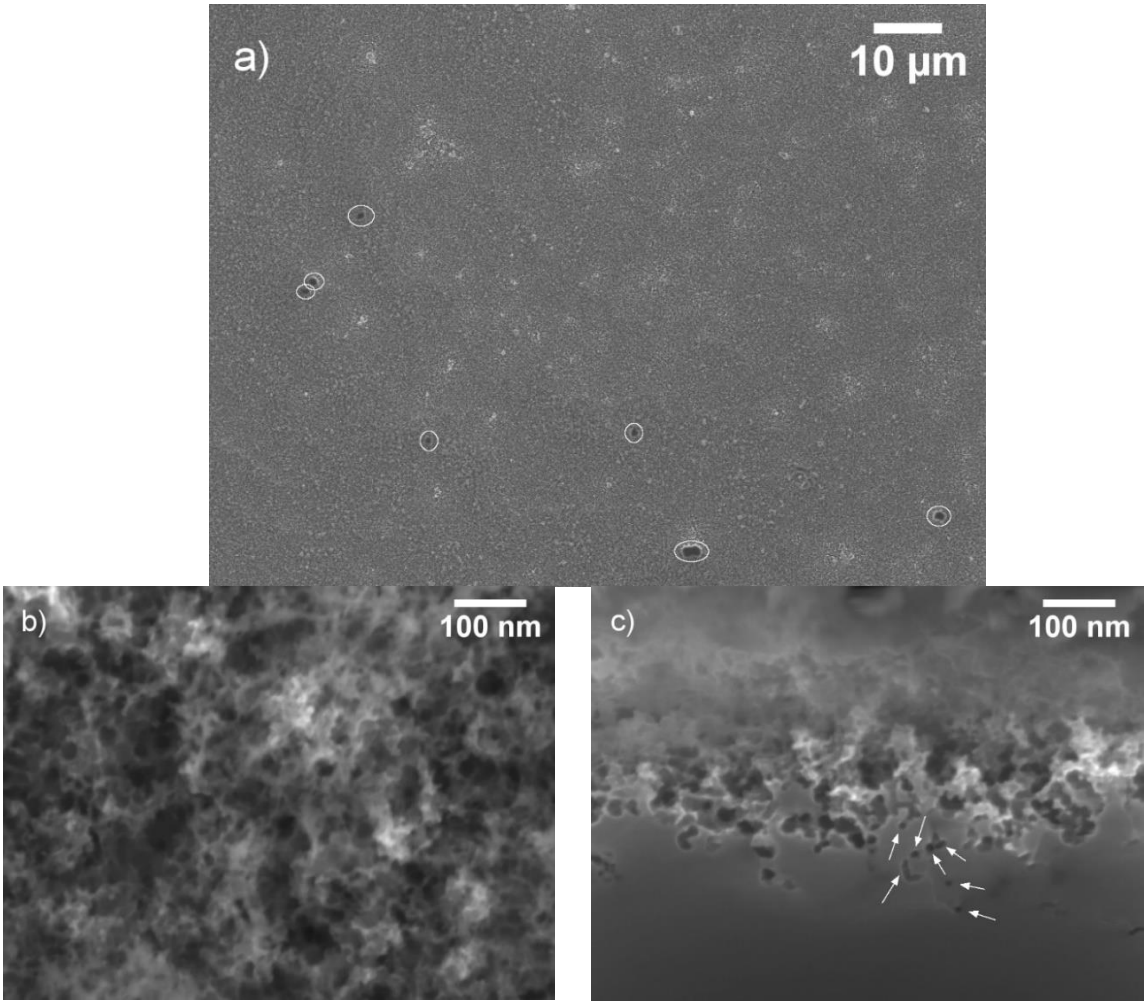

Figure 5.24 SEM images of the microstructure of samples textured using the stabilised precursor a) top-down view at low-magnification, dark regions indicated with white circles b) top-down view at high-magnification c) cross-sectional view at high magnification.

To conclude, a uniform, reproducible texturing technique has been created to texture the entirety of a full-sized Si wafer, using an acid-stabilised colloidal silica and IPA precursor sprayed onto the substrate surface before texturing. Using this method, surface reflectance was reduced to approximately 3% in 10 minutes of texturing.

5.4 Process Optimisation to determine Industrial Applicability

One key aspect of developing GaPTex was determining its industrial applicability. Minimising processing time was key, where a typical metric for batch processes is 1 second per wafer, whilst maintaining uniformity and reflectance. Thus, the target total processing time target for GaPTex was 16 minutes and 40 seconds (batches of up to 1000 wafers), with the uniformity and reflectance achieved in section 5.3.3. Thus far, the GaPTex process takes approximately 35 minutes including spraying (using the recipe from Table 5.6). A

variety of experimental methods were trialled, but only those with significant time reduction (1 minute or more) are presented.

Two operating parameters were found to reduce total processing time the greatest. The first was the precursor drying time after spraying. When spray time was decreased from 45s to 10s, dry time was reduced from 20 mins to 10 mins. To maintain the number of colloidal silica particles deposited on the substrate surface, the precursor dilution was decreased from 1:200 to 1:50. All other processing parameters are the same as in Table 5.6. Figure 5.25 shows the sample appearance post-texture and the corresponding reflectance. With these adjustments, neither surface reflectance nor uniformity was compromised, achieving a WAR of 2.6% and a narrow standard deviation of ± 0.2%. Uniformity is additionally confirmed visually in Figure 5.25a), where the sample surface appears uniform to the naked eye with no imperfections.

The second parameter to significantly reduce total processing time was texturing time. The texturing and spraying conditions are given in Table 5.7. As reducing spray time and increasing the concentration of the colloidal silica had already proven beneficial to reducing total processing time whilst maintaining optical properties, both improvements were included in the sample processing when testing the reduction in texturing time, as shown in Table 5.7. Figure 5.25 shows the sample's appearance post-texturing as well as its reflectance as a function of wavelength. Decreasing texturing time from 10 mins to 2 mins had no negative impact on the surface uniformity, as no imperfections were observed across the sample surface in Figure 5.25b). High texturing uniformity was also demonstrated by the small standard deviation of the reflectance spectra in Figure 5.25c), at ± 0.3%. An increase in reflectance was observed for the 2 mins 'Texture Time' reflectance profile in Figure 5.25c) compared to the 10 min 'Spray Time' reflectance curve. The difference in reflectance was greatest at short wavelengths (~ 1% reflectance difference at 400 nm) and decreased until, at 700 nm and beyond, the reflectance profiles were effectively equal. These changes in reflectance resulted in a small increase of WAR from 2.6% ± 0.2%, when processing for 10 mins, to 3.2% ± 0.3% when reducing processing time

to 2 mins. However, this increase in WAR was still within range of the three samples that demonstrated reproducibility with the stabilised precursor and deemed acceptable in Figure 5.23 and replotted in Figure 5.25c). Thus, the reduction in texturing time was accepted into the optimised texturing conditions. With these two changes to the sample processing recipe, the total processing time was reduced from 35 minutes to less than 15 mins.

Table 5.7 Spraying conditions and texturing conditions for the sample that demonstrated a decrease in texture processing time did not negatively impact texturing.

Operating Parameter	**Value**
Processing Time (min)	2
HF Temperature (°C)	80
Flow Rate (L/min)	1
Sample Temperature	250
Ozone Concentration (wt%)	20

Precursor Spraying Parameter	**Value**
Precursor Concentration	1:50
Infusion Rate (ml/hr)	400
Atomising Pressure (bar)	1.4
Sample Spray Time (s)	10

a)

b)

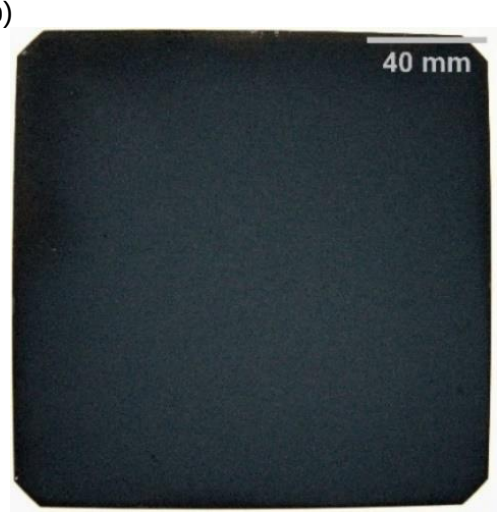

c)

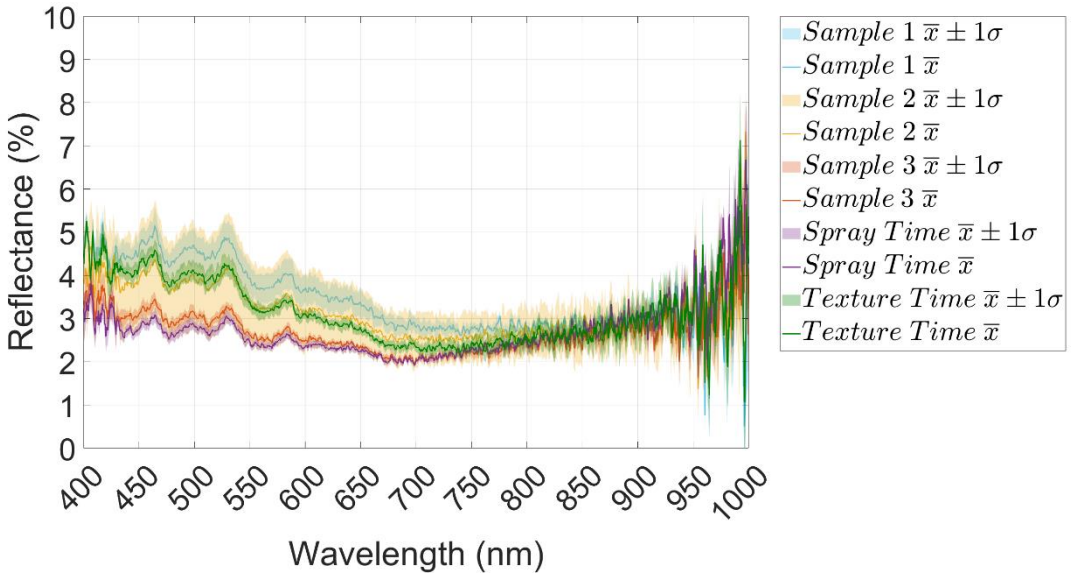

Figure 5.25 Post-texture appearance a) after decreased spray time b) after shortening texturing process time c) the corresponding reflectance spectrums for a) and b). Reflectance spectra from Figure 5.23 are included for reference.

During processing time optimisation, reaction gas flow rate was found to compromise surface uniformity and reflectance, independently of processing time. The texturing recipe in Table 5.7 was used, varying the flow rate varied between 1 L/min and 5 L /min. Figure 5.26 presents the five post-textured surfaces of wafers from 1 L/min to 5 L/min and Figure 5.27 presents the corresponding reflectance.

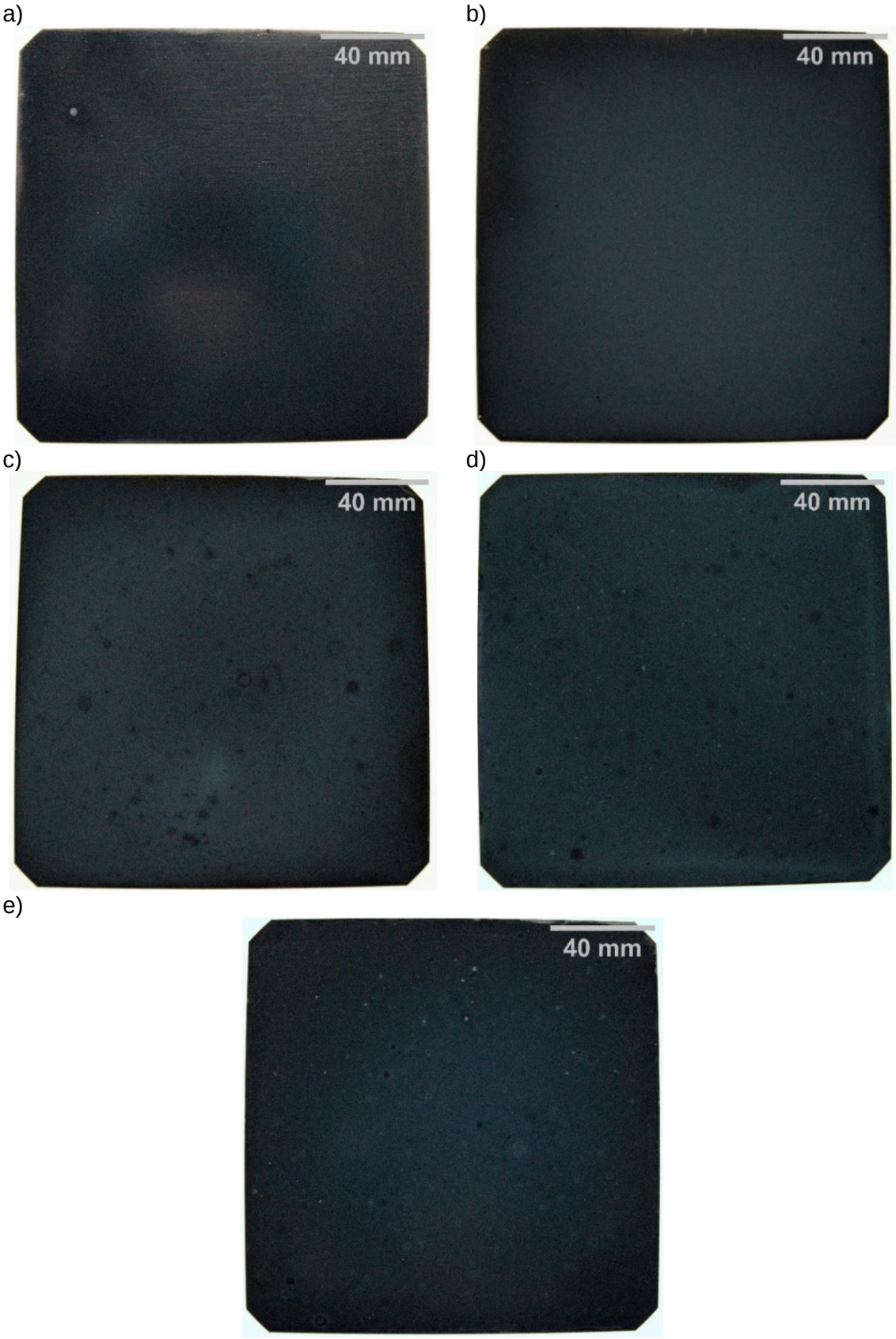

Figure 5.26 Post-texture of samples with flow rates a) 1 L/min b) 2 L/min c) 3 L/min d) 4 L/min e) 5 L/min.

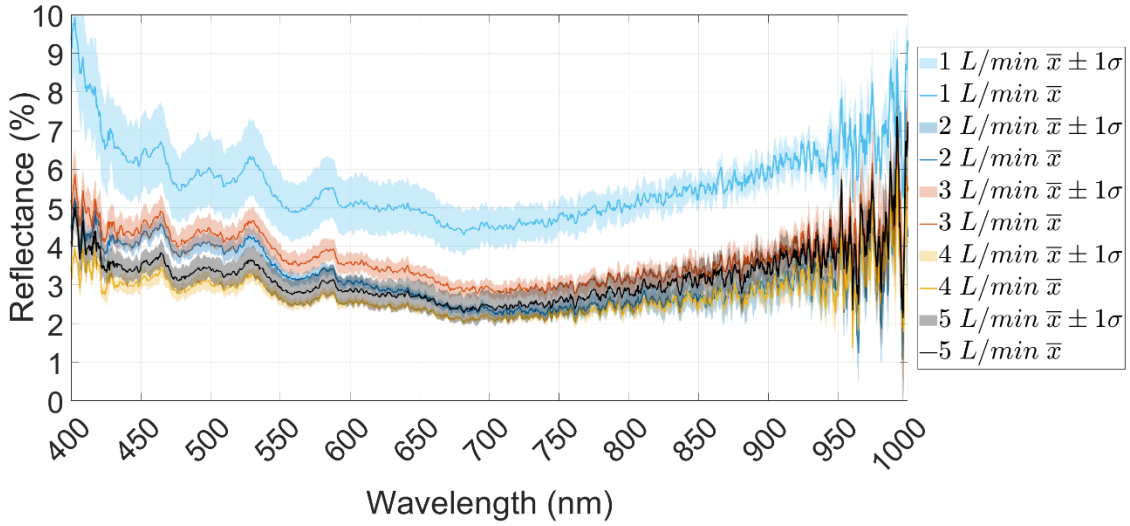

Figure 5.27 Reflectance of samples textured with gas flow rates 1-5 L/min.

Figure 5.27 shows that a low reflectance of 3 – 4% was achieved for all flow rates except 1 L/min, where it increased to 6%. From 400 nm – 700 nm, the reflectance of all specimens decreases with increasing wavelength. This phenomenon could be an artifact of incomplete texturing, as the 1 L/min specimen demonstrates a reflectance greater than 3.5%, implying an increase in the number of regions of incomplete nanotexturing previously demonstrated in Figure 5.24a), and also the largest change in reflectance between 400 nm - 700 nm. In comparison, the reflectance of the other specimens in Figure 5.27 are lower, indicating more complete nanotexturing with fewer regions of untextured material, these spectra also exhibit a smaller change in reflectance values between 400 nm – 700 nm. Therefore, it is plausible that the regions of untextured material contribute to decrease in reflectance between 400 nm and 700 nm, where more untextured material correlates to a larger drop in reflectance. Beyond 700 nm reflectance rises for all the specimens. This effect is not uncommon to nanoscale textures and is typically an indication that the total texture depth is shallow and thus is unable to minimise reflectance at longer wavelengths as effectively as for short wavelengths [235]–[241]. Figure 5.26 shows sufficient surface uniformity was only observed for lower flow rates of 1 and 2 L/min; at flow rates beyond 2 L/min, spots marred the surface. The spotting at high flow rates is attributed to increased gas flow, causing HF to escape the HF drip-cup and fall onto the sample surface. The flow rate of 2 L/min balanced low reflectance and high texturing uniformity with a WAR of 3.1% ± 0.4%

and no observable spotting on the surface. Using all the texturing recipe optimisations, the final optimised texturing recipe for high processing speed, low reflectance and consistent uniformity is presented in Table 5.8.

Table 5.8 Optimised spraying texturing conditions for low reflectance, high uniformity, and quick processing speed.

Operating Parameter	**Value**
Processing Time (min)	2
HF Temperature (°C)	80
Flow Rate (L/min)	2
Sample Temperature	250
Ozone Concentration (wt%)	20

Precursor Spraying Parameter	**Value**
Precursor Concentration	1:50
Infusion Rate (ml/hr)	400
Atomising Pressure (bar)	1.4
Sample Spray Time (s)	10

The optimisation of GaPTex presented here has not only achieved a great reduction in WAR but also in processing time compared with prior work. In M. Cohen's work [183], the lowest WAR achieved on DWS material was 11.7% in 30 mins texturing time. Within this work, WAR has been reduced to 3.1% ± 0.4% in 2 mins of texturing time, a reduction of ~×4 in reflectance and ×15 in texturing time against prior work. This initial optimisation has already made GaPTex more industrially applicable, particularly with the reduction in processing time. To further industrial applicability, future work should focus on demonstrating HF/O_3 GaPTex on multiple wafers at once.

The optical performance of GaPTex is equal to some of the best texturing techniques for ultra-low surface reflectance. Figure 5.28 compares WAR values of a variety of B-Si texturing techniques including MACE, RIE, F_2 gas-phase texturing, and HF/O_3 GaPTex. Both MACE and RIE can produce some of the lowest reflectance morphologies on Si, commonly demonstrating ultra-low sub-5% surface reflectivity [123], [125], [126]. Typical GaPTex is comparable to MACE, achieving approximately the same WAR in Figure 5.28, but the champion GaPTex outperforms MACE with a WAR of 2.6% ± 0.2%. RIE surpasses GaPTex optically, achieving a WAR of 0.2%. Finally, the alternative gas-phase texturing

techniques presented in Chapter 1 are all outperformed in terms of WAR and processing time by HF/O_3 GaPTex, except for the work of B. Kafle et al. [172]. Figure 5.28 shows a comparable WAR of F_2 gas-phase texturing to GaPTex of approximately 2% for the former with an 1100 nm deep texture [172].

In addition to ultra-low reflectance, GaPTex provides processing benefits over other nanotexturing techniques. GaPTex mitigates the drawbacks of MACE and RIE, as it does not require the expense of noble metals, costly equipment, or more than one etching phase to achieve ultra-low reflectance. A processing time comparison between GaPTex and F_2 gas-phase texturing is difficult as the total processing time for F_2 gas-phase texturing was not commented on [172], instead, sample belt speed was quoted, and the belt length was not defined. In conclusion, GaPTex has demonstrated comparable or more desirable processing requirements than other industrially relevant nanotexture techniques, without any compromise to optical properties of the textured Si.

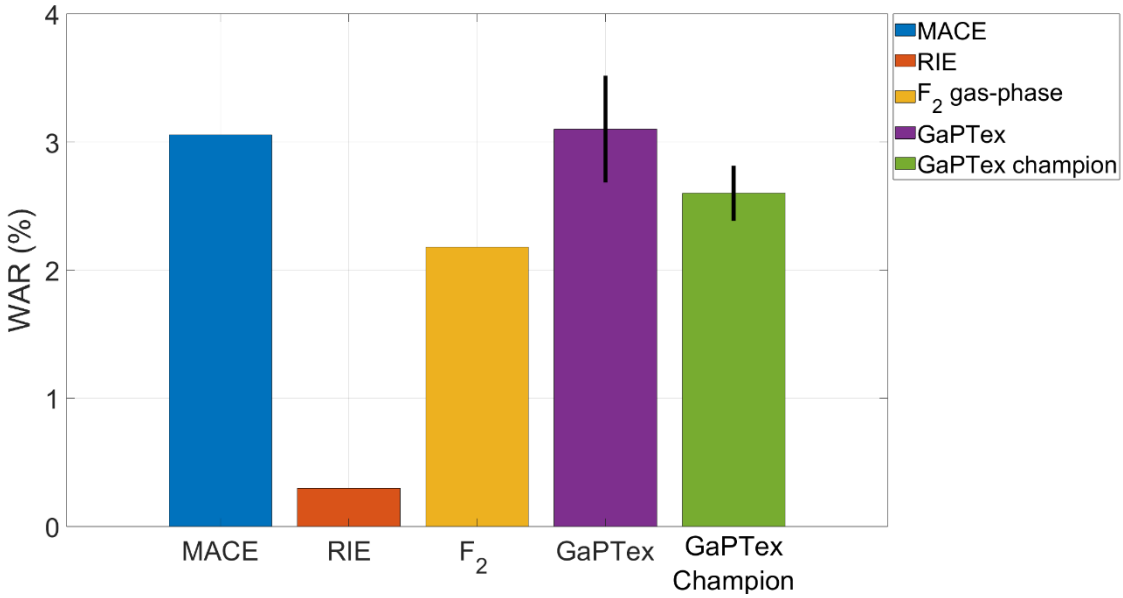

Figure 5.28 WAR comparison of different B-Si techniques. MACE data is reproduced from J. Oh et al. [139]*, RIE data is reproduced from T. Fung et al.* [242]*, F_2 gas-phase texturing data is reproduced from B. Kafle et al.* [172]*.*

GaPTex showed sensitivity to its operating parameters during the texturing optimisation process, therefore experimental checks had to be implemented to verify an experimental session's results were reproducible and meaningful. At the start of each experimental session, a wafer was textured using the recipe presented in Table 5.8, the subsequent

reflectivity and surface finish of the wafer indicated if any adjustments were needed to any equipment. For example, large, seemingly random, dots on the wafer surface indicated that HF was being spat from the drip-cup and the cup needed adjustment or emptying. Conversely, much smaller, darker, and more regular dots indicated the sample dried too quickly after spraying and the spray unit needed adjustment (for example, the spray nozzle needed re-seating). Once any adjustments were made to the overall process and a sample achieved 2-3% reflectance with a uniform surface finish, further experimental work was deemed to be meaningful and reproducible.

5.5 Chapter Summary

In this chapter, an acid-stabilised precursor of colloidal silica in IPA was created, enabling uniform, reproducible texturing, resulting in ultra-low reflectance from Si surfaces. Application methods for the precursor were reviewed, and the greatest texturing uniformity was achieved with an optimised spray-unit set-up to spray the precursor onto the substrate surface before texturing. Texturing reproducibility was resolved with the stabilisation of the precursor and the implementation of engineering controls at the start of each experimental session. Additionally, GaPTex was successfully optimised for an industrial application, where a 156 mm × 156 mm wafer was textured to 3% WAR in 2 minutes texturing time and less than 15 minutes total processing time. Further investigations into the role the precursor has in enabling texturing will be investigated in the next chapter.

6 The Role of Colloidal Silica in Gas-Phase Texturing

6.1 Investigating Individual Precursor Components

Before further optimising the texture morphology of GaPTex for solar cells, the hypothesis of the role of the precursor was verified. The hypothesis in Chapter 5 proposed that the texturing nucleation rate could be accelerated by increasing the number of microscopic variations on the surface. Silica nanoparticles were chosen to fulfil this role. However, when texturing was displayed for the first time, using the non-stabilised precursor, there were three other components in the colloidal silica aside from the silica nanoparticles: ethylene glycol, NaOH (Na^+ counter-ions around silica particles and OH^- ions in the bulk solution), and IPA. To verify that texturing was caused by the nanoparticles, the four components of the non-stabilised precursor were split up and tested individually to isolate their effect on texturing.

The concentrations of the isolated components were made to match their concentrations in the Kemet Col-K NC colloidal silica. IPA used in forming the precursor was shown in Chapter 5 to not produce significant texturing and thus was not tested further. For nanoparticles, 2 g of fumed silica nanoparticles were mixed with 10 ml of deionised water to recreate the colloidal silica concentration of 200 g/L. For ethylene glycol, 1 ml of ethylene glycol was mixed with 9 ml of deionised water concentration for a 10 vol% solution. The entirety of the alkaline pH in the colloidal silica was attributed to NaOH, as all other components were neutral pH. A solution of pH 10 NaOH was made from a NaOH pellet and deionised water, and pH was measured with the Hanna Instruments HI-98100 Checker Plus pH Tester. Each component was subsequently diluted with IPA, recreating the 1:50 colloidal silica to IPA dilution of the precursor from Chapter 5; 1 ml of each of the three components was mixed with 50 ml IPA and shaken by hand for 30 s. 1 ml of each of the diluted component solutions was pipetted onto three different sample surfaces and air-dried. Substrates used were 4 cm × 4 cm from Trina 2 wafers, cleaved using a diamond-tipped

pen, rinsed with IPA, and dried with compressed air. Samples were textured using the conditions in Table 6.1. Sample appearance post-texturing is presented in Figure 6.1, surface reflectance in Figure 6.2, and micrographs in Figure 6.3.

Table 6.1 Operating parameters in the texturing tool to test individual components of the precursor.

Operating Parameter	**Value**
Processing time (min)	3
HF Temperature (°C)	80
Flow Rate (L/min)	2
Sample Temperature (°C)	250
Ozone Concentration (wt%)	20

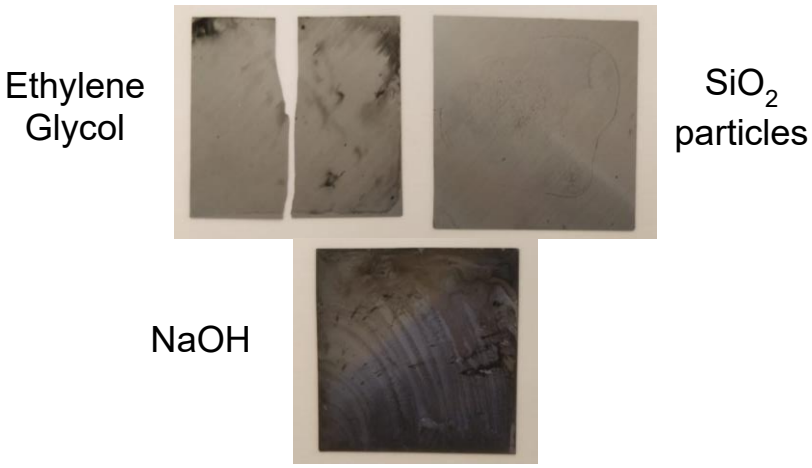

Figure 6.1 Post-texture appearance of the three individual components of the colloidal silica used in the non-stabilised precursor.

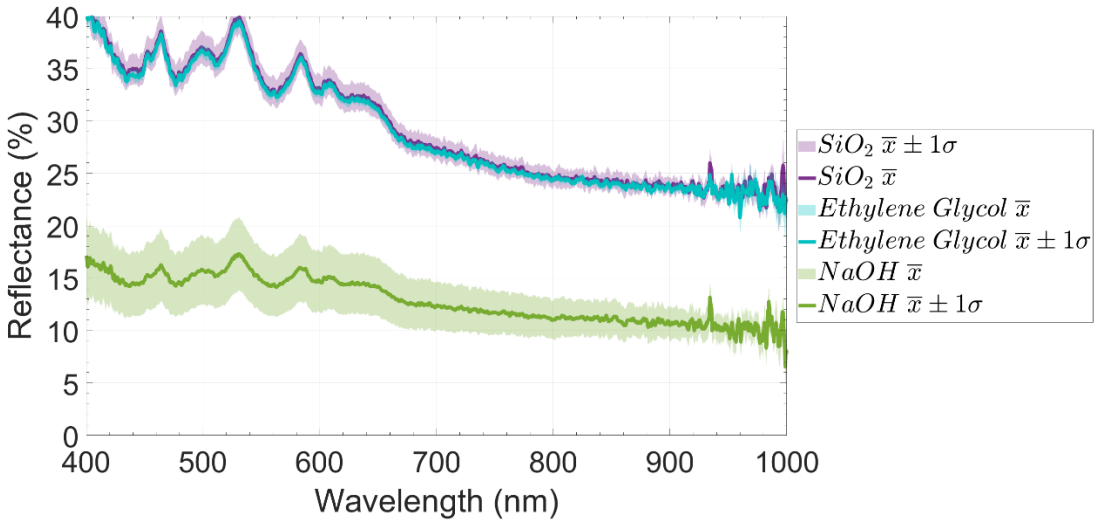

Figure 6.2 Post-texture reflectance of the three individual components of the colloidal silica used in the non-stabilised precursor.

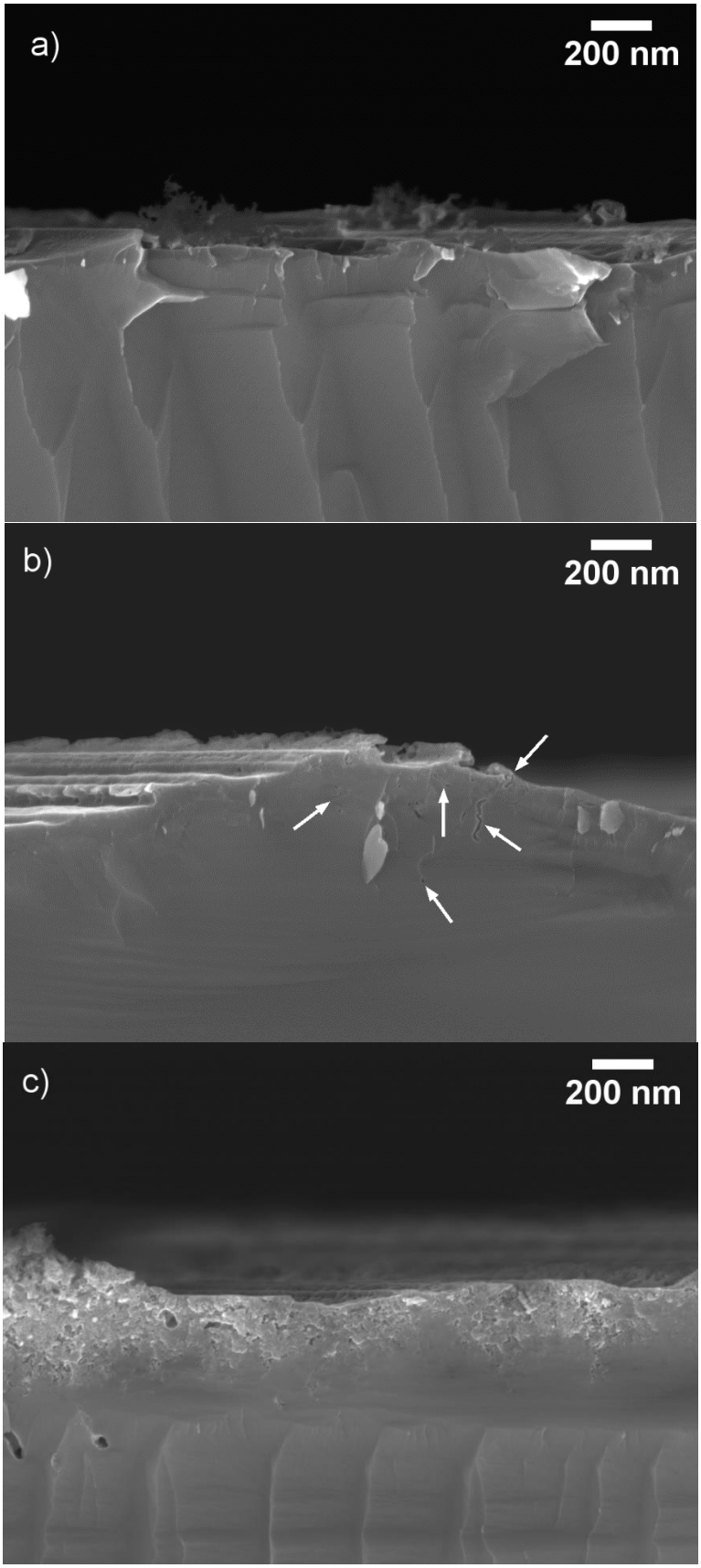

Figure 6.3 SEM images of the texture produced by the three colloidal silica components a) silica nanoparticles b) ethylene glycol c) NaOH solution.

In Figure 6.1, when only the silica nanoparticles were present on the surface, there was no significant change in appearance after texturing. For ethylene glycol, the post-texture appearance in Figure 6.1 showed trace amounts of non-uniform texturing. Contrastingly, the sample with NaOH darkened most of the three components, where with bands of varying reflectance radiating from the bottom left corner of the sample are visible in Figure 6.1. Figure 6.2 and Figure 6.3 corroborate the findings in Figure 6.1. The WAR for NaOH from Figure 6.2 is less than half of the other components at 13.6% ± 2.6%, while the WAR for the SiO_2 nanoparticle sample was 31.2% ± 1.3% and the ethylene glycol sample was 30.9% ± 0.5%. However, the WAR of the sample textured with NaOH is greater than for samples textured with the full precursor, as evidenced in Chapter 5. Considering the morphology of each of the three component samples, Figure 6.3a) shows effectively no texturing occurs for the silica nanoparticle sample, as no etch-pits are observed in the micrograph. Little texturing occurred for the ethylene glycol specimen, where a limited number of etch-pits are indicated in Figure 6.3b). The NaOH specimen in Figure 6.3c) shows many more etch-pits in comparison to the other two components, yet once again this is not as many etch-pits as when the full precursor was used in Chapter 5. From testing the non-stabilised precursor components individually, the component that appeared to aid texturing the most was NaOH.

To corroborate the initial findings that texturing was predominantly caused by NaOH, and not due to other precursor components or any other surface species, two further specimens were prepared. Two substrates of 4 cm × 4 cm were cut from Trina 2 wafers using a diamond-tipped pen. Instead of the IPA cleaning used for samples in Figure 6.1, all specimens were cleaned with RCA1, RCA2, and a HF dip to completely remove any chemical species on the surface that may have influenced subsequent texturing. After cleaning, one sample underwent no further preparation before texturing. The second sample re-tested the response of NaOH in IPA; the preparation of this specimen is the same as described earlier in this section. Both samples were textured using the conditions

presented in Table 6.1. Post-texturing appearance and surface reflectance are presented in Figure 6.4 and Figure 6.5 respectively.

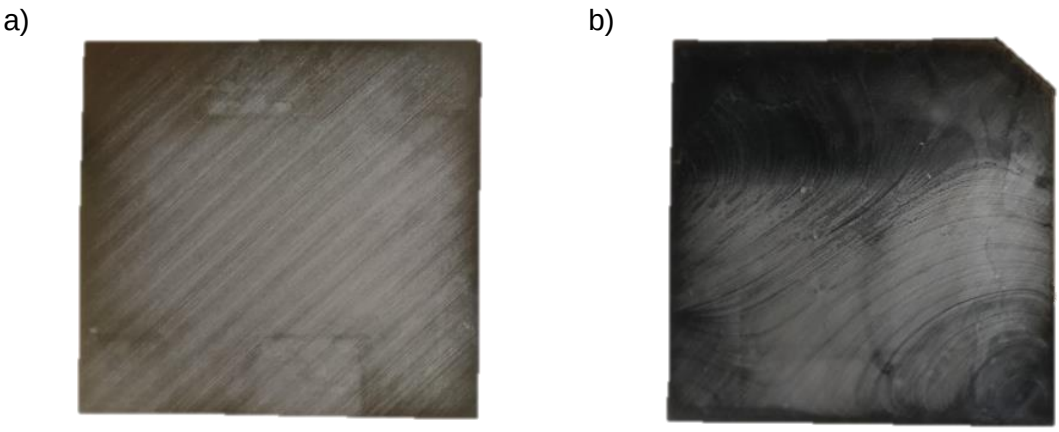

Figure 6.4 Post-texture appearance of a) a RCA cleaned surface b) a RCA cleaned and NaOH surface.

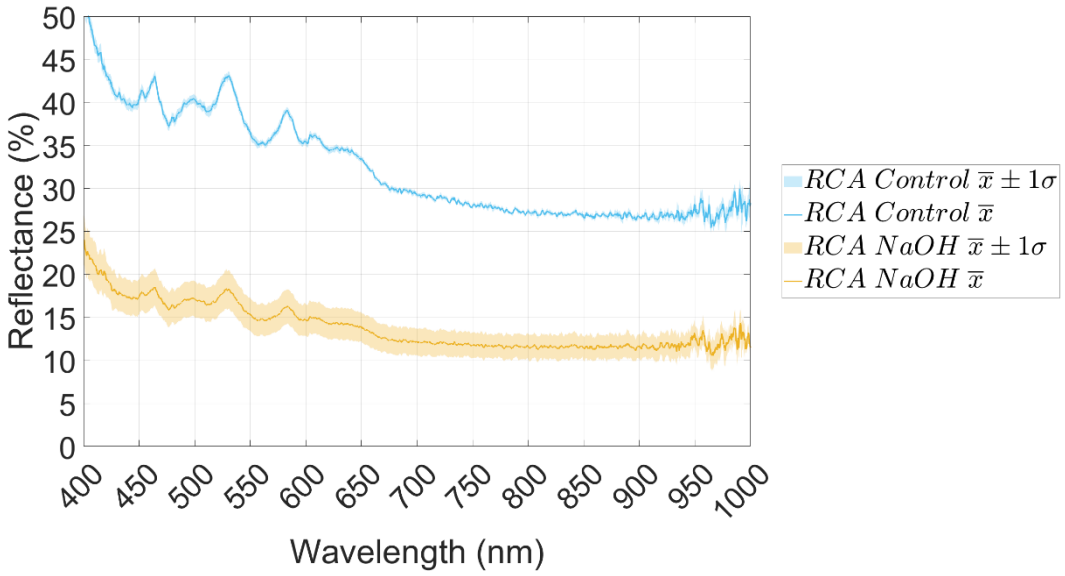

Figure 6.5 Post-texture reflectance of the RCA control sample and the RCA with NaOH sample.

Once more, the presence of NaOH on the Si surface induced texturing, whilst the control sample remained unchanged. Figure 6.4 shows a darkened surface when NaOH was present during texturing, whilst the RCA-cleaned control specimen was effectively unchanged by the texturing process. Figure 6.5 supports these findings where WAR remained at 34.6% ± 0.6% for the control specimen, whilst reflectance decreased to 14.8% ± 1.9% for the NaOH sample. Texturing non-uniformity again occurred when only using NaOH as a precursor. Figure 6.4 shows the bands of varying darkness from the upper left corner to the lower right corner for the NaOH textured sample; similar to the corresponding

NaOH sample in Figure 6.1. However, in contrast to Figure 6.1, a horizontal band of darker material also occurs at the top of the NaOH sample in Figure 6.4.

Thus far in this chapter, the precursor component that has a dominant effect on texturing has been narrowed to NaOH. However, both the Na^+ and OH^- ions in aqueous NaOH do not appear in the final, fully stabilised precursor, only Na^+ counter ions are present (see section 5.3.3). To determine if only Na^+ ions aided texturing, fully acid stabilised precursors with and without Na^+ as the counter-ion were prepared. In addition, by testing a precursor without Na^+ as the counter-ion, it can be ascertained if the sum of the precursor components that did not produce significant texturing in this chapter thus far, could produce texturing once combined. Two acid-stabilised precursors were made as described in Chapter 2, using two different colloidal silicas. The first precursor used colloidal silica stabilised with ammonium counter-ions from Ludox with a particle size of 22 nm, termed AS-40 by the company. The second precursor used the Ludox colloidal silica TM-40 with a 22 nm particle size and Na^+ as the stabilising counter-ion. The particle size of AS-40 differs from the Kemet colloidal silica used thus far in this work, thus the second precursor, TM-40, accounted for a change in particle size, disentangling the effects of particle size and counter-ion on texturing. Both precursors were made to a 1:50 colloidal silica to IPA dilution. Two substrates of 4 cm × 4 cm were cut from Trina 1 wafers using a diamond-tipped pen, then rinsed with IPA and dried with compressed air. Spraying conditions used to apply the two precursors to the substrates are presented in Table 6.2. The texturing recipe used is presented in Table 6.1. Post-texture appearance, surface reflectance, and micrographs of the two specimens are presented in Figure 6.6, Figure 6.7, and Figure 6.8 respectively.

Table 6.2 Spraying conditions of the precursors made with the colloidal silicas AS-40 and TM-40.

Precursor Spraying Parameter	**Value**
Precursor Dilution (Colloidal Silica : IPA)	1:50
Infusion Rate (ml/hr)	400
Atomising Pressure (bar)	1.4
Sample Spray Time (s)	10

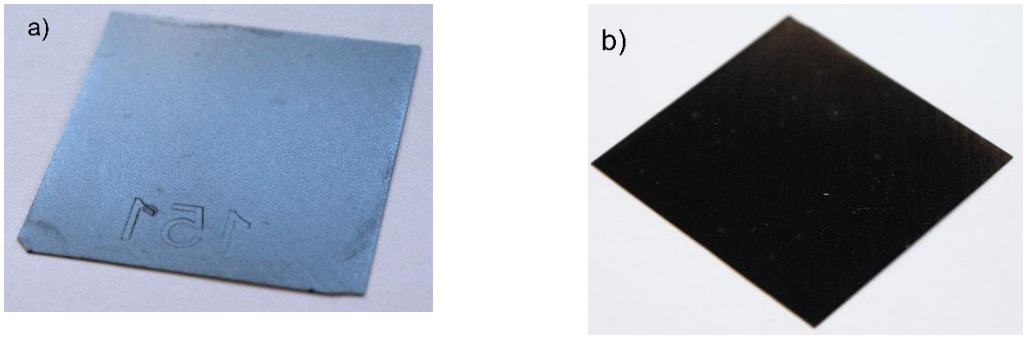

Figure 6.6 Post-texture appearance of samples sprayed with precursors containing colloidal silicas a) AS-40 b) TM-40.

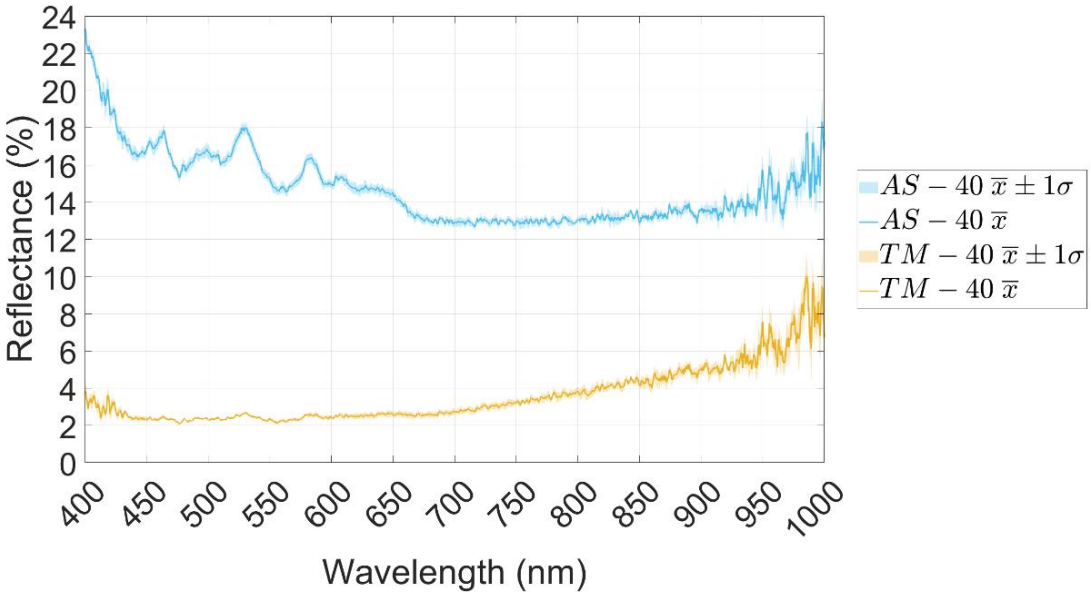

Figure 6.7 Post-texture reflectance of precursors made with AS-40 or TM-40 colloidal silicas.

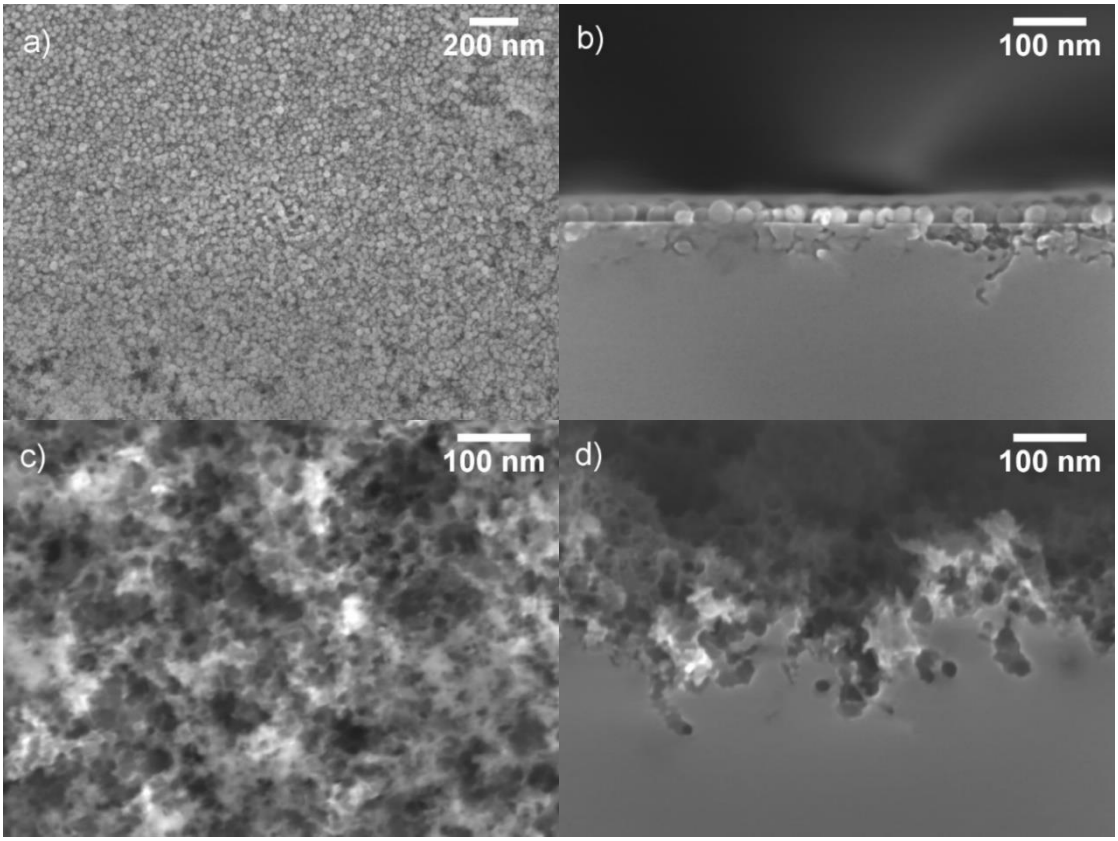

Figure 6.8 SEM images of the microstructure of samples textured with colloidal silica AS-40 a) top-down view b) cross-sectional view and with colloidal silica TM-40 c) top-down view d) cross-sectional view.

Figure 6.6, Figure 6.7, and Figure 6.8 demonstrate the ammonium counter-ion precursor produced little to no texturing in comparison to the Na^+ counter-ion precursor. In Figure 6.6, there is no apparent visual change from GaPTex when using AS-40 in the precursor, whilst the specimen with TM-40 darkened. Figure 6.7 shows the reflectance of the AS-40 specimen is less than a bare Si surface, at 15.5% ± 0.5%, but still not as low as when the Na^+ counter-ion is present, as the reflectance of the TM-40 sample was 3.5% ± 0.4%. Upon examining the microstructures in Figure 6.8, the AS-40 specimen underwent less texturing than the TM-40 sample for the same processing time. In addition, the silica particles on the AS-40 specimen underwent etching but were not fully etched away, as was apparent for the TM-40 specimen.

6.1.1 Discussion

The hypothesis of the precursor promoting texturing due to nanoparticles is contradicted by the findings shown in this chapter. Texturing became limited when only silica nanoparticles were present on the sample surface; as shown by the lack of visual changes

to the sample surface post-texturing in Figure 6.1, the high reflectance post-texturing in Figure 6.2 (when compared to a GaPTex sample textured with a fully stabilised precursor as in Chapter 5), and the effectively unchanged morphology in Figure 6.3. Contrastingly, the component that did cause texturing provided no physical variation on the surface but instead was a chemical. Figure 6.1 - Figure 6.3 again demonstrates texturing only occurring when a solution of NaOH was present on the sample surface. The sample surface darkened when NaOH was present in Figure 6.1, correspondingly, the surface reflectance for the NaOH specimen was lower than either the silica nanoparticles or the ethylene glycol in Figure 6.2.

However, the WAR and texturing uniformity when using only NaOH as a precursor was poorer than when the full precursor was used to texture in Chapter 5. Figure 6.1 and Figure 6.4 demonstrate the lack of texturing uniformity for specimens textured solely with NaOH, where bands of grey can be seen across the surface. Figure 6.2 and Figure 6.5 show that WAR reduced to approximately 15% when texturing with NaOH, greater than the WAR when texturing with the full precursor in Chapter 5. Two possibilities could attribute to the increase in WAR and the lack of texturing uniformity observed: how NaOH was deposited onto the surface and how it dried on the surface. Firstly, considering how uniform texturing occurs, section 5.3.1 showed that Na^+ counter-ions in colloidal silica localise around the silica particles in the stern layer and the diffuse layer, while OH^- ions predominantly remain in the bulk solution. When using the complete and stabilised precursor during texturing, uniform and ultra-low reflectance textures were achieved when a uniform distribution of nanoparticles was created on the surface. In turn, a uniform distribution of Na^+ was created across the surface with the uniform distribution of the nanoparticles, as Na^+ counter-ions localise around the nanoparticles in the EDL. Contrastingly, when the nanoparticles were not present, as in the NaOH solution, the Na^+ ions were free to move across the surface, thus a uniform distribution of Na^+ on the surface after application was no longer not guaranteed. Secondly, the drying of the deposited solution also influenced the distribution of Na^+ on the surface. In the full precursor, the Na^+ can be considered to be ‘anchored’ to

the nanoparticles, due to the electrostatic attraction between the surface of the nanoparticle and the Na^+ counter-ion, thus enabling Na^+ to dry in a uniform distribution on the surface alongside the nanoparticles. However, without the particles present in the NaOH solution, there is no cause for the Na^+ to dry in a uniform distribution across the surface. Instead, the ions are likely influenced by the next strongest force: the surface tension of the drying solution. The effect of the surface tension would likely move the ions in the NaOH solution across the surface, with the drying film, in a non-uniform manner. The non-uniform drying of the NaOH solution accounts for the bands of dark grey present on the sample surface in both Figure 6.1 and Figure 6.4. The bands of dark grey would also imply that texturing using Na^+ is a local effect, otherwise, there would have been no change in texturing uniformity between Na^+ in a uniform or non-uniform distribution on the substrate surface during texturing.

Finally, the typical GaPTex texture morphology, when using the full precursor, was not achieved when only the NaOH solution was present on the surface. Figure 6.3 showed the original Si surface remained after texturing with the NaOH solution. However, nanoscale etch-pits with a circular cross-section were present beneath the original Si surface which was also seen when texturing with the full precursor in Chapter 5. This again indicates that texturing can occur by NaOH, but it does not yield identical results to using the full precursor. Thus, silica nanoparticles do not fulfil the original hypothesis of directly causing texturing, instead this effect is attributed to the Na^+ counter-ions of the colloidal silica. However, silica nanoparticles play an important supporting role to achieve high texture uniformity and the darkest of textured surfaces.

Texturing also appeared chemically selective, specifically to Na^+. The other two non-suspension components, ethylene glycol and IPA, demonstrated only trace texturing when isolated, demonstrated visually in Figure 6.1, microstructurally in Figure 6.3, and by a high surface reflectance in Figure 6.2. Chemical selectivity to Na^+ is further supported by XPS measurements from Chapter 4, where Na^+ was found as contamination on sample surfaces that textured. The last indication texturing is specific to Na^+ was shown when an otherwise

identical precursor except for the counter-ion, was used to texture. Texturing effectively stopped when the ammonium-stabilised precursor, AS-40, was used instead of the Na^+-stabilised precursor, TM-40, as demonstrated in Figure 6.6 - Figure 6.8. Figure 6.6 visually demonstrated that a full precursor with Na^+ counter-ions darkened Si to black, while an ammonium counter-ion precursor caused little change to the surface colour from silver. Figure 6.7 supports the findings of Figure 6.6, where the WAR of the specimen prepared with TM-40 was 3.5% ± 0.4%, typical to WARs achieved by fully stabilised precursors in Chapter 5; however, the ammonium stabilised AS-40 precursor yielded a higher WAR of 15.5% ± 0.5%, atypical from the results in Chapter 5. When texturing with AS-40, some texture typical to GaPTex morphologies formed, as shown in Figure 6.8(a,b), but this texture did not cover the entire surface, as was shown when Na^+ counter-ions were present in the precursor in Figure 6.8(c,d), leaving areas of un-textured Si after texturing. The type of etch-pits that formed when texturing with AS-40 were the same as when texturing with TM-40, where they were nanoscale and circular in cross-section. The total texture depth when using AS-40 was greatly reduced in comparison to when TM-40 was used, achieving approximately a quarter of the total texture depth in comparison to the sample textured with TM-40 in Figure 6.8. It may be possible if processing time was increased, for the specimen textured with AS-40, the texture would have developed to the texture of the samples prepared with the Na^+ counter-ion precursor. Finally, Figure 6.8(c,d) showed when the Na^+ counter-ion colloidal silica TM-40 was used, that the typical GaPTex morphology when using a stabilised precursor was achieved, with a typical total texture depth, feature size, and none of the original un-etched Si surface remaining. This again supports the previous statement that the full precursor, containing both the nanoparticles and the Na^+ counter-ions, must be applied on the Si surface to cause the most uniform and lowest reflectance textures. Thus, Na^+ counter-ions are the dominant effect of the precursor aiding GaPTex, not the nanoparticles. However, the combination of the nanoparticles and Na^+ counter-ions are required to achieve the darkest and most uniformly textured surfaces by GaPTex.

Thus far Na^+ has been shown to be necessary for texturing to occur, but its role within texturing has not been well defined. There are two possibilities of the type of aid Na^+ offers to GaPTex. First is physical assistance to the texturing reaction, by methods such as increasing the number of texturing reaction sites (as the nanoparticles were originally proposed to do), such as roughening the surface. Alternatively, chemical assistance may be offered to texturing, analogous to the difference between wet acidic chemical etching and MACE. However, Na^+ cannot offer physical assistance to GaPTex. Section 1.6.1.1 demonstrated that any roughening of Si using alkali metal hydroxides relied on the presence of OH^- ions in solution, not the alkali metal cation. From section 5.3.3 it was shown that during the preparation of the acid stabilised precursor, any OH^- ions neutralised with the H_3O^+ ions to form water. Therefore, Na^+ does not physically aid GaPTex.

Instead, the role of Na^+ in GaPTex is likely chemically based, where its presence on the substrate surface during texturing is necessary for significant texturing to occur. From the experiments in this section, texturing only occurred when specimens had Na^+ present on the surface; when Na^+ was not present on sample surfaces, texturing effectively ceased. Considering the two halves of the texturing reaction, oxidation and oxide-etching, Na^+ has been shown to aid oxide-etching. Figure 6.8(a,b) showed that the silica nanoparticles underwent minimal etching without the presence Na^+ of in the reaction chamber, whilst effectively all nanoparticles were etched away in Figure 6.8(c,d) when Na^+ was present on the surface. All these effects indicate the role of Na^+ in GaPTex to be chemical.

To define the chemical role of Na^+ in texturing further, the thermodynamics and kinetics of GaPTex oxidation and oxide-etching reactions were considered, including the effect Na^+ may have upon them.

6.2 Thermodynamics and Kinetics of Si Oxidation

To determine the spontaneity of silicon oxidation without Na^+, the change in Gibbs Free Energy (ΔG) was calculated for both O_3 and O_2 using the equation:

$$\Delta G_{reaction} = \Delta H_{reaction} - T\Delta S_{reaction} \quad (6.1)$$

where $\Delta G_{reaction}$ is the change in Gibbs Free Energy of a reaction in kJ/mol, $\Delta H_{reaction}$ is the change in Enthalpy of Reaction in kJ/mol, T is reaction temperature in K, and $\Delta S_{reaction}$ is the change in Entropy of Reaction in J/K.mol. Full details of the calculation are found in Appendix II. $\Delta G_{reaction}$ for oxidation using O_3 or O_2 is:

$$\Delta G_{Si-O_3} = -2878.5\ kJ/mol$$

$$\Delta G_{Si-O_2} = -849.1\ kJ/mol$$

$\Delta G_{reaction}$ was negative for both oxidation scenarios, indicating that Si oxidation is spontaneous with either oxygen species, causing Si to exist in a lower free energy state by oxidising. The driving force for oxidation is greater when using O_3 than O_2, as $\Delta G_{reaction}$ was a larger negative value, indicating a greater energy reduction occurs when O_3 is used to oxidise the Si surface. Thus, Na^+ is unlikely to affect oxidation thermodynamically, as a driving force is already present.

Regardless of a reaction being thermodynamically favourable, it can still be prevented from occurring to any significant extent if the kinetics are unfavourable. To assess if any significant oxidation occurred under the texturing experimental conditions thus far, oxidation reaction rates were examined. C. K. Fink et al. [196] demonstrated in their review of oxidation using ozone, that oxidation rates have extreme sensitivity to temperature, pressure, surface termination, and the ozone generator used; however, no trends were presented in the four-parameter space. Thus, an accurate calculation of oxidation rates for GaPTex using literature cannot be made.

To determine oxidation rates on a bare Si surface in the GaPTex tool, four 3 cm × 3 cm samples of Trina 1 material were cleaved using a diamond-tipped pen. Samples were rinsed in IPA and dried with a compressed air gun, then dipped in 1:10 40 wt% HF and de-ionised water, and subsequently rinsed in de-ionised water. The surface oxide of the samples was measured with the ellipsometer and the “0 min” measurement was used as a baseline to measure subsequent oxide growth. One sample was left in air at room temperature as a

control and the oxide thickness was measured after 15 mins, 30 mins, and 60 mins. The other three samples were used to measure oxidation at elevated temperature with O_3 where samples were removed after 15 mins, 30 mins, and 60 mins for oxide growth measurements. The recipe used for oxidising samples at high temperatures in O_3 was based on the recipe in Table 6.1 with adjustments for O_3 to bypass the HF reservoirs, thus only O_3 was present in the texturing chamber. The thickness of oxide grown as a function of time is presented in Figure 6.9. The accuracy of oxide thickness measurements was monitored using the 'fit difference' provided by the ellipsometer software. For all measurements, this fell within an acceptable range of 0.0019 – 0.0025.

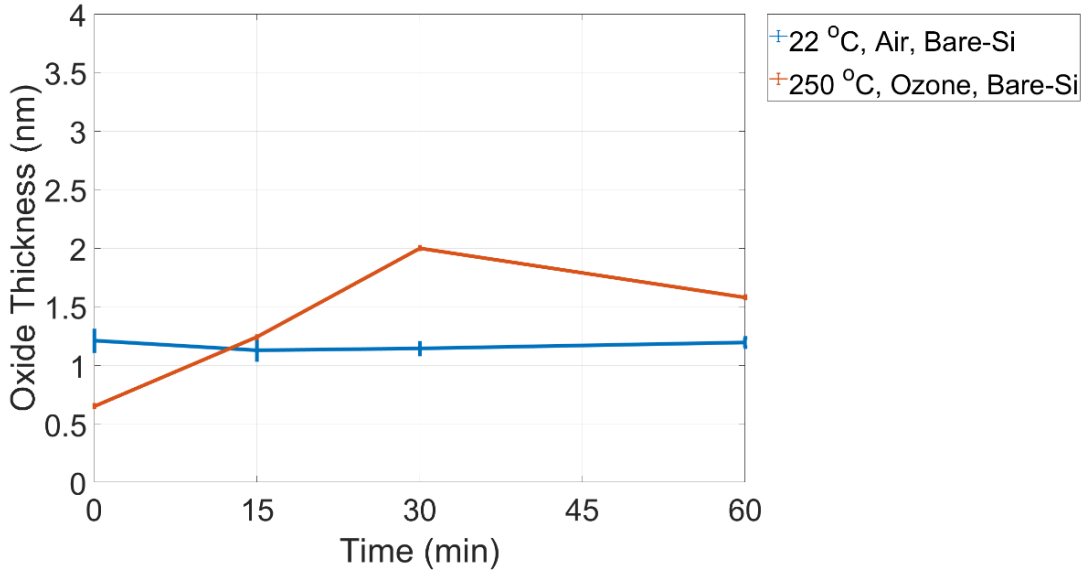

Figure 6.9 Si-oxide growth of bare Si either in air at room temperature or 250 °C in O_3.

The oxide growth thicknesses presented in Figure 6.9 show that SiO_2 no greater than 2 nm was grown with O_3 at elevated temperatures. A small decrease in the oxide thickness was observed when using O_3 at elevated temperatures between 30 mins and 60 mins from 2 nm to 1.6 nm. This decrease is unlikely to be caused experimentally, as there were not any species in the environment to cause etching of the surface oxide. The source of the decrease may originate from the increased 'fit difference' experienced for this value, indicating more error was introduced to the measurement by the parameters of the ellipsometer [186]. Comparing the oxide grown at high temperature with O_3 to the control sample at room temperature showed the oxide thickness of the high-temperature, O_3

sample was greater than the room temperature control, but the greatest difference in thickness between the two specimens was less than 1 nm.

Temperature has been shown to kinetically aid Si oxidation rates, where higher temperatures yield thicker oxides more quickly [243]–[245]. Thus, by performing oxidation at an elevated temperature of 250 °C, the oxidation rate should be quicker than at room temperature. However, the increase in oxidation rates and thickness in literature are explored at temperatures greater than 800 °C, up to 1200 °C [243]–[245], not at temperatures as low as 250 °C. Thus, it is unknown from the literature if increasing the temperature from room temperature to 250 °C would be sufficient to change the kinetics of Si oxide growth for quicker oxide growth. Instead, the oxide thickness grown at 250 °C with O_3 in Figure 6.9 is comparable to native oxides grown in air at room temperature for the same time, demonstrated by S. Raider et al. [246] and C. Bohling et al. [206]. Therefore, little to no benefit was achieved for Si oxide growth by increasing the temperature to 250 °C and using O_3 as the oxidation species over a sample at room temperature in air. Considering the whole GaPTex reaction, the total texture depth of 200 nm after 3 mins of texturing cannot be attained with the limited oxide growth at 250 °C with O_3. Thus, without the presence Na^+ on the sample surface, the surface oxidation in GaPTex appears to be kinetically limited.

6.2.1 Na and Si Oxidation Kinetics

Na^+ may be increasing GaPTex efficacy by acting as an oxidation catalyst. Alkali metals have been shown as effective oxidation catalysts for Si, being of particular interest for the microelectronics industry in generating low temperatures gate oxides with sub-100 Å thickness [247]–[254]. The process of increasing Si oxidation involved depositing the alkali metal atop the surface forming adatoms, where the alkali metal atoms sat atop the Si surface in a new crystallographic layer [250], [252]. After the deposition of the alkali metal the substrate was exposed to oxygen where the alkali metal acted as a ‘sponge’ and absorbed up to $\times 10^6$ more oxygen than a bare Si surface under the same conditions [250].

Both the alkali metal deposition and the exposure to oxygen were performed at temperatures as low as room temperature [250], [252]. The store of oxygen in the alkali metal 'sponge' was then transferred to the Si upon heating, thus oxidising the Si surface [250], [252]. The dissemination of oxygen from the alkali metal to the Si surface has been shown to occur locally to the alkali metal [252]. In addition, during the heating phase, the alkali metal entirely desorbed from the Si surface after oxygen transferal to the Si with a flash heat of 600 °C for 3 minutes [250]. While the alkali metal coverage was shown to be proportional to the thickness of oxide grown on the Si surface, coverages of as little as 0.15 of a monolayer have been shown to aid in Si surface oxidation [252]. At such coverages, the alkali metal is no longer in a metallic phase, which was shown to occur at 1 monolayer or more, but instead are isolated adatoms on the Si surface. XPS measurements have shown at sub-monolayer alkali metal coverages of less than 0.5 of a monolayer, that it is atomic oxygen bonding with the alkali metal adatoms on the Si surface [252]. Therefore, even atomic alkali metals on the Si surface can greatly benefit Si oxidation.

The above literature showed benefits to Si oxidation when the alkali metal atoms were specifically bonded to the Si surface. In GaPTex, after precursor deposition, the Na^+ ions are not bonded to the substrate surface but are in solution and are attracted to the surface of the nanoparticles. To determine if Na^+ ions in the precursor would aid Si-oxidation, four 3 cm × 3 cm specimens were cleaved from Trina 1 wafers using a diamond-tipped pen. All four samples followed the same procedure as in section 6.2, but after the HF-dip and de-ionised water rinse, the samples were sprayed using the conditions in Table 6.2, with a spray time of 20 s. The precursor used for spraying was 0.037 M NaOH and IPA in a 1:10 respective dilution. Samples were air-dried in the spray chamber. Post-spray, surface oxide-thickness was measured and used as the '0 min' value. One sample was used as a control in air at room temperature and the oxide thickness was measured after 15 mins, 30 mins, and 60 mins. The other three samples were individually inserted into the reaction chamber and were removed after 15 mins, 30 mins, or 60 mins for oxide measurements. Figure 6.10 presents the oxide growth for the room temperature, air control and the elevated

temperature, O_3 sample. the y-axis of Figure 6.10 differs from Figure 6.9, as the surface was sprayed with NaOH, thus it is termed 'film thickness'. The fit difference of oxide thickness measurements slightly increased when NaOH was present to 0.0073 - 0.0190 but was still in acceptable ranges.

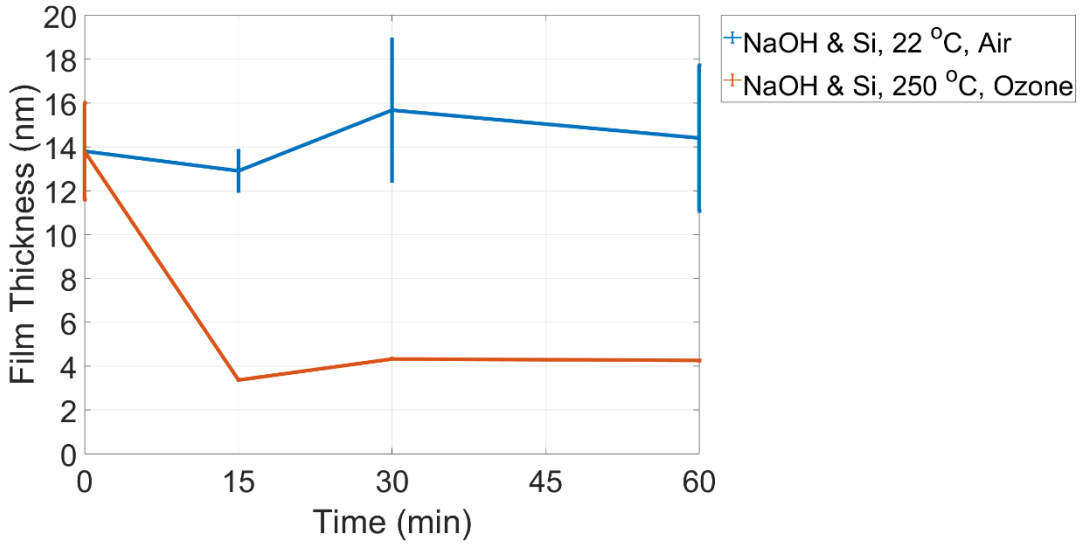

Figure 6.10 Film thickness variation of a Si surface sprayed with NaOH, either at room temperature in air or 250 °C in O_3.

The presence of an alkali metal caused the film thickness to vary. The initial thickness of the film for both samples in Figure 6.10 was much greater than the specimens in Figure 6.9. As the only difference between these two specimens is the NaOH deposited by spraying, the additional ~ 13 nm measured at 0 min in Figure 6.10 is attributed to the air-dried NaOH layer. After 15 mins of processing, the film thickness of the high-temperature, NaOH sprayed sample reduced from 13.8 nm to 3.4 nm in Figure 6.10. This reduction in film thickness is likely due to the elevated temperature causing any remaining IPA on the surface to evaporate. By 30 mins, the film thickness of the NaOH sprayed sample at high temperature has grown to a thickness of 4.3 nm and self-limits at this thickness for the last 30 mins. The increase in film thickness from 15 mins to 60 mins is attributed to oxide growth as there are no other methods of the film thickening. The film thickness of the control sample in Figure 6.10 remained effectively constant across the 60 mins, indicating little to no oxide growth.

One could argue that at high temperature, with O_3, Na^+ doubled the Si oxide growth, as more than 4 nm was achieved in 60 mins in Figure 6.10 compared to an oxide thickness of less than 2 nm for the counterpart sample in Figure 6.9 for the same time. However, the 'oxide' grown for the specimen at high temperature with O_3 in Figure 6.10 likely still contains Na^+, as only partial desorption of Na^+ occurs at temperatures less than 600 °C [248]–[250]. Thus the thickness of 4 nm measured in Figure 6.10 cannot be solely attributed to silicon oxide. Instead, the additional 2 nm measured for the high-temperature, O_3 specimen in Figure 6.10 (in comparison to its counterpart in Figure 6.9), is split between additional oxide growth and Na^+. From this 2 nm, 1 nm can be contributed to oxide growth from the increase in thickness measured between 15 mins and 30 mins in Figure 6.10, as there are no means for the film to increase in thickness unless it is with O_2/O_3. Thus, the minimum oxide thickness growth with Na^+ at high temperatures in O_3 is 3 nm, with 1 nm possibly due to Na^+. Thus, Na^+ in the precursor aids surface oxidation kinetically, increasing maximum oxide thickness grown by a factor of 1.5 to 2.

6.3 Thermodynamics and Kinetics of Si Oxide Etching

To determine the Si-oxide-etching reaction spontaneity, the equation for $\Delta G_{reaction}$ (6.1) was applied to the oxide-etching reaction. The full calculation is found in Appendix II. $\Delta G_{reaction}$ for oxide-etching is:

$$\Delta G_{oxide-etching} = -94.5\ kJ/mol$$

As $\Delta G_{reaction}$ is negative, Si oxide etching is energetically favourable to proceed in GaPTex.

To establish if the oxide-etching kinetics were impeded, SiO_2 etch rates of HF-vapour etching were considered. Williams et al. [255] measured gaseous etching of SiO_2 with HF-vapour at a rate of 66 nm/min by holding a piece of oxidised Si 1 cm over a dish containing 49 wt% HF at room temperature and pressure for 1 minute. Applying this oxide etch rate to GaPTex, in 3 minutes a total depth of 198 nm of SiO_2 could be etched, which is analogous to the etch depth presented in Figure 6.8d). Thus, GaPTex appears unimpeded by the etching component of the total reaction.

However, GaPTex should become limited at high sample temperatures, as oxide etching with HF-vapour has been shown to only proceed if a liquid phase containing HF forms on the substrate surface. C. R. Helmes and B. E. Deal [256] present the mechanism of etching SiO_2 using HF vapour. The first phase of etching is for HF and H_2O gases to condense on the SiO_2 surface, where the condensed H_2O is a solvent for the HF. If condensation could not occur then no etching took place [255], [256]. In HF/O_3 GaPTex, texturing has successfully proceeded at temperatures above both boiling points of HF and H_2O, where micro-droplets would not be able to form on the sample surface. This implies a liquid phase containing HF is being stabilised on the substrate surfaces during texturing, at temperatures above the boiling points of HF and H_2O.

To understand how oxide-etching could occur at temperatures above the boiling point of both HF and H_2O in GaPTex, oxide etching was performed in the texturing reactor at room temperature and 250 °C, with and without Na^+ present on the surface. Ox 2 wafers, with a 100 nm SiO_2 oxide atop the Si, were cleaved into four 15 mm × 15 mm samples using a diamond-tipped pen, rinsed with IPA, and dried with compressed air. 1 ml of NaOH (aq) at pH 10 was deposited atop the SiO_2 on two samples, which were then air-dried. Samples were split into two groups, each containing a sample with and without NaOH on the surface, where the oxide thickness was measured after etching at room temperature for one group and at elevated temperature for the other group. The two oxide-etching recipes used are presented in Table 6.3. Oxide thickness measurements are presented in Table 6.4.

Table 6.3 Operating parameters in the texturing tool for testing oxidation rates at room temperature and elevated temperatures.

Operating Parameter	**Value**	
Reaction gases	N_2/HF	N_2/HF
Processing time (min)	3	3
HF Temperature (°C)	80	80
Flow Rate (L/min)	2	2
Sample Temperature (°C)	250	22
Ozone Concentration (wt%)	20	20

Table 6.4 Remaining oxide thickness, from a 100 nm thick surface oxide, after etching in HF/N_2 gas with and without NaOH on the surface.

		Sample Temperature	
		Room Temperature (22 °C)	**250 °C**
Surface Composition	**No NaOH**	30 nm	100 nm
	NaOH	70 nm	80 nm

Various thicknesses of oxide were yielded after etching from the specimen groups. From Table 6.4, at room temperature without NaOH present, 70 nm of oxide was removed leaving 30 nm on the surface. But with the presence of NaOH, only 30 nm was removed at room temperature, leaving 70 nm remaining. At 250 °C, no measurable amount of oxide was etched without NaOH present, whilst 20 nm was removed with NaOH on the surface.

6.3.1 Discussion

The presence of NaOH has been shown to allow oxide etching to occur at temperatures beyond the boiling points of HF and H_2O in GaPTex. The results from Table 6.4 illustrate that without NaOH deposited on the surface at temperatures above the boiling point of HF and H_2O, the oxide remains effectively unetched. This lack of etching stems from the necessary microdroplets required for etching being unable to condense on the SiO_2 surface at such temperatures [255], [256]. When the temperature was below the boiling points of HF and H_2O, Table 6.4 showed that etching occurred, regardless of if NaOH was present. At such temperatures, microdroplets from the HF vapour can condense on the surface to enable etching. Both results agree with the etching mechanism suggested in [255], [256]. The presence of NaOH demonstrates more curious findings. At 250 °C, no liquid state should be able to form on the surface and therefore etching should not occur. However, 20 nm of oxide was removed at high temperature when NaOH was present. In accordance with the mechanism of HF-vapor etching [255], [256], this etching implies NaOH induces and stabilises the necessary HF liquid phase for etching to occur at elevated temperatures. Such a property is termed deliquescence, defined by the Britannic dictionary [257] as “The process by which a substance absorbs moisture from the atmosphere until it dissolves in

the absorbed water and forms a solution. Deliquescence occurs when the vapour pressure of the solution that is formed is less than the partial pressure of water vapour in the air."

To quantify that the vapour pressure of a NaOH solution was less than the partial pressure of water in air at 250 °C to cause deliquescence, the Clausius-Clapeyron equation was used:

$$\ln\left(\frac{P_2}{P_1}\right) = -\frac{\Delta H_{vap}}{R}\left(\frac{1}{T_2} - \frac{1}{T_1}\right) \qquad (6.2)$$

Here T_1 and T_2 are two different temperatures, P_1 are P_2 the partial pressures of the chemical species at T_1 and T_2 respectively, R is the gas constant, and ΔH_{vap} is the enthalpy of vaporisation of the chemical species in question. Full calculation details can be found in Appendix III. Table 6.5 presents the partial pressures for water and NaOH at 25 °C from [258] and [259], and partial pressures calculated using equation (6.2) at 250 °C.

Table 6.5 Vapour pressure for NaOH and H_2O at 25 °C and 250 °C using the Clausius-Clapeyron equation

		Temperature	
		25 °C	**250 °C**
Species	**H_2O**	23.8 mm Hg	49.4×10^{3} mm Hg
	NaOH	1.82×10^{-21} mm Hg	2.86×10^{-8} mm Hg

Table 6.5 shows that the vapour pressure of NaOH is less than water for both temperatures. Therefore, NaOH undergoes deliquescence at both temperatures, enabling a H_2O liquid phase to condense on the Si surface, acting as a solvent for HF. Thus, oxide-etching can proceed at temperatures beyond the boiling points of H_2O and HF, up to at least 250 °C. However, the deliquescence of NaOH at room temperature appears to hinder oxide-etching in comparison to when NaOH is not present. Table 6.4 illustrates this effect, where the total oxide etched reduced from 70 nm to 30 nm when NaOH was present. C. Helms and B. Deal [256], suggested that HF-vapor etch rates were slowed by a reaction production build-up in the condensed phase, limiting HF diffusion to the SiO_2 surface for etching. Such an effect would account for the reduction in oxide etching when NaOH was present at room temperature in Table 6.4.

However, the exact form of NaOH is not present in the GaPTex precursor for oxide-etching during texturing. Na^+ ions are present in the precursor, but the OH^- ions in NaOH are not present in GaPTex (see section 5.3.3). Nevertheless, the precursor must be stabilising a liquid phase for oxide-etching to occur so that texturing is not impeded, otherwise texturing after acid stabilisation would have remained limited and the ultra-low reflectance surfaces in Chapter 5 would not have been possible. In addition, it was demonstrated that Na^+ counter-ions specifically brought about significant oxide-etching during GaPTex; Figure 6.8 showed the complete etching of the silica nanoparticles when Na^+ counter-ions were present, whilst the silica nanoparticles remained effectively unetched when the Na^+ counter-ions were not present. Na^+ is required in the precursor for oxide-etching to occur in GaPTex, thus the Na^+ counter-ions are the dominant factor in the stabilisation of a liquid phase on the surface.

To consider how Na^+ stabilises a liquid phase during GaPTex, let us first consider how deliquescence occurs with NaOH. When water interacts with solid NaOH it undergoes the reaction:

$$NaOH(s) + H_2O \rightarrow Na^+(aq) + OH^-(aq) + H_2O$$

The absorption of the water molecules causes the solid structure of NaOH to break apart into the ionic components of Na^+ and OH^- in solution. These ions stabilise the liquid phase via electrostatic attraction between them and the absorbed water molecules. Figure 6.11 demonstrates the liquid phase stabilisation where both Na^+ and OH^- ions are surrounded by the water molecules in solution: Na^+ ions are attracted to the negative charge of the oxygen in the water molecules, the oxygen of the water molecules are attracted to the hydrogen of the OH^- ions, and the hydrogen in the water molecules are attracted to the oxygen of the OH^- ions. Considering the GaPTex process, the majority of IPA and water molecules likely evaporate upon heating samples in excess of 200 °C. Yet, as Na^+ ions are present in the precursor, a liquid phase can be stabilised local to the Na^+ counter-ions. Therefore, oxide-etching proceeds in GaPTex. It is unclear if the sample heating causes any other processes to occur during GaPTex, such as the possibility of Na^+ bonding to the

Si surface with heating. Future work should consider measurement techniques such as XPS to confirm the electronic state of the Na^+ after substrate heating.

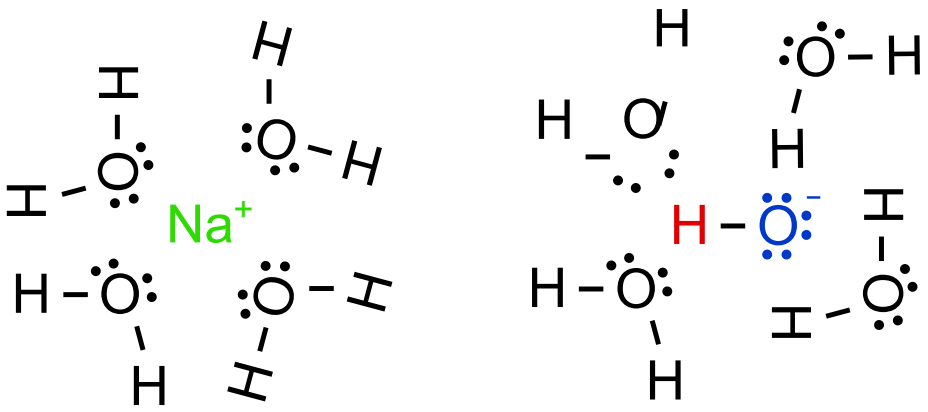

Figure 6.11 The arrangement between water and Na^+ or OH^- ions in solution.

Finally, the water surrounding Na^+ ions may provide an additional benefit to oxide-etching. HF can react with Na^+ to form NaF. However, if this were the dominant reaction, no oxide-etching would occur and no texturing would be observed. Therefore, the dominant reaction is unlikely to be HF reacting with Na^+ to form NaF. Instead, this reaction may be prevented by the water molecules surrounding the Na^+ acting as a screen to the HF absorbed into the liquid phase. Thus, NaF is prevented from forming and the dominant reaction is HF etching the Si oxide, resulting in surface texture forming.

To conclude, Na^+ is unlikely to thermodynamically aid oxide-etching, instead it is likely to be offering kinetic aid by stabilising the necessary liquid phase, via deliquescence, for oxide-etching to occur at temperatures beyond the boiling points of HF and H_2O.

6.4 Chapter Summary

This chapter has further investigated the role of colloidal silica aiding GaPTex. The original hypothesis of SiO_2 nanoparticles acting as nucleation points for texturing has been dismissed after individually testing the components of colloidal silica. Instead, the Na^+ counter-ions of the precursor were revealed to induce texturing. However, uniformly textured surfaces were only generated when using the full precursor, whereby the nanoparticles acted to evenly distribute the Na^+ counter-ions across the surface. The function of Na^+ in GaPTex was explored and was shown to be chemical, where it kinetically

supported both surface oxidation and oxide-etching. The next chapter will explore the effect GaPTex operating parameters have on the resulting morphology to optimise surface texture for solar cells.

7 HF/O_3 Gas-Phase Texturing Microstructures

The development of GaPTex in previous chapters has demonstrated only one morphology, and its performance in a solar cell has not been verified; there may be alternative GaPTex microstructures that yield better final cell properties. This chapter presents the variation in microstructural and optical properties of GaPTex, caused by altering operating parameters. In addition, a texturing mechanism is proposed and the impact of operating parameters on the mechanism is discussed. Operating parameters investigated include the alkali metal of the precursor, the alkali metal concentration, sample temperature, and O_3 concentration.

7.1 Alkali Metal

7.1.1 Type

In Chapter 6, it was shown that Na^+ aided texturing through oxidation catalysis, as well as supporting oxide-etching by stabilising liquid HF on the wafer surface. The other alkali metals of group I have been documented to catalyse Si oxidation, as well as being deliquescent [248]–[254], [260]–[263]. However, it was found that the oxidation catalysis efficacy of the alkali metals varied with metal [248], [249], [252]. By altering the rate of one-half of the total texturing reaction, oxidation, precursors using a different alkali metal ions to Na^+ may produce a differing texture morphology.

Li, K, or Cs ions were tested in the precursor, instead of Na, to determine if they could also produce texturing and if any alternative microstructures were produced. Trina 1 wafers were cut into 4 cm × 4 cm specimens, rinsed with IPA and dried with compressed air. Precursors were prepared as described in Chapter 2, using AS-40 as the colloidal silica and solutions of LiOH, KOH, or CsOH. The final concentration of the alkali hydroxide solution in the precursor was the same concentration as Na^+ in the Col-K (NC) colloidal silica of 0.0033 M. Each precursor was sprayed onto a specimen using the conditions shown in Table 7.1 and then textured using the operating parameters in Table 7.2. When

discussing the effects produced by each precursor, they are referred to by their alkali metal. The wafers used, their preparation, the spray conditions, and the texturing conditions are the same throughout this chapter unless stated otherwise. The resulting reflectance is presented in Figure 7.1, microstructures in a top-down view in Figure 7.2 and cross-sectional view in Figure 7.3. Two magnifications are presented for each metal in both top-down and cross-sectional views. Figure 7.4 shows the mean etch-pit diameter from the cross-sectional views in Figure 7.3. Etch-pit diameter and total texture depth are calculated as described in Chapter 2.

Table 7.1 Precursor spraying conditions.

Precursor Spraying Parameter	**Value**
Colloidal Silica:IPA	1:50
Infusion Rate (ml/hr)	400
Atomising Pressure (bar)	1.4
Sample Spray Time (s)	10

Table 7.2 Texturing conditions

Operating Parameter	**Value**
Processing Time (min)	3
HF Temperature (°C)	80
Flow Rate (L/min)	2
Sample Temperature	250
Ozone Concentration (wt%)	20

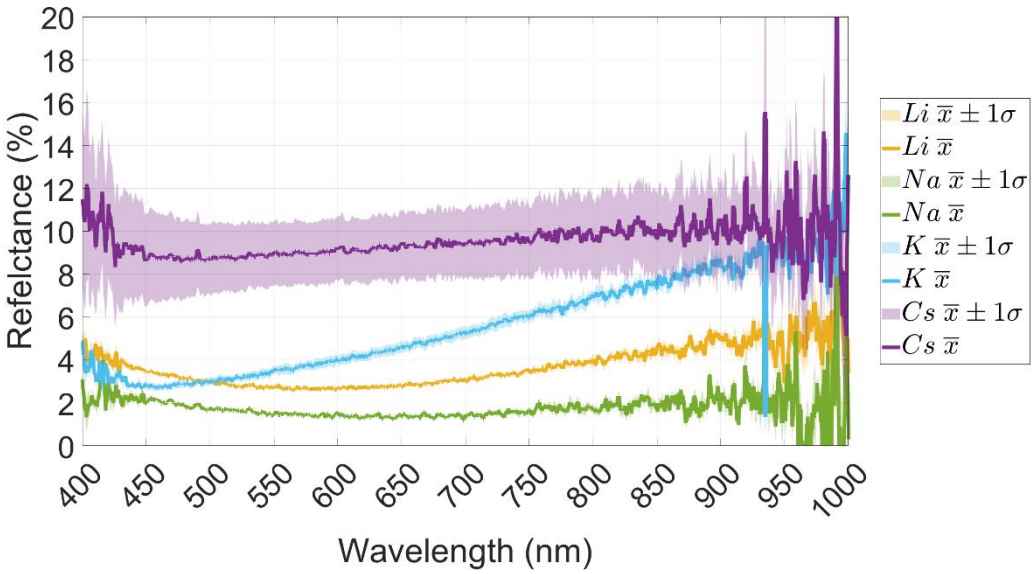

Figure 7.1 Reflectance spectra for precursors made with Li, Na, K, or Cs.

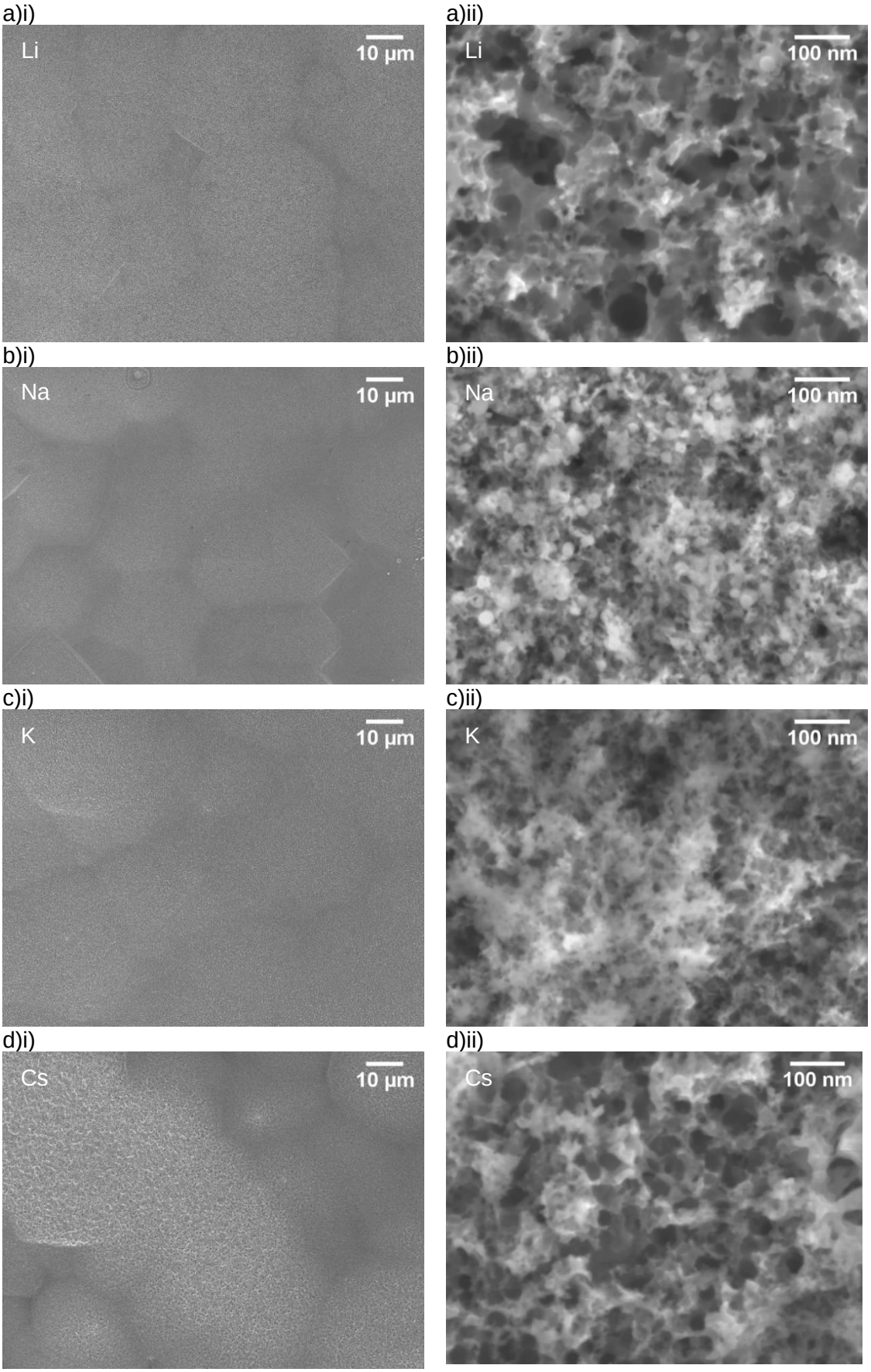

Figure 7.2 Textured surfaces using different alkali metals in the precursor in a top-down view a) Li b) Na c) K d) Cs.

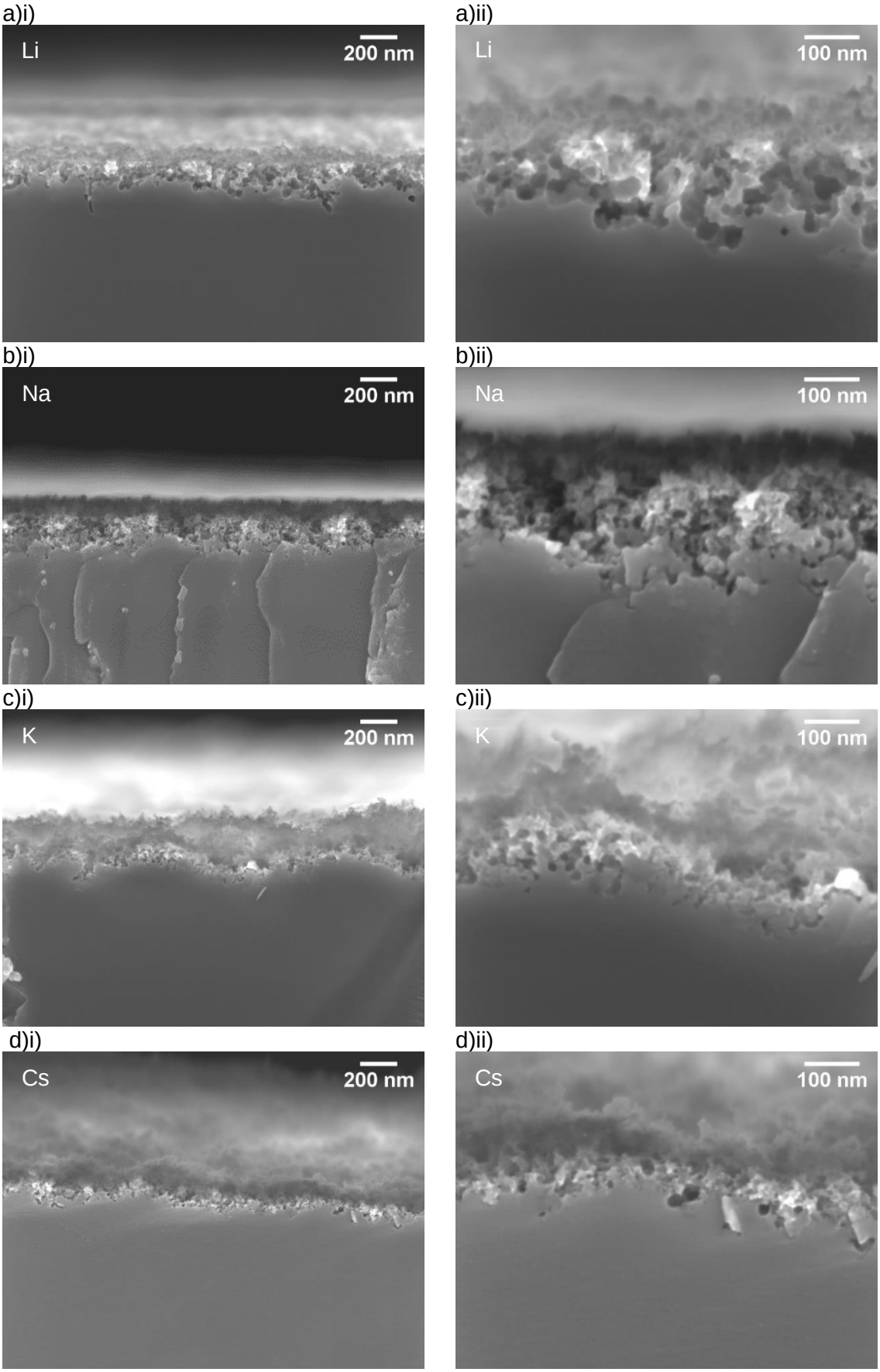

Figure 7.3 Textured surfaces using different alkali metals in the precursor in cross-section a) Li b) Na c) K d) Cs.

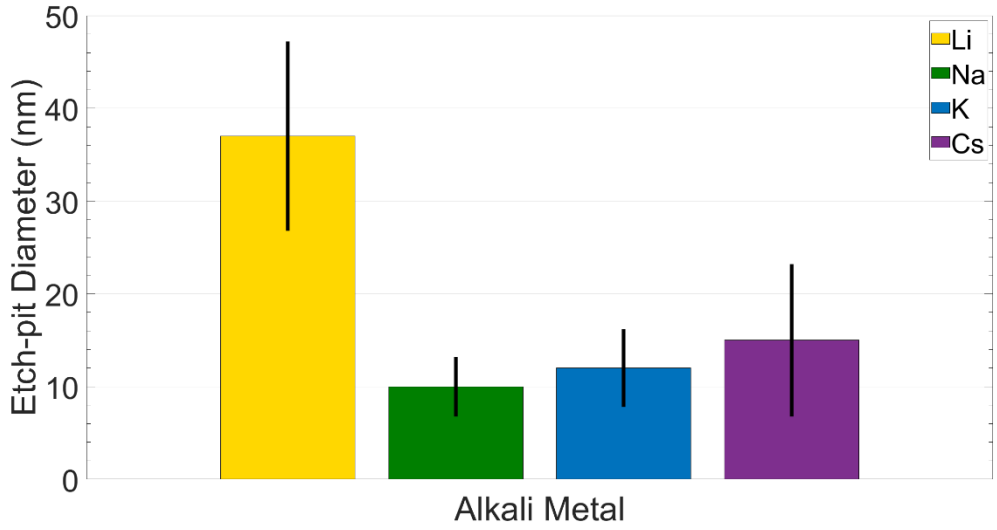

Figure 7.4 Mean etch-pit diameters for each of the four alkali metal precursors with an error of one standard deviation.

The other alkali metals enabled similar texturing as Na when under the same texturing conditions. The reflectance spectra shown in Figure 7.1 shows that while Na produced the lowest WAR at 1.8% ± 0.2%, the other metals also produced reflectance reductions to Si surfaces: Li at 3.5% ± 0.2%, K with 4.9% ± 0.3%, and Cs at 9.4% ± 1.9%. Additionally, the reflectance profile of the K specimen in Figure 7.1 differed from the other three metals. Its reflectance increased with increasing wavelength, whereas the other three metal's reflectance was approximately invariant with wavelength from 450 nm onwards. Textures for all metals were uniform across the surface, as demonstrated by the uniform brightness in the low-magnification images in Figure 7.2. The texturing coverage was also complete, with no areas of untextured material. Similar texture morphologies were produced by the other alkali metals as Na^+ had previously demonstrated. The high-magnification images in Figure 7.2 showed in top-down views the alkali metals all produced the same fibrous (the etched Si appeared to consist of thin strands, like fibres, across the surface) morphology as Na^+ did, and Figure 7.3 showed the etch-pits had the same circular cross-section as when texturing with Na^+. However, there were some subtle differences. Qualitatively, at high magnification in Figure 7.2, both Li and Cs appear the least fibrous out of the four metals. In addition, a secondary texture occurred for K of microscale 'waves' with the

nanoscale GaPTex sitting atop the ‘wave’. Furthermore, the average etch-pit diameter in Figure 7.4 for Li was more than double the next largest average etch-pit diameter, at 37 nm ± 10 nm. The other three alkali metals average etch-pit diameter ranged between 10 – 15 nms.

While changing the alkali metal in the precursor produced some morphological changes, the resulting textures were approximately the same between all four metals. However, the morphology must contribute to the variation in WAR measured in Figure 7.1. Reflection reduction efficacy by nano-textures is dictated by the total texture depth, where deeper textures produce lower reflectance [235]–[241], [264]. The largest total texture depth is achieved by Li and Na, both at ~230 nm, corroborating the findings in Figure 7.1, where Li and Na achieved the lowest WARs out of the four metals. When measuring the total texture depth for K, measurements from two different locations were made. The distance between the peak and the trough of the ‘wave’ yielded ~ 240 nm, and the distance between bulk Si and the top of the texture at a ‘wave’ peak yielded ~ 110 nm. These two measurements can account for the variation in WAR for K observed across the wavelength spectrum in Figure 7.1. The larger texture of the ‘wave’ would enable a reduction in reflectance by multiple photon-surface interactions, as it is too large to be considered a diffuse interface with a gradual transition in density as nanostructures typically are. Thus, the reflectance reduction mechanism of nanostructures cannot be applied and therefore the ultra-low reflectance of nanostructures cannot be achieved. However, the thinner texture atop the ‘wave’ creates a pseudo-hybrid surface texture, enabling a decrease to surface reflectance as observed in Figure 7.1 [151]–[155]. The thinner nanotexture is shallower in depth than Li or Na, thus cannot reduce reflectance at longer wavelengths (see section 1.4.2), therefore accounting for the increase in reflectance observed with increasing wavelength for K in Figure 7.1. Cs also achieved a texture depth of ~ 110 nm but no ‘wave-like’ secondary texture was observed, thus the reflectance in Figure 7.1 is considerably higher than for the other three metals.

No further than a semi-quantitative analysis can be made for total texture depth at this time as it cannot be confirmed that the cross-sectional images are truly orthogonal to the viewing plane to obtain accurate depth measurements of the texture. In addition, defining what texture belongs to the immediate cleaved surface is error-prone when performed only from SEM micrographs. The long depth of focus achieved by SEM causes texture behind the cleaved surface to appear in focus, as though it could be part of the immediate texture at the cleaved surface. Therefore, texture deeper into the sample, away from the cleaved surface, could contribute to the measurement of total texture depth at the cleaved surface, introducing inaccuracy to the measurement. To circumvent this issue, a focussed ion beam (FIB) can be used to mill a thin slice of the sample, beyond what is possible with cleaving using a diamond-tipped pen. To eliminate the issue of non-orthogonal viewing, manual mounting of samples for the SEM must be discarded, as it cannot guarantee orthogonal mounting.

Texture feature size can also impact the nanostructure reflectance reduction mechanism. If the circular etch-pits of GaPTex became sufficiently large (hundreds of nms, or even microns), surface texture would more closely resemble a wet, acid textured surface. With such a texture, the diffuse interface layer nanotextures rely on to achieve ultra-low reflectance would no longer occur and surface reflectance would increase. Thus, texture feature-size for GaPTex needs to be taken into consideration to maintain ultra-low reflectance. Considering the etch-pit diameters in Figure 7.4, Li has the largest etch-pit size, followed by Cs, K, and Na with the smallest etch pit size. However, even with the largest etch-pit size, Li maintains an ultra-low reflectance, achieving the second lowest reflectance after Na in Figure 7.1. Thus, the etch-pit size of all the four alkali metals is sufficiently small to maintain the diffuse nanotexture layer for ultra-low surface reflectance.

7.1.2 Concentration

The concentration of the alkali metals in the precursor was varied to determine if texturing morphology would change. For each alkali metal, four precursors were prepared

using AS-40 colloidal silica and alkali metal hydroxide concentrations. The alkali metal concentrations in the four precursors were: 0.0017 M, 0.0033 M, 0.0047 M, and 0.0084 M. The full top-down and cross-sectional views of the microstructures are presented in Appendix IV, while a specific selection is included in Figure 7.5 and Figure 7.6. Post-texturing WAR is presented in Figure 7.7.

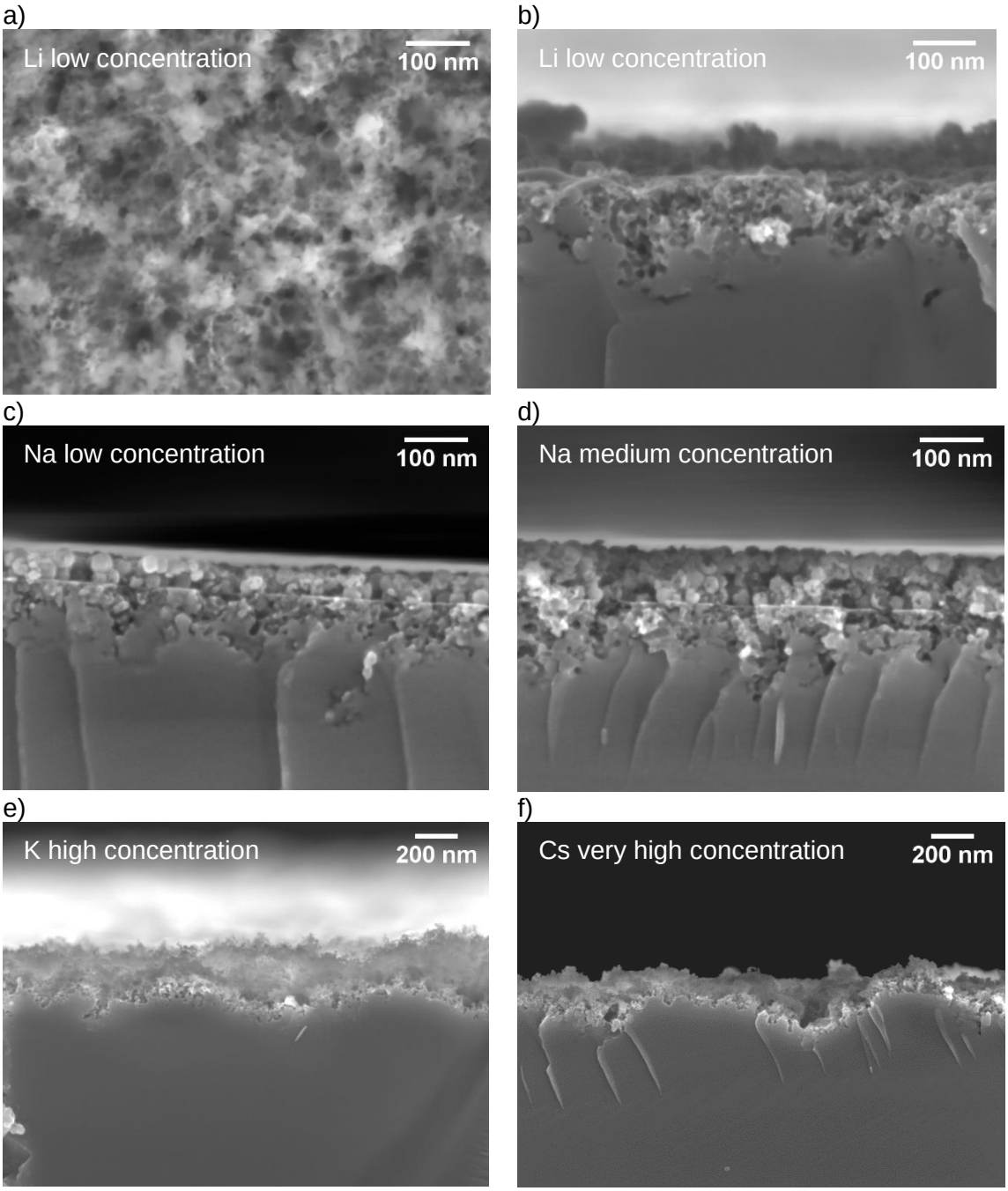

Figure 7.5 Micrographs of texturing using different concentrations of Li, Na, K, or Cs. a) top-down view using 0.0017 M Li, all other micrographs are cross-sectional b) 0.0017 M Li c) 0.0017 M Na d) 0.0033 M Na e) 0.0047 M K f) 0.0084 M Cs.

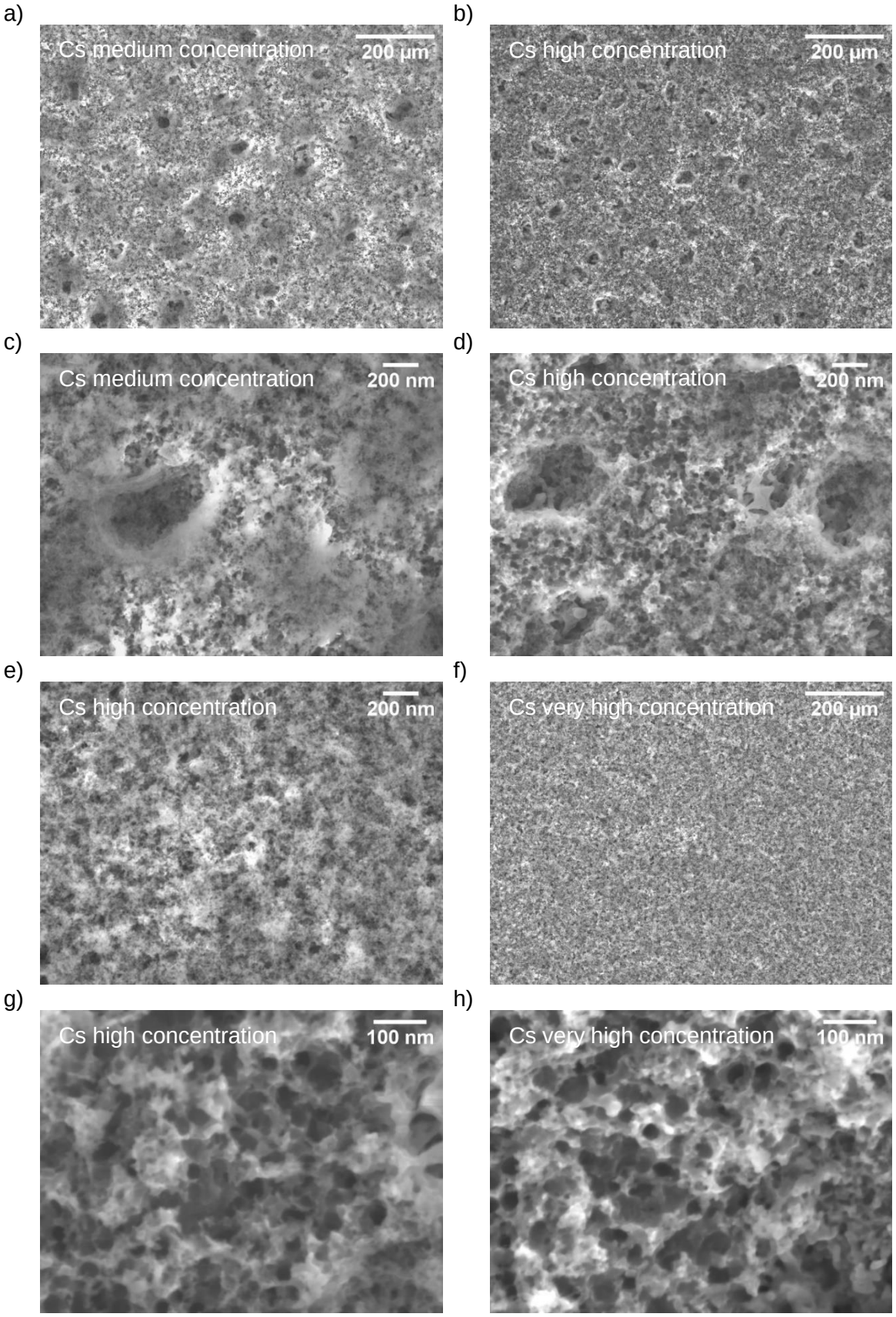

Figure 7.6 Micrographs of texturing using different concentrations of Cs a) low-magnification using 0.0033 M b) low-magnification using 0.0047 M c) intermediate-magnification using 0.0033 M d) intermediate-magnification using 0.0047 M e) high-magnification using 0.0047 M f) low-magnification using 0.0084 M g) high-magnification using 0.0047 M h) high-magnification using 0.0084 M.

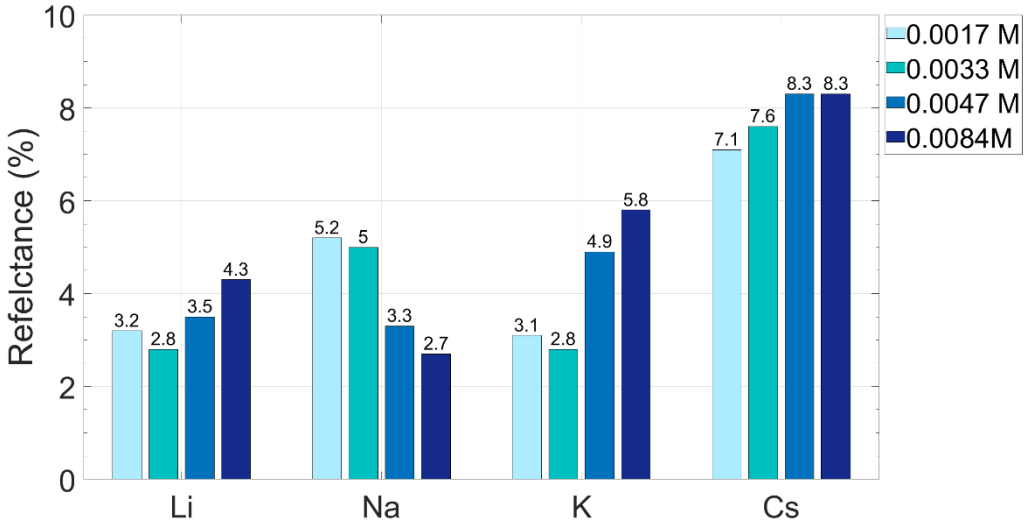

Figure 7.7 WAR as a function of varying alkali metal concentration for Li, Na, K, Cs. From lightest to darkest in each group: 0.0017 M, 0.0033 M, 0.0047 M, 0.0084 M.

The WAR in Figure 7.7 showed three different trends. Firstly, Li and K exhibited the lowest WAR at 0.0033M and subsequently increased at concentrations higher and lower than 0.0033M, where the highest WAR for both metals occurred at 0.0084 M. Secondly, WAR for Na progressively decreased with increasing concentration. Thirdly, WAR for Cs progressively increased with increasing concentration.

Most concentrations produced the same morphologies previously seen in section 7.1.1, but there were some changes with concentration. The etch-pit diameter of Li reduced with concentration from 37 nm ± 10 nm at 0.0033M in Figure 7.4 to 13 nm ± 2 nm at 0.0017 M in Figure 7.5a) and b), which was within the same range as the other three metals at 0.0033 M in Figure 7.4. With regards to Na, Figure 7.5c) and d) showed that the original Si surface did not completely etch for concentrations less than 0.0047 M. This is likely responsible for the drop in reflectance between concentrations 0.0033 M to 0.0047 M shown in Figure 7.7. In Figure 7.5e), K once again demonstrated the additional larger scale 'wave-like' microstructure. Cs also demonstrated the 'wave-like' structure at 0.0084 M in Figure 7.5f). Cs produced a further two microstructural features not observed in any of the other three metals. Figure 7.6a) - d) showed that for 0.0033 M and 0.0047 M, larger pits appeared with approximately 400 nm in diameter. However, upon increasing the concentration to 0.0084

M, these pits were no longer observed as shown in Figure 7.6e) and f). Figure 7.6g) and h) showed the secondary texture of circular pits, the order of 10s nm, for concentrations 0.0047 M and 0.0084 M.

The WAR trends of all metals are dictated by the total texture depth. For Na, the total texture depth is proportional to concentration, generating the largest texture depth at high concentration, corresponding to the lowest WAR. Li and K present a more complex trend between morphology and WAR, depending not only on the textured Si but the silica nanoparticles as well. At 0.0017 M, silica particles are effectively un-etched and only a small texture depth is generated, producing the second lowest WAR. When increasing concentration to 0.0033M, the silica particles are still effectively un-etched but the Si texture depth increases, producing the lowest WAR. At 0.0047 M, the silica particles undergo greater etching, but the Si texture depth does not appear to increase, causing an increase in WAR. At the highest concentration, the silica particles appear complete removed but there is still no apparent increase in the Si texture depth, thus yielding the highest WAR. The unique morphological changes observed only for Cs with varied concentration are to be responsible for the range of WAR at higher values than the other three metals. Na and K produced similar microstructures across the concentration range with K structures yielding higher reflectance. Therefore, going forwards, precursors containing K will no longer be investigated.

7.2 Sample Temperature

Thus far GaPTex has only been performed at a sample temperature of 250 °C. Varying processing temperature has been demonstrated to produce different texture morphologies by other GaPTex techniques [172]–[174]. Thus, the sample temperature in GaPTex was varied to determine if alternative microstructures were produced.

Li, Na, and Cs-based precursors were used to test variations in sample temperature with alkali metal concentrations of 0.0033 M. Sample processing temperature was varied in 50 °C increments from 50 °C to 250 °C. All other processing conditions were kept the

same as presented in Table 7.2. The WAR for each temperature is presented in Figure 7.8. A selection of the microstructures is presented in Figure 7.9 - Figure 7.13 and the full complement of microstructures is presented in Appendix IV.

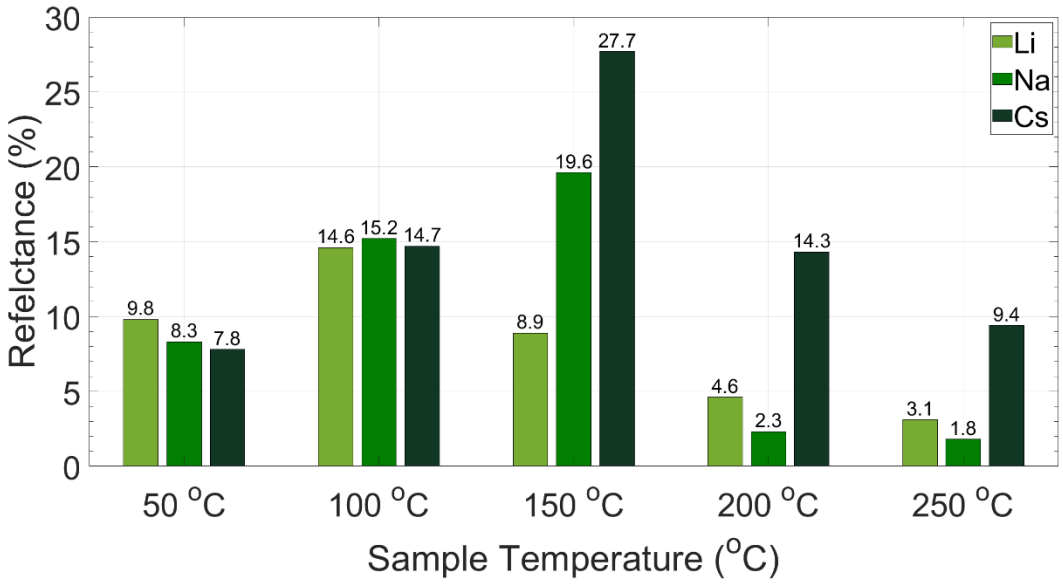

Figure 7.8 WAR for samples processed with a precursor containing Li, Na, or Cs, processed between 50 °C and 250 °C. Light green is Li, intermediate green Na, and dark green Cs.

a)i)

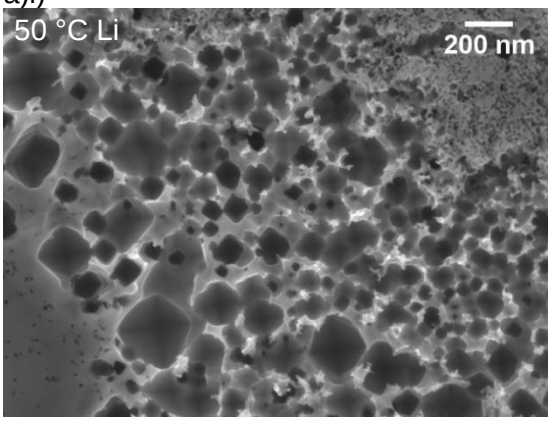

a)ii)

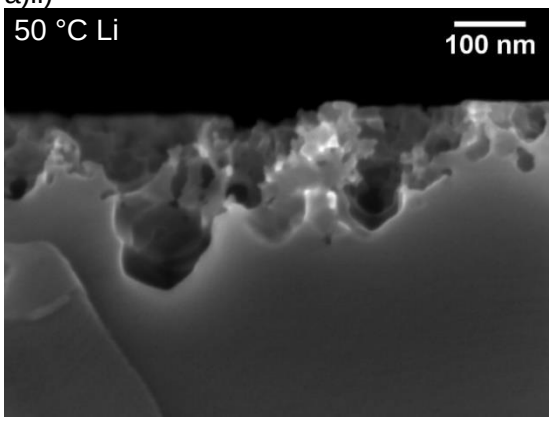

b)i)

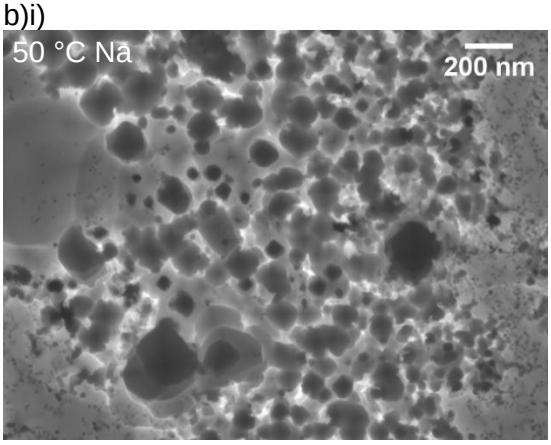

b)ii)

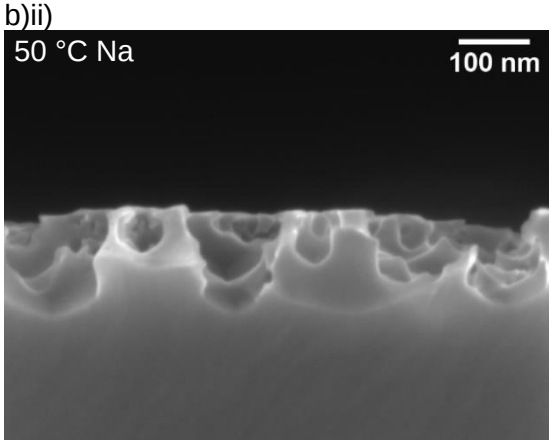

c)i)

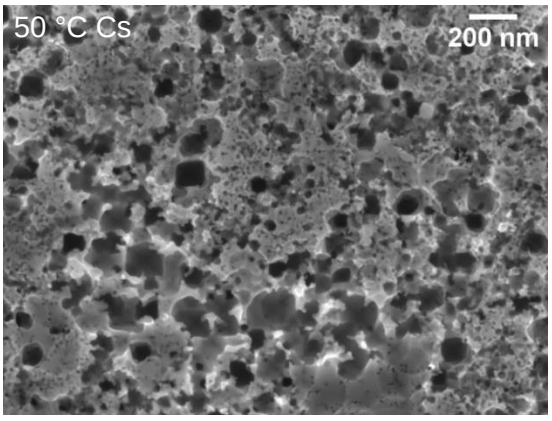

c)ii)

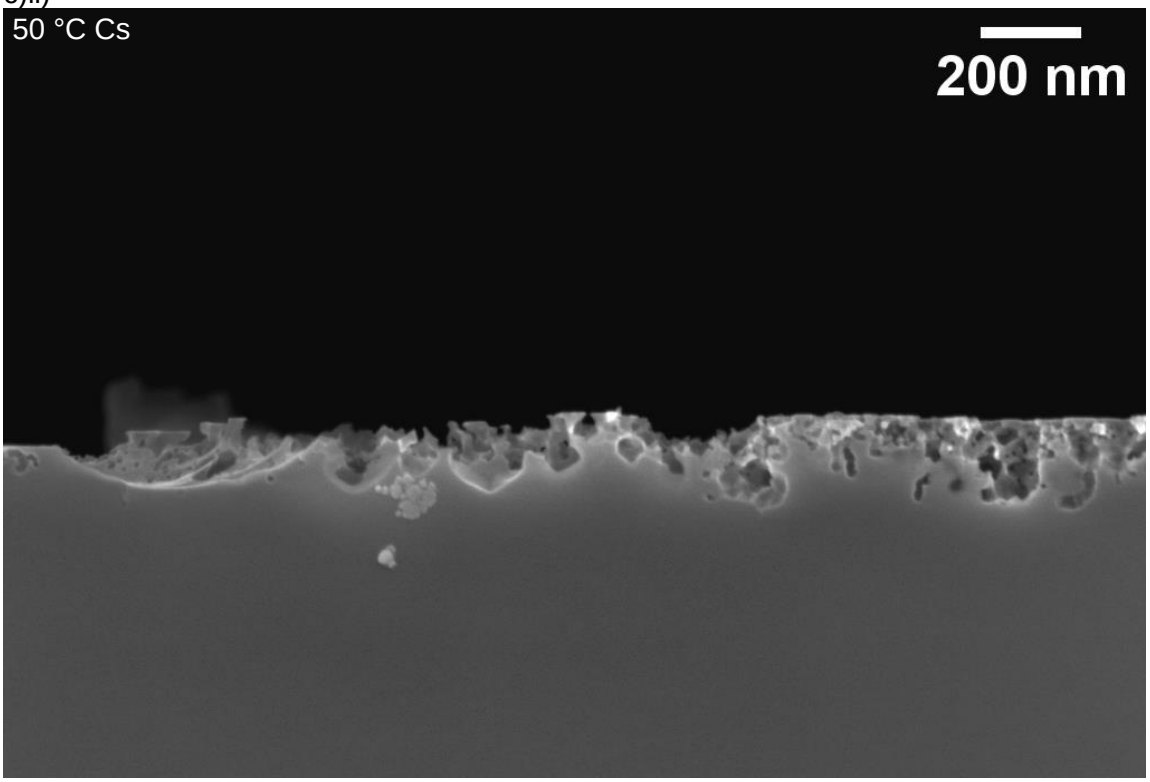

Figure 7.9 Microstructures for processing at 50 °C with different alkali metals in the precursor a) Li-precursor b) Na-precursor c) Cs-precursor i) top-down views ii) cross-sectional views.

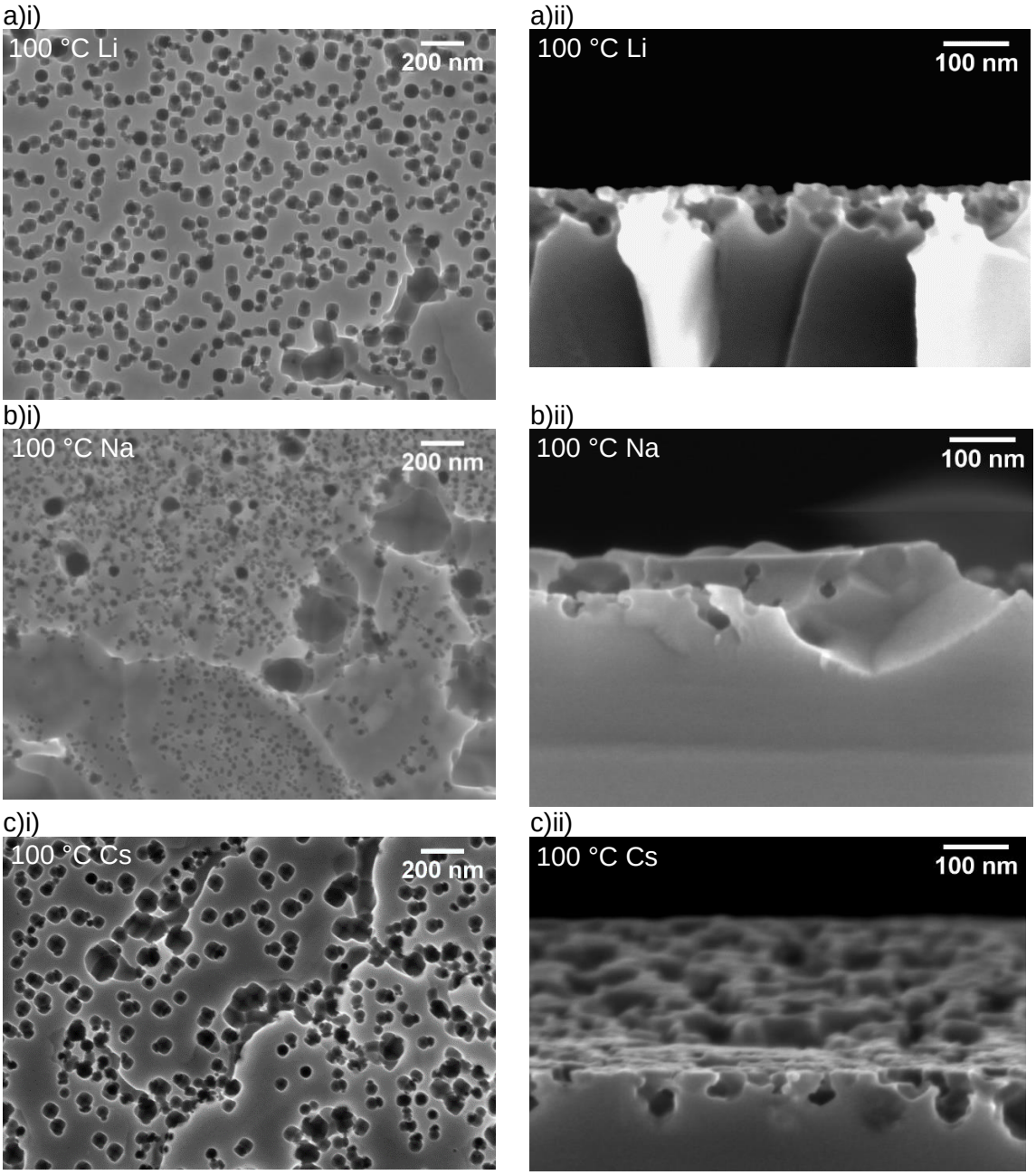

Figure 7.10 Microstructures when sample processing temperature was 100 °C with different alkali metals in the precursor a) Li-precursor b) Na-precursor c) Cs-precursor i) top-down views ii) cross-sectional views.

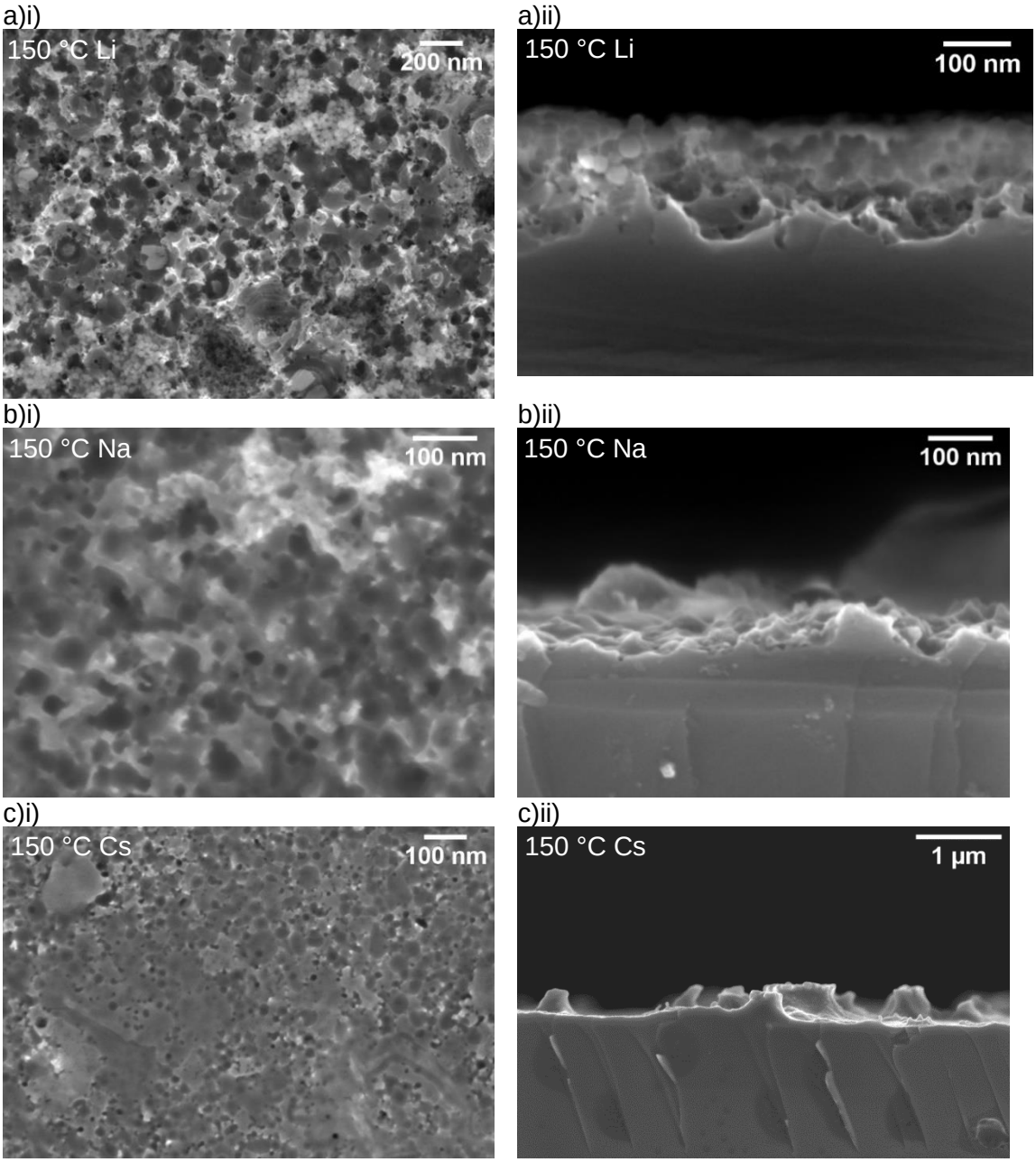

Figure 7.11 Microstructures when sample processing temperature was 150 °C with different alkali metals in the precursor a) Li-precursor b) Na-precursor c) Cs-precursor i) top-down views ii) cross-sectional views.

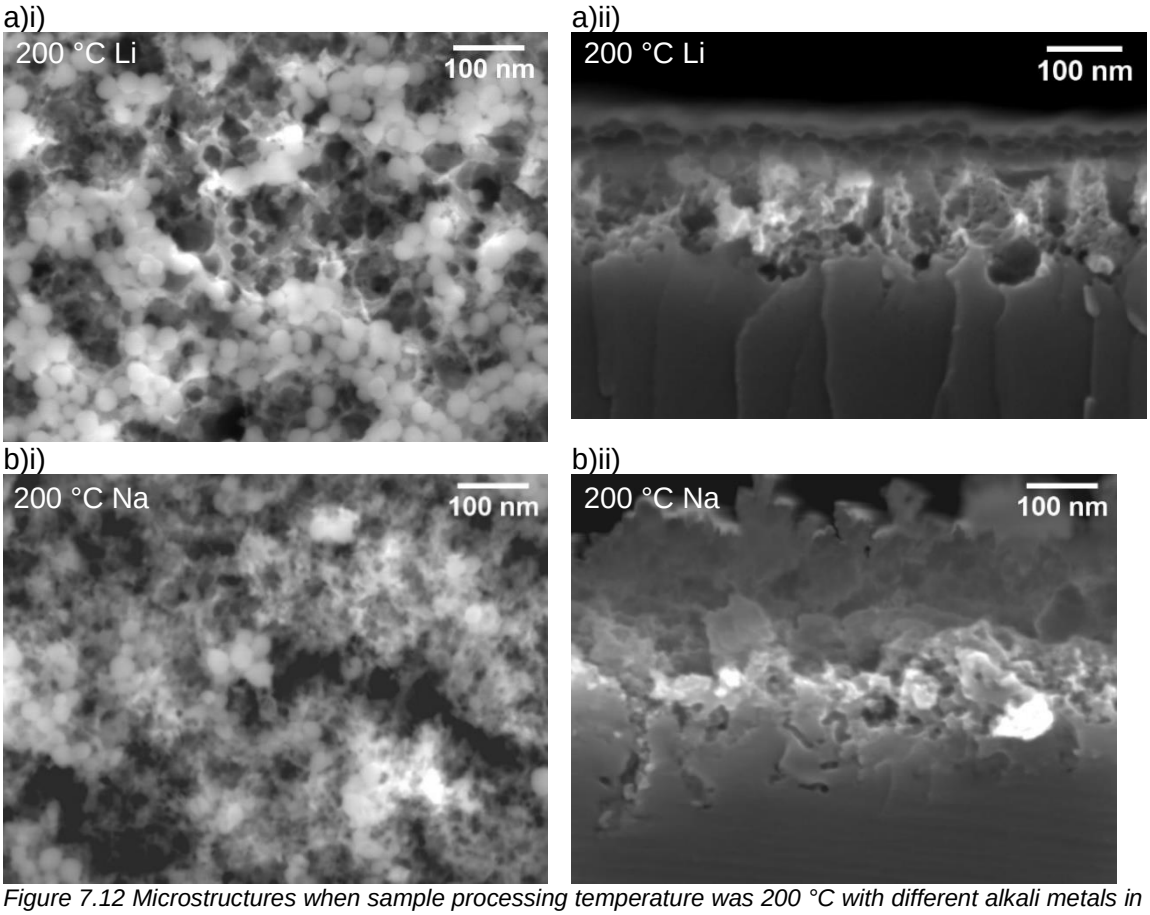

Figure 7.12 Microstructures when sample processing temperature was 200 °C with different alkali metals in the precursor a) Li-precursor b) Na-precursor i) top-down views ii) cross-sectional views.

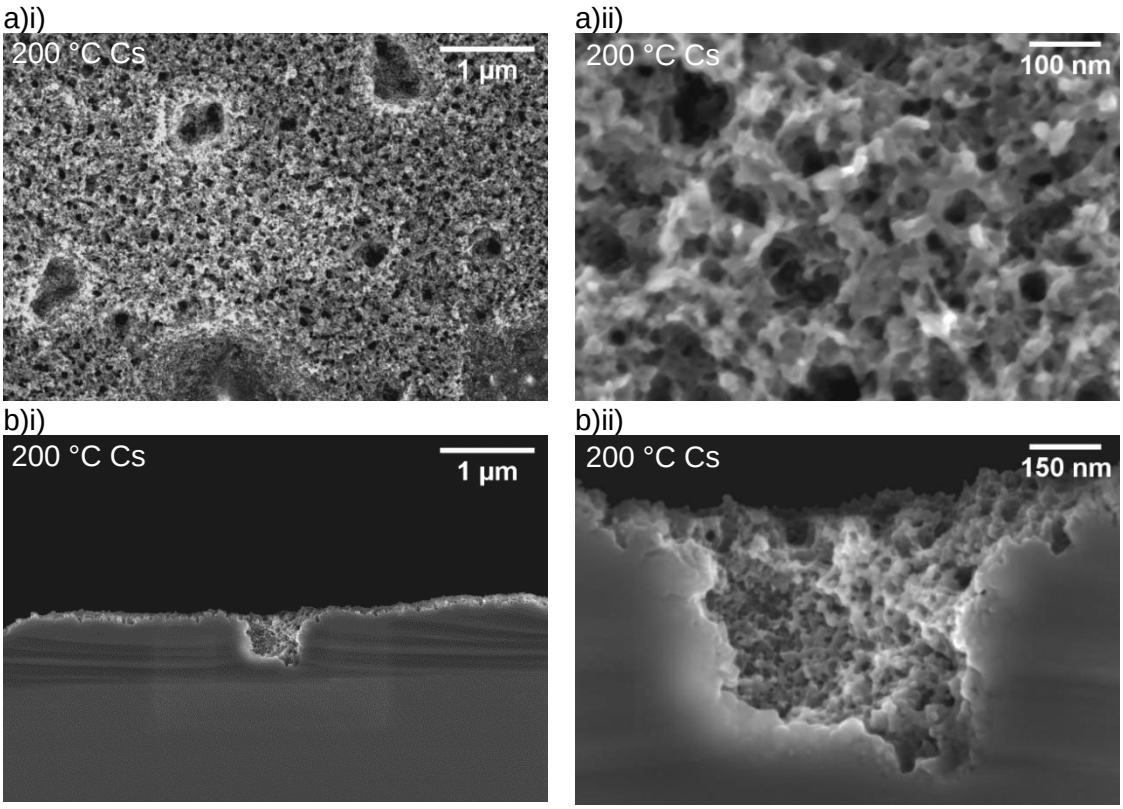

Figure 7.13 Microstructures when sample processing temperature was 200 °C for Cs in the precursor a) top-down views b) cross-sectional views i) low-magnification ii) high-magnification.

Changing the sample texturing temperature caused marked variation in the corresponding reflectance. Figure 7.8 shows that at 50 °C and 100 °C, WAR was greater than at 250 °C and the alkali metal used did not influence the resulting reflectance. Cs was the only one to deviate from this rule, as a lower WAR was achieved at 50 °C than at 250 °C. The variation in WAR between all three metals at 50 °C was 2%, from 7.8% ± 0.3% to 9.8% ± 0.6%, and for 100 °C was 0.6%, from 14.6% ± 1.1% to 15.2% ± 0.7%. Beyond 100 °C, the effect of different alkali metals became significant again. Figure 7.8 shows that at 150 °C, the variation in WAR between the three metals increased to 18.8%, where Li achieved the lowest WAR of 8.9% ± 2.5% and Cs achieved the highest WAR of 27.7% ± 1.2%. The variation in WAR between the three metals reduced to 7.6% by 250 °C, from 1.8% ± 0.2% for Na to 9.8% ± 1.9% for Cs. Li progressively reduced in reflectance from 100 °C, whereas the WAR for both Na and Cs increased at 150 °C from 100 °C, but then reduced as the temperature increased further. Both Li and Na achieved sub-5% WAR by 200 °C and by 250 °C achieved 3.1% ± 0.5% and 1.8% ± 0.2% respectively. Na underwent a 17.3% decrease in WAR when the temperature was increased from 150 °C to 200 °C, the largest change in WAR between two temperatures for any metal. From 150 °C onwards, Cs had the greatest reflectance of the three metals, achieving the lowest WAR at 50 °C of 7.8% ± 0.3%.

The corresponding microstructures aid understanding of the WAR invariance between the three metals at lower temperatures. Figure 7.9 and Figure 7.10 show the microstructures at ≤ 100 °C for all three metals, which are alike but very different to the microstructures shown thus far. Inverted square-based pyramids occur for Li and Na at 50 °C, shown in Figure 7.9a)i) and b)i). However, the individual etch-pits of Cs at 50 °C in Figure 7.9c)i) appear to be closer to a circle in cross-section. Li and Na presented a similar feature size of >100 nm in Figure 7.9a)i) and b)i), while Cs feature size was <100 nm shown in Figure 7.9c)i). The cross-sectional views in Figure 7.9 reveal that the etch-pits are not truly square-based inverted pyramids at 50 °C. In cross-section, the inverted pyramid occurs at the bottom of the etch-pit, but vertical walls occur at the top of the etch-pit.

When increasing the temperature to 100 °C, all three metals possess similar microstructures to one another, but with varying feature sizes. In Figure 7.10, the inverted square-based pyramid structure appears for all metals again, where Li and Cs show an approximate etch-pit diameter of 50 nm while Na demonstrates a smaller diameter of 20 nm. These square etch-pits also appeared at a larger scale for 100 °C, most notably demonstrated in Figure 7.10b) for Na where the larger etch-pits were approximately 200 nm in diameter. However, as the etch-pits increased in size, the base of the larger pyramids became irregular in shape, as observed in both images of Figure 7.10b). The cross-sectional images in Figure 7.10 confirm the inverted square-based pyramid with vertical walls after a certain etch depth. The similar feature size and shape between the three alkali metals at ≤ 100 °C accounts for the invariance in reflectance shown in Figure 7.8.

Above 100 °C, the three metals' texture no longer resembles one another. The microstructure of Li at 150 °C in Figure 7.11a) shows a texture resembling that seen at 50 °C, of larger square-based pyramids than achieved at 100 °C. Etch-pit diameter for Na in Figure 7.11b)i) undergoes broadening to a typical etch-pit size up to 40 nm. Contrastingly, Figure 7.11c)i) presents a range of feature sizes for Cs, where etch-pits less than 10 nm and over 100 nm are observed. The corresponding cross-sectional images in Figure 7.11b)ii) and c)ii) show etch-pit depth decreasing and the etch-pit characteristic angle broadening from the inverted pyramid observed at lower temperatures. These morphology changes from 100 °C to 150 °C cause the increase in reflectance observed for both Na and Cs. Reflectance reduction for nanostructures relies upon feature size being much smaller than total texture depth, typically by an order of magnitude [235]–[241], [264]. Therefore, as features have broadened and the total texture depth decreased with the increase in processing temperature, reflectance can no longer be minimised as effectively, thus WAR increases.

The microstructures in Figure 7.12 for Na and Li at 200 °C both resemble microstructures previously seen at 250 °C in Figure 7.2 and Figure 7.3. However, Figure 7.12a)i) and b)i) show incomplete etching of the silica nanoparticles occurs for both metals

at 200 °C, as well as in complete etching of the original Si surface. Meanwhile, the morphology of Cs at 200 °C in Figure 7.13 was similar to that demonstrated when the concentration was 0.0033 M or 0.0047 M at 250 °C presented in Figure 7.6; larger etch-pits of the order of 1 µm with complete nanoscale texturing across the surface, including the larger etch-pits. Altogether, varying the sample temperature has shown to cause significant changes to the texturing microstructure.

7.3 O_3 concentration

The effect of reaction gas composition on morphology was investigated by changing the O_3 concentration used in the reaction gas. The O_3 concentration was varied at the O_3-generator by the 'power' setting. The power could be changed from 10% to 100%, corresponding to a change of 10 wt% to 20 wt% O_3 in the output gas (where the remaining 90-80 wt% consisted of O_2). O_3 power settings investigated were 10%, 20%, 40%, 70% and 100%. Apart from the changes to the O_3 concentration, the sample recipe was the same as shown in Table 7.2. A control specimen was made using N_2 gas as a non-oxidising species and bypassed the O_3-generator, straight to the reaction chamber, all other texturing parameters are found in Table 7.2. Only the Na-precursor was used for this investigation. WAR for all samples is shown in Figure 7.14 while a selection of microstructures for various O_3 concentrations is shown in Figure 7.15.

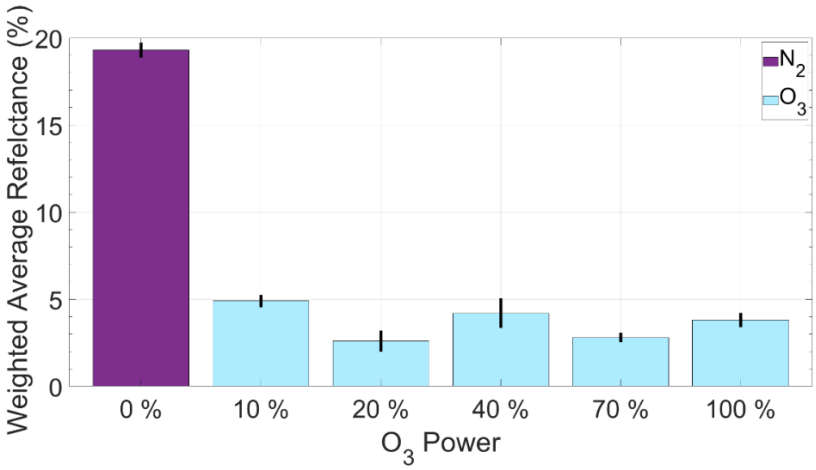

Figure 7.14 WAR for samples where O_3 concentration was varied during texturing using the power setting from 0% to 100% power and the N_2 control.

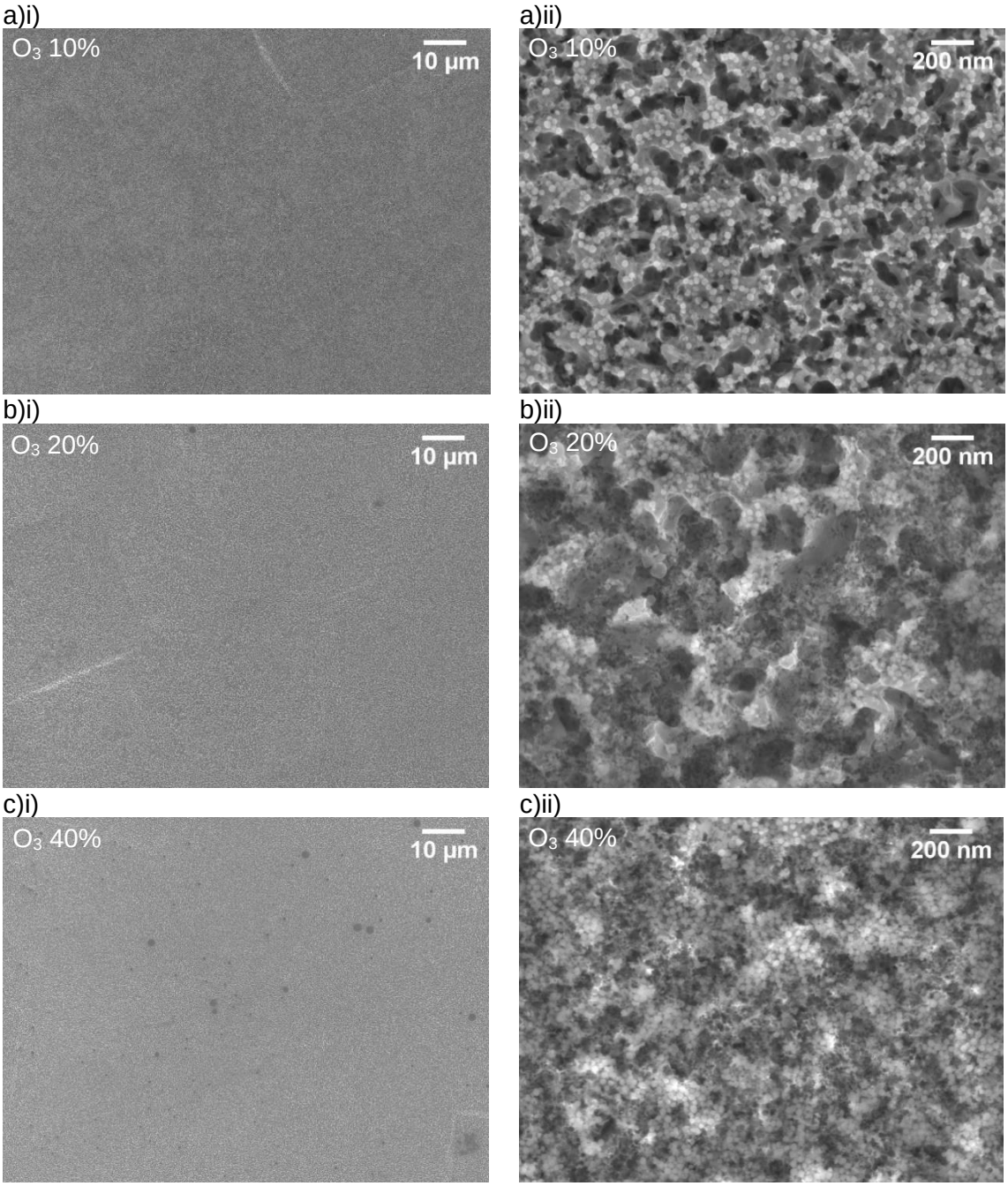

Figure 7.15 Samples textured where O_3 power was a) 10% b) 20% c) 40% at i) low-magnification ii) high-magnification.

Figure 7.14 shows that varying O_3 concentration only produced a small variation in WAR. The WAR of all the O_3 samples was sub-5%. However, the WAR results in Figure 7.14 demonstrated that the presence of O_3 was important to providing a low surface reflectance, as the N_2 control was 19.3% ± 0.4%. While there was little variation in reflectance with changing O_3 concentration, the morphology underwent several changes with O_3 variation. Figure 7.15a) shows for 10% O_3 power, etching occurred but it was not the typical fibrous structure seen when 100% O_3 power was used for Na precursors with this recipe. Instead,

larger etch-pits of ~ 100 nm are seen along with unetched silica particles remaining on the surface. Unfortunately, cross-sectional images could not be captured as the surface melted under the electron beam, caused by the focussing of the electron beam at high magnification [265], thus indicating a shallow total texture depth. Figure 7.15b) shows when power was increased to 20%, the resulting morphology changed to a more complex structure. Firstly, individual etch-pits observed in Figure 7.15b)ii) decreased in size from those seen in Figure 7.15a)ii). Secondly, a macro-texture appears in Figure 7.15b)ii) of an irregular shape and distribution. This secondary texture may have resulted from the further etching of the already textured areas, deepening the structure, whilst some areas remained un-etched. By 40% O_3 power, the typical fibrous structure associated with Na precursors at high temperatures was observed. All low magnification images in Figure 7.15 demonstrate that, regardless of O_3 concentration, texturing uniformity remained high. Some small islands of un-etched material are seen in Figure 7.15c)i) for the 40% power sample, which corresponds to the increase in standard deviation shown for WAR in Figure 7.14. However, O_3 power variation affected the etching of the silica nanoparticles. The high-magnification micrographs in Figure 7.15 show an increase in the number of silica particles on the Si surface as O_3 power is increased. While this effect does not appear to be detrimental to WAR, it may incur an additional cleaning step during cell manufacture to remove the silica particles from the surface. To confirm the initial findings of varying O_3 concentration in the reaction gas future work should focus on further testing, as this preliminary study contained one sample per O_3 concentration.

7.4 Discussion and Proposed Texturing Mechanism

HF/O_3 GaPTex can make different textures by varying operating parameters. The most influential parameter, in terms of creating alternative microstructures, was found to be the sample processing temperature. Texturing at temperatures ≤ 100 °C produced an inverted, square-based pyramid at the bottom of etch-pits, where the base width appeared to be limited to a maximum size as vertical walls formed higher up the etch-pit. Pyramidal textures

are typically associated with wet alkaline etchants for texturing Si, such as NaOH or KOH. As alkali metals ions were present on the sample surfaces during GaPTex, from the precursor, it is plausible that some of the effects observed for wet alkaline etchants apply to HF/O_3 GaPTex. Alkaline wet etches demonstrate a temperature dependency on the morphology produced, where lower temperatures yield upright pyramids and elevated temperatures produce smooth surfaces [266]. This change in morphology is caused by the different atomic arrangements between crystallographic planes [94], [266]. Each Si surface atom on Si(100) possesses two unsatisfied surface bonds and two Si-Si per surface atom whilst Si(111) possess one unsatisfied surface bond and three Si-Si per surface atom. The decrease in the number of Si-Si bonds to be broken for Si(100) than Si(111) results in a lower activation energy for etching, thus at lower temperatures, Si(100) etches quicker than Si(111), resulting in a pyramidal texture [94]. At elevated temperatures, the higher activation energy of Si(111) can be met; thus, etching becomes isotropic with increasing temperature [94], [266]. HF/O_3 GaPTex experiences a similar effect. Where, at lower temperatures, there is only sufficient energy to etch Si(100), causing pyramidal textures to occur, but the temperature is increased, etching can occur on more crystallographic planes, thus the structure tends to isotropy at temperatures of ≥ 200 °C. However, one difference remains between the textures produced by GaPTex and wet alkaline etching; GaPTex produces inverted pyramids with vertical walls, not upright random pyramids. To explain these differences, a mechanism is proposed for HF/O_3 GaPTex that considers the morphology variation with temperature.

The GaPTex mechanism is explained by a micro-droplet etching model, previously considered in Chapter 6. Figure 7.16 shows the proposed etching model for both low and high temperatures. In Chapter 6 it was discussed that GaPTex proceeded due to HF micro-droplet stabilisation on the Si surface, otherwise no measurable oxide-etching occurred. This is the first proposed stage of etching for all temperatures and is shown in Figure 7.16a). The second stage is surface oxidation. Similar to alkaline etching Si(100) fastest at low temperatures, alkali metal oxidation catalysis may also be limited (or preferential) to Si(100)

at low temperature. Si(100) has double the number of unsatisfied surface bonds than Si(111), thus double the number of sites for oxidation. Therefore oxidation could proceed quicker on Si(100), resulting in a faster overall etch rate on Si(100) over Si(111), yielding a pyramidal texture as shown in Figure 7.16b). At high temperatures there is no such constraint, thus the etch-pit is hemispherical as shown in Figure 7.16c). Alkali metal oxidation catalysis is a local effect [251], [252], [260], thus further etching is local to the etch-pit where the alkali metal is contained, as shown by the growth of the etch-pits from Figure 7.16i) to ii). At a certain etch-pit size, all liquid will be contained by the etch-pit, as demonstrated in Figure 7.16ii). For the case of 50 °C and 100 °C, Figure 7.16b)ii), when etching proceeds there will be a certain depth where the deliquesced liquid no longer contacts the top of the etch pit; etching can continue at the bottom of the bit but no further widening of the pyramid's base can occur at the top of the pit. Thus, the width of the pyramid's base self-limits and vertical walls occur at the top of the etch-pit, demonstrated in Figure 7.16b)iii).

The same etching process as described for lower temperatures occurs for elevated temperatures and is shown in Figure 7.16c). However, the constraint of etching Si(100) is lifted, as with increased temperature there is sufficient energy to overcome the higher activation energy of Si(111). Thus, morphology is no longer confined to pyramidal with vertical walls. Figure 7.16c)iii) shows etching proceeding in any direction, thus the direction of etch-pits seems random, as observed in cross-sectional images of etching ≥ 200 °C. Nevertheless, the same constraint of constant etch-pit width at low temperature also applies to high-temperature etching, as the volume of deliquesced liquid within an etch-pit remains the same. Yet etch-pit width for high and low-temperature etching is not equal. The diameter of etch pits in cross-section at 200 ˚C is less than the etch pits at 50 °C, shown in Figure 7.9 and Figure 7.3 respectively. This effect can be attributed to a smaller volume of liquid being stabilised by the alkali metal at higher temperatures, as discussed and demonstrated in Chapter 6.

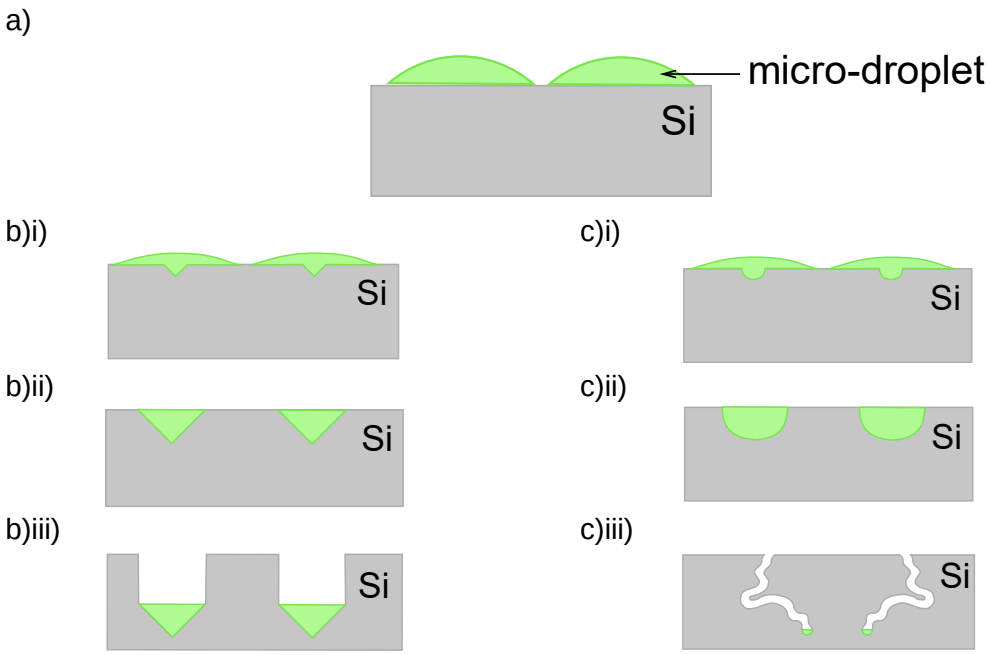

Figure 7.16 Proposed HF/O_3 GaPTex mechanism as a function of temperature. Regardless of temperature, the first stage a) shows micro-droplets forming on the surface. The etching mechanisms at b) 50 °C – 100 °C and c) ≥ 200 °C. Note that c)iii) is a zoomed-out perspective; the width of the etch pit in c)ii) and iii) is the same.

Other parameters investigated appeared to have a lesser impact on changing morphology, such as the differing alkali metals, their concentration, and varying O_3 concentration. However, all three investigations were conducted at 250 °C and alternative effects may have occurred in concert with temperature variation. For example, by increasing the concentration of the alkali metals at low temperatures, the size of the inverted pyramids may have been enlarged as a greater pool of liquid could be deliquesced with more alkali metal present. As such, these parameters should not be discarded from future investigations.

7.5 Chapter Summary

In this chapter, it was shown that GaPTex can produce different texture morphologies by altering operating parameters. The most significant change to texture morphology was caused by varying sample temperature, where pyramidal textures were produced at ≤ 100 °C. A texturing mechanism was proposed, incorporating the morphology changes observed with sample temperature. While the optical properties of GaPTex have been well defined thus far, an assessment of the performance of GaPTex in the final application of a

PERC has yet to be assessed. The next chapter will address the cell performance of GaPTex.

8 Solar Cells Fabricated using HF/O_3 Gas-Phase Texturing

GaPTex has demonstrated excellent optical properties; however, the performance of the texture has not been assessed in the final application of a solar cell. In this chapter, GaPTex undergoes PERC fabrication to analyse its current industrial feasibility. PERC fabrication was performed with the aid of the industrial facility SIRF at UNSW, thus many of the fabrication method recipes were confidential and operating details are not included here. The work with UNSW SIRF occurred before the texture development of Chapter 7, thus only the high-temperature, fibrous texture was made into cells. Figure 8.1 presents schematics of PERC, either with a front surface texture of pyramids or a nanotexture, to illustrate the differences in cell architecture between the two textures.

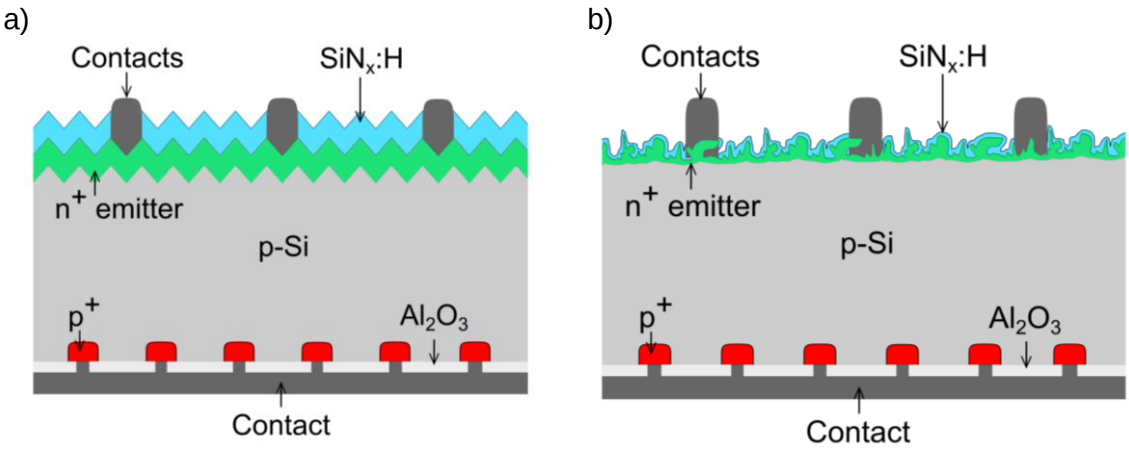

Figure 8.1 PERC schematic using a) a pyramidal surface texture b) a nanotexture.

8.1 Emitters

The first fabrication method tested after texturing was the emitter-formation on the front surface. Two emitter recipes were tested, both optimised to achieve the highest cell performance when using microscale upright pyramids as the front surface texture. Firstly, a standard PERC recipe, typically achieving a sheet resistance (R_{sh}) of 80 - 90 Ω/□ on upright pyramids. Secondly, a lighter doping recipe, termed laser doped selective emitter (LDSE), typically achieves a R_{sh} of 115 - 125 Ω/□ on upright pyramids. All measurements

for LDSE were performed before the laser process and thus analysed the lighter-doped, homogenous emitter. Emitters were formed using the Tempress TS81004 Tube Furnace using a $POCl_3$ source at the SIRF facility in UNSW [69]. Fourteen 156 mm × 156 mm UNSW wafers were textured using the recipe in Table 8.1. A precursor of Col-K (NC) colloidal silica and IPA in a 1:50 respective dilution was used for GaPTex, but due to time constraints, it was applied to the surface using a pipette. Post-texturing, nine of the GaPTex wafers and eighteen UNSW Control wafers underwent PERC emitter-diffusion. UNSW Control wafers were textured with upright pyramids for the front surface texture. The remaining five GaPTex wafers underwent LDSE diffusion. One wafer from each group was removed for testing after the emitter-diffusion, the remainder underwent further fabrication steps. R_{sh} for all three groups is presented in Figure 8.2, reflectance in Figure 8.3 with the reflectance of the PERC pyramids coated in a SiN_x:H ARC, and SEM micrographs in Figure 8.4 - Figure 8.7.

Table 8.1 GaPTex parameters used to texture wafers for cell fabrication

Operating Parameter	**Value**
Processing Time (min)	3
HF Temperature (°C)	80
Flow Rate (L/min)	2
Sample Temperature	250
Ozone Concentration (wt%)	20

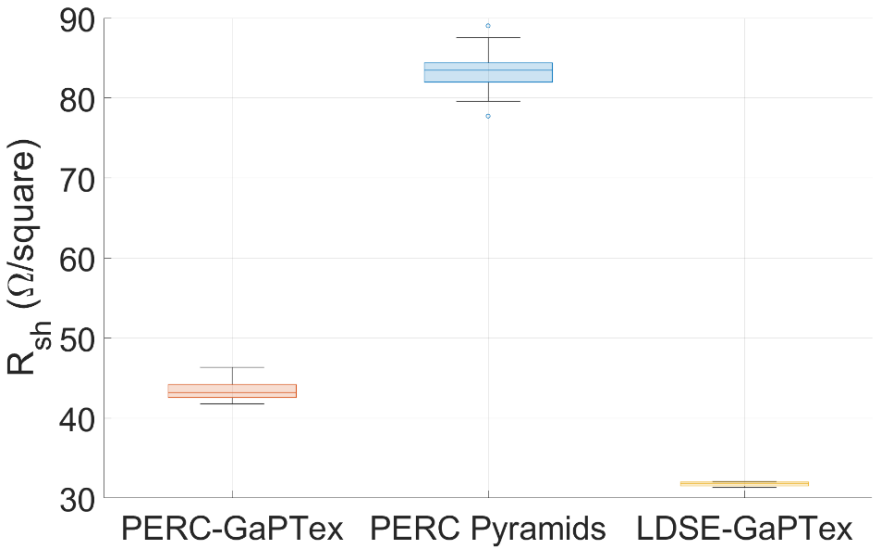

Figure 8.2 R_{sh} of samples after emitter-formation for PERC, LDSE emitter-diffusions on GaPTex and pyramids.

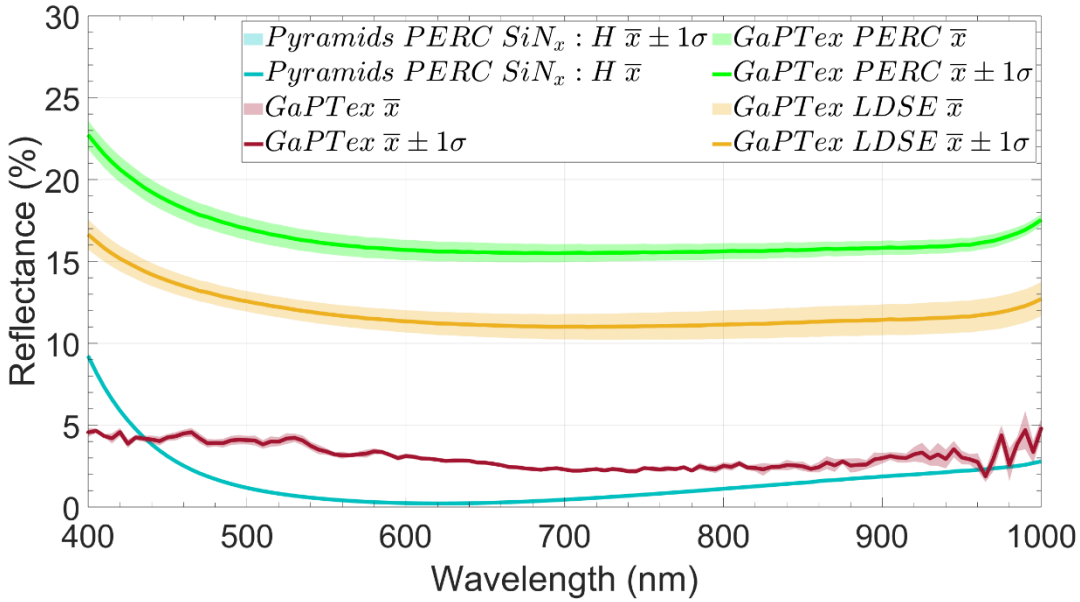

Figure 8.3 Front surface reflectance after emitter-formation for GaPTex with a PERC diffusion or LDSE diffusion, as well as a reference of GaPTex prior to emitter-formation.

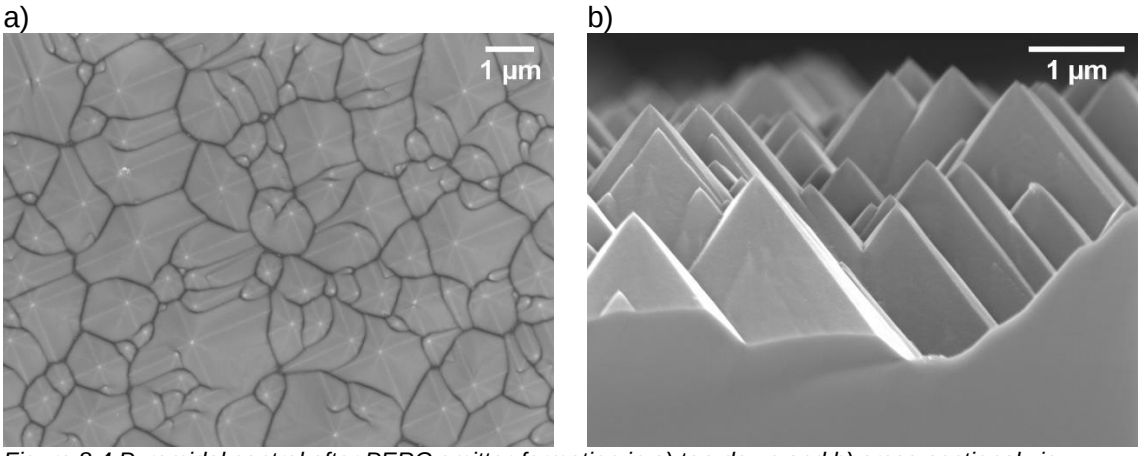

Figure 8.4 Pyramidal control after PERC emitter-formation in a) top-down and b) cross-sectional view.

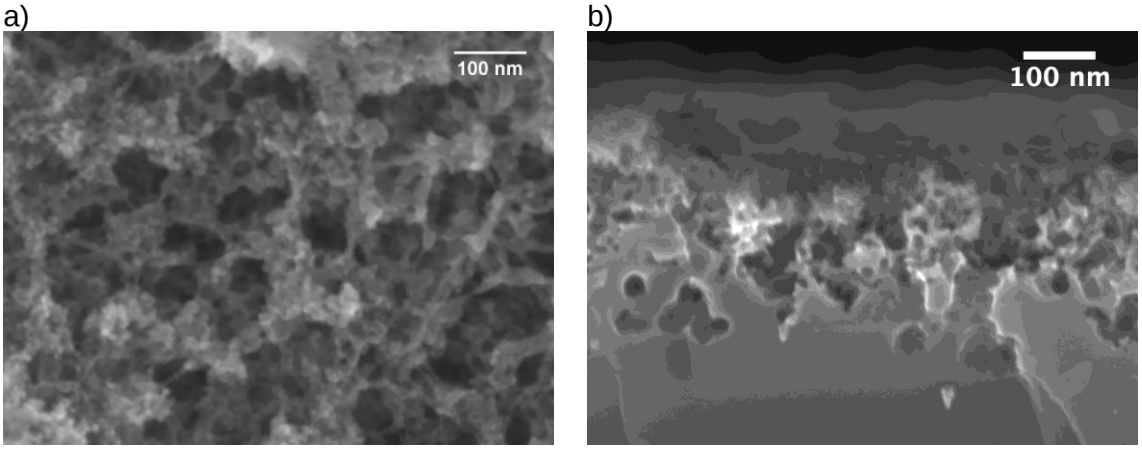

Figure 8.5 Microstructure of GaPTex before emitter fabrication in a) top-down and b) cross-sectional views.

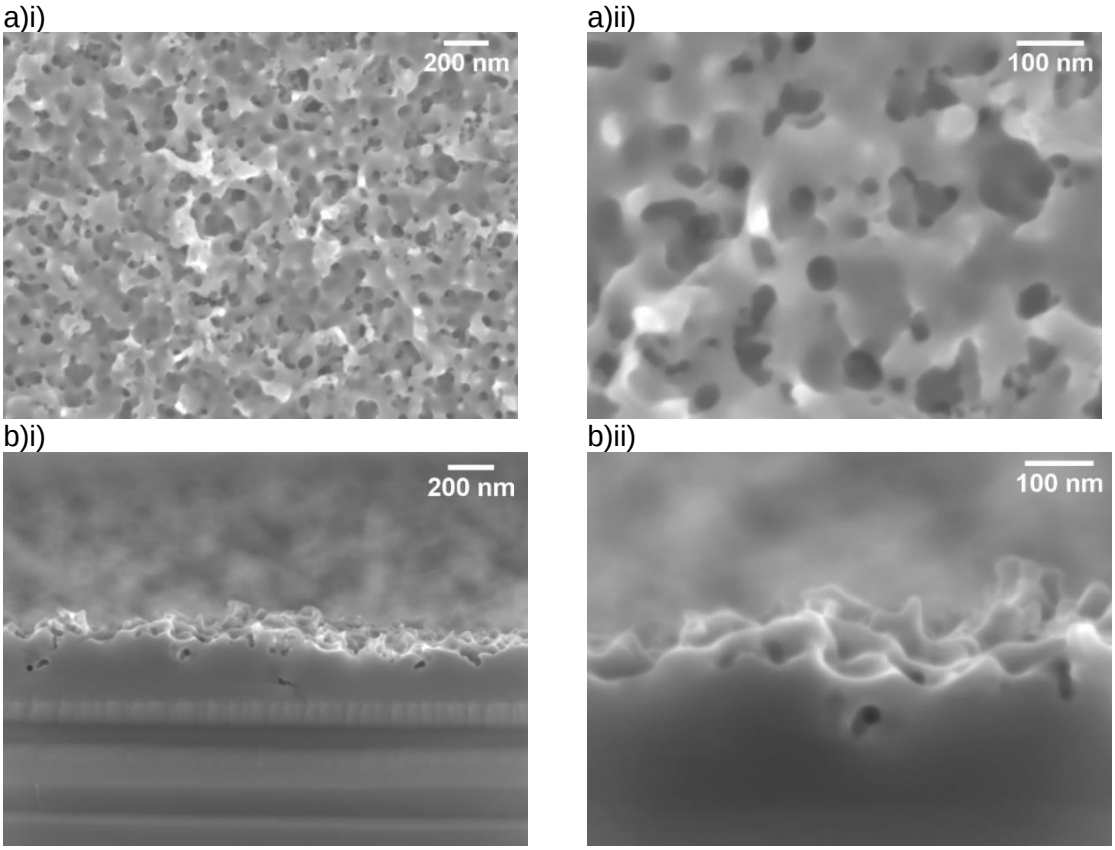

Figure 8.6 GaPTex after PERC emitter-formation in a) top-down and b) cross-sectional views in i) low-magnification and ii) high-magnification.

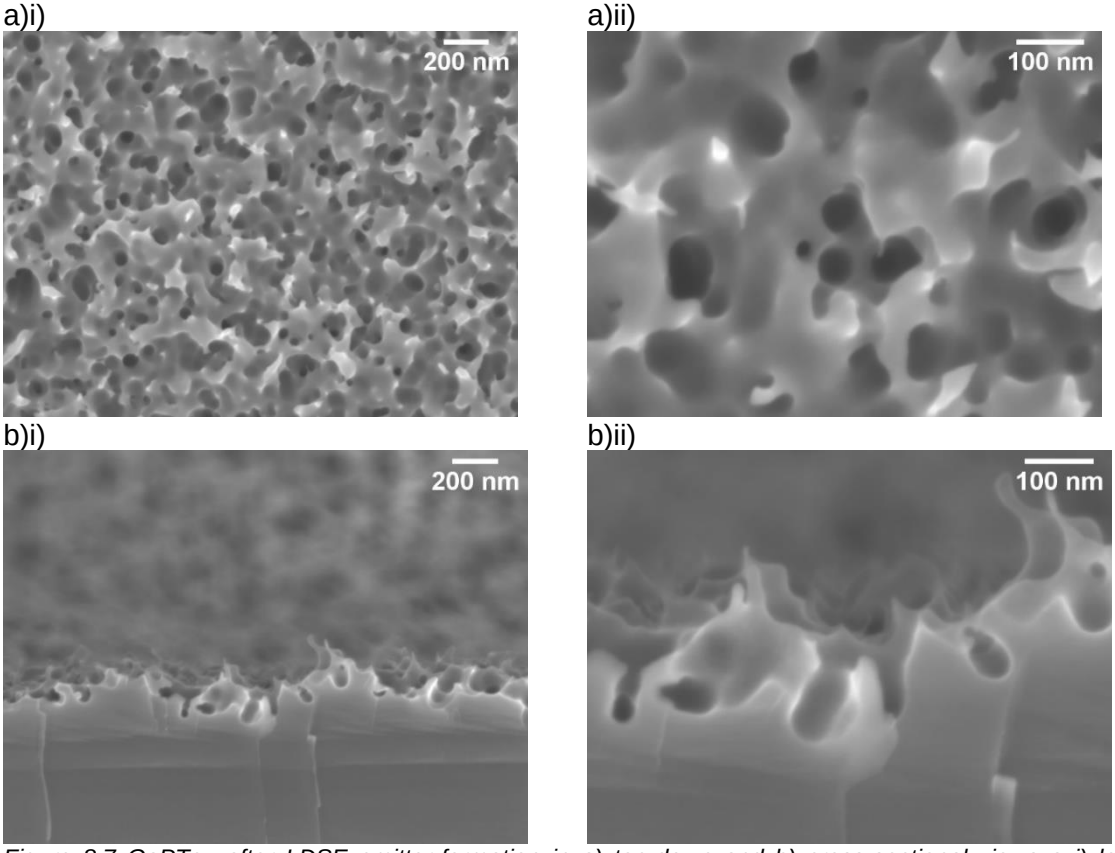

Figure 8.7 GaPTex after LDSE emitter-formation in a) top-down and b) cross-sectional views a i) low-magnification and ii) high-magnification.

Electrical, optical, and physical changes occurred from emitter-formation. Firstly, both R_{sh} values for GaPTex in Figure 8.2 were less than for the microscale pyramidal control. The R_{sh} median values from Figure 8.2 were 43.20 Ω/□ for PERC-GaPTex, 83.47 Ω/□ for pyramidal PERC, and LDSE-GaPTex was 31.80 Ω/□. Secondly, Figure 8.3 showed a reflectance increase for both GaPTex samples from the post-textured reflectance after emitter-formation. The WAR of PERC-GaPTex increased from 3.2% ± 0.2% post-texturing to 16.7% ± 0.6% post-emitter, while LDSE-GaPTex increased to 12.2% ± 0.8% post-emitter. The WAR of the PERC-pyramids with a SiN_x:H ARC in Figure 8.3 was 1.7% ± 0.1%. This low reflectance is caused by the combination of the pyramids and ARC, as a typical reflectance of bare pyramids on Si is ~ 10% [36]. Lastly, the microstructure of PERC-GaPTex and LDSE-GaPTex in Figure 8.6 and Figure 8.7, respectively, shows a change in texture when compared to the post-textured surface of GaPTex in Figure 8.5. Cross-sectional images reveal a reduction in the total texture depth for post-emitter GaPTex against the pre-emitter total texture depth. In addition, the emitter-formation process changed texture morphology. Qualitatively, both textures in Figure 8.6 and Figure 8.7 appear smoother than the pre-emitter texture in Figure 8.5, where PERC-GaPTex appears to have undergone greater smoothing than LDSE-GaPTex. The pyramidal control in Figure 8.4 still contains sharp pyramidal features post-emitter formation.

8.2 Surface Passivation

8.2.1 PECVD SiN_x:H Passivation Post-Emitter-Formation

After fabricating the front surface emitter, the remaining wafers from section 8.1 were passivated to minimise surface recombination. A MAiA XS PECVD tool at SIRF was used to passivate all wafer surfaces using SiN_x:H optimised for microscale upright pyramids. Typical SiN_x:H thickness on upright pyramids was quoted at 70 nm. One wafer from each group was removed for testing after passivation, while the remainder underwent further fabrication steps. SEM micrographs of the passivated surfaces are shown in Figure 8.8 and corresponding effective carrier lifetimes in Figure 8.9. The SEM micrographs in Figure 8.8

are labelled with blue arrows to indicate areas of good coating conformality with the Si surface and orange arrows to indicate bare-Si.

a)

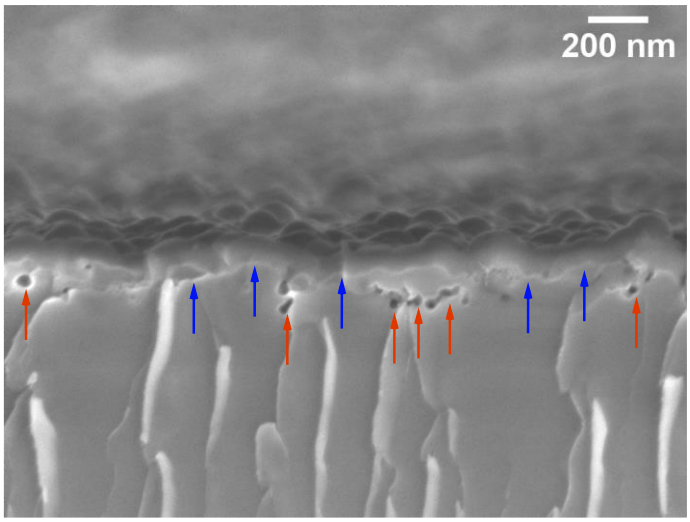

b)i)

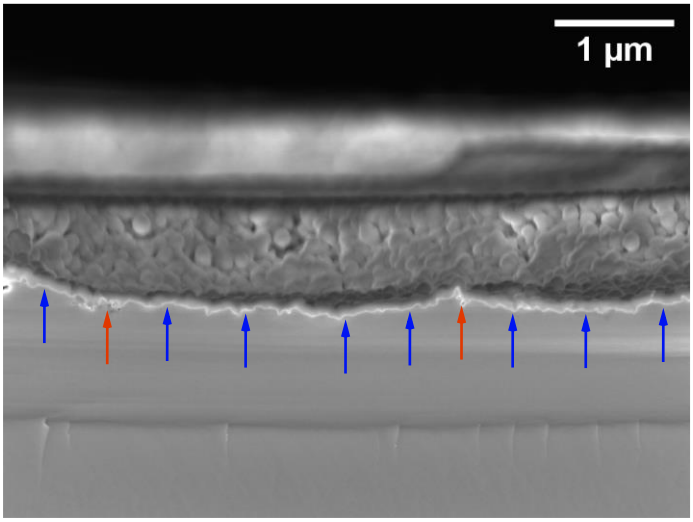

b)ii)

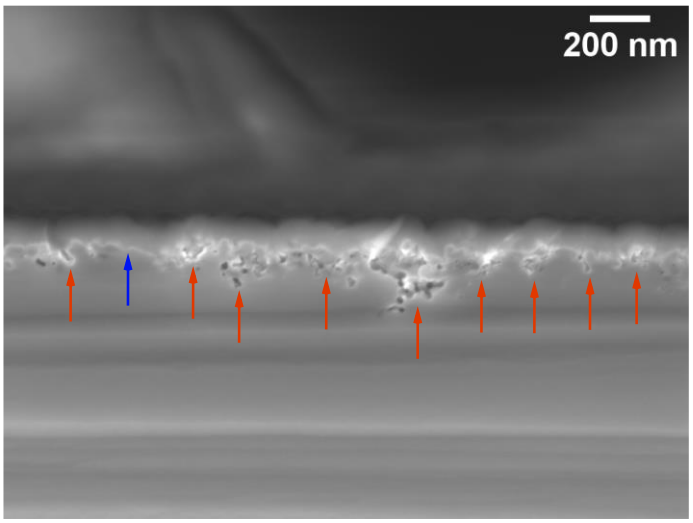

c)

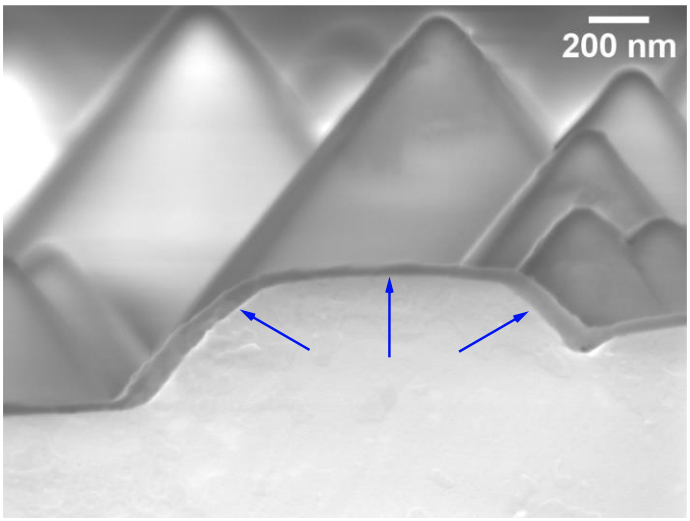

Figure 8.8 PECVD SiN_x:H atop GaPTex with a) PERC emitter-diffusion b) LDSE diffusion for two different areas and c) pyramids with a PERC emitter-diffusion. Blue arrows indicate good coating conformality regions, orange arrows indicate poor or a lack of coating conformality.

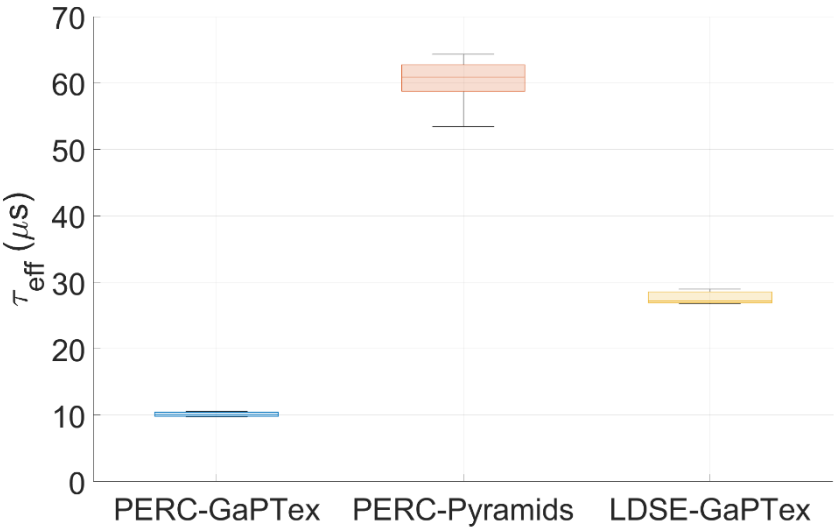

Figure 8.9 Effective lifetime of GaPTex or pyramidally textured wafers with either a PERC emitter or LDSE and SiN_x:H surface passivation. Lifetime values are extracted at minority carrier densities of 1 × 10^{15} cm^{-3}.

Coating conformality of the PECVD SiN_x:H varied for GaPTex surfaces. Figure 8.8a) shows good cohesion across much of the surface between the passivating SiN_x:H layer and the PERC-GaPTex structure, as indicated by the blue arrows; however, there were also areas of bare-Si present on the PERC-GaPTex, pointed out by the orange arrows. The LDSE-GaPTex structures in Figure 8.8b) demonstrated two types of passivation schemes, effectively full surface passivation in Figure 8.8b)i) and partial passivation in Figure 8.8b)ii) with bare-Si etch-pits beneath the surface. The passivation morphology for both GaPTex structures results in a 'ball-pit' like structure on top, where rounded features can be seen

most clearly in Figure 8.8a) and b)i). The passivation for the pyramidal control in Figure 8.8c) appeared to be complete with no bare-Si. The corresponding effective lifetimes in Figure 8.9 corroborate the findings from Figure 8.8 with respect to passivation-surface coating conformality; PERC pyramids achieved the highest lifetime with a median of 60.9 µs followed by LDSE-GaPTex at 27.2 µs and PERC-GaPTex at 10.0 µs.

8.2.2 ALD AlO_x Passivation Post-Texturing

Surface passivation for nano-textures can be improved by using ALD, as its layer-by-layer deposition enables coating conformality of high-aspect-ratio textures [52], [267], [268]. J_0 was extracted to determine surface passivation efficacy, and higher quality material was used so that samples were limited by the surface recombination, not by bulk recombination. N-type, 10 Ω.cm wafers were cleaved into 4 cm × 4 cm specimens using a diamond-tipped pen, sprayed with the precursor using the conditions in Table 8.2, and textured using the recipe in Table 8.1. This was the first use of GaPTex on n-type material. The morphology of n-type and p-type textured with GaPTex was the same, indicating dopant type did not affect the texturing process. The control was a flat, untextured surface. Warwick University used an Ultratech Fiji plasma-enhanced ALD tool to apply a thin film of Al_2O_3 for surface passivation. All samples were cleaned using an RCA2 for 10 mins, dipped in 2 wt% HF for 1 min, and rinsed with de-ionised water. The ALD performed used 200 cycles to generate a 20 – 25 nm thick Al_2O_3 at 200 °C with O_2 plasma. All samples were then heated to 440 °C in air for 30 mins. The mean effective carrier lifetime and J_0 values are presented in Table 8.3 with their respective standard deviations, as well as the champion values for GaPTex. The microstructure in top-down and cross-sectional views are presented in Figure 8.10.

Table 8.2 Precursor spraying conditions.

Precursor Spraying Parameter	**Value**
Precursor Concentration	1:50
Infusion Rate (ml/hr)	400
Atomising Pressure (bar)	1.4
Sample Spray Time (s)	10

Table 8.3 Mean and champion values for effective carrier lifetime and J_0 for the ALD passivated GaPTex samples and control specimen.

	Mean τ_{eff} (µs)	Champion τ_{eff} (µs)	Mean J_0 (fA/cm^2)	Champion J_0 (fA/cm^2)
GaPTex	256.8 ± 43.2	315.2	32.95 ± 2.08	30.89
Control	-	851.5	-	2.82

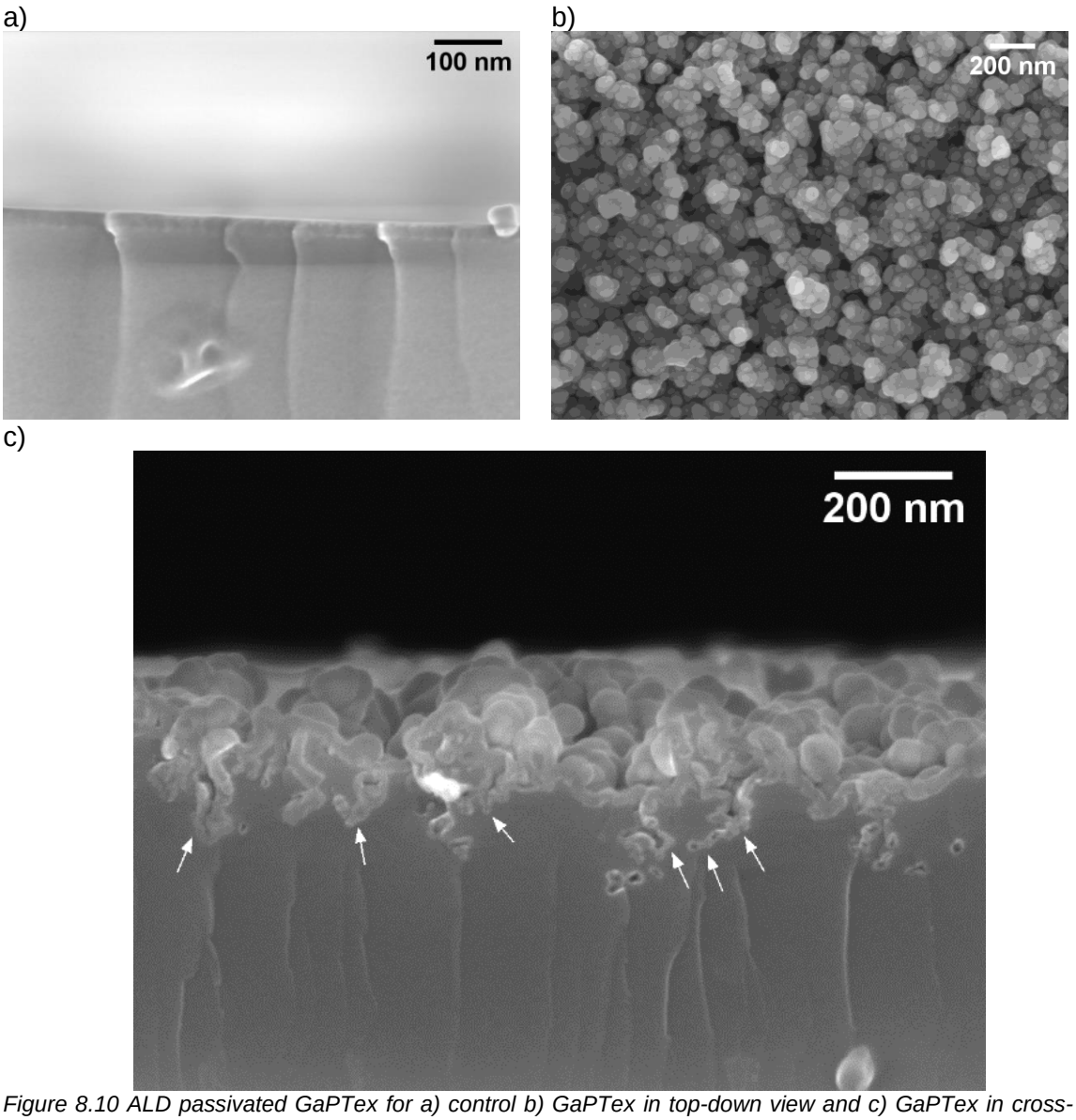

Figure 8.10 ALD passivated GaPTex for a) control b) GaPTex in top-down view and c) GaPTex in cross-sectional view.

Figure 8.10 shows Al_2O_3 passivation successfully adhering to an increased proportion of the surface in comparison to PECVD passivation. ALD Al_2O_3 was able to passivate many of the deeper etch-pits occurring into the bulk-Si, as indicated in Figure 8.10c), which PECVD was unable to do. Figure 8.10b) shows the same 'ball-pit' structure occurred for ALD passivation as did for PECVD passivation. Figure 8.10a) shows ALD completely

adhering to the smooth control surface, where Al_2O_3 thickness was measured at 23 nm ± 2 nm. Table 8.3 shows the corresponding lifetime values to the micrographs in Figure 8.10, where GaPTex achieved an average J_0 of 32.95 ± 2.08 fA/cm^2 and a champion value of 30.89 fA/cm^2, while the flat control specimen achieved a J_0 of 2.82 fA/cm^2. A direct comparison cannot be made between the lifetimes using PECVD passivation presented in Figure 8.9 and the lifetimes using ALD passivation in Table 8.3, as two variables were altered. The first variable altered was the type of passivation scheme, which affects the surface lifetime component of the total lifetime. In addition, the bulk lifetime component was also altered between experiments due to the change in material type and resistivity. Thus, a direct comparison of lifetime cannot be made between the two passivation experiments, as two variables were altered that both affect the total lifetime.

8.3 Final PERC Devices

The remaining wafers from section 8.2.1 underwent the final stages of PERC fabrication at SIRF. EQE and front surface reflectance are presented in Figure 8.11. Figure 8.12 shows cell J_{sc}, V_{oc}, efficiency, FF, pseudo-FF (pFF), series resistance (R_s), and shunt resistance (R_{shunt}) for GaPTex and the pyramidal control wafers.

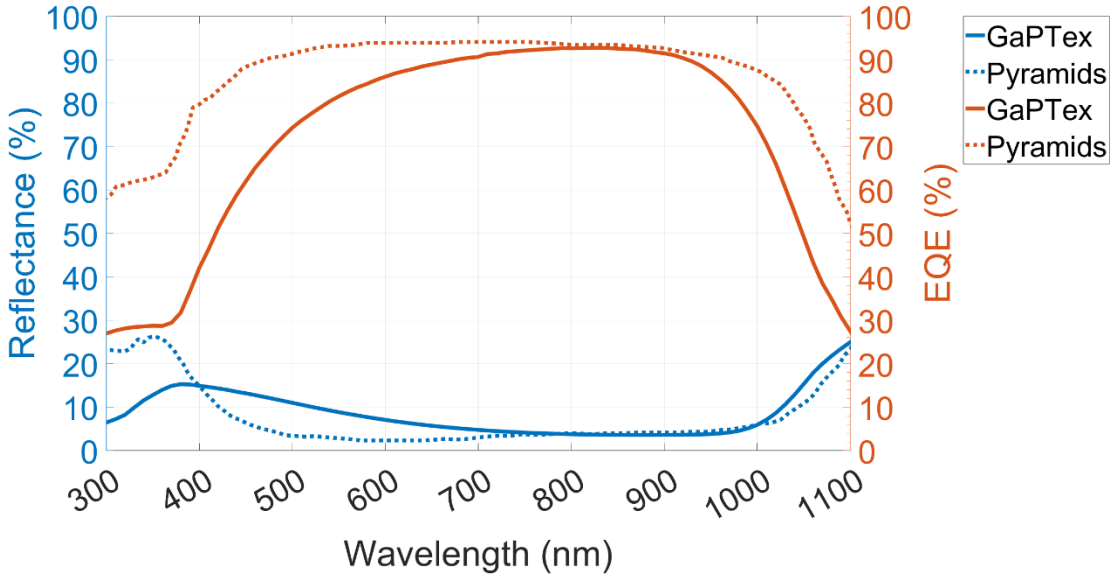

Figure 8.11 EQE and front surface reflectance for PERC made using GaPTex and upright pyramids.

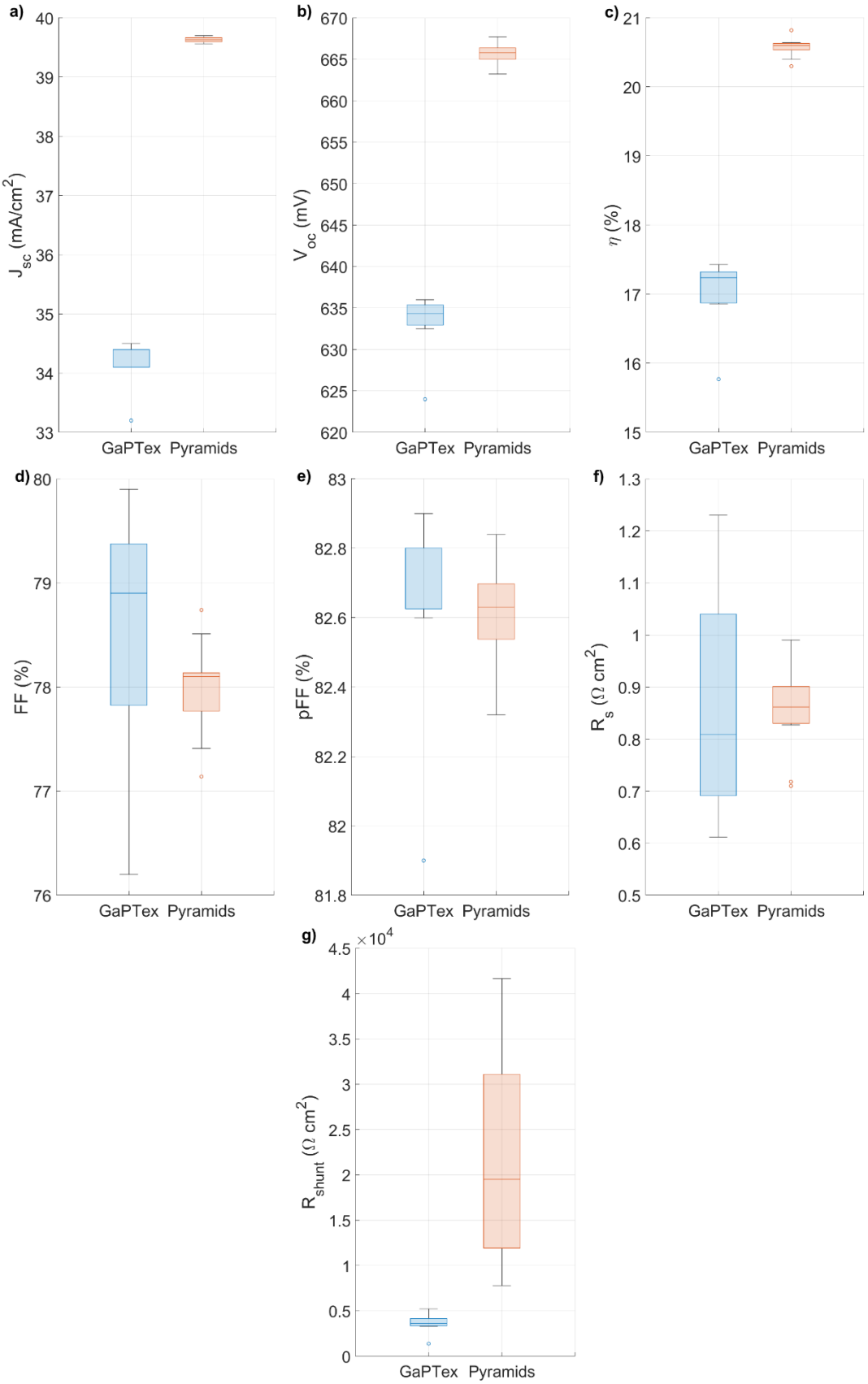

Figure 8.12 GaPTex and upright pyramidal PERC a) J_{sc} b) V_{oc} c) efficiency d) FF e) pFF f) R_s g) R_{shunt}.

The results in Figure 8.12 show that PERC-GaPTex cell properties are inferior, yet of moderate level considering this was the first unoptimized cell fabrication. From Figure 8.12,

the median values of PERC-GaPTex for efficiency, J_{sc}, and V_{oc} are 17.24%, 34.4 mA/cm^2, and 634.3 mV respectively. In addition, the FF presented in Figure 8.12d) shows that the median for GaPTex is greater than for upright pyramids at 78.90% and 78.10% respectively. However, the spread of data for FF, shown by the increased boxplot range in Figure 8.12d), is approximately four times that of the upright pyramids, exceeding both the smallest and largest values of FF for the upright pyramids. Thus, whilst the median FF for GaPTex is greater than for the upright pyramids there are still GaPTex specimens where the FF is less than any of the pyramidal specimens. This spread in data is likely caused by the precursor application in the GaPTex process, where the precursor was deposited onto the substrate surface via manual pipetting. Therefore, a uniform distribution of the precursor across the surface was not guaranteed, causing variations in the subsequent texturing uniformity, hence making a variation in cell properties more likely than the pyramidal counterpart. For pFF in Figure 8.12e), the median values are approximately equal where GaPTex has a slightly larger pFF of 82.80% while the pyramids median value is 82.63%. Yet unlike FF, the spread of both data sets for pFF are similar in size, where GaPTex is approximately half that of upright pyramids. For R_s in Figure 8.12f), the trend reverses where the GaPTex median is less than the pyramids with 0.809 Ω.cm^2, while the upright pyramids yield 0.862 Ω.cm^2. The data range for R_s mimics the trend of FF, where the data spread of GaPTex is more than three times that of the pyramids. Finally, GaPTex presents lower R_{shunt} values than pyramids in Figure 8.12g), where the GaPTex median is 3598 Ω.cm^2 and pyramidal median 19,500 Ω.cm^2. Contrastingly to FF and R_s, the data spread in R_{shunt} for GaPTex is small, 1378 - 5211 Ω.cm^2, whilst the pyramids have a large spread, 7793 - 41,630 Ω.cm^2.

Both GaPTex and pyramids had similar reflectance and EQE responses with respect to wavelength in Figure 8.11. Both GaPTex and pyramids demonstrate increased reflectance at short (<450 nm) and long (>1000 nm) wavelengths in comparison to the wavelengths between (450 – 1000 nm). However, while both reflectance curves are approximately equal in shape, there is a difference in the absolute values. GaPTex reflectance in Figure 8.11 is less than pyramids for wavelengths < 400 nm and 1000 – 1100 nm, but between 400 nm

and 800 nm, GaPTex reflectance is greater than pyramids. At ~ 800 - 1000 nm, both reflectance' are effectively equal. A similar trend is observed for EQE in Figure 8.11. Both EQE curves have lower efficiency at short and long wavelengths whilst increasing the EQE efficiency at the wavelengths between. However, GaPTex EQE is less than that of the pyramids for effectively the whole spectra, except for ~ 800 - 900 nm where the two EQEs are approximately equal.

8.4 Discussion

To understand the difference in morphological and electrical results between the two different textures and emitter recipes, the mechanism of doping using a $POCl_3$ source must be examined. Gases of $POCl_3$ and O_2 are used to form a liquid phosphosilicate-glass (PSG) on the Si surface, surrounding all topographical features [269]. The drive-in of dopant atoms is performed after PSG-formation, where the temperature is increased to enable phosphorous diffusion from the PSG into the Si according to:

$$2P_2O_5(l) + 5Si(s) \rightarrow 5SiO_2(s) + 4P(s) \qquad (8.1)$$

After the drive-in, the surface is cleaned with HF to remove the PSG and SiO_2. The reduction in doping for a LDSE recipe is caused by increasing the oxide thickness, through an oxidation step before forming the PSG, or by reducing the temperature of the drive-in stage. Figure 8.13 presents the PSG formation, drive-in, and cleaning stages on pyramids and GaPTex for a PERC emitter diffusion on both textures and a LDSE diffusion on GaPTex.

For the same emitter recipe, nanostructures will undergo enhanced doping compared to microstructures. Due to the increase in surface area, nanostructures have a higher number of PSG/Si interfaces per unit volume, enabling a greater number of phosphorous atoms to diffuse into the nano-texture [143], [268], [270], [271]. Increased phosphorous doping reduces R_{sh}, as it is inversely proportional to carrier concentration (N), as shown by equation (8.2) in terms of carrier mobility (μ), charge (q), and emitter thickness (t). Carrier mobility has been shown to decrease with increasing doping density, which would increase R_{sh}, but such changes are orders of magnitude less than carrier concentration, making the

latter the dominant term for R_{sh} in this case [31]. As a result, both emitter recipes yielded lower R_{sh} for GaPTex in comparison to the pyramidal control.

$$R_{sh} = \frac{1}{q}\int_0^t \frac{1}{\mu N}\,dt = \frac{1}{q}\left[\frac{t}{\mu N}\right]_0^t \qquad (8.2)$$

The two different emitter recipes used on GaPTex caused differing morphological and electrical results. The supposedly lighter doping of the LDSE recipe yielded a lower R_{sh} than the PERC emitter counterpart in Figure 8.2. Additionally, the LDSE recipe produced a rougher surface on GaPTex than PERC, shown by the micrographs in Figure 8.6 and Figure 8.7, corresponding to a lower reflectance for LDSE-GaPTex than PERC-GaPTex in Figure 8.3. These effects are all accounted for by the differences in the emitter recipes between PERC and LDSE. The oxidation of Si during emitter formation is dependent on processing conditions but is typically of the order of <10 nm [272], thus accounting for the smoothing effect observed in Figure 8.6, as the surface feature size is of an equivalent scale. The rougher texture after LDSE diffusion on GaPTex Si in Figure 8.7 - than after a PERC emitter-diffusion in Figure 8.6 - indicates that less of the surface was oxidised during LDSE diffusion, thus the more fibrous GaPTex features remain. Figure 8.13c)ii) shows that as less of the surface was oxidised with the LDSE emitter recipe, an increased amount of radial diffusion of phosphorous, from the PSG into the Si, occurs. This increased doping accounts for the lower R_{sh} measured for LDSE-GaPTex in Figure 8.2, while the reduction in surface oxidation accounts for the lower reflectance in Figure 8.3.

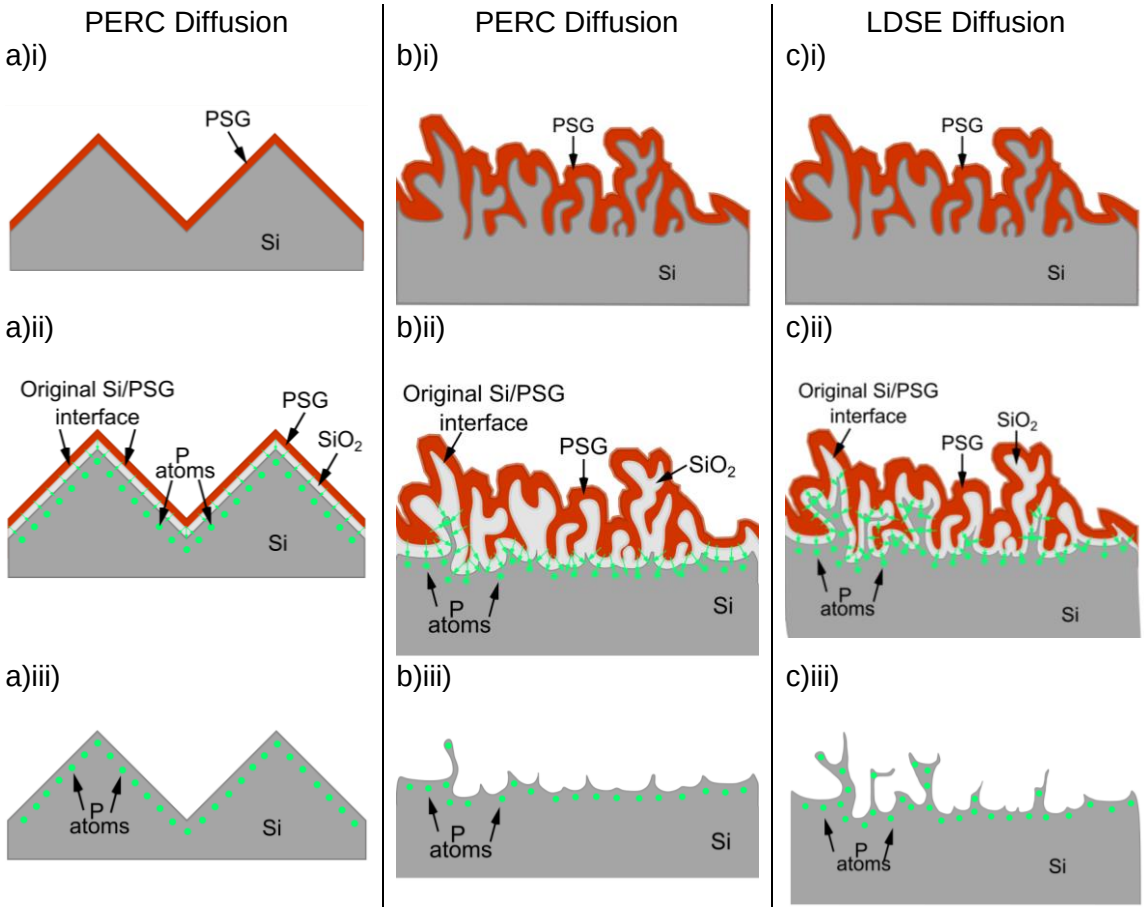

Figure 8.13 Emitter-formation for a) microscale pyramids b) GaPTex with a PERC diffusion and c) GaPTex with a LDSE for the three steps of i) PSG deposition ii) phosphorous drive-in ii) final doped surface.

The lifetime results from SiN_x:H surface passivation for PERC-GaPTex and LDSE-GaPTex are the result of three competing effects. Firstly, the increased doping from emitter-formation for both GaPTex structures is likely sufficient to cause Auger recombination at the surface. B-Si structures can yield doping concentrations $>10^{19}$ cm^{-3}, which makes Auger recombination likely to become a dominant factor to carrier lifetime [31], [143]. Secondly, Figure 8.8 shows regions of bare Si surfaces for both GaPTex samples after surface passivation. Incomplete surface passivation is not uncommon for nano-texture passivation when using PECVD. Y. Liu et al [122] and X. Ye et al [143] demonstrate the same lack of coating conformality between nano-textures and PECVD SiN_x:H, where the SiN_x:H is unable to passivate the bottom of the etch-pits and only coats the top of the nanostructure. Increased Auger, and surface recombination account for the reduction in the lifetime of both GaPTex samples compared to the lifetime for pyramids in Figure 8.9. However, LDSE-GaPTex has a higher lifetime than PERC-GaPTex in Figure 8.9, even though the doping is

higher for LDSE-GaPTex, as demonstrated by R_{sh} in Figure 8.2. The third competing effect contributing to lifetime, responsible for the difference in lifetime between the two GaPTex emitter recipes, is field-effect passivation (FEP). Due to the increased surface area of B-Si over other textures, the effective surface charge density from the passivation layer is larger for B-Si than either a flat surface or micro-textures. Thus, the surface passivation of B-Si generates an electric field sufficient to repel carriers away from the surface for recombination [141], [142]. As more of the texture survived emitter-formation for LDSE-GaPTex than PERC-GaPTex, FEP would be enhanced, causing the increase in lifetime exhibited for LDSE-GaPTex in Figure 8.9.

ALD passivation almost entirely overcame the conformality limitations of PECVD passivation for GaPTex. Due to monolayer deposition caused by self-limiting reactions, ALD is an effective passivation method for high-aspect-ratio structures, such as nano-textures [141], [142], [273]. Figure 8.10 showed ALD passivating a greater proportion of the surface than PECVD passivation by growing on the deep etch-pits and not just the top of the nanostructures. However, the 'ball-pit' structure from PECVD passivation in Figure 8.8 was still present for ALD passivation in Figure 8.10, regardless of the latter's self-limiting, monolayer deposition. This may be caused by the unique morphology of high-temperature GaPTex, which may prevent a smooth layer application from occurring for any dielectric passivation technique.

ALD passivation yielded good electrical properties, without any optimisation of the texture or passivation method, where the champion J_0 of GaPTex was 30.89 fA/cm^2. ITRPV predicted J_0 for a variety of n-type cell architectures in 2022 of 17-20 fA/cm^2 [9]; therefore, achieving a J_0 value less than a factor of two away from industry standards, without any texture optimisation for the passivation method, is an excellent initial result. To obtain even lower J_0 values, the etch-pit depth needs to be reduced for full surface passivation. This could either be achieved by trialling one of the other textures found in Chapter 7, or by performing a light front surface etch after GaPTex to reduce total texture depth.

The final cell properties of PERC-GaPTex show encouraging initial results. With regards to optical properties, both textures had similar responses at the different wavelengths in Figure 8.11, yet pyramids outperform GaPTex for J_{sc} in Figure 8.12a). A closer inspection of where reflectance is minimised with respect to wavelength reveals the source of the difference in J_{sc}. The highest photon density occurs at green wavelengths ~ 500 – 700 nm, Figure 8.11 shows at such wavelengths the pyramidal texture's reflectance was minimised whilst GaPTex's was not. Thus, to improve GaPTex J_{sc} further, reflectance at 500 – 700 nm must further be reduced. This could either be achieved by optimisation of the ARC for the nanoscale structures to ensure reflectance is reduced at 600 nm, as originally designed, or by increasing the total texture depth that remains after cell fabrication to maximise reflectance reduction.

Both front surface reflectance and surface passivation impact EQE results. The overall lowering of EQE curves is associated with an increase in reflectance, as fewer of the incident photons can transmit into the cell to contribute to carrier generation. However, GaPTex specifically shows a lower EQE than upright pyramids between 400 – 800 nm. Such decreases in EQE are caused by increased recombination at the front surface due to higher emitter doping for nanostructures and lack of dielectric surface passivation [139]. In addition, poor front surface passivation increases surface recombination, particularly for short-wavelength carriers, as they are absorbed nearer to the front surface. Both causes reduce the number of carriers that are collected from the solar cell, thus reducing EQE. V_{oc} is also negatively affected by these two factors due to its dependency on the recombination current and the light-generated current. At long wavelengths, EQE may be reduced for GaPTex due to recombination at the rear of the cell and the reduced absorption of longer wavelengths in Si. To improve EQE and V_{oc}, GaPTex cells made with ALD passivation would reduce surface recombination, due to improved adhesion between the passivation and the nano-textured surface, shown in Figure 8.10. Optimisation of the emitter recipe for nano-textures to reduce Auger recombination would also be beneficial, as the PERC emitter

recipe was optimised for the microscale pyramids and thus was not necessarily optimum for any nano-texture.

While the V_{oc} and J_{sc} aided to explain the optical and electrical properties of the cell, the FF can describe the resistive effects. FF has a dependency on both V_{oc} and J_{sc}, yet not all the GaPTex specimens possess a lower FF than the pyramidal specimens. FF can be better understood by examining its components of pFF, describing losses due to recombination, R_s, describing the resistive losses carriers experience on route to extraction from the cell, and R_{shunt} describing the losses due to carriers travelling unintended paths in the solar cell. Figure 8.12e) shows GaPTex possesses a greater pFF than pyramids, which is counterintuitive as V_{oc} and lifetime for GaPTex are both lower than for pyramids. The R_s losses of FF, shown in Figure 8.12f), demonstrate a lower median R_s for GaPTex than pyramids. However, the range of R_s for GaPTex exceeds both the upper and lower bounds of the R_s range for upright pyramids, indicating that carriers in some GaPTex cells had less resistance when travelling to the contacts, while others possessed more. Lower R_s may be explained by differing emitter shapes. For pyramids, the emitter follows the Si/air interface, undulating across the surface with the rise and fall of the slopes of the pyramid. However, for nanostructures, the emitter has been shown to finish well below the Si/air interface into the bulk of the Si in a planar fashion [52]. With a planar emitter, carriers can diffuse a shorter distance to the contacts compared to pyramids, incurring a reduction to R_s. With regards to an increase in R_s for some of the GaPTex cells compared to pyramids, this may be caused by the quality of the contact formed on the front surface. All PERC fabrication steps were optimised for microscale pyramids and therefore the contacts formed on GaPTex may not be performing optimally and thus incurring higher R_s than intended. To reduce R_s for PERC-GaPTex, the contact fabrication would be further investigated to ensure no unnecessary resistances were being introduced. Incidentally, the quality of contact may also account for the lower R_s values of GaPTex than pyramids, alongside the change in the change of the emitter shape. During cell fabrication, the GaPTex wafers underwent smoothing after emitter formation, as evidenced by Figure 8.6. The smoothing of the surface may have

aided to form a higher quality contact than the pyramidal counterpart, thus reducing recombination and decreasing R_s. The smaller R_{shunt} values for GaPTex in comparison to RPD in Figure 8.12 indicate carriers can take alternative routes in the cell, not necessarily to the contacts for extraction. Manufacturing defects are the typical cause of low R_{shunt}, therefore manufacturing optimisation for the GaPTex nanotexture would likely improve R_{shunt}. After reviewing the components of FF, it is still somewhat unclear why the FF values for GaPTex and pyramids are comparable and yet the difference in the J_{sc} and V_{oc} values is so great. Both the R_s and R_{shunt} values of GaPTex would indicate it to have a poorer FF performance than the pyramid cells, yet this is not the case. However, the calculation of FF does not solely depend on V_{oc} and J_{sc}. FF is the ratio of V_{mp}, I_{mp} to V_{oc}, J_{sc}; therefore, having a large V_{oc} and J_{sc} does not guarantee a large FF. The results imply that the ratio between the maximum power point (V_{mp}, I_{mp}) and V_{oc}, J_{sc} for each texture is similar. In future studies of GaPTex applications to solar cells, the IV properties should be investigated in further detail, including analysis of the maximum power point for further clarity on the affect GaPTex has on final electrical properties.

Lastly, cell efficiency is directly proportional to V_{oc} and J_{sc}, thus it is unsurprising that GaPTex produced lower median efficiency than pyramids at 17.24% against 20.60%. As has previously been discussed, the PERC fabrication performed was optimised specifically for microscale upright pyramids, thus it would be unlikely for any nanostructure to outperform the pyramidal PERC control. In addition, this was the first-ever study of implementing GaPTex into a solar cell, thus achieving a 17.24% median efficiency provides a suitable starting point for future research. With the previously suggested alterations to fabrication from this initial study, nano-textured cells could surpass micro-textured cells with their superior optical properties.

8.5 Chapter Summary

GaPTex was successfully implemented into a PERC architecture for the first time, achieving a median efficiency of 17.24%. Of the two types of emitter recipes investigated,

the lighter doping of the LDSE recipe was found to improve the electrical and optical properties of the GaPTex nanostructures in comparison to the PERC emitter diffusion tested. ALD provided high coating conformality for the nanotextures of GaPTex, achieving a J_0 of 30.9 fA/cm^2, which is less than a factor of two from the predicted industrial standards for 2022. No optimisation between the ALD and surface texture was performed, thus this initial J_0 result is an excellent starting point for future research. Lastly, whilst the efficiency achieved by GaPTex was less than the microscale upright pyramids, the PERC fabrication used was optimised for microscale upright pyramids, making it improbable for any nanotexture to outperform the pyramids. In conclusion, a foundation has been provided for focusing future research on optimising GaPTex, and the fabrication methods used, to produce the highest cell efficiency possible.

9 Conclusions & Further Work

Within this thesis, a texturing technique for Si solar cells was developed. This technique was able to produce ultra-low reflectance surfaces at low temperatures, and atmospheric pressure, all in an industrially appropriate time frame.

Texturing has been a vital aspect of Si-based solar cell performance ever since it was first demonstrated in the 1974 COMSAT solar cell [93]. The optical benefits a front surface texture provides solar cells are increased photon transmission into the cell, by reducing the front surface reflectance, and aiding in retaining photons within the cell resulting in increased carrier generation [31], [53]. However, current industrial texturing is still dominated by microscale textures, which do not eliminate front surface reflectance across the entirety of the relevant photon wavelengths for solar cell carrier generation. Nanoscale texturing techniques have demonstrated that effectively all incident light on the front surface of a solar cell can be transmitted into the cell for carrier generation, forming what is known as black-Si (B-Si). Nevertheless, each B-Si texturing technique has at least one drawback preventing significant industrial implementation, including difficult and costly waste disposal, multi-step processing, the use of expensive metals, or expensive equipment. Thus, there is still a need to develop an alternative, industrially feasible B-Si texturing method to increase cell efficiency beyond what is possible with microscale texturing.

In this thesis, a B-Si texturing technique in the gas phase, termed gas-phase texturing (GaPTex), was developed to produce the beneficial ultra-low surface reflectance of other B-Si techniques without their drawbacks. GaPTex used ozone (O_3) and hydrofluoric acid (HF) vapours to oxidise the surface and etch the surface oxide away. Other gas-phase texturing techniques have been presented in literature but either the time to achieve a suitable texture was too great for industrial uptake or the techniques were designed for in-line processing, as opposed to the preferred batch processing by manufacturers [172], [173], [175], [177]–[180]. Thus, the benefits of texturing in the gas phase had yet to be truly realised.

The aims of this thesis, as set out in Chapter 1, were:

1. Develop a new GaPTex tool.
2. Reproducibly make uniform ultra-low reflectance Si in an industrially suitable time frame.
3. Propose the GaPTex texturing reaction mechanism.
4. Investigate the range of morphologies GaPTex could produce and their optical properties.
5. Define GaPTex solar cell performance for the first time.

The design and development of a new GaPTex tool were addressed in Chapter 3. Chapters 4 and 5 show the progression to a final texturing recipe that, with the aid of a precursor, could reproducibly fabricate ultra-low reflectance Si within minutes. Chapters 6 and 7 delved into how and why the precursor was so effective at aiding texturing and culminated in proposing the GaPTex reaction mechanism. Chapter 7 also focussed on determining what range of morphologies GaPTex could produce and the resulting optical properties. Finally, Chapter 8 contained the first-ever results of GaPTex in the final application of a solar cell, achieving a 17.24% efficient passivated emitter rear cell (PERC) without any processing optimisation to accommodate the nanoscale texture. The summary of each aim is detailed below as well as avenues for future work to enable GaPTex to aid in maximising cell efficiency in the fight against climate change.

9.1 B-Si with a Newly Developed Gas-Phase Texturing Tool

The prior investigation into GaPTex was limited by the operating parameter space of the texturing tool. Chapter 3 presented the development of a new GaPTex tool, where the new tool design, and subsequent tool refinements, increased the parameter space to allow for a deeper exploration of GaPTex. The new design of the GaPTex tool also incorporated features to increase industrial feasibility, thus making GaPTex competitive with other gas phase texturing techniques. One concern of industry, with regards to process desirability, is the wafer processing time. The new GaPTex tool design enabled higher sample

processing temperatures from sub-80 °C to 250 °C, thus increasing the texturing kinetics for faster sample processing. The reaction gas temperature in the reaction chamber was also increased to shorten wafer processing time, from 35 °C in the prior tool to 56 °C in the new tool. Both increases in operating temperature are still regarded as low-temperature processing in solar cell manufacture, thus GaPTex gains the benefit of reducing processing time without compromising on its industrial desirability.

The first use of the new GaPTex tool in Chapter 4 showed that the surface chemistry of Si played a crucial role in texturing. A variety of sample cleaning methods demonstrated that while the cleanest samples could reproduce reflectance the best, the blackest samples were not the cleanest samples. XPS measurements confirmed the presence of surface contaminants, both from the manufacturer and the dicing machine used to cut wafers. Due to the impurities not being intentionally added to the surface by the manufacturer, or the dicing machine, the impurity distribution on a wafer surface, and between wafers, accounted for the lack of texturing uniformity across a wafer surface and the lack of reproducibility between wafers.

The role of surface impurities was harnessed for the creation of uniform, reproducible B-Si. It was hypothesised, in Chapter 5, that by deliberately introducing a non-native chemical species to the surface, the rate of GaPTex would increase, as the introduced chemical species would act as heterogeneous nucleation sites for the texturing reaction. A precursor containing colloidal silica and IPA was chosen to fulfil this role, where the SiO_2 nanoparticles were intended to act as the heterogeneous nucleation sites. In addition, as the reaction gas included HF, the SiO_2 nanoparticles would be etched away during texturing, necessitating no additional processing steps post-texture. Chapter 5 also explored the use and application of the precursor in GaPTex and resulted in achieving reproducible and uniform B-Si, with a typical weighted average reflectance (WAR) of 3.1% and a standard deviation of 0.4% in as little as 2 mins texturing time. Two factors were found to be crucial in producing this ultra-low reflectance. Firstly, the precursor stability. Settling occurred when placing colloidal silica into IPA; such precursors did not yield reproducible texturing. Once

the precursor underwent stabilisation with sulphuric acid to form chains of polysilicic acid at the surface of the nanoparticles, texturing became reproducible. The second factor was the precursor application method. Texturing uniformity was dependent on how the precursor was distributed across the surface. Precursor application methods such as painting, dipping, and spinning all yielded a lack of uniformity across the sample surface, producing standard deviations above 1% reflectance. The final application method of atomising the precursor and spraying it onto the surface, creating a uniform surface distribution of micro-droplets, produced highly uniform textured samples, with standard deviations < 1%. The combination of spraying and using a stabilised precursor was used to create the ultra-low reflectance GaPTex B-Si.

The optimisation of GaPTex in this thesis achieved a reduction of ×4 in WAR and a reduction of ×15 to total processing time versus prior work. GaPTex was able to produce sub-5% reflectance without the need for expensive manufacturing equipment, or cost-intensive noble metals, while avoiding the drawbacks of wet chemical texturing methods such as difficult and expensive waste disposal. Furthermore, the texturing time of GaPTex to achieve sub-5% reflectance was less than the industry standard of 7 mins, for the commonly used wet chemical methods, and comparable to the quicker processing times of other B-Si techniques, which were typically < 5 mins. With regards to other gas-phase texturing techniques, GaPTex produced a lower WAR than all except for the work by B. Kafle et al. [172] where 2% WAR was produced. The processing time from that study was not stated thus a comparison to processing time could not be made, but the compromise of 1% higher reflectance in favour of GaPTex's short processing time is an attractive avenue to manufacturers.

9.2 The Texturing Reaction Mechanism

The original hypothesis that the SiO_2 nanoparticles induced the rapid texturing seen in Chapter 5 was disproved in Chapter 6. By testing all the components of the colloidal silica individually, it was demonstrated that the Na^+ counter-ions in the colloidal silica caused

texturing, not the silica particles. Furthermore, it was shown that Na^+ aided the texturing process chemically and not physically as the nanoparticles had originally been hypothesised to do. The chemical effect of Na^+ was further refined and determined to be kinetic, not thermodynamic. Alkali metals had previously been demonstrated to act as an oxidation catalyst in literature, and oxidation experiments in Chapter 6 using Na^+ showed oxidation rates increased by a factor of 1.5 to 2 in the GaPTex tool. From the oxide-etching experiments in Chapter 6, Na^+ was determined to stabilise the necessary water micro-droplets on the Si surface for oxide-etching via HF to occur at temperatures above the evaporation point of H_2O and HF. Using these factors and the morphology data resulting from different operating parameters in Chapter 7, a complete reaction mechanism for GaPTex was proposed for the first time. The first stage of the texturing mechanism was the stabilisation of micro-droplets on the surface. Secondly, etching occurred in micro-droplet locations due to the requirement of HF needing to be in the liquid phase for oxide-etching to occur. Thirdly, the etch pits would continue to grow in all dimensions until they completely contained their respective micro-droplet. Lastly, etching continued where the liquid was in contact with the Si, creating a uniform etch-pit cross-section except at the bottom of the etch-pit where etching was still occurring.

9.3 Texture Morphology

The key result of Chapter 7 was that etch-pit morphology was dominated by the sample temperature. Processing samples at temperatures ≤ 100 °C caused an inverted pyramidal texture at the base of the etch-pit, with vertical walls to the surface. Whilst at temperatures ≥ 200 °C, etch-pit cross-sections became circular with seemingly random etch-pit direction. The change in morphology with temperature was linked to the role of Na^+ in the oxidation phase of the texturing reaction. It was proposed that oxidation by alkali metals, such as Na^+, became confined to specific crystallographic planes at lower temperatures, akin to the well-documented wet alkali metal etching of Si [94], [266]. At decreased temperatures, wet alkali metal etching proceeds quicker on Si(100) than Si(111), due to the difference in bonding

strength of the Si-Si back-bonds on each set of planes [94], resulting in an upright pyramid texture. Therefore, it was proposed that the oxidation catalysis caused by Na^+ occurred quicker on Si(100) than Si(111), causing the inverted pyramidal etch-pits to form. Upon increasing temperature, the activation energy to oxidise a greater number of crystallographic planes could be met. Thus, the etch-pit shape was no longer confined to specific crystallographic planes but by the contact between the surface to the deliquesced liquid.

Other operating parameters such as alkali metal species, alkali metal concentration, and O_3 concentration were also investigated in Chapter 7 for their effect on morphology. However, none caused dramatic changes to morphology to the extent as the sample temperature did. Nevertheless, it was noted that all investigations were undertaken at a sample temperature of 250 °C, and the investigations could have yielded different results at lower sample temperatures.

9.4 Solar Cell Implementation

The last aim of this thesis was to determine the performance of GaPTex-Si in a solar cell for the first time. The median cell efficiency for the first implementation of GaPTex into a PERC was 17.24%. While the control PERC of microscale, upright pyramids achieved a median cell efficiency of 20.60%, all the cell fabrication steps were optimised for microscale pyramids, not the nanoscale texture of GaPTex. Thus, it would have been unlikely for any nano-texture to outperform the microscale pyramid PERC, if not any other texture, regardless of scale. However, the primary goal of this first implementation of GaPTex was not to achieve a record cell efficiency but to gain an understanding of how GaPTex interacted with cell fabrication steps and use it for optimisation in future work.

In addition to the fabrication of PERC from GaPTex-Si, an alternative passivation method, known to perform well with nanotextures, was tested on as-textured GaPTex-Si. Atomic layer deposition (ALD) Al_2O_3 improved the adhesion between the Si surface and the passivation layer beyond what was possible with the PERC fabrication. A champion

recombination current of 30.89 fA/cm^2 was achieved, approximately a factor of two away from the current predicted industrial standard of 17-20 fA/cm^2 [9]. Therefore, GaPTex-Si has demonstrated industrial applicability with a single implementation, without optimisation. However, it would still be beneficial to continue to reduce recombination to achieve record cell efficiencies.

9.5 Further Work

For GaPTex to gain significant industrial traction it must demonstrate multi-wafer etching. This may involve a redesign of the current texturing tool, to maintain aspects such as sample temperature, as well as new challenges such as uniform gas flow across the surface of multiple wafers.

Further investigations into the effect of operating parameters should be undertaken at lower temperatures. In Chapter 7, sample temperature produced the most significant morphology change. However, the effect of temperature may have masked the effect of the other tested operating parameters, as all experiments (except sample temperature) were conducted at 250 °C. The effect of operating parameters on morphology should be re-evaluated at lower temperatures to determine what other morphologies GaPTex can produce.

To increase the efficiency of cells generated by GaPTex, two avenues must be explored. Firstly, cell fabrication methods designed or optimised for nanoscale textures must be investigated. Within this thesis only methods optimised for microscale upright pyramids were tested on GaPTex, thus it was unlikely that GaPTex would have yielded better-performing cells or any other nanoscale texture. Specific attention should be paid to the emitter-formation to ensure retention of the exceptional optical properties of GaPTex, as well as reducing the front surface doping to diminish recombination. Passivation using ALD should also be trialled in a full cell, as the initial results from Chapter 8 already demonstrated an improvement when using ALD. Lastly, the contact design must be investigated, as it may have contributed to resistive losses in the GaPTex PERC. The second avenue to explore

for improved cell efficiency is the GaPTex morphology. Only one texture was trialled in a cell during this thesis due to time constraints, but GaPTex has presented alternative textures yet to be tested in a full solar cell. Once the investigation into the effect of operating parameters on morphology is completed, a selection of textures should be implemented into a cell, with appropriate fabrication steps for the texture scale, and the performance re-evaluated.

10 Appendix I: Chapter 4 Complete Data Sets

10.1 Cleaned Specimens Post-Texturing Appearance

Figure 10.1 Camera images of samples that underwent different pre-texturing cleans.

		Sample 1	Sample 2	Sample 3
No Cleaning – Diamond Pen	Pre-Texture			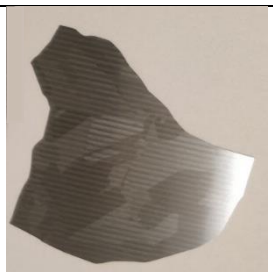
	Post-Texture			
Acetone Cleaning	Pre-Texture			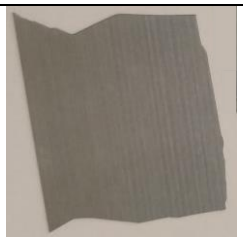
	Post-Texture			

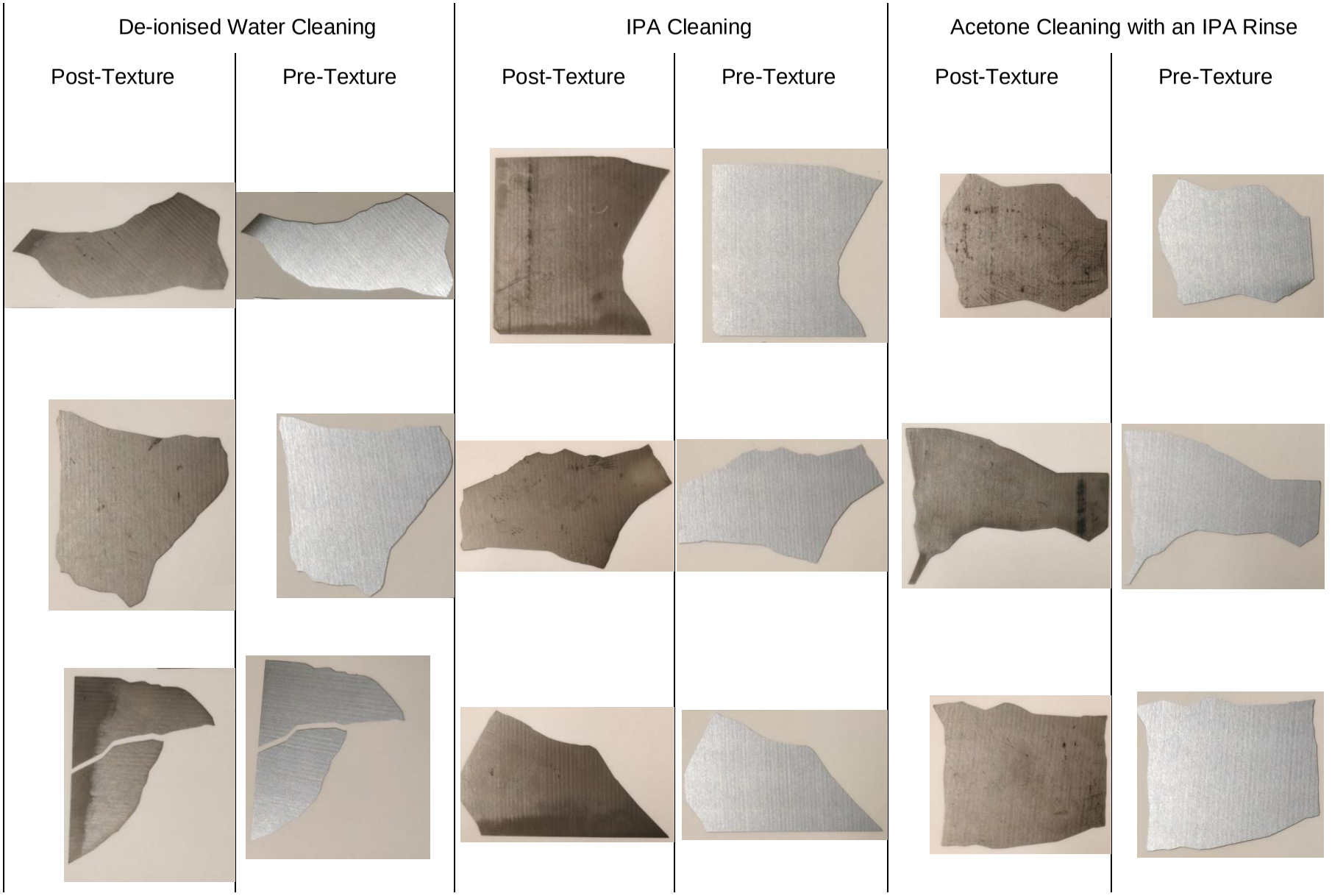
De-ionised Water Cleaning
IPA Cleaning
Acetone Cleaning with an IPA Rinse
Post-Texture
Pre-Texture
Post-Texture
Pre-Texture
Post-Texture
Pre-Texture

RCA Cleaning	Pre-Texture		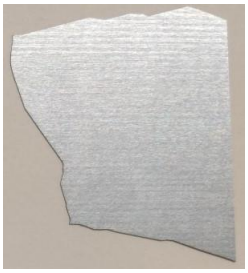	
	Post-Texture			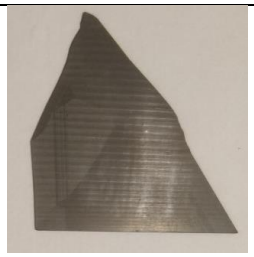

10.2 XPS Spectra of Sample Surface Chemistry

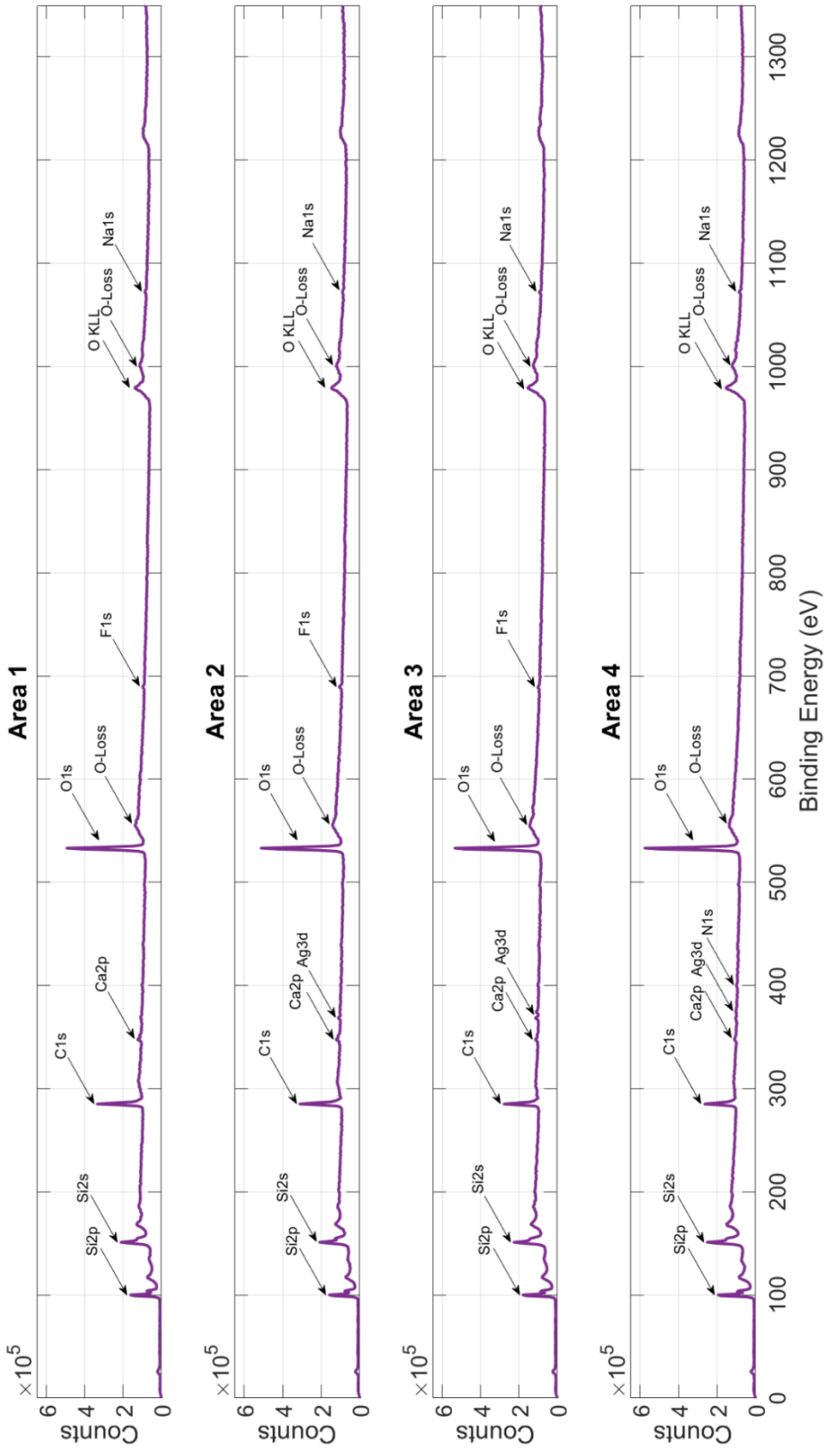

Figure 10.2 XPS spectra of 4 points across the uncleaned specimen that was cut using the MicroAce3 dicer.

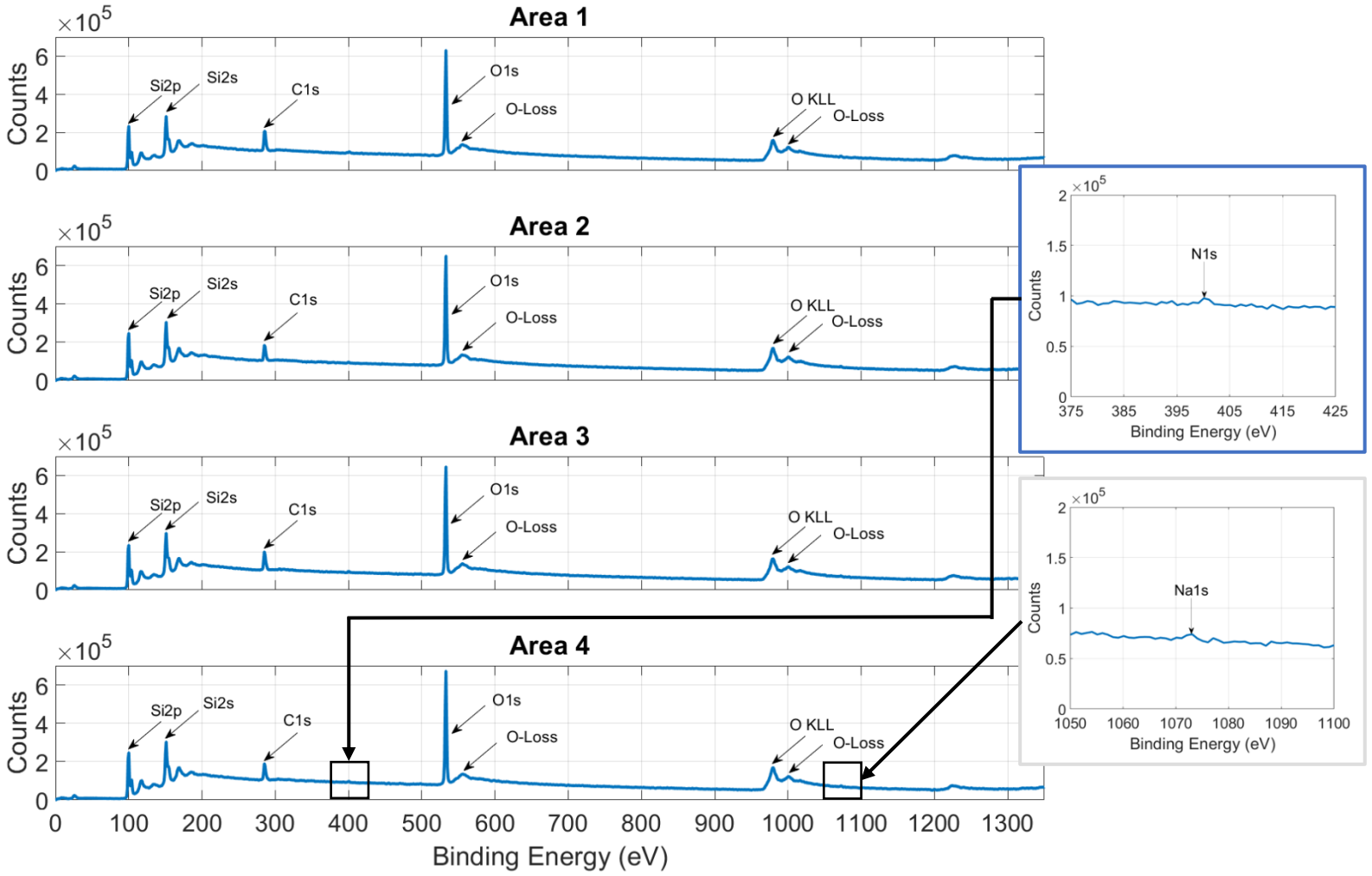

Figure 10.3 XPS spectra of 4 points across the uncleaned specimen that was cut using the diamond-tipped pen. Exploded views are included of the N1s and Na1s peaks as an example on Area 4, but these peaks also appear in Areas 1-3.

11 Appendix II: Gibbs Free Energy Calculations

$$\Delta G_{reaction} = \Delta H_{reaction} - T\Delta S_{reaction}$$

$$\Delta H_{reaction} = \sum n\Delta H_{formation}(products) - \sum m\Delta H_{formation}(reactants)$$

$$\Delta S_{reaction} = \sum n\Delta S_{formation}(products) - \sum m\Delta S_{formation}(reactants)$$

- $\Delta G_{reaction}$ – change in gibbs free energy of a reaction in kJ/mol
- $\Delta H_{reaction}$ – Enthalpy of Reaction in kJ/mol
- T – reaction temperature in K
- $\Delta S_{reaction}$ – Entropy of Reaction in J/Kmol
- $\Delta H_{formation}$ – Enthalpy of formation in kJ/mol
- $\Delta S_{formation}$ – Entropy of formation in kJ/mol
- n – number of moles of the products
- m – number of moles of the reactants

All calculations were performed under standard temperature and pressure conditions (298 K, 1 atm), data obtained from M.W. Chase [1].

11.1 Si Oxidation Using O_3

$$3Si + 2O_3 \rightarrow 3SiO_2$$

11.1.1 $\Delta H_{reaction}$

$$\Delta H_{formation}(SiO_2) = -898.1\ kJ/mol$$

$$\Delta H_{formation}(Si) = 0\ kJ/mol$$

$$\Delta H_{formation}(O_3) = +152.4\ kJ/mol$$

$$\Delta H_{reaction} = \{(3) \times (-898.1\ kJ/mol)\} - \{[(3) \times (0\ kJ/mol)] + [(2) \times (+152.4\ kJ/mol)]\}$$

$$\Delta H_{reaction} = \{(-2694.3\ kJ/mol)\} - \{(+304.8\ kJ/mol)\}$$

$$\Delta H_{reaction} = -2999.1\ kJ/mol$$

11.1.2 $\Delta S_{reaction}$

$$\Delta S_{formation}(SiO_2) = 70.9\ J/(Kmol)$$

$$\Delta S_{formation}(Si) = \ 30.2\ J/(Kmol)$$

$$\Delta S_{formation}(O_3) = \ 263.4\ J/(Kmol)$$

$$\Delta S_{reaction} = \{(3) \times (70.9\ J/(Kmol))\} - \{[(3) \times (30.2\ J/(Kmol))] + [(2) \times (263.4\ J/(Kmol))]\}$$

$$\Delta S_{reaction} = \{(212.7\ J/(Kmol))\} - \{(617.4\ J/(Kmol))\}$$

$$\Delta S_{reaction} = -404.7\ J/(Kmol)$$

11.1.3 $\Delta G_{reaction}$

$$\Delta G_{reaction} = (-2999.1\ kJ/mol) - (298K)(-404.7\ J/mol)$$

$$\Delta G_{reaction} = -2878.4\ kJ/mol$$

Si oxidation using O_3 is spontaneous as the Gibbs free energy is negative. The reaction will proceed of its own accord.

11.2 Si Oxidation Using O_2

$$Si + O_2 \rightarrow SiO_2$$

11.2.1 $\Delta H_{reaction}$

$$\Delta H_{formation}(SiO_2) = -898.1\ kJ/mol$$

$$\Delta H_{formation}(Si) = \ 0\ kJ/mol$$

$$\Delta H_{formation}(O_2) = \ 0\ kJ/mol$$

$$\Delta H_{reaction} = \{(-898.1\ kJ/mol)\} - \{(0\ kJ/mol) + (0\ kJ/mol)\}$$

$$\Delta H_{reaction} = -898.1\ kJ/mol$$

11.2.2 $\Delta S_{reaction}$

$$\Delta S_{formation}(SiO_2) = 70.9\ J/(Kmol)$$

$$\Delta S_{formation}(Si) = \ 30.2\ J/(Kmol)$$

$$\Delta S_{formation}(O_2) = \ 205.2 \ J/(Kmol)$$

$$\Delta S_{reaction} = \{(70.9\,J/(Kmol))\} - \ \{(30.2\,J/(Kmol)) + (205.2\,J/(Kmol))\}$$

$$\Delta S_{reaction} = \{(70.9\,J/(Kmol))\} - \ \{(235.4\,J/(Kmol))\}$$

$$\Delta S_{reaction} = -164.5\,J/(Kmol)$$

11.2.3 $\Delta G_{reaction}$

$$\Delta G_{reaction} = (-898.1\ kJ/mol) - (298K)(-164.5\,J/mol)$$

$$\Delta G_{reaction} = -849.1\ kJ/mol$$

Si oxidation using O_2 is spontaneous as the Gibbs free energy is negative. The reaction will proceed of its own accord.

11.3 HF etching SiO_2

$$4HF + SiO_2 \ \rightarrow \ SiF_4 + \ 2H_2O$$

11.3.1 $\Delta H_{reaction}$

$$\Delta H_{formation}(H_2O) = \ -285.8\ kJ/mol$$

$$\Delta H_{formation}(SiF_4) = -1615.0 \ \ kJ/mol$$

$$\Delta H_{formation}(SiO_2) = \ -898.1\ kJ/mol$$

$$\Delta H_{formation}(HF) = \ -272.7\ kJ/mol$$

$$\Delta H_{reaction} = \{[(2) \times (-285.8\ kJ/mol)] + [(1) \times (-1615.0\ kJ/mol)]\}$$
$$- \ \{[(1) \times (-898.1\ kJ/mol)] + [(4) \times (-272.7\ kJ/mol)]\}$$

$$\Delta H_{reaction} = \{(-2186.6\ kJ/mol)\} - \ \{(-1988.9\ kJ/mol)\}$$

$$\Delta H_{reaction} = -197.7\ kJ/mol$$

11.3.2 $\Delta S_{reaction}$

$$\Delta S_{formation}(H_2O) = 70.0 \ \ J/(Kmol)$$

$$\Delta S_{formation}(SiF_4) = \ 282.8 \ \ J/(Kmol)$$

$$\Delta S_{formation}(SiO_2) = 70.9\ J/(Kmol)$$

$$\Delta S_{formation}(HF) = 173.8\ \ J/(Kmol)$$

$$\Delta S_{reaction} = \{[(2) \times (70.0\ J/(Kmol))] + [(1) \times (282.8\ \ J/(Kmol))]\}$$

$$- \ \{[(1) \times (70.9\ J/(Kmol))] + [(4) \times (173.8\ \ J/(Kmol))]\}$$

$$\Delta S_{reaction} = \{(422.8\ J/(Kmol))\} - \ \{(766.1\ J/(Kmol))\}$$

$$\Delta S_{reaction} = -343.3\ J/(Kmol)$$

11.3.3 $\Delta G_{reaction}$

$$\Delta G_{reaction} = (-197.7\ kJ/mol) - (298K)(\ -343.3\ J/mol)$$

$$\Delta G_{reaction} = -95.4\ kJ/mol$$

Etching SiO_2 using HF is spontaneous as the Gibbs free energy is negative. The reaction will proceed of its own accord.

12 Appendix III: Vapour Pressure Calculations for NaOH and H_2O at Elevated Temperature

Clausius-Claperyron Equation:

$$\ln\left(\frac{P_2}{P_1}\right) = -\frac{\Delta H_{vap}}{R}\left(\frac{1}{T_2} - \frac{1}{T_1}\right)$$

$T_1 = 298\ K$

$T_2 = 523\ K$

$R = 8.3145\ J/mol.K$

12.1 Vapour Pressure for H_2O at 523 K

$P_1 = 23.8\ mmHg$

$\Delta H_{vap} = 43.988\ kJ/mol$

$$\ln\left(\frac{P_2}{23.8\ mmHg}\right) = -\frac{43.988\ kJ/mol}{8.3145\ J/mol.K}\left(\frac{1}{523\ K} - \frac{1}{298\ K}\right)$$

$$\ln\left(\frac{P_2}{23.8\ mmHg}\right) = 7.6377$$

$$P_2 = 23.8\ mmHg \exp(7.6377)$$

$$P_2 = 49.4 \times 10^3\ mmHg$$

12.2 Vapour Pressure for NaOH at 523 K

$P_1 = 1.82 \times 10^{-21}\ mmHg$

$\Delta H_{vap} = 175\ kJ/mol$

$$\ln\left(\frac{P_2}{1.82 \times 10^{-21}\ mmHg}\right) = -\frac{175\ kJ/mol}{8.3145\ J/mol.K}\left(\frac{1}{523\ K} - \frac{1}{298\ K}\right)$$

$$\ln\left(\frac{P_2}{1.82\ \times 10^{-21}\ mmHg}\right) =\ 30.3855$$

$$P_2 = 1.82\ \times 10^{-21}\ mmHg \exp\ (30.3855)$$

$$P_2 =\ 2.86\ \times 10^{-8}\ mmHg$$

13 Appendix IV: Full Micrograph Sets of Chapter 7

13.1 Alkali Metal Concentration

13.1.1 Li

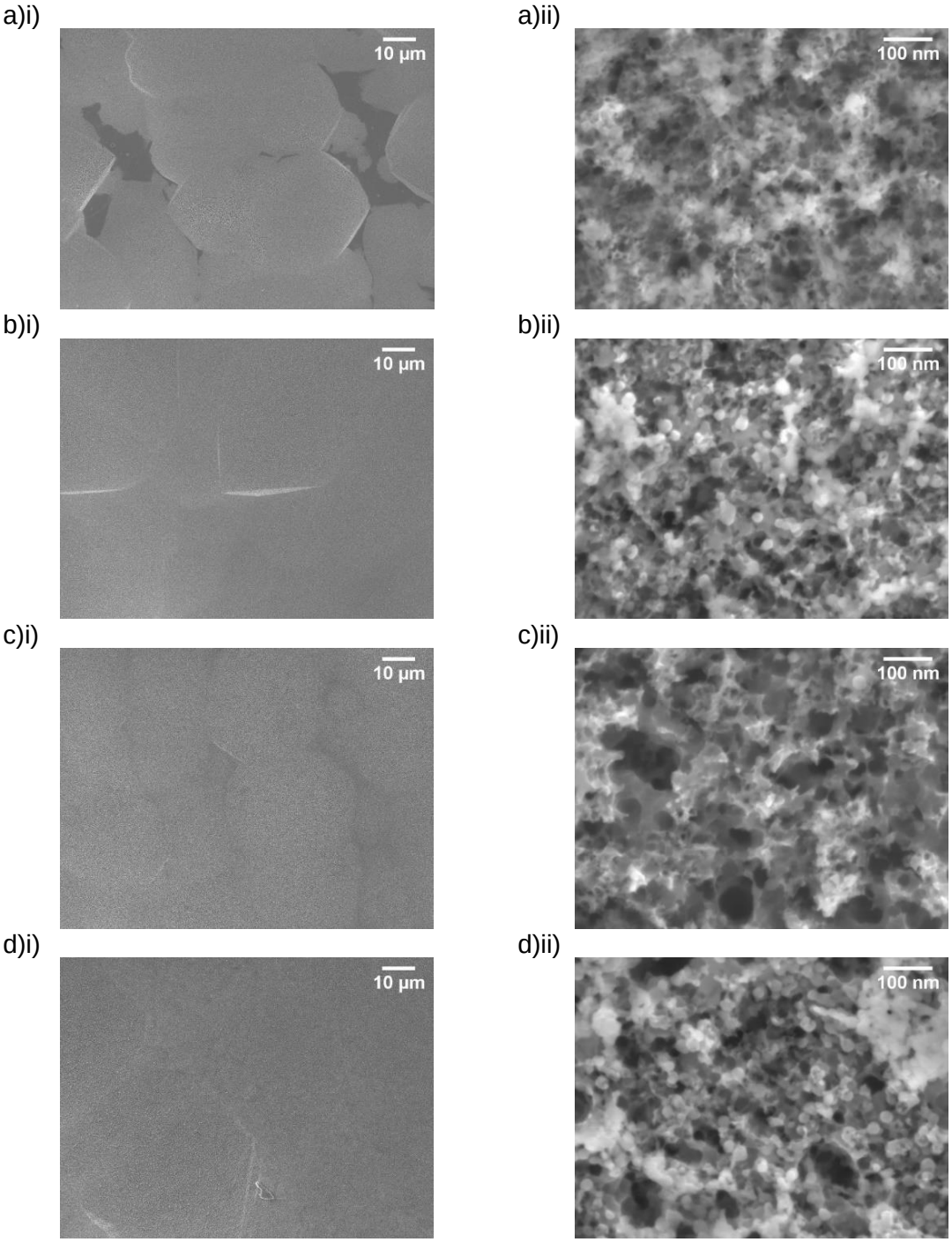

Figure 13.1 Microstructures in a top-down view of varying Li concentration in the precursor by a) 0.0017 M, b) 0.0033 M, c) 0.0047 M, d) 0.0084 M at i) low-magnification and ii) high-magnification.

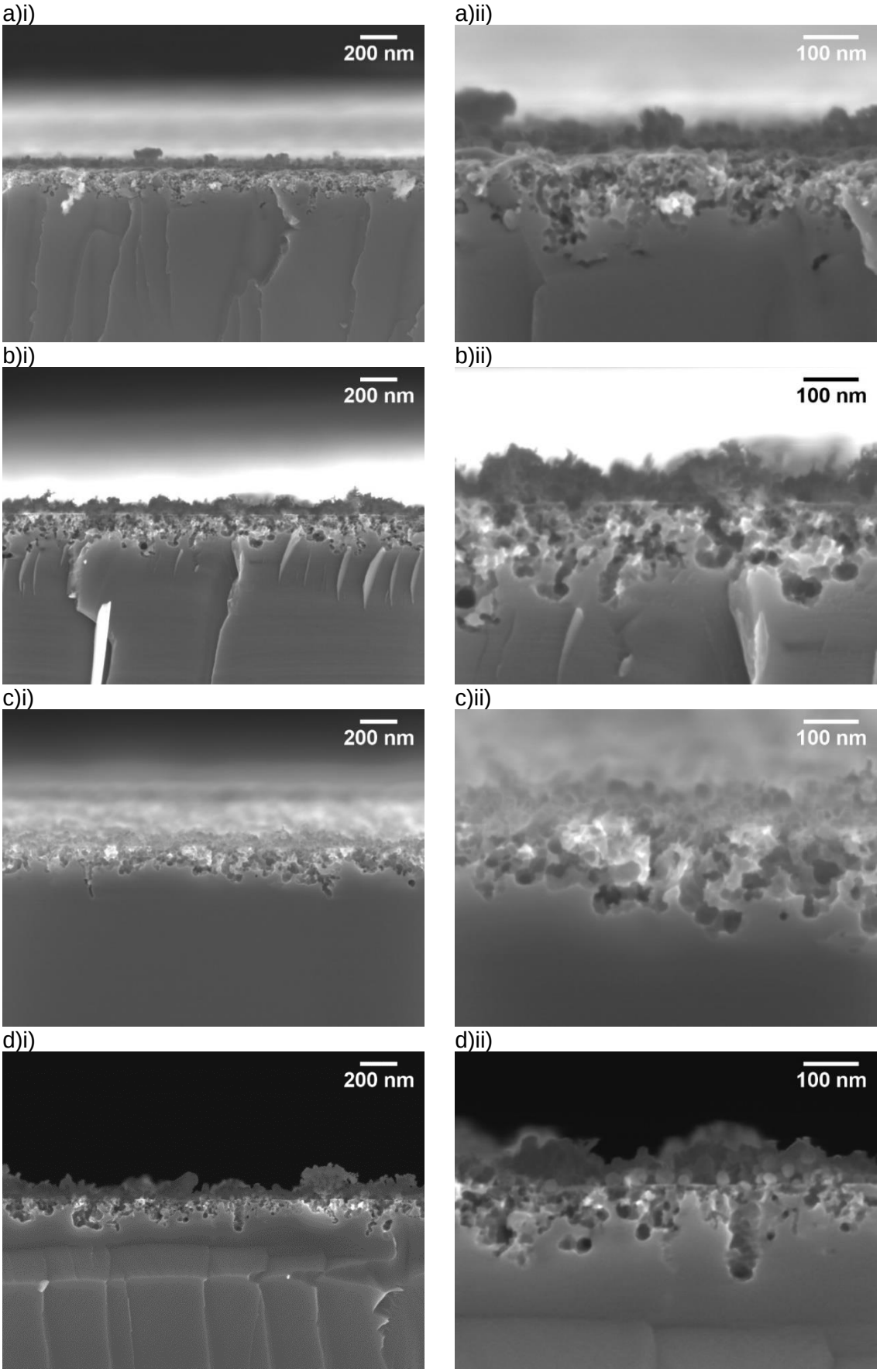

Figure 13.2 Microstructures in a cross-sectional view as a function of varying Li concentration by a) 0.0017 M, b) 0.0033 M, c) 0.0047 M, d) 0.0084 M at i) low-magnification and ii) high-magnification.

13.1.2 Na

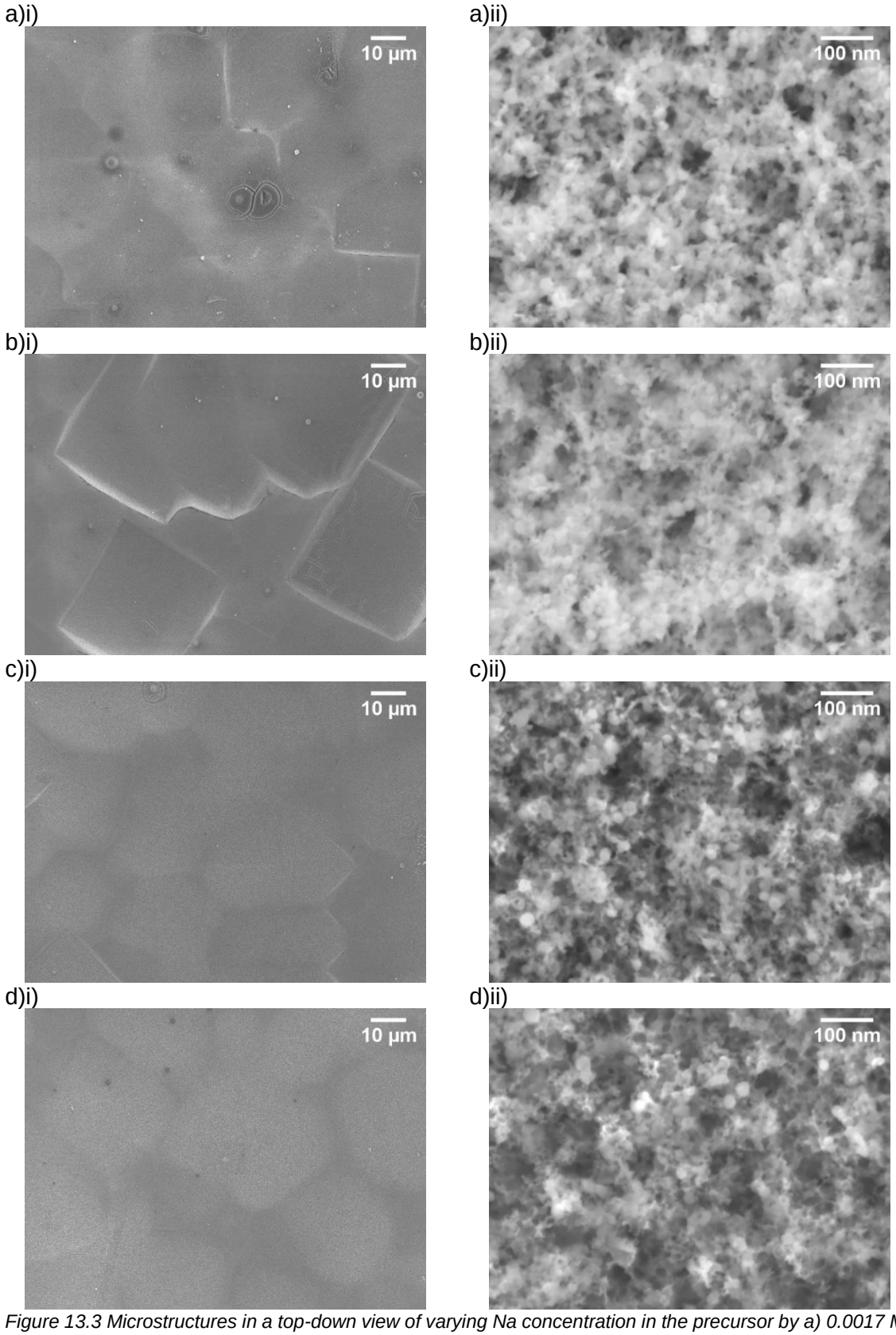

Figure 13.3 Microstructures in a top-down view of varying Na concentration in the precursor by a) 0.0017 M, b) 0.0033 M, c) 0.0047 M, d) 0.0084 M at i) low-magnification and ii) high-magnification.

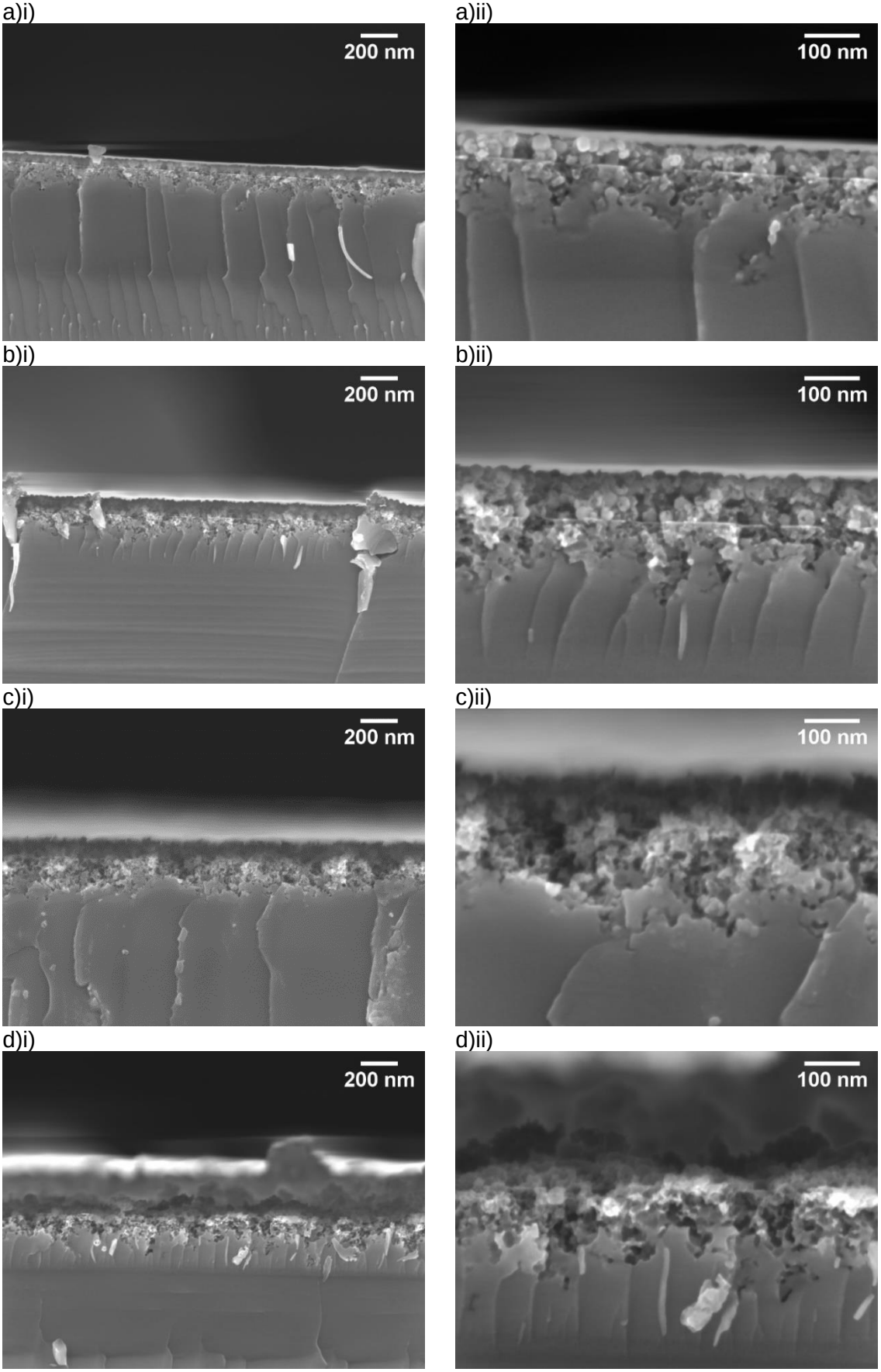

Figure 13.4 Microstructures in a cross-sectional view as a function of varying Na concentration by a) 0.0017 M, b) 0.0033 M, c) 0.0047 M, d) 0.0084 M at i) low-magnification and ii) high-magnification.

13.1.3 K

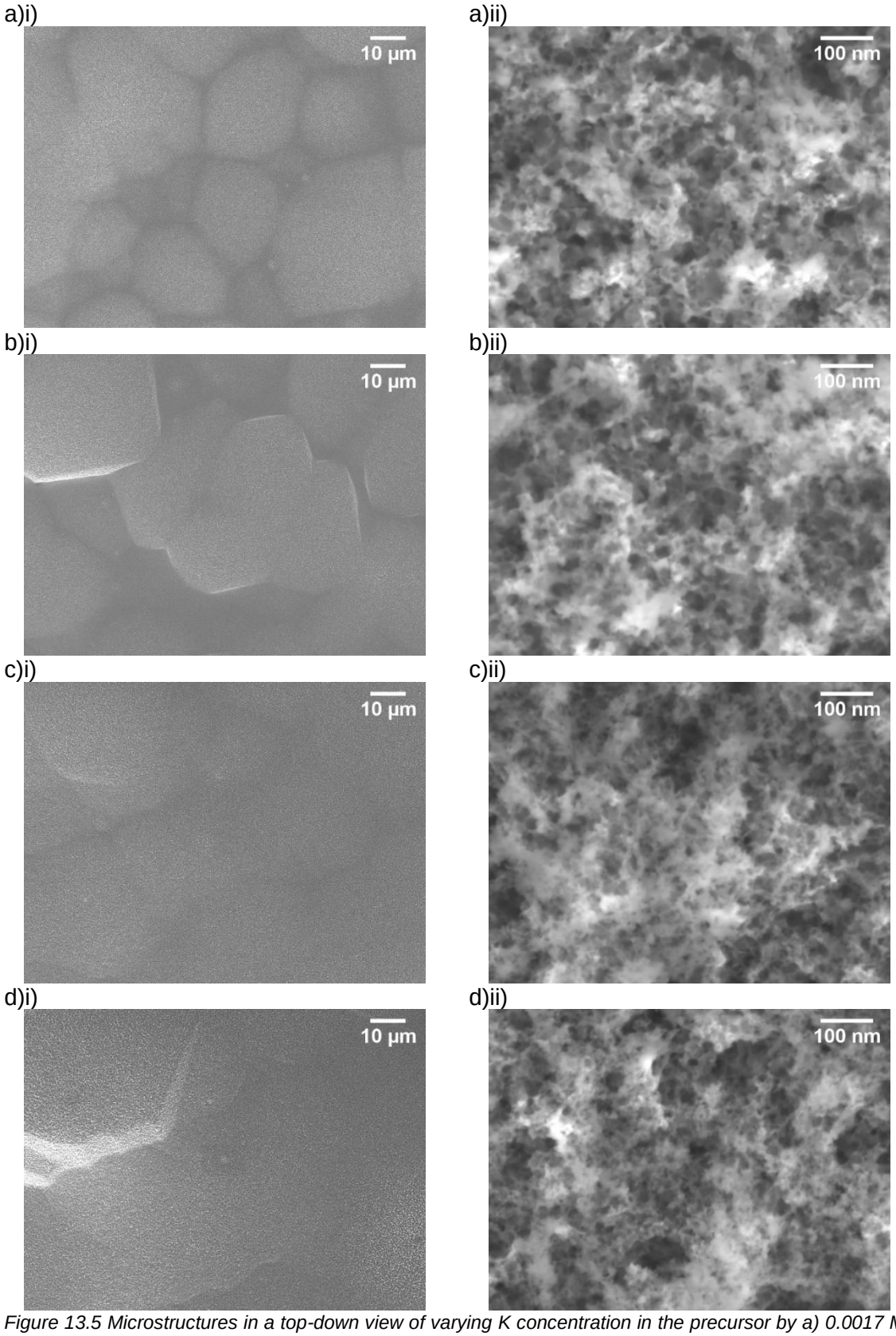

Figure 13.5 Microstructures in a top-down view of varying K concentration in the precursor by a) 0.0017 M, b) 0.0033 M, c) 0.0047 M, d) 0.0084 M at i) low-magnification and ii) high-magnification.

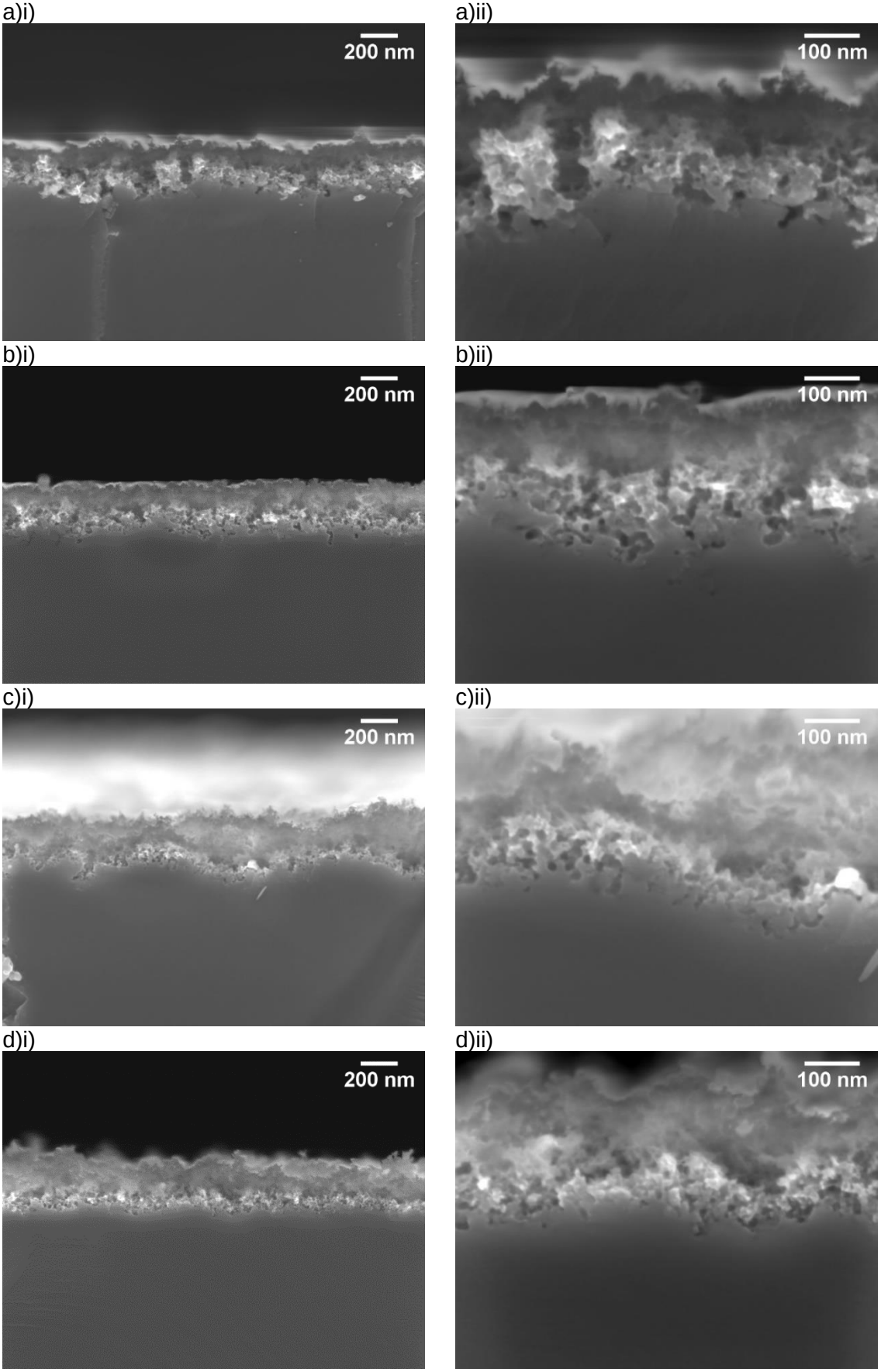

Figure 13.6 Microstructures in a cross-sectional view as a function of varying K concentration by a) 0.0017 M, b) 0.0033 M, c) 0.0047 M, d) 0.0084 M at i) low-magnification and ii) high-magnification.

13.1.4 Cs

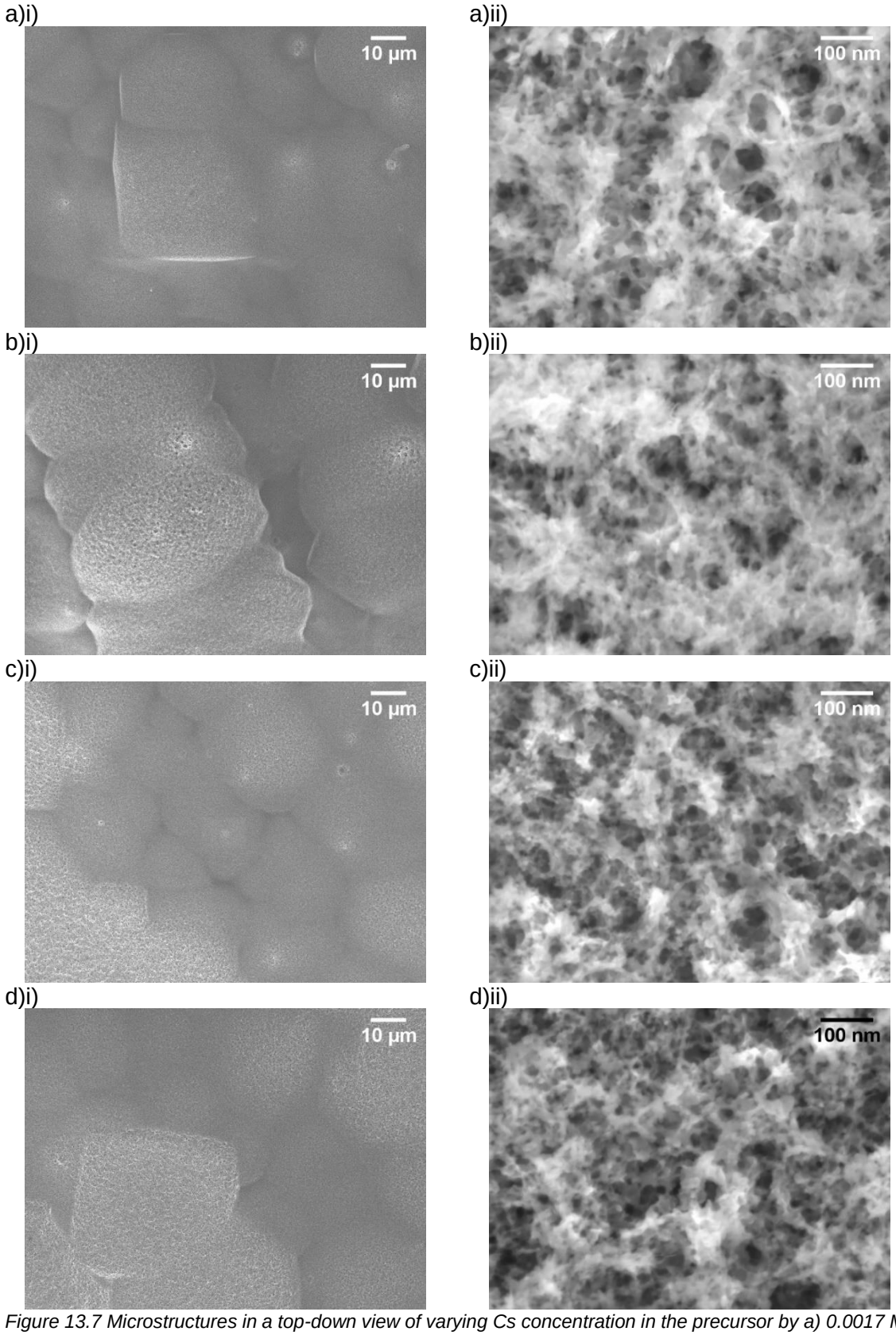

Figure 13.7 Microstructures in a top-down view of varying Cs concentration in the precursor by a) 0.0017 M, b) 0.0033 M, c) 0.0047 M, d) 0.0084 M at i) low-magnification ii) high-magnification.

a)i)

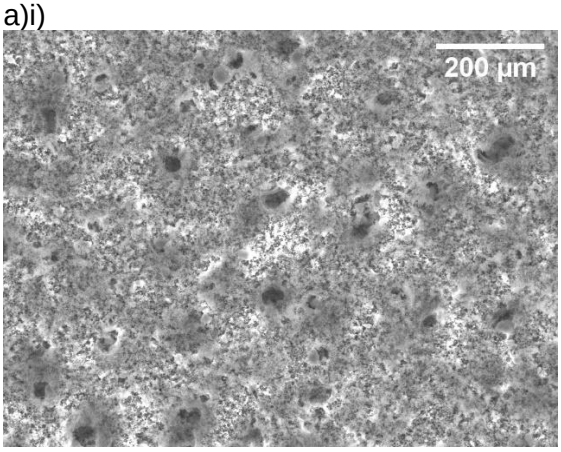

a)ii)

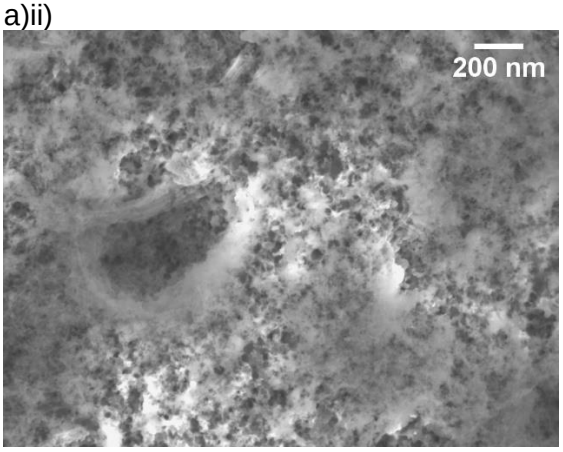

a)iii)

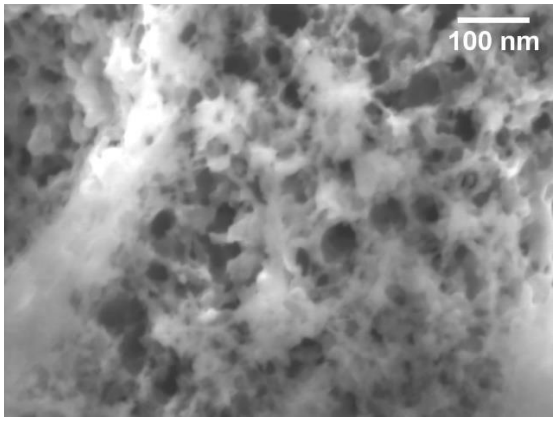

b)i)

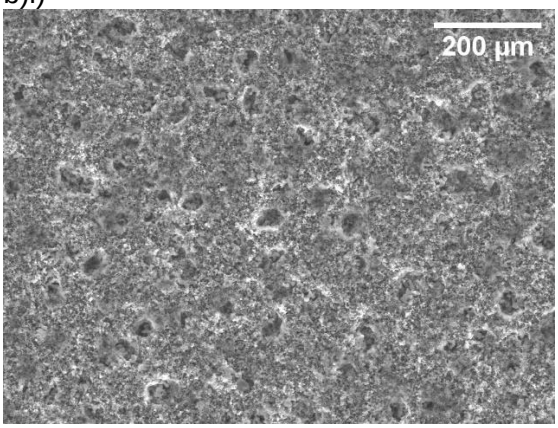

b)ii)

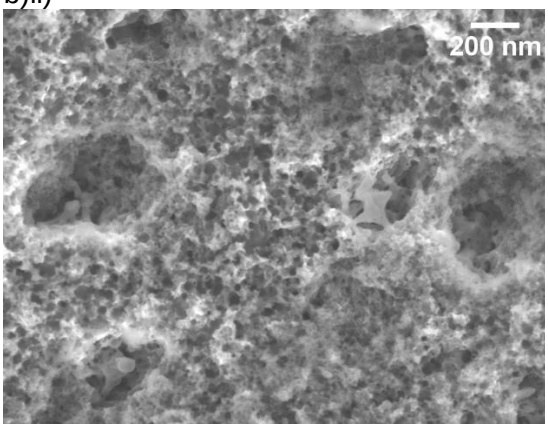

b)iii)

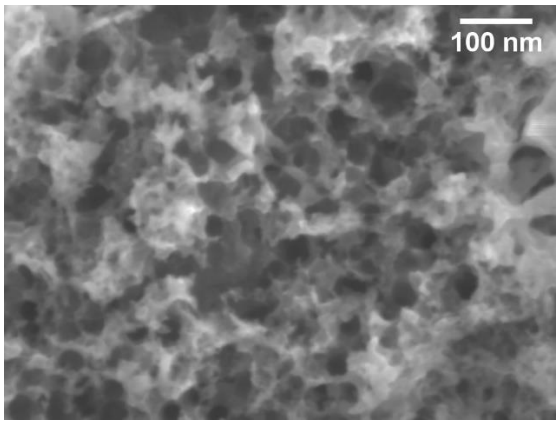

c)i)

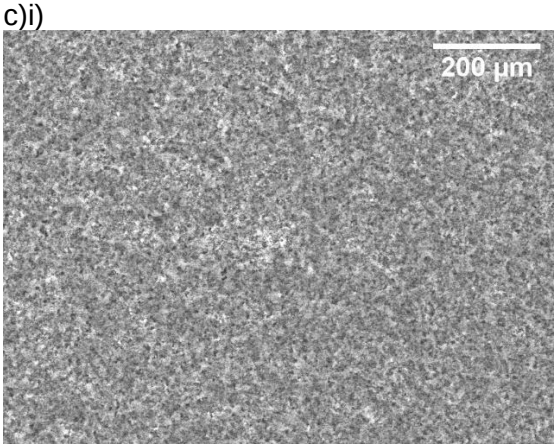

c)ii)

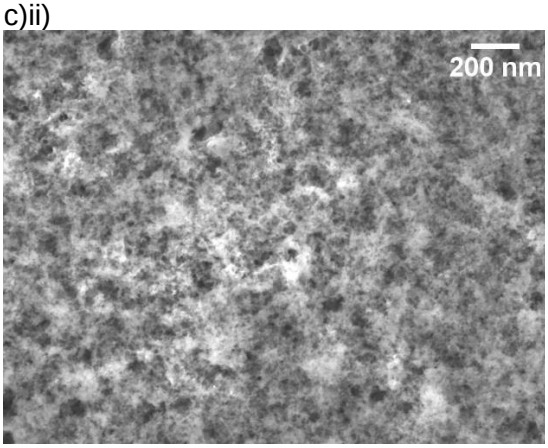

c)iii)

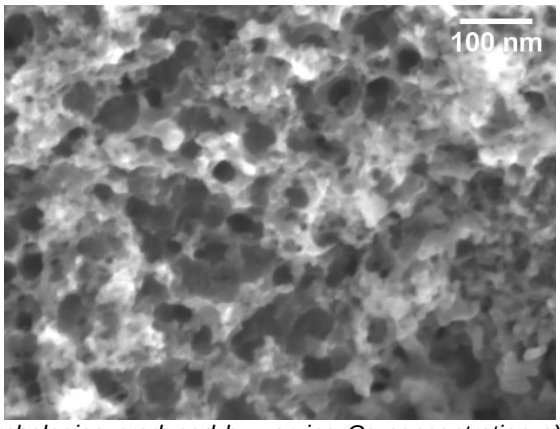

Figure 13.8 Additional morphologies produced by varying Cs concentration a) 0.0033 M b) 0.0047 M c) 0.0084 M at i) low-magnification ii) intermediate-magnification iii) high-magnification.

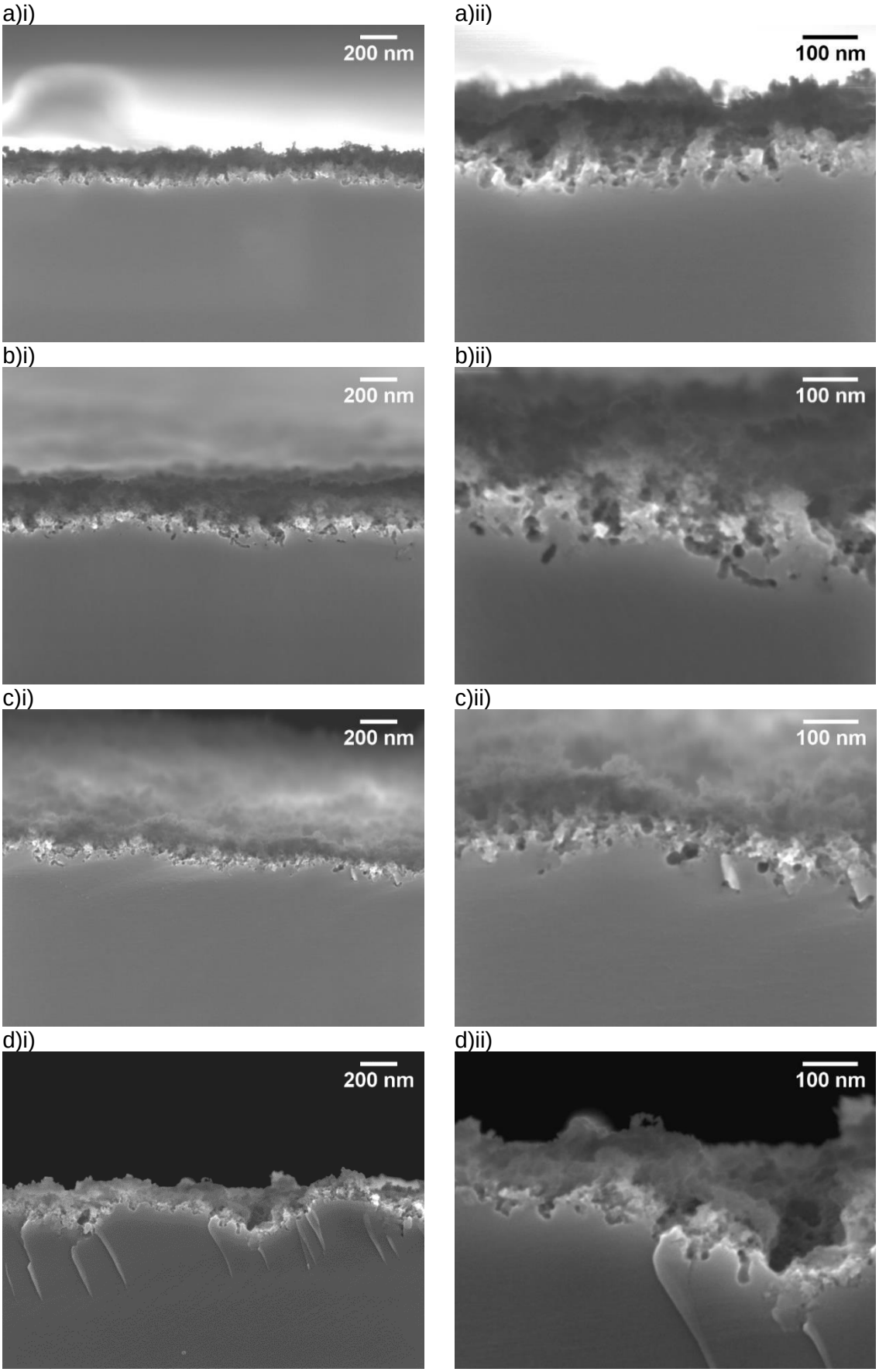

Figure 13.9 Microstructures in a cross-sectional view as a function of varying Cs concentration by a) 0.0017 M, b) 0.0033 M, c) 0.0047 M, d) 0.0084 M at i) low-magnification and ii) high-magnification.

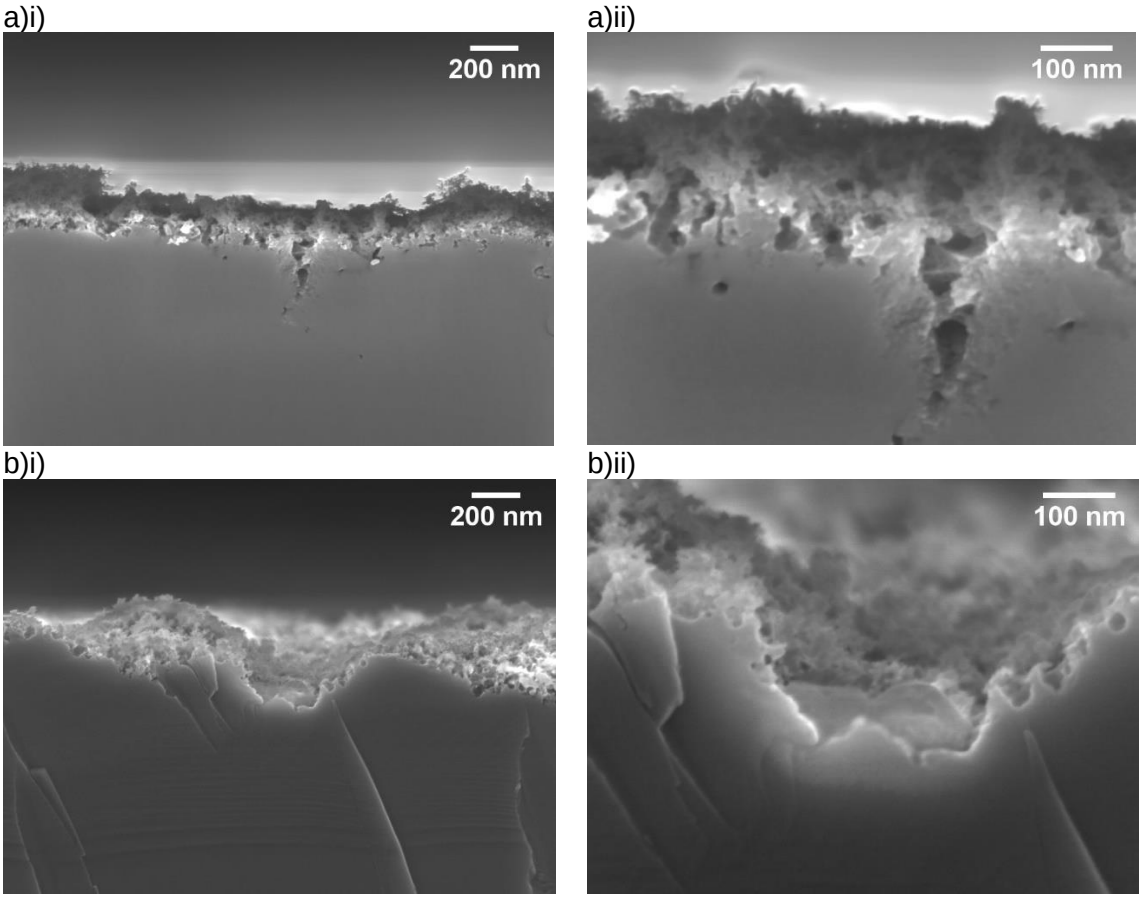

Figure 13.10 Additional morphologies produced by varying Cs concentration a) 0.0033 M b) 0.0084 M at i) low-magnification and ii) high-magnification.

13.2 Sample Temperature

13.2.1 50 °C

a)i)

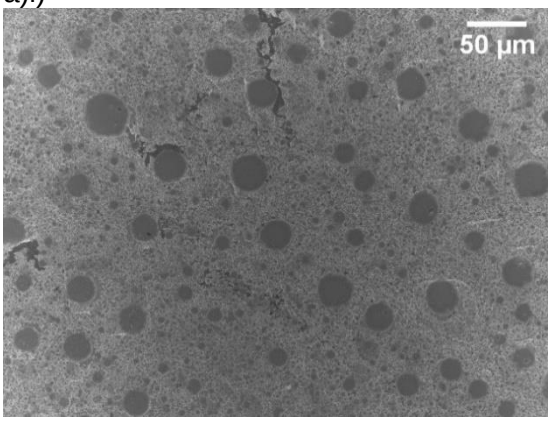

a)ii)

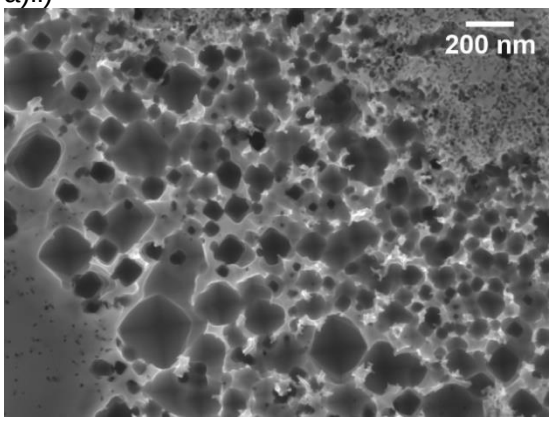

b)i)

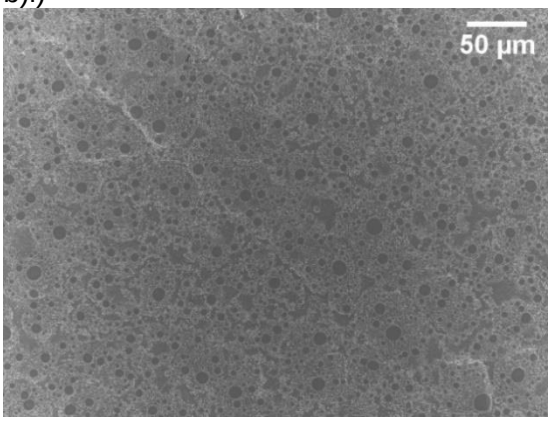

b)ii)

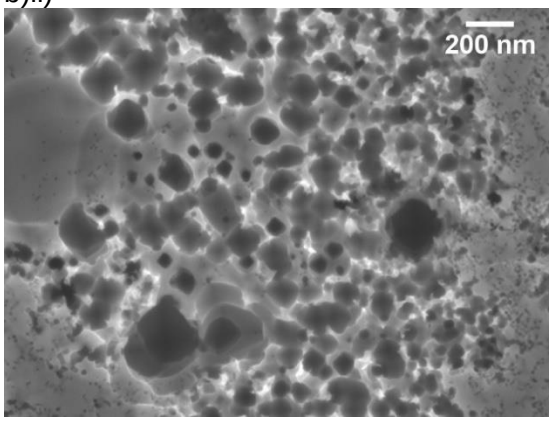

b)iii)

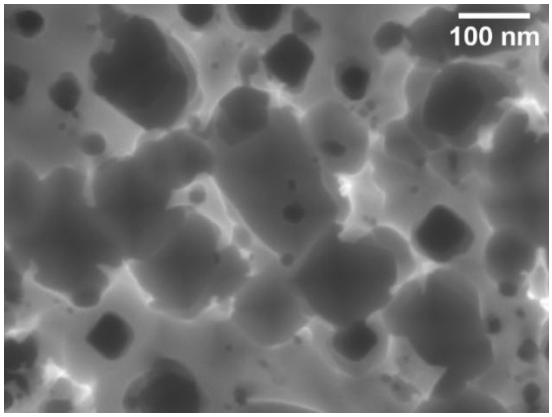

c)i)

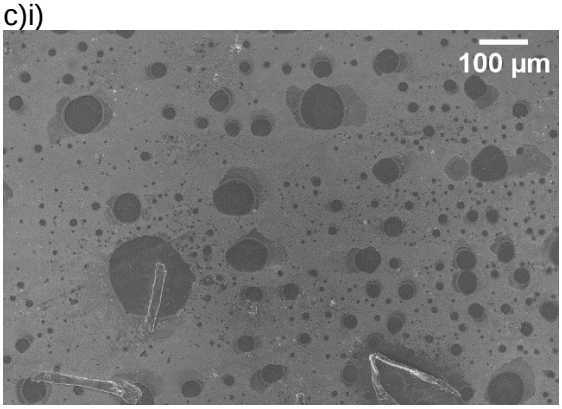

c)ii)

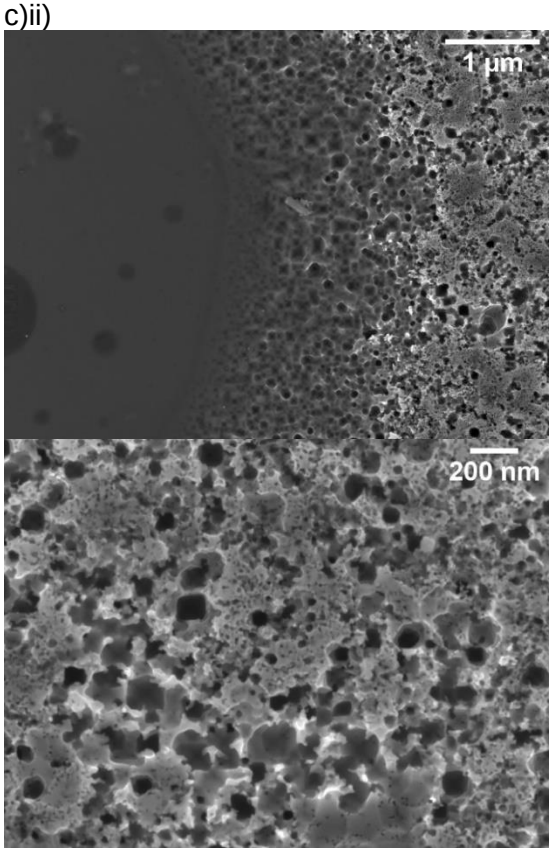

c)iii)

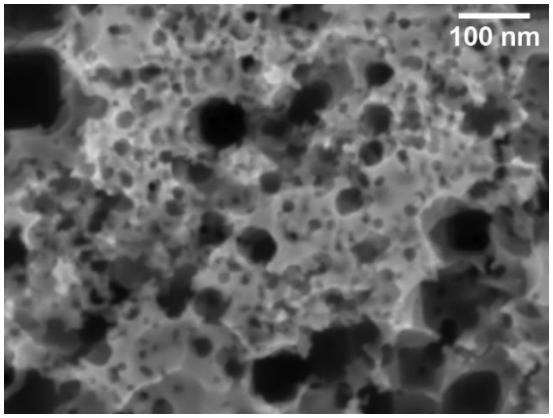

Figure 13.11 Microstructures produced at 50 °C sample processing temperature using the different alkali metals a) Li b) Na c) Cs at i) low-magnification ii) intermediate-magnification iii) high-magnification.

a)i)

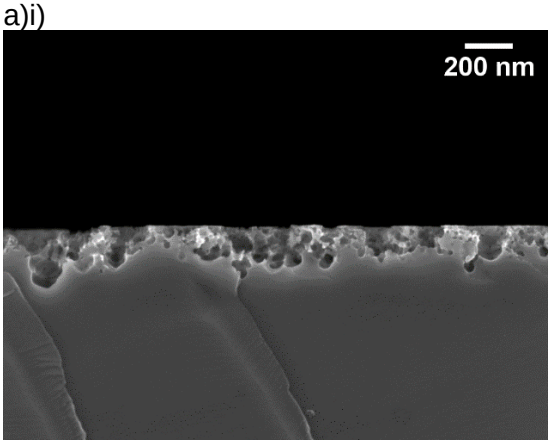

a)ii)

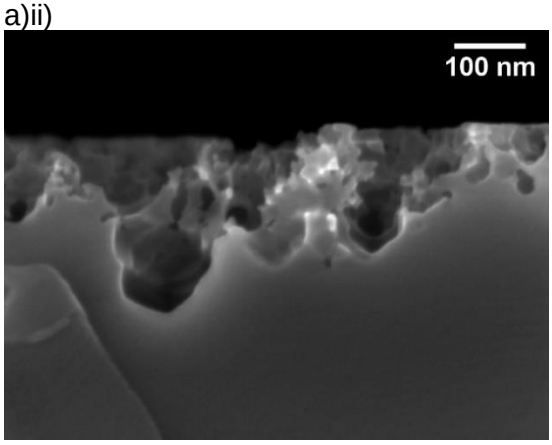

b)i)

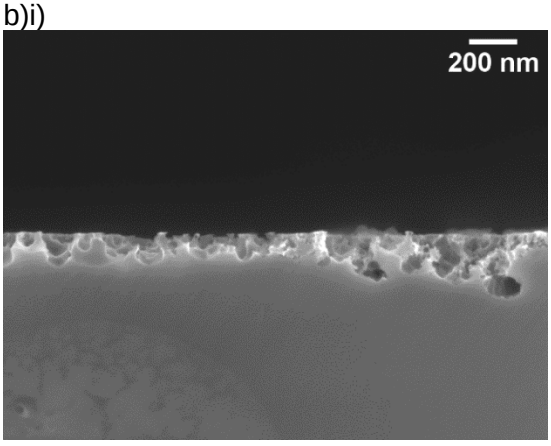

b)ii)

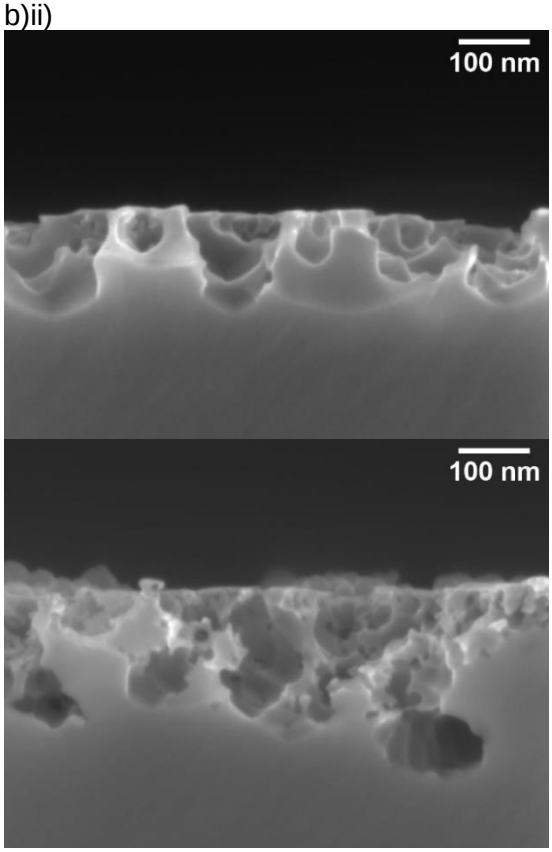

c)i)

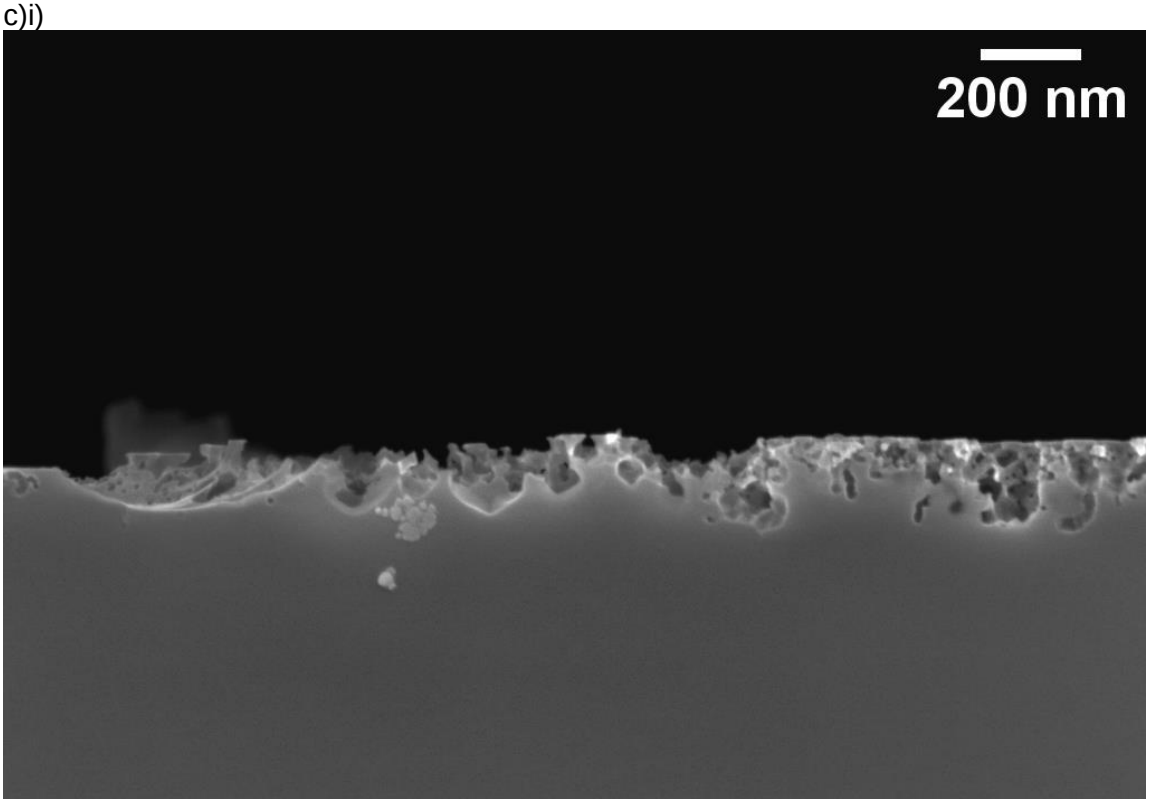

Figure 13.12 Microstructures produced at 50 °C sample processing temperature using the different alkali metals a) Li b) Na c) Cs at i) low-magnification ii) high-magnification.

13.2.2 100 °C

a)i)

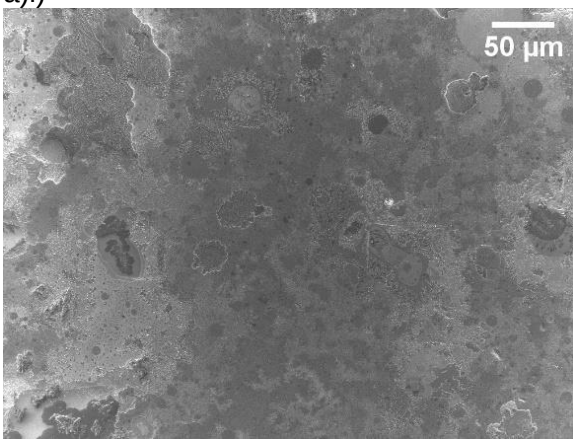

a)ii)

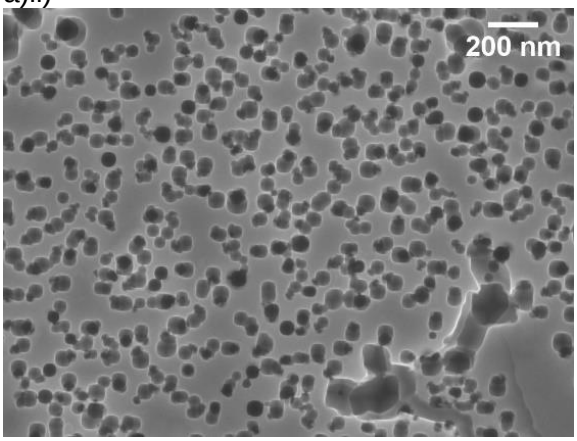

b)i)

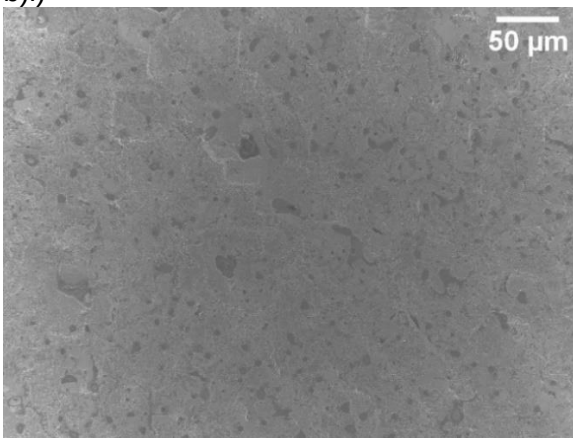

b)ii)

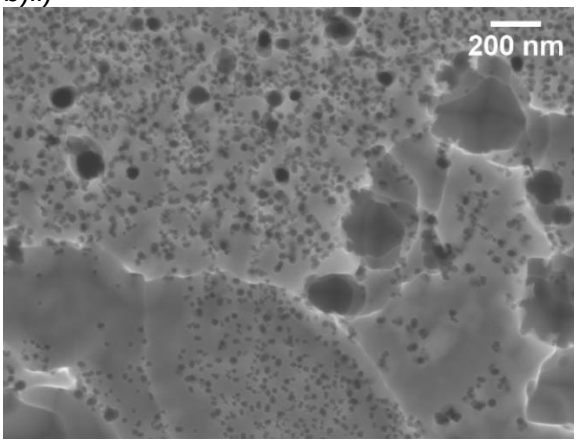

b)iii)

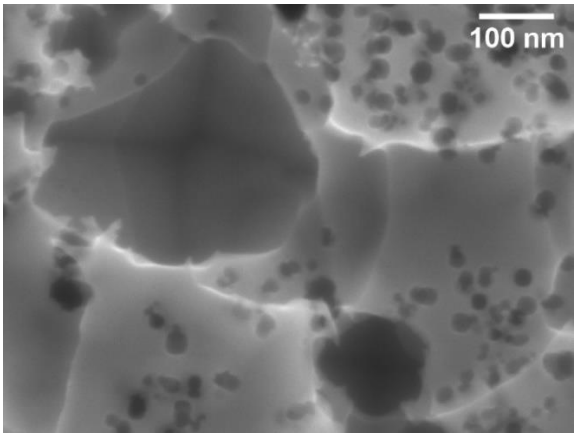

c)i) c)ii)

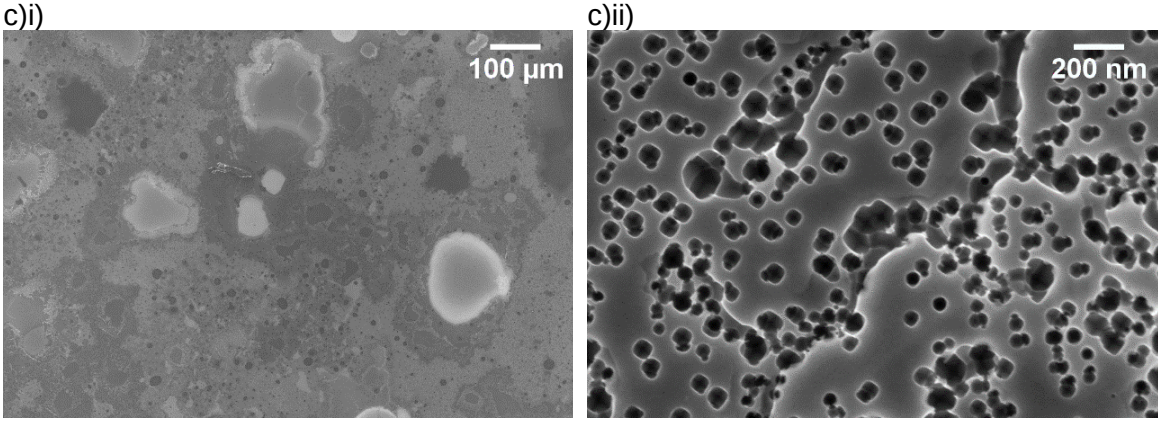

Figure 13.13 Microstructures produced at 100 °C sample processing temperature using the different alkali metals a) Li b) Na c) Cs at i) low-magnification ii) intermediate-magnification iii) high-magnification.

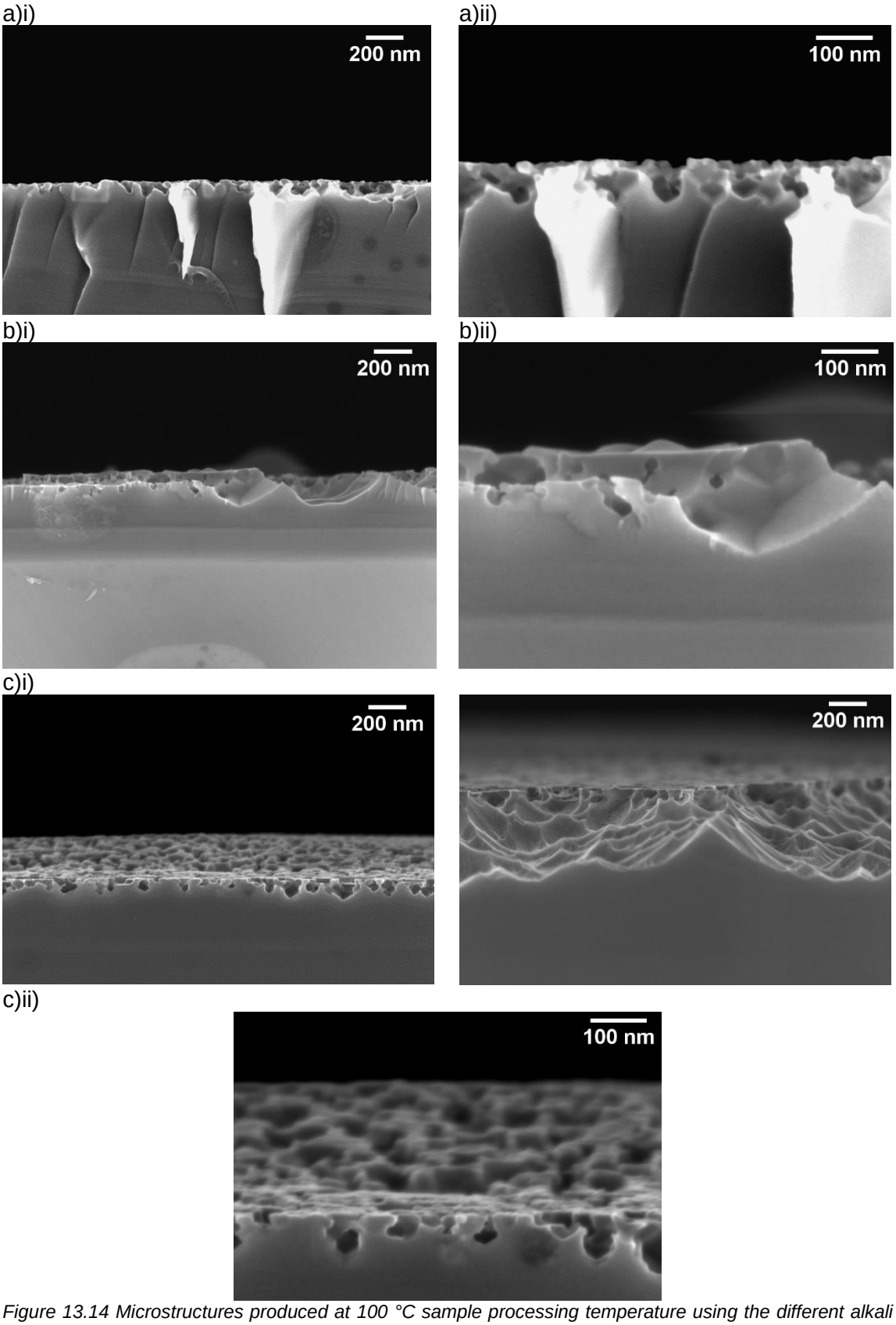

Figure 13.14 Microstructures produced at 100 °C sample processing temperature using the different alkali metals a) Li b) Na c) Cs at i) low-magnification ii) high-magnification.

13.2.3 150 °C

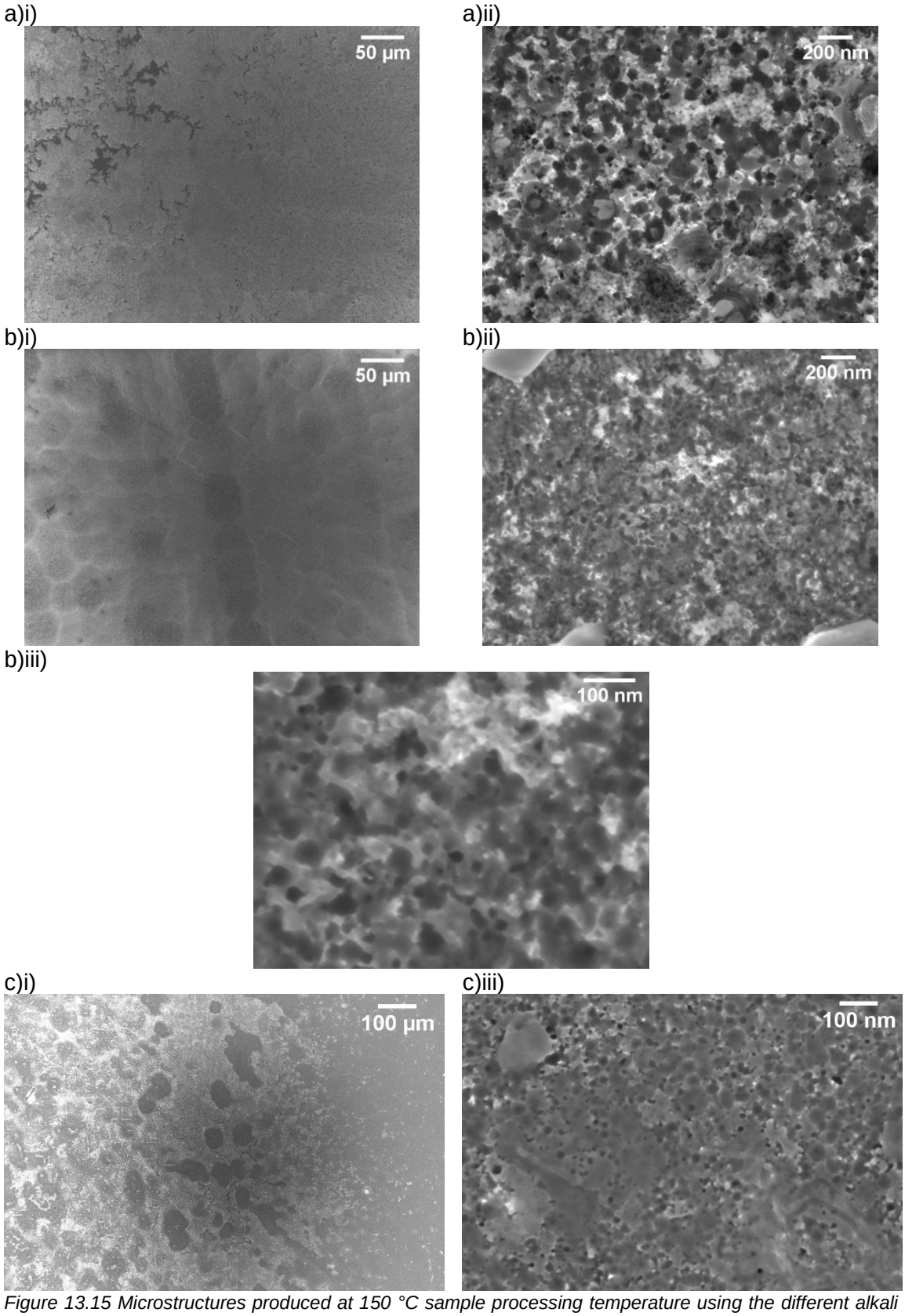

Figure 13.15 Microstructures produced at 150 °C sample processing temperature using the different alkali metals a) Li b) Na c) Cs at i) low-magnification ii) intermediate-magnification iii) high-magnification.

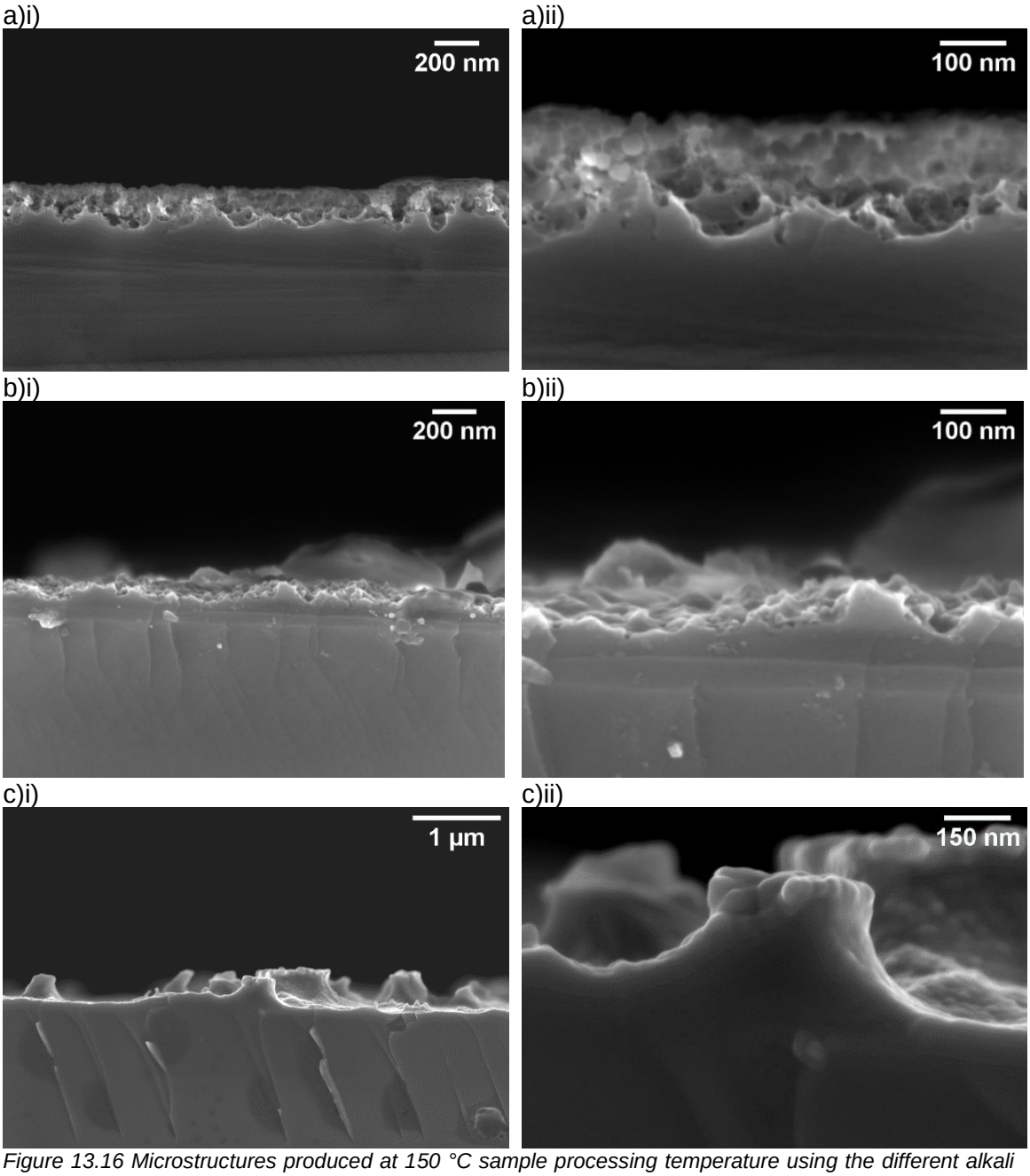

Figure 13.16 Microstructures produced at 150 °C sample processing temperature using the different alkali metals a) Li b) Na c) Cs at i) low-magnification ii) high-magnification.

13.2.4 200 °C

a)i)

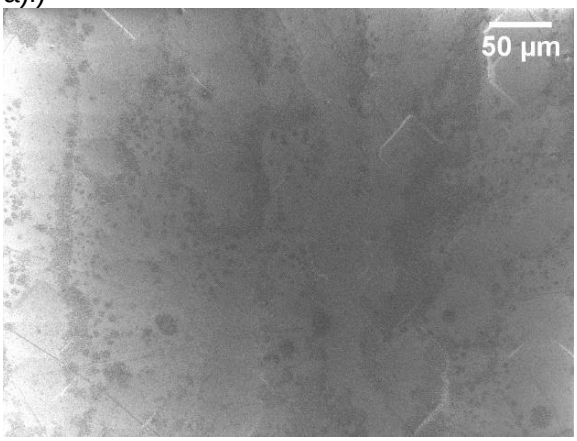

a)ii)

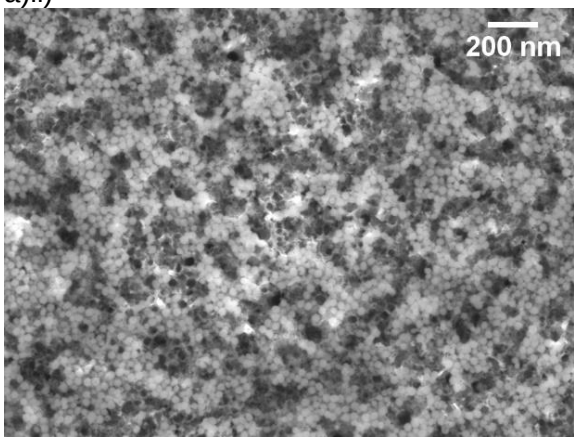

a)iii)

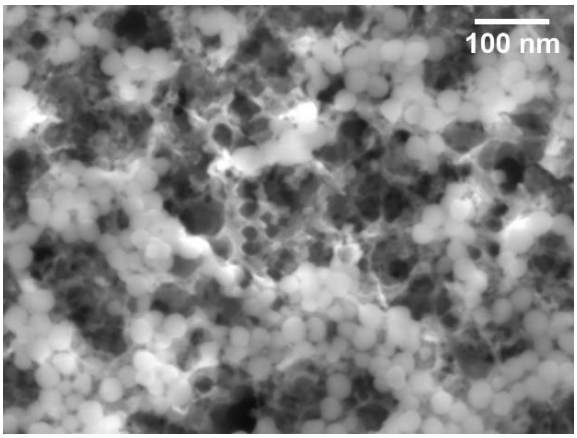

b)i)

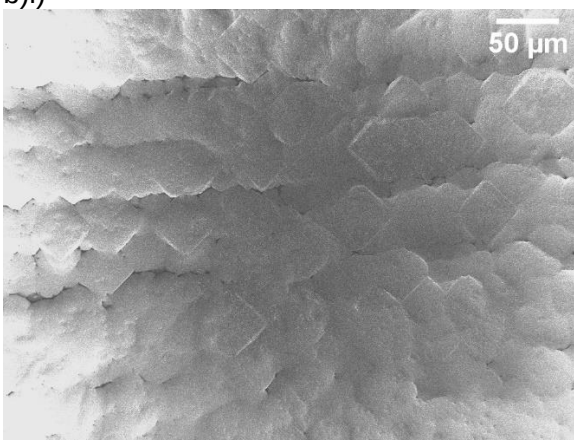

b)ii)

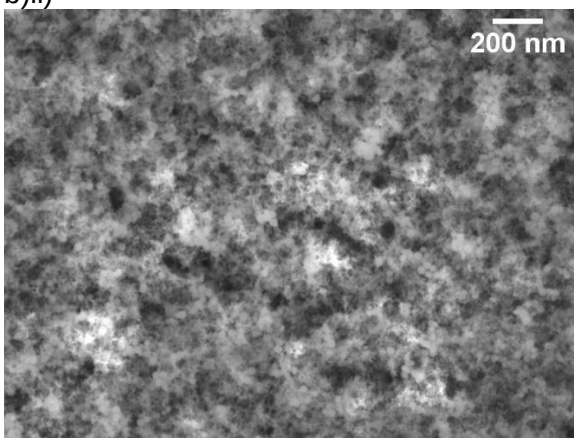

b)iii)

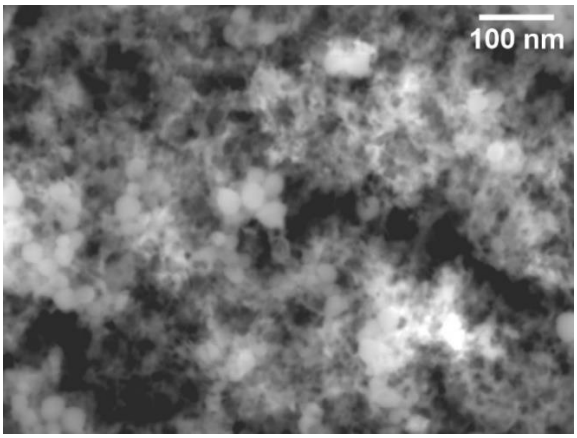

c)i)

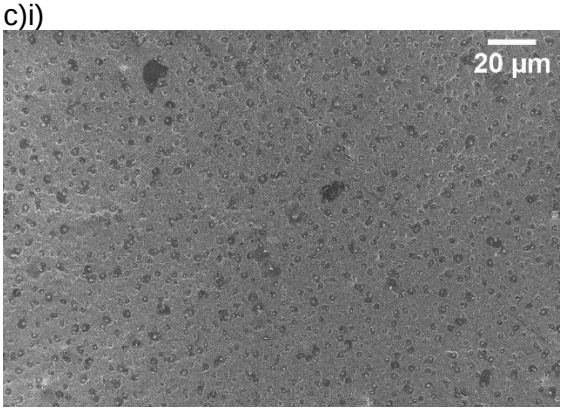

c)ii)

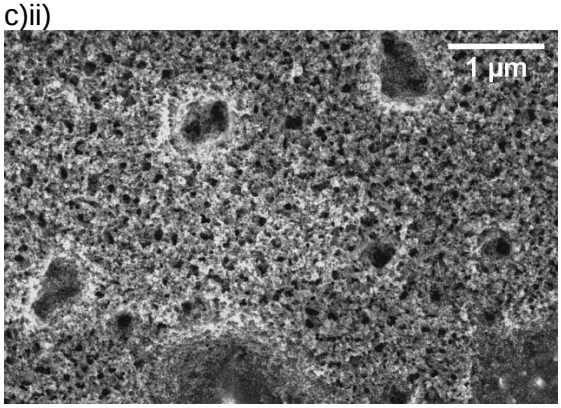

c)iii)

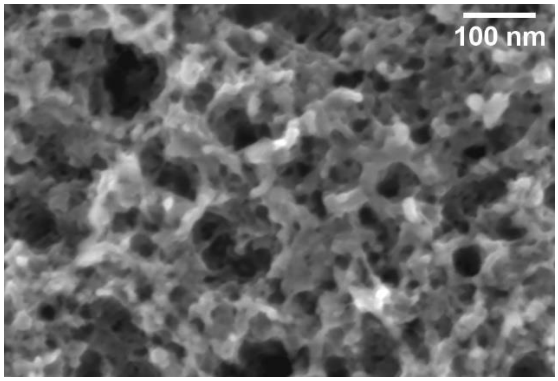

Figure 13.17 Microstructures produced at 200 °C sample processing temperature using the different alkali metals a) Li b) Na c) Cs at i) low-magnification ii) intermediate-magnification iii) high-magnification.

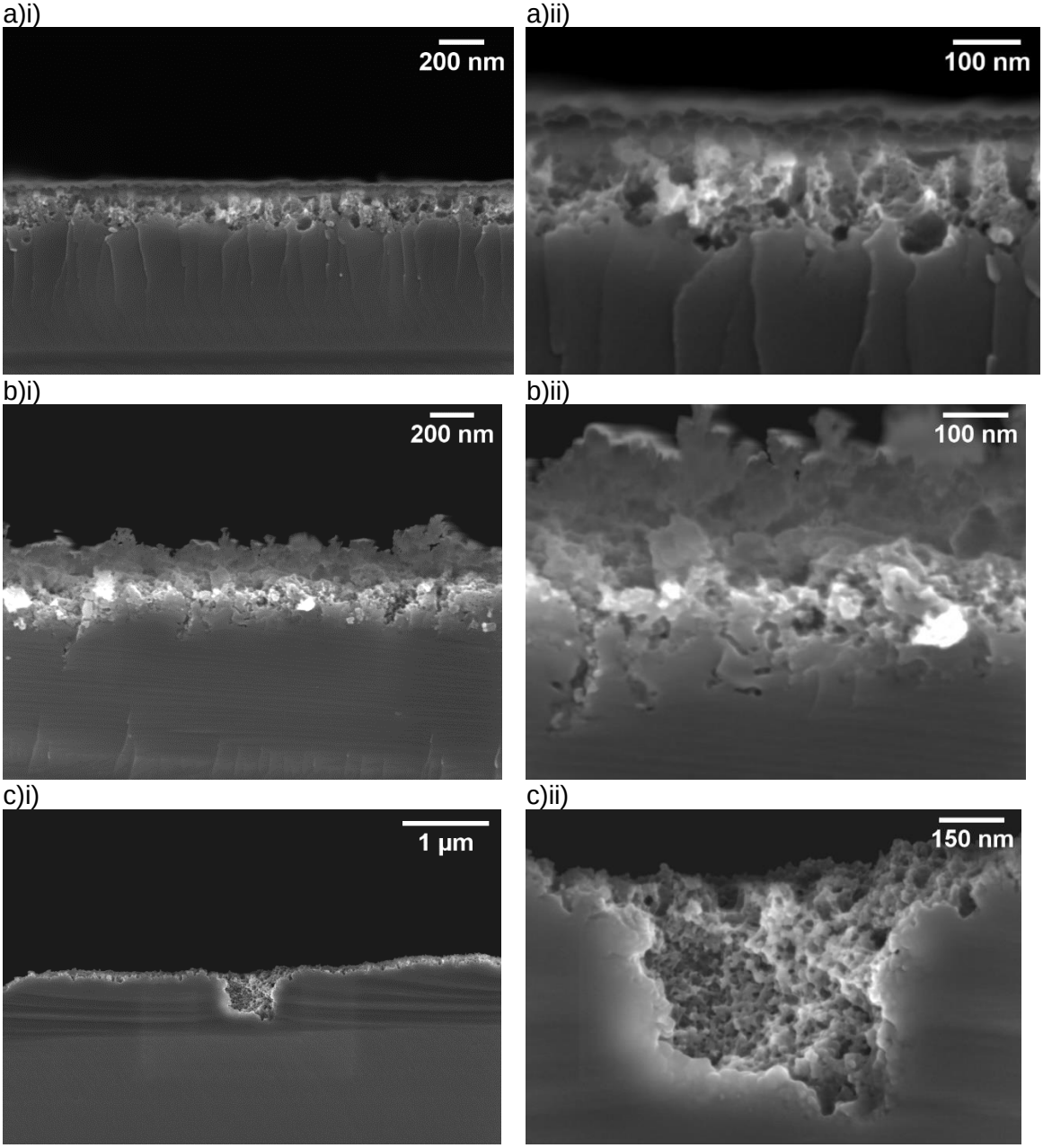

Figure 13.18 Microstructures produced at 200 °C sample processing temperature using the different alkali metals a) Li b) Na c) Cs at i) low-magnification ii) high-magnification.

13.2.5 250 °C

a)i)

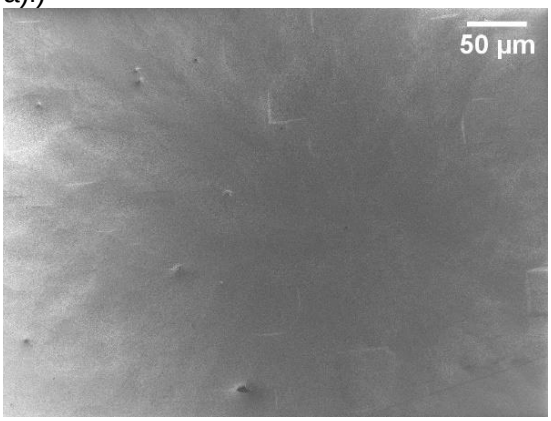

a)ii)

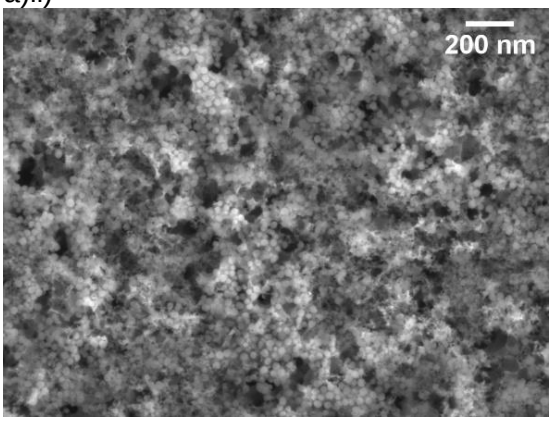

a)iii)

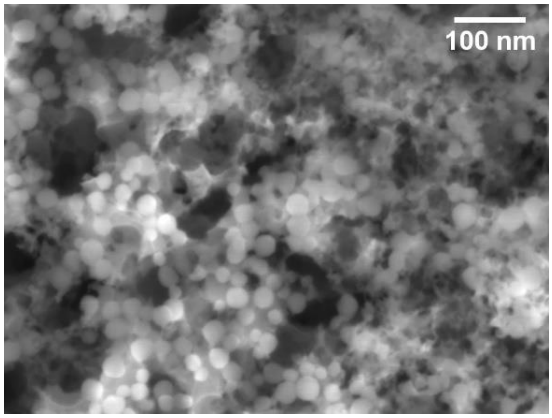

b)i)

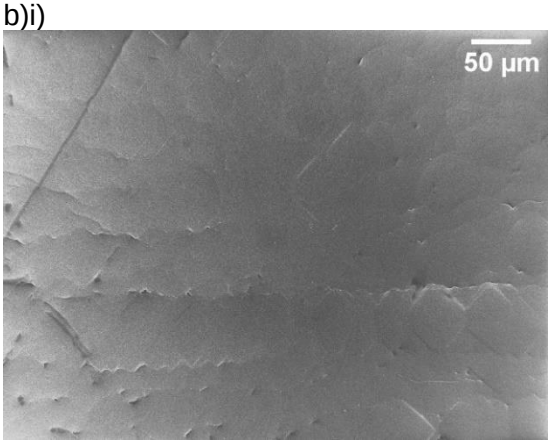

b)ii)

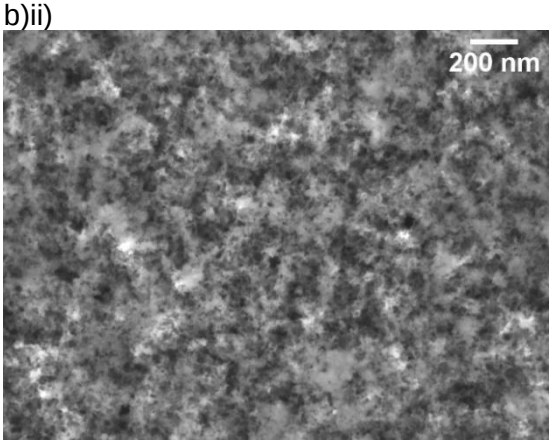

b)iii)

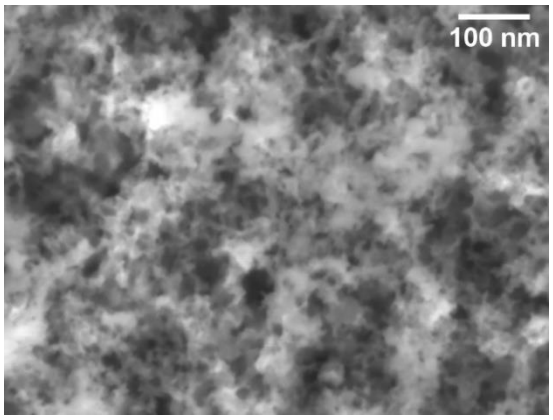

c)i)

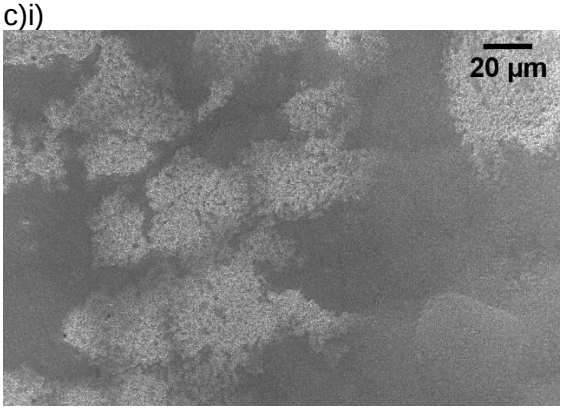

c)ii)

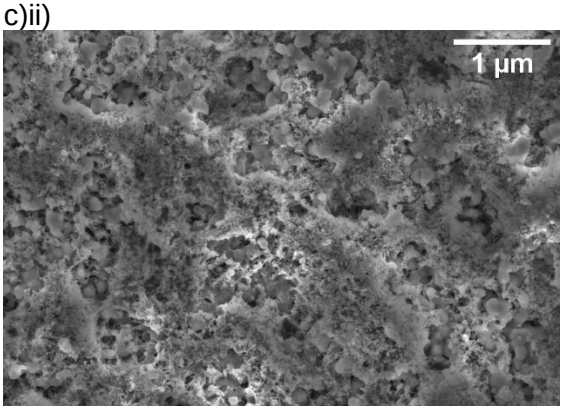

c)iii)

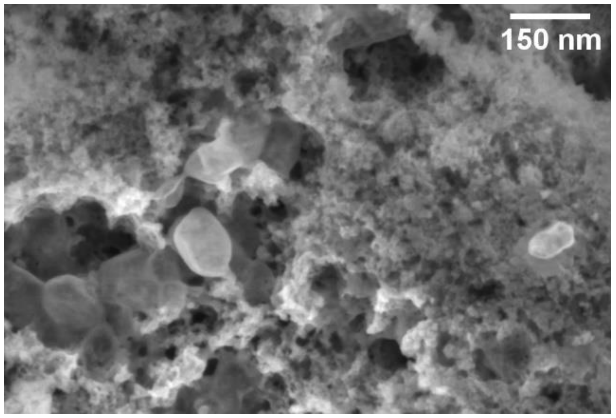

Figure 13.19 Microstructures produced at 250 °C sample processing temperature using the different alkali metals a) Li b) Na c) Cs at i) low-magnification ii) intermediate-magnification iii) high-magnification.

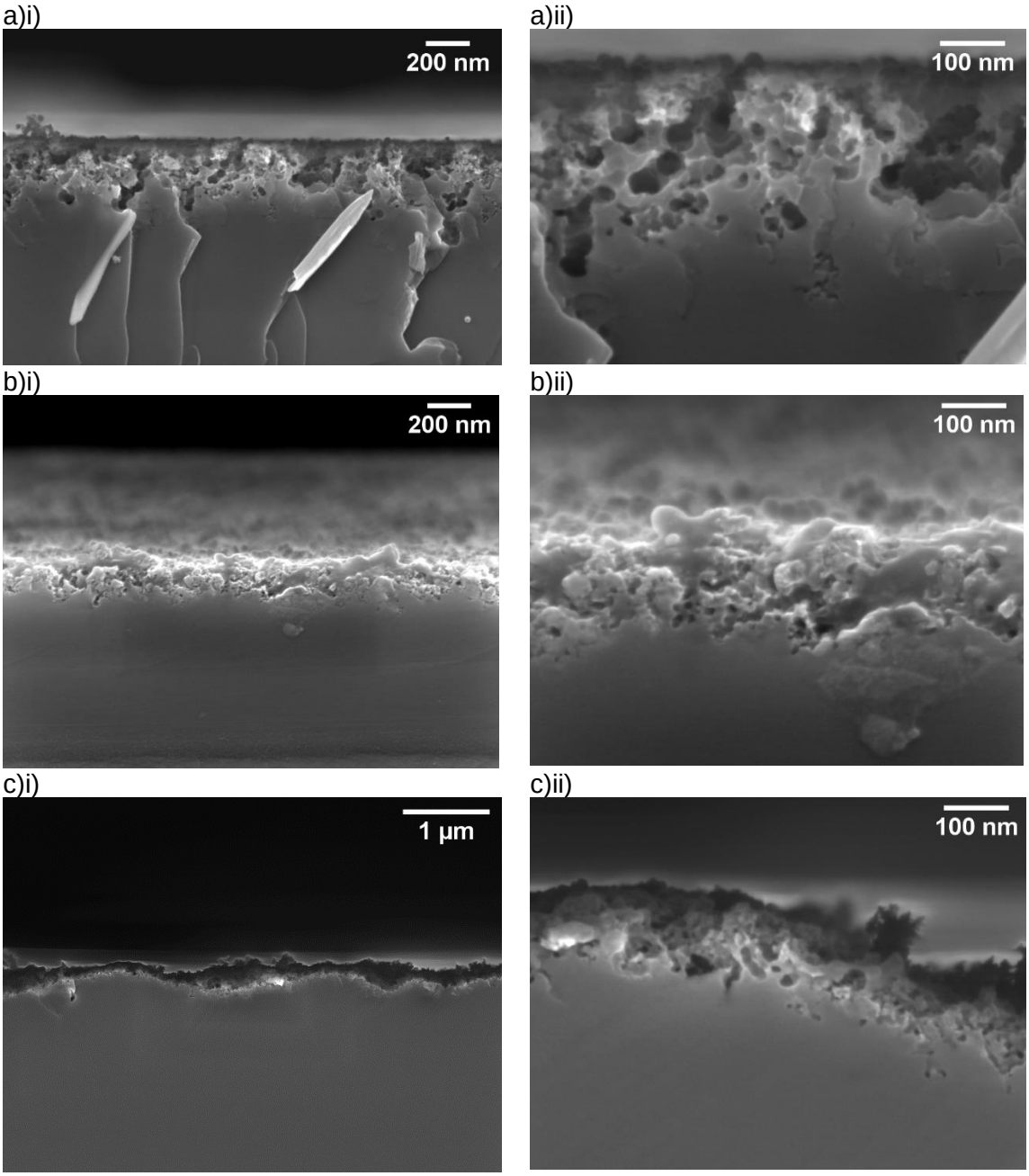

Figure 13.20 Microstructures produced at 250 °C sample processing temperature using the different alkali metals a) Li b) Na c) Cs at i) low-magnification ii) high-magnification.

13.3 O_3 concentration

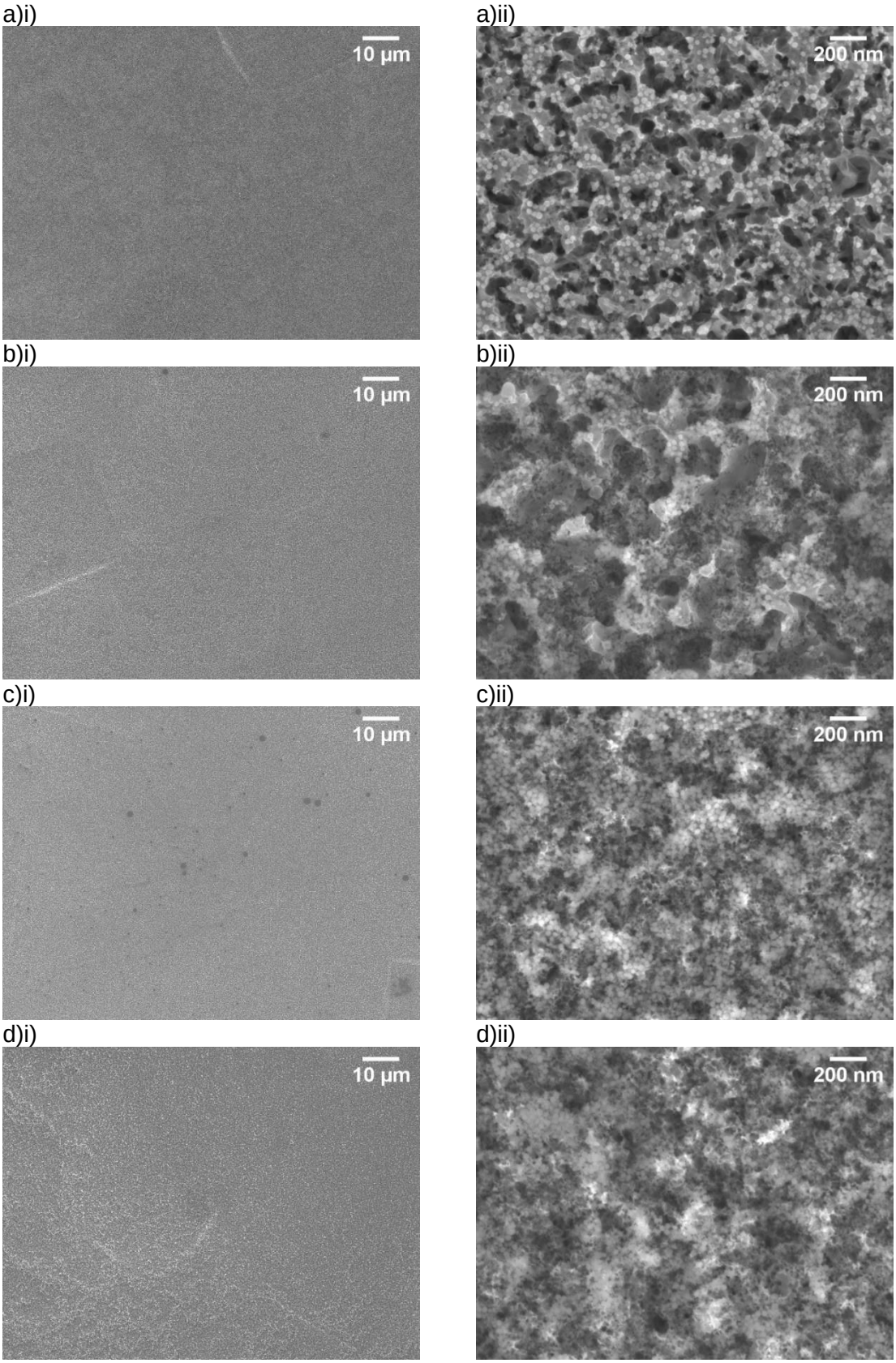

Figure 13.21 Samples textured with a) 10 % b) 20 % c) 40 % d) 70 % O_3 at i) low-magnification ii) high-magnification.

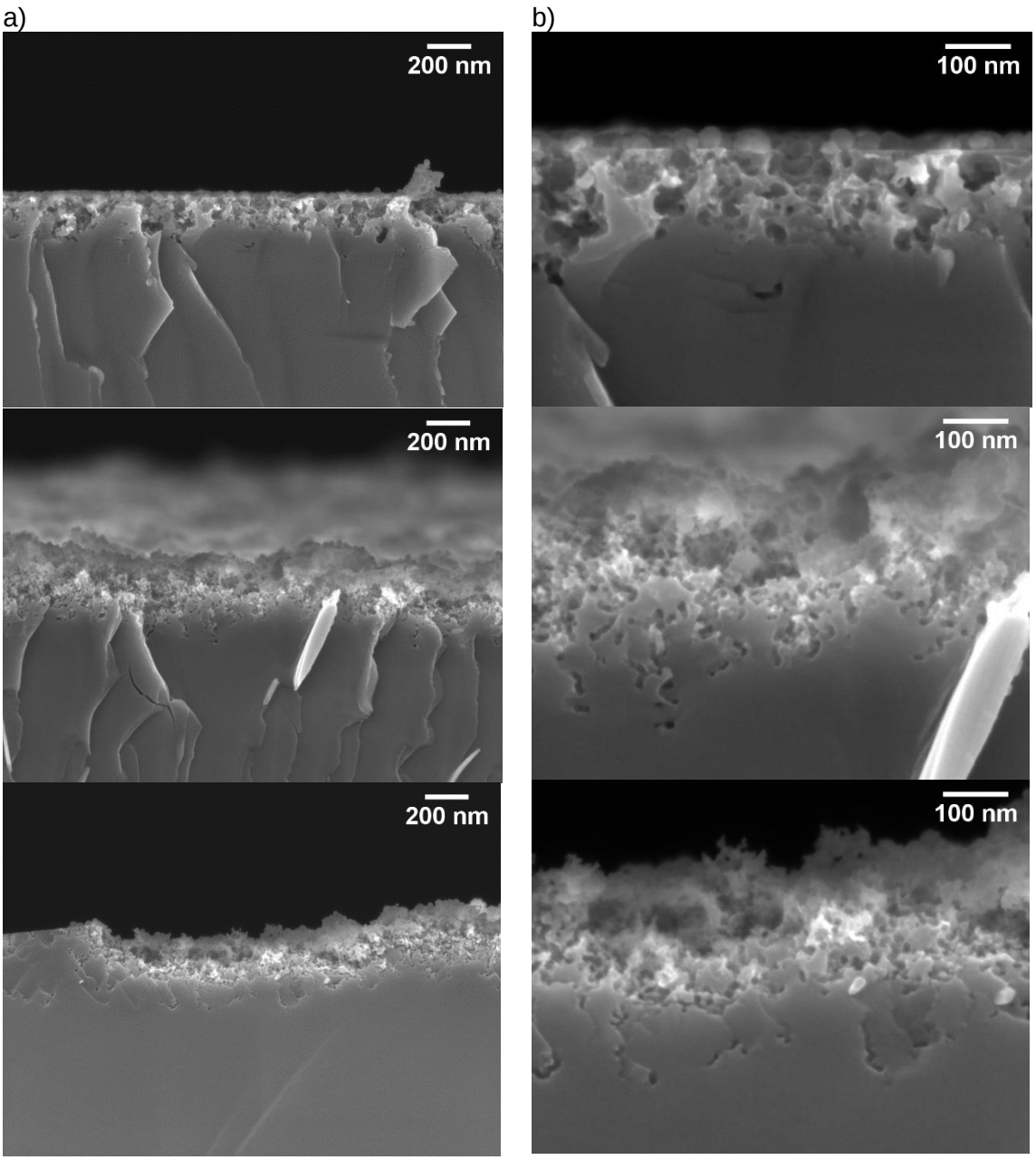

Figure 13.22 Cross-section morphology when samples were textured with 20 % O_3 concentration at a) low-magnification and b) high-magnification.

14 References

[1] I. P. on C. C. (IPCC), “Climate Change 2022: Impacts, Adaptation and Vulnerability Summary for Policymakers,” 2022.

[2] V. Smil, *Energy Transitions: Global and National Perspectives*, 2nd ed. ABC-CLIO, LLC, 2016.

[3] British Petroleum, “Statistical Review of World Energy globally consistent data on world energy markets . and authoritative publications in the field of energy,” *BP Energy Outlook 2021*, vol. 70, pp. 8–20, 2021.

[4] H. Ritchie, M. Roser, and P. Rosado, “Energy: Fossil Fuels,” *Our World in Data*, 2020. https://ourworldindata.org/fossil-fuels (accessed May 15, 2022).

[5] GISTEMP-Team, “GISS Surface Temperature Analysis (v4),” *NASA Goddard Institute for Space Studies*, 2022. https://data.giss.nasa.gov/gistemp/graphs_v4/ (accessed May 15, 2022).

[6] H. Ritchie, M. Roser, and P. Rosado, “Energy: Climate Change,” *Our World in Data*, 2020. https://ourworldindata.org/explorers/climate-change (accessed May 15, 2022).

[7] IRENA, *World energy transitions outlook: 1.5 degrees pathway*. 2021.

[8] J. D. Farmer and F. Lafond, “How predictable is technological progress?,” *Res Policy*, vol. 45, no. 3, pp. 647–665, 2016, doi: 10.1016/j.respol.2015.11.001.

[9] “International Technology Roadmap for Photovoltaic (ITRPV) - Results 2021,” ITRPV, 2022.

[10] IRENA, *Future of solar photovoltaic: Deployment, investment, technology, grid integration and socio-economic aspects (A Global Energy Transformation: paper)*, vol. November. 2019. [Online]. Available: https://www.irena.org/-/media/Files/IRENA/Agency/Publication/2019/Oct/IRENA_Future_of_wind_2019.pdf

[11] “International Technology Roadmap for Photovoltaic (ITRPV) - Results 2020,” 2021. [Online]. Available: https://itrpv.vdma.org/documents/27094228/29066965/20210ITRPV/08ccda3a-585e-6a58-6afa-6c20e436cf41

[12] “International Technology Roadmap for Photovoltaic (ITRPV) - Results 2019,” 2020. [Online]. Available: https://itrpv.vdma.org/en/ueber-uns

[13] “International Technology Roadmap for Photovoltaic (ITRPV) - Results 2018,” 2019. [Online]. Available: http://www.itrpv.net/

[14] IRENA and ILO, *Renewable Energy and Jobs – Annual Review 2021*. 2021.

[15] M. Graham *et al.*, “Partial shading by solar panels delays bloom, increases floral abundance during the late-season for pollinators in a dryland, agrivoltaic ecosystem,” *Sci Rep*, vol. 11, no. 1, pp. 1–13, 2021, doi: 10.1038/s41598-021-86756-4.

[16] J. J. Buonocore *et al.*, “Health and climate benefits of different energy-efficiency and renewable energy choices,” *Nat Clim Chang*, vol. 6, no. 1, pp. 100–106, 2016, doi: 10.1038/nclimate2771.

[17] J. J. Buonocore, E. J. Hughes, D. R. Michanowicz, J. Heo, J. G. Allen, and A. Williams, “Climate and health benefits of increasing renewable energy deployment in the United States,” *Environmental Research Letters*, vol. 14, no. 11, 2019, doi: 10.1088/1748-9326/ab49bc.

[18] J. Yang, X. Li, W. Peng, F. Wagner, and D. L. Mauzerall, “Climate, air quality and human health benefits of various solar photovoltaic deployment scenarios in China in 2030,” *Environmental Research Letters*, vol. 13, no. 6, 2018, doi: 10.1088/1748-9326/aabe99.

[19] B. Hallam, M. Kim, R. Underwood, S. Drury, L. Wang, and P. R. Dias, “A Silicon learning curve and polysilicon requirements for broad-electrification with photovoltaics by 2050,” in *2022 IEEE 49th Photovoltaics Specialists Conference (PVSC)*, 2022, pp. 1177–1177.

[20] M. P. Cenci *et al.*, “Eco-Friendly Electronics — A Comprehensive Review,” *Adv Mater Technol*, vol. 7, no. 2001263, pp. 1–34, 2022, doi: 10.1002/admt.202001263.

[21] B. Hallam, M. Kim, R. Underwood, S. Drury, L. Wang, and P. Dias, “A Polysilicon Learning Curve and the Material Requirements for Broad Electri fi cation with Photovoltaics by 2050,” *Solar RRL*, vol. 6, no. 2200458, pp. 1–8, 2022, doi: 10.1002/solr.202200458.

[22] S. Weckend, A. Wade, and G. Heath, “End-Of-Life Management: Solar Photovoltaic Panels,” 2016.

[23] M. M. Lunardi, J. P. Alvarez-Gaitan, J. I. Bilbao, and R. Corkish, “Comparative life cycle assessment of end-of-life silicon solar photovoltaic modules,” *Applied Sciences (Switzerland)*, vol. 8, no. 8, 2018, doi: 10.3390/app8081396.

[24] M. M. Lunardi, J. P. Alvarez-Gaitan, J. Bilbao, and R. Corkish, “A review of recyling processes for photovoltaic modules,” in *Solar Panels Photovoltaic Materials*, IntechOpen, 2018, pp. 9–27.

[25] M. M. Lunardi, J. P. Alvarez-Gaitan, N. L. Chang, and R. Corkish, “Life cycle assessment on PERC solar modules,” *Solar Energy Materials and Solar Cells*, vol. 187, no. August, pp. 154–159, 2018, doi: 10.1016/j.solmat.2018.08.004.

[26] P. R. Dias *et al.*, “High yield, low cost, environmentally friendly process to recycle silicon solar panels: Technical, economic and environmental feasibility assessment,” *Renewable and Sustainable Energy Reviews*, vol. 169, no. August 2021, p. 112900, 2022, doi: 10.1016/j.rser.2022.112900.

[27] Z. W. Zhong, B. Song, and P. E. Loh, “LCAs of a polycrystalline photovoltaic module and a wind turbine,” *Renew Energy*, vol. 36, no. 8, pp. 2227–2237, 2011, doi: 10.1016/j.renene.2011.01.021.

[28] M. M. Lunardi, P. R. Dias, R. Deng, and R. Corkish, *Life Cycle Environmental Assessment of Different Solar Photovoltaic Technologies*. AIP Publishing LLC, 2021. doi: 10.1063/9780735423152_005.

[29] Y. Zhang, M. Kim, L. Wang, P. Verlinden, and B. Hallam, “Design considerations for multi-terawatt scale manufacturing of existing and future photovoltaic technologies: Challenges and opportunities related to silver, indium and bismuth consumption,” *Energy Environ Sci*, vol. 14, no. 11, pp. 5587–5610, 2021, doi: 10.1039/d1ee01814k.

[30] Fraunhofer ISE and PSE Projects GmbH, “Photovoltaics Report -2022- Fraunhofer ISE,” no. February, p. https://www.ise.fraunhofer.de/conte%0Ant/dam/ise/d, 2022, [Online]. Available: https://www.ise.fraunhofer.de/en/publications/studies/photovoltaics-report.html%0Ahttps://www.ise.fraunhofer.de/conte%0Ant/dam/ise/de/documents/publications/studies/Photovoltaics-Report.pdf%0Awww.ise.fraunhofer.de

[31] M. A. Green, *Silicon Solar Cells: Advanced Principles & Practice*. Sydney: Centre for Photovoltaic Devices and Systems, University of New South Wales, Sydney, N.S.W, 2052, 1995.

[32] C. Honsberg and S. Bowden, “Fill Factor,” *PV Education*, 2019. https://www.pveducation.org/pvcdrom/solar-cell-operation/fill-factor (accessed Feb. 16, 2023).

[33] R. Chen *et al.*, “23.83% efficient mono-PERC incorporating advanced hydrogenation,” *Progress in Photovoltaics: Research and Applications*, vol. 28, no. 12, pp. 1239–1247, 2020, doi: 10.1002/pip.3243.

[34] M. Jonasz and G. R. Fournier, “Basic principles of the interaction of light with matter,” *Light Scattering by Particles in Water*, pp. 1–32, 2007, doi: 10.1016/b978-012388751-1/50001-6.

[35] M. Fox, *Optical Properties of Solids*. Oxford University Press, 2010.

[36] S. Baker-Finch, “Opal 2 Calculator,” *PV Lighthouse*, 2013. https://www2.pvlighthouse.com.au/calculators/opal 2/opal 2.aspx (accessed Aug. 09, 2021).

[37] S. M. Sze and M. K. Lee, *Semiconductor Devices: Physics and Technology*, 3rd ed. New York: John Wiley and Sons Ltd, 2006. doi: 10.1002/9780470068328.

[38] Y. P. Varshni, “Band-to-Band Radiative Recombination in Groups IV, 81, and HI-V Semiconductors (I) ’1,” 1967.

[39] P. Altermatt, J. Schmidt, G. Heiser, and A. G. Aberle, “Assessment and parameterisation of Coulomb-enhanced Auger recombination coefficients in lowly injected crystalline silicon,” *J Appl Phys*, vol. 82, no. 10, pp. 4938–4944, Nov. 1997, doi: 10.1063/1.366360.

[40] W. Shockley and W. T. Read, “Statistics of the recombinations of holes and electrons,” *Physical Review*, vol. 87, no. 5, pp. 835–842, 1952, doi: 10.1103/PhysRev.87.835.

[41] R. N. Hall, “Electron-Hole Recombination in Germanium,” *Physical Review*, vol. 87, no. 2, pp. 387–387, 1952.

[42] A. A. Istratov *et al.*, “Metal content of multicrystalline silicon for solar cells and its impact on minority carrier diffusion length,” *J Appl Phys*, vol. 94, no. 10, pp. 6552–6559, Nov. 2003, doi: 10.1063/1.1618912.

[43] J. Chen *et al.*, “Electron-beam-induced current study of small-angle grain boundaries in multicrystalline silicon,” *Scr Mater*, vol. 52, no. 12, pp. 1211–1215, 2005, doi: 10.1016/j.scriptamat.2005.03.010.

[44] D. Cavalcoli, D. Cavallini, and C. Capperdoni, “Influence of dislocation density on recombination at grain boundaries in multicrystalline silicon Related content On the electrical activity of first-and second-order twin boundaries in silicon,” 1993.

[45] M. Seibt, R. Khalil, V. Kveder, and W. Schröter, “Electronic states at dislocations and metal silicide precipitates in crystalline silicon and their role in solar cell materials,” *Appl Phys A Mater Sci Process*, vol. 96, no. 1, pp. 235–253, Jul. 2009, doi: 10.1007/s00339-008-5027-8.

[46] S. Woo *et al.*, “An insight into dislocation density reduction in multicrystalline silicon,” *Solar Energy Materials and Solar Cells*, vol. 155. Elsevier B.V., pp. 88–100, Oct. 01, 2016. doi: 10.1016/j.solmat.2016.03.040.

[47] L. Euler, “4 . 6 The Electromagnetic Approach,” no. 2016, pp. 121–132, 2022.

[48] J. Hofstetter, C. Cafiizo, and A. Luque, “Optimisation of SINx : H anti-reflection coatings for silicon solar cells,” in *2007 Spanish Conference on Electron Devices*, 2007, pp. 131–134.

[49] A. El amrani, I. Menous, L. Mahiou, R. Tadjine, A. Touati, and A. Lefgoum, “Silicon nitride film for solar cells,” *Renew Energy*, vol. 33, no. 10, pp. 2289–2293, 2008, doi: 10.1016/j.renene.2007.12.015.

[50] S. Duttagupta, F. Ma, B. Hoex, T. Mueller, and A. G. Aberle, “Optimised antireflection coatings using silicon nitride on textured silicon surfaces based on measurements and multidimensional modelling,” *Energy Procedia*, vol. 15, no. 2011, pp. 78–83, 2012, doi: 10.1016/j.egypro.2012.02.009.

[51] Y. Zhang, L. Wang, D. Chen, M. Kim, and B. Hallam, “Pathway towards 24% efficiency for fully screen-printed passivated emitter and rear contact solar cells,” *J Phys D Appl Phys*, vol. 54, no. 21, 2021, doi: 10.1088/1361-6463/abe900.

[52] T. H. Fung *et al.*, “Improved emitter performance of RIE black silicon through the application of in-situ oxidation during POCl3 diffusion,” *Solar Energy Materials and Solar Cells*, vol. 210, no. March, Jun. 2020, doi: 10.1016/j.solmat.2020.110480.

[53] P. Campbell and M. A. Green, “Light trapping properties of pyramidally textured surfaces,” *J Appl Phys*, vol. 62, no. 1, pp. 243–249, 1987, doi: 10.1063/1.339189.

[54] E. Yablonovitch, “Statistical ray optics,” *Journal of Optical Society of America*, vol. 72, no. 7, pp. 899–907, 1982.

[55] T. E. Scheul, E. Khorani, T. Rahman, M. D. B. Charlton, and S. A. Boden, “Light scattering from black silicon surfaces and its benefits for encapsulated solar cells,” *Solar Energy Materials and Solar Cells*, vol. 235, no. October 2021, p. 111448, 2022, doi: 10.1016/j.solmat.2021.111448.

[56] T. E. Scheul, E. Khorani, T. Rahman, M. D. B. Charlton, and S. A. Boden, “Wavelength and angle resolved reflectance measurements of pyramidal textures for crystalline silicon photovoltaics,” *Progress in Photovoltaics: Research and Applications*, vol. 28, no. 12, pp. 1248–1257, 2020, doi: 10.1002/pip.3319.

[57] B. Sopori *et al.*, “Characterizing damage on Si wafer surfaces cut by slurry and diamond wire sawing,” *Conference Record of the IEEE Photovoltaic Specialists Conference*, pp. 945–950, 2013, doi: 10.1109/PVSC.2013.6744298.

[58] K. Chen, Y. Liu, X. Wang, L. Zhang, and X. Su, “Novel texturing process for diamond-wire-sawn single-crystalline silicon solar cell,” *Solar Energy Materials and Solar Cells*, vol. 133, pp. 148–155, 2015, doi: 10.1016/j.solmat.2014.11.016.

[59] A. Bidiville, “DIAMOND WIRE WAFERING: WAFER MORPHOLOGY IN COMPARISON TO SLURRY SAWN WAFERS,” in *25th European Photovoltaic Solar Energy Conference and Exhibition*, 2010, no. September, pp. 1673–1676.

[60] A. Bidiville, K. Wasmer, R. Kraft, and C. Ballif, “DIAMOND WIRE-SAWN SILICON WAFERS-FROM THE LAB TO THE CELL PRODUCTION.”

[61] J. Il Jang, M. J. Lance, S. Wen, T. Y. Tsui, and G. M. Pharr, “Indentation-induced phase transformations in silicon: Influences of load, rate and indenter angle on the transformation behavior,” *Acta Mater*, vol. 53, no. 6, pp. 1759–1770, 2005, doi: 10.1016/j.actamat.2004.12.025.

[62] I. Zubel and I. Barycka, “Silicon anisotropic etching in alkaline solutions I. The geometric description of figures developed under etching Si (100) in various solutions,” *Sens Actuators A Phys*, vol. 70, no. 3, pp. 250–259, 1998, doi: 10.1016/S0924-4247(98)00141-1.

[63] Y. Wang, R. Luo, J. Ma, and S.-Q. Man, “Fabrication of the pyramidal microstructure on silicon substrate using KOH solution,” 2015.

[64] E. Vazsonyi *et al.*, “Improved anisotropic etching process for industrial texturing of silicon solar cells,” 1999.

[65] P. K. Singh, R. Kumar, M. Lal, S. N. Singh, and B. K. Das, “Effectiveness of anisotropic etching of silicon in aqueous alkaline solutions,” *Solar Energy Materials and Solar Cells*, vol. 70, no. 1, pp. 103–113, 2001, doi: 10.1016/S0927-0248(00)00414-1.

[66] H. Seidel, L. Csepregi, A. Heuberger, and H. Baumgärtel, “Anisotropic Etching of Crystalline Silicon in Alkaline Solutions I. Orientation Dependence and Behavior of Passivation Layers,” *J Electrochem Soc*, vol. 137, no. 11, pp. 3626–3632, 1990, doi: 10.1149/1.2086278.

[67] B. Hoex *et al.*, “Acid Texturing,” *PV Manufacturing*, 2017. https://pv-manufacturing.org/acid-texturing/ (accessed May 20, 2022).

[68] J. Acker, T. Koschwitz, B. Meinel, R. Heinemann, and C. Blocks, “HF/HNO3 etching of the saw damage,” *Energy Procedia*, vol. 38, pp. 223–233, 2013, doi: 10.1016/j.egypro.2013.07.271.

[69] H. Li, K. Kim, B. Hallam, B. Hoex, S. Wenham, and M. Abbott, “POCl3 diffusion for industrial Si solar cell emitter formation,” *Frontiers in Energy*, vol. 11, no. 1, pp. 42–51, Mar. 2017, doi: 10.1007/s11708-016-0433-7.

[70] H. Li, F. J. Ma, Z. Hameiri, S. Wenham, and M. Abbott, “On elimination of inactive phosphorus in industrial POCl3 diffused emitters for high efficiency silicon solar cells,” *Solar Energy Materials and Solar Cells*, vol. 171, pp. 213–221, Nov. 2017, doi: 10.1016/j.solmat.2017.06.040.

[71] B. Min, H. Wagner, A. Dastgheib-Shirazi, A. Kimmerle, H. Kurz, and P. P. Altermatt, “Heavily doped Si: P emitters of crystalline Si solar cells: Recombination due to phosphorus precipitation,” *Physica Status Solidi - Rapid Research Letters*, vol. 8, no. 8, pp. 680–684, 2014, doi: 10.1002/pssr.201409138.

[72] A. Dastgheib-Shirazi, M. Steyer, G. Micard, H. Wagner, P. P. Altermatt, and G. Hahn, “Relationships between diffusion parameters and phosphorus precipitation during the POCl3 diffusion process,” in *Energy Procedia*, 2013, vol. 38, pp. 254–262. doi: 10.1016/j.egypro.2013.07.275.

[73] “Morris, Katz - 1978 - Reduction of Excess Phosphorus and Elimination of Defects in Phosphorus Emitter Diffusions-annotated”.

[74] K. Misiakos and F. A. Lindholm, “Toward a Systematic Design Theory for Silicon Solar Cells Using Optimization Techniques,” *Solar Cells*, vol. 17, pp. 29–52, 1986.

[75] F. Miao, S. Zhang, W. Lian, B. Zhao, and Q. Wei, “Improvement of PERC solar cell efficiency based on laser-doped selective emitter,” *AIP Conf Proc*, vol. 2147, no. August, 2019, doi: 10.1063/1.5123838.

[76] A. Wolf *et al.*, “STATUS AND PERSPECTIVE OF EMITTER FORMATION BY POCl3-DIFFUSION,” *31st European PV Solar Energy Conference and Exhibition*, no. September, pp. 14–18, 2015.

[77] K. Birmann, “25th European Photovoltaic Solar Energy Conference and Exhibition / 5th World Conference on Photovoltaic Energy Conversion, 6-10 September 2010, Valencia, Spain,” *Solar Energy*, no. September, pp. 6–10, 2010.

[78] Aberle, Armin G, “Overview on SiN surface passivation of crystalline silicon solar cells,” *Solar Energy Materials and Solar Cells*, vol. 65, no. 1–4, pp. 239–248, 2001.

[79] F. Duerinckx and J. Szlufcik, “Defect passivation of industrial multicrystalline solar cells based on PECVD silicon nitride,” *Solar Energy Materials and Solar Cells*, vol. 72, no. 1–4, pp. 231–246, 2002, doi: 10.1016/S0927-0248(01)00170-2.

[80] G. E. Jellison and P. C. Joshi, “Crystalline silicon solar cells,” *Springer Series in Optical Sciences*, vol. 212, no. May, pp. 201–225, 2018, doi: 10.1007/978-3-319-75377-5_8.

[81] S. Dauwe, L. Mittelstädt, A. Metz, and R. Hezel, “Experimental evidence of parasitic shunting in silicon nitride rear surface passivated solar cells,” *Progress in Photovoltaics: Research and Applications*, vol. 10, no. 4, pp. 271–278, 2002, doi: 10.1002/pip.420.

[82] G. Agostinelli *et al.*, “Very low surface recombination velocities on p-type silicon wafers passivated with a dielectric with fixed negative charge,” *Solar Energy Materials and Solar Cells*, vol. 90, no. 18–19, pp. 3438–3443, 2006, doi: 10.1016/j.solmat.2006.04.014.

[83] P. K. Liu, Y. L. Cheng, and L. Wang, “Crystalline silicon PERC solar cell with ozonized AlOx passivation layer on the rear side,” *International Journal of Photoenergy*, vol. 2020, 2020, doi: 10.1155/2020/6686797.

[84] B. Hoex, S. B. S. Heil, E. Langereis, M. C. M. Van De Banden, and W. M. M. Kessels, “Ultralow surface recombination of c-Si substrates passivated by plasma-assisted atomic layer deposited Al2O3,” *Appl Phys Lett*, vol. 89, no. 4, pp. 5–8, 2006, doi: 10.1063/1.2240736.

[85] B. Veith *et al.*, “Comparison of ICP-AlOx and ALD-Al2O3 layers for the rear surface passivation of c-Si solar cells,” *Energy Procedia*, vol. 27, pp. 379–384, 2012, doi: 10.1016/j.egypro.2012.07.080.

[86] T. Dullweber *et al.*, “Inductively coupled plasma chemical vapour deposited AlO x/SiNy layer stacks for applications in high-efficiency industrial-type silicon solar cells,” *Solar Energy Materials and Solar Cells*, vol. 112, pp. 196–201, 2013, doi: 10.1016/j.solmat.2013.01.036.

[87] E. Cornagliotti *et al.*, “Large-Area n-Type PERT Solar Cells Featuring Rear p+ Emitter Passivated by ALD Al2O3,” *IEEE J Photovolt*, vol. 5, no. 5, pp. 1366–1372, 2015, doi: 10.1109/JPHOTOV.2015.2458041.

[88] P. Saint-Cast *et al.*, “High-efficiency c-si solar cells passivated with ALD and PECVD aluminum oxide,” *IEEE Electron Device Letters*, vol. 31, no. 7, pp. 695–697, 2010, doi: 10.1109/LED.2010.2049190.

[89] B. Veith *et al.*, “Comparison of ICP-AlOx and ALD-Al2O3 layers for the rear surface passivation of c-Si solar cells,” *Energy Procedia*, vol. 27, pp. 379–384, 2012, doi: 10.1016/j.egypro.2012.07.080.

[90] J. Schmidt *et al.*, “Industrially Relevant Al2O3 Deposition Techniques for the Surface Passivation of Si Solar Cells,” in *25th European Photovoltaic Solar Energy Conference and Exhibition/ 5th Wold Conference on Photovoltaic Energy Conceersion*, 2010, pp. 1130–1133.

[91] V. I. Kuznetsov, M. A. Ernst, and E. H. A. Granneman, “Al2O3 surface passivation of silicon solar cells by low cost ald technology,” *2014 IEEE 40th Photovoltaic Specialist Conference, PVSC 2014*, pp. 608–611, 2014, doi: 10.1109/PVSC.2014.6924995.

[92] D. Kray, M. Hermle, and S. W. Glunz, “Theory and Experiments on the Back Side Reflectance of SSilicon Wafer Solar Cells,” *Progress in Photovoltaics: Research and Applications*, vol. 16, pp. 1–15, 2008, doi: 10.1002/pip.

[93] J. Haynos, J. Alllson, R. Arndt, and A. Meulenberg, “The Comsat Non Reflective Silicon Solar Cell: A Second Generation Improved Cell,” in *Conference on Prhotovoltaic Power Generation*, 1974, p. 487.

[94] T. Baum and D. J. Schiffrin, “Mechanistic aspects of anisotropic dissolution of materials: Etching of single-crystal silicon in alkaline solutions,” *Journal of the Chemical Society - Faraday Transactions*, vol. 94, no. 5, pp. 691–694, 1998, doi: 10.1039/a707473e.

[95] H. Seidel, “The mechanism of anisotropic, electrochemical silicon etching in alkaline solutions,” *IEEE 4th Technical Digest on Solid-State Sensor and Actuator Workshop*, pp. 86–91, 1990.

[96] L. Zhu *et al.*, “Ultrafast Random-Pyramid Texturing for Efficient Monocrystalline Silicon Solar Cells,” *Solar RRL*, p. 2200204, 2022, doi: 10.1002/solr.202200204.

[97] P. K. Basu, D. Sarangi, K. D. Shetty, and M. B. Boreland, “Liquid silicate additive for alkaline texturing of mono-Si wafers to improve process bath lifetime and reduce IPA consumption,” *Solar Energy Materials and Solar Cells*, vol. 113, pp. 37–43, 2013, doi: 10.1016/j.solmat.2013.01.037.

[98] H. Park, J. S. Lee, H. J. Lim, D. Kim, S. Kwon, and S. Yoon, “The effect of tertiary-butyl alcohol on the texturing of crystalline silicon solar cells,” *Journal of the Korean Physical Society*, vol. 55, no. 5 PART 1, pp. 1767–1771, 2009, doi: 10.3938/jkps.55.1767.

[99] W. Sparber *et al.*, “Comparison of texturing methods for monocrystalline silicon solar cells using KOH and Na2CO3,” *Proceedings of the 3rd World Conference on Photovoltaic Energy Conversion*, vol. B, no. February 2015, pp. 1372–1375, 2003, doi: 10.1109/WCPEC.2003.1306177.

[100] E. Abdur-Rahman, I. Alghoraibi, and H. Alkurdi, “Effect of isopropyl alcohol concentration and etching time on wet chemical anisotropic etching of low-resistivity crystalline silicon wafer,” *Int J Anal Chem*, vol. 2017, 2017, doi: 10.1155/2017/7542870.

[101] Z. Xi, D. Yang, W. Dan, C. Jun, X. Li, and D. Que, “Investigation of texturization for monocrystalline silicon solar cells with different kinds of alkaline,” *Renew Energy*, vol. 29, no. 13, pp. 2101–2107, 2004, doi: 10.1016/j.renene.2004.03.003.

[102] M. F. Abdullah *et al.*, “Research and development efforts on texturization to reduce the optical losses at front surface of silicon solar cell,” *Renewable and Sustainable Energy Reviews*, vol. 66, pp. 380–398, 2016, doi: 10.1016/j.rser.2016.07.065.

[103] S. Baker-Finch and K. McIntosh, “Reflection distributions of textured monocrystalline silcon: impilcations for silicon solar cells,” *Progress in Photovoltaics: Research and Applications*, vol. 21, pp. 960–971, 2013, doi: 10.1002/pip.

[104] J. D. Hylton, A. R. Burgers, and W. C. Sinke, “Alkaline Etching for Reflectance Reduction in Multicrystalline Silicon Solar Cells,” *J Electrochem Soc*, vol. 151, no. 6, p. G408, 2004, doi: 10.1149/1.1738137.

[105] D. R. Turner, “On the Mechanism of Chemically Etching Germanium and Silicon,” *J Electrochem Soc*, vol. 107, no. 10, p. 810, 1960, doi: 10.1149/1.2427519.

[106] E. S. Kooij, K. Butter, and J. J. Kelly, “Silicon Etching in HNO3/HF Solution: Charge Balance for the Oxidation Reaction,” *Electrochemical and Solid-State Letters*, vol. 2, no. 2–4, pp. 178–180, 1999, doi: 10.1149/1.1390775.

[107] B. Schwartz and H. Robbins, “Chemical Etching of Silicon: III . A Temperature Study in the Acid System,” *J Electrochem Soc*, vol. 108, no. 4, pp. 365–372, 1961.

[108] K. P. Sreejith, A. K. Sharma, P. K. Basu, and A. Kottantharayil, “Etching methods for texturing industrial multi-crystalline silicon wafers: A comprehensive review,” *Solar Energy Materials and Solar Cells*, vol. 238, no. January, p. 111531, 2022, doi: 10.1016/j.solmat.2021.111531.

[109] R. Einhaus, E. Vazsonyi, J. Szlufcik, J. Nijs, and R. Mertens, “Isotropic texturing of multicrystalline silicon wafers with acidic texturing solutions,” *Conference Record of the IEEE Photovoltaic Specialists Conference*, pp. 167–170, 1997.

[110] D. H. Macdonald *et al.*, “Texturing industrial multicrystalline silicon solar cells,” *Solar Energy*, vol. 76, no. 1–3, pp. 277–283, 2004, doi: 10.1016/j.solener.2003.08.019.

[111] E. Stensrud Marstein, H. Jsrgen Solheim, D. Nilsen Wright, and A. Holt, “ACIDIC TEXTURING OF MULTICRYSTALLINE SILICON WAFERS.”

[112] K. P. Sreejith, A. K. Sharma, S. Kumbhar, A. Kottantharayil, and P. K. Basu, “An additive-free non-metallic energy efficient industrial texturization process for diamond wire sawn multicrystalline silicon wafers,” *Solar Energy*, vol. 184, no. March, pp. 162–172, 2019, doi: 10.1016/j.solener.2019.03.062.

[113] Y. Nishimoto, T. Ishihara, and K. Namba, “Investigation of Acidic Texturization for Multicrystalline Silicon Solar Cells,” 1999.

[114] Y. T. Cheng *et al.*, “Efficiency improved by acid texturization for multi-crystalline silicon solar cells,” *Solar Energy*, vol. 85, no. 1, pp. 87–94, 2011, doi: 10.1016/j.solener.2010.10.020.

[115] M. Lippold, F. Buchholz, C. Gondek, F. Honeit, E. Wefringhaus, and E. Kroke, “Texturing of SiC-slurry and diamond wire sawn silicon wafers by HF-HNO 3-H2SO4 mixtures,” *Solar Energy Materials and Solar Cells*, vol. 127, pp. 104–110, 2014, doi: 10.1016/j.solmat.2014.04.006.

[116] Z. Huang, N. Geyer, P. Werner, J. de Boor, and U. Gösele, “Metal-assisted chemical etching of silicon: A review,” *Advanced Materials*, vol. 23, no. 2. pp. 285–308, Jan. 11, 2011. doi: 10.1002/adma.201001784.

[117] F. Toor *et al.*, “Nanostructured silicon via metal assisted catalyzed etch (MACE): Chemistry fundamentals and pattern engineering,” *Nanotechnology*, vol. 27, no. 41, 2016, doi: 10.1088/0957-4484/27/41/412003.

[118] X. Li and P. W. Bonn, “Metal-assisted chemical etching in HF/H2O2 produces porous silicon,” *Appl Phys Lett*, vol. 77, no. 16, pp. 2572–2574, 2000, doi: 10.1063/1.1319191.

[119] K. Peng *et al.*, “Fabrication of single-crystalline silicon nanowires by scratching a silicon surface with catalytic metal particles,” *Adv Funct Mater*, vol. 16, no. 3, pp. 387–394, 2006, doi: 10.1002/adfm.200500392.

[120] C. Chartier, S. Bastide, and C. Lévy-Clément, “Metal-assisted chemical etching of silicon in HF-H2O2,” *Electrochim Acta*, vol. 53, no. 17, pp. 5509–5516, 2008, doi: 10.1016/j.electacta.2008.03.009.

[121] B. Douglas, D. H. McDaniel, and J. J. Alexander, *Concepts and Models of Inorganic Chemistry*, 2nd ed. New York: Wiley, 1983.

[122] Y. Liu *et al.*, “Nanostructure formation and passivation of large-area black silicon for solar cell applications,” *Small*, vol. 8, no. 9, pp. 1392–1397, 2012, doi: 10.1002/smll.201101792.

[123] S. Koynov, M. S. Brandt, and M. Stutzmann, “Black nonreflecting silicon surfaces for solar cells,” *Appl Phys Lett*, vol. 88, no. 20, 2006, doi: 10.1063/1.2204573.

[124] S. Zou *et al.*, “Complementary etching behavior of alkali, metal-catalyzed chemical, and post-etching of multicrystalline silicon wafers,” *Progress in Photovoltaics: Research and Applications*, vol. 27, no. 6, pp. 511–519, 2019, doi: 10.1002/pip.3125.

[125] K. P. Sreejith, A. K. Sharma, B. Siddarth, S. Kumbhar, P. Basu, and A. Kottantharayil, “Optimization of MACE black silicon surface morphology in multi-crystalline wafers for excellent opto-electronic properties,” in *47th IEEE Photovoltaic Specialists Conference (PVSC)*, 2020, pp. 0839–0842.

[126] K. Chen, T. P. Pasanen, V. Vähänissi, and H. Savin, “Effect of MACE Parameters on Electrical and Optical Properties of ALD Passivated Black Silicon,” *IEEE J Photovolt*, vol. 9, no. 4, pp. 974–979, 2019, doi: 10.1109/JPHOTOV.2019.2917787.

[127] S. Li, W. Ma, Y. Zhou, X. Chen, Y. Xiao, and O. Mace, “Fabrication of p-type porous silicon nanowire with oxidized silicon substrate through one-step MACE,” *J Solid State Chem*, vol. 213, pp. 242–249, 2014, doi: 10.1016/j.jssc.2014.02.037.

[128] W. To, H. Li, and Z. Huang, “Fabrication of n-Type Mesoporous Silicon Nanowires by One-Step Etching,” *ACS Nano Letters*, vol. 11, pp. 5252–5258, 2011.

[129] Z. G. Huang *et al.*, “Solar Energy Materials & Solar Cells One-step-MACE nano / microstructures for high-ef fi cient large-size multicrystalline Si solar cells,” *Solar Energy Materials and Solar Cells*, vol. 143, pp. 302–310, 2015, doi: 10.1016/j.solmat.2015.07.017.

[130] F. Bai, M. Li, D. Song, H. Yu, B. Jiang, and Y. Li, “One-step synthesis of lightly doped porous silicon nanowires in HF/AgNO3/H2O2 solution at room temperature,” *J Solid State Chem*, vol. 196, pp. 596–600, 2012, doi: 10.1016/j.jssc.2012.07.029.

[131] Y. Qu, L. Liao, Y. Li, H. Zhang, Y. Huang, and X. Duan, “Electrically Conductive and Optically Active Porous Silicon Nanowires,” pp. 8–12, 2009.

[132] B. Harris, C. White, and V. Aprahamian, “Method for recovering nitric acid and purifying silver nitrate electrolyte,” US 8282903 B2, 2012

[133] G. Zante, R. Marin Rivera, J. M. Hartley, and A. P. Abbott, “Efficient recycling of metals from solar cells using catalytic etchants,” *J Clean Prod*, vol. 370, no. May, p. 133552, 2022, doi: 10.1016/j.jclepro.2022.133552.

[134] M. Otto *et al.*, “Black silicon photovoltaics,” *Advanced Optical Materials*, vol. 3, no. 2. Wiley-VCH Verlag, pp. 147–164, Feb. 01, 2015. doi: 10.1002/adom.201400395.

[135] T. H. Pei, S. Thiyagu, and Z. Pei, “Ultra high-density silicon nanowires for extremely low reflection in visible regime,” *Appl Phys Lett*, vol. 99, no. 15, pp. 2009–2012, 2011, doi: 10.1063/1.3650266.

[136] M. Lajvardi, H. Eshghi, M. E. Ghazi, M. Izadifard, and A. Goodarzi, “Structural and optical properties of silicon nanowires synthesized by Ag-assisted chemical etching,” *Mater Sci Semicond Process*, vol. 40, pp. 556–563, 2015, doi: 10.1016/j.mssp.2015.07.032.

[137] P. Repo *et al.*, “Effective passivation of black silicon surfaces by atomic layer deposition,” *IEEE J Photovolt*, vol. 3, no. 1, pp. 90–94, 2013, doi: 10.1109/JPHOTOV.2012.2210031.

[138] P. K. Parashar, “Effective suppression of nano-textured black silicon surface recombination channels through sputtered aluminum oxide: A comparison study with ALD grown films,” *Nanotechnology*, Jun. 2020, doi: 10.1088/1361-6528/aba141.

[139] J. Oh, H. C. Yuan, and H. M. Branz, “An 18.2%-efficient black-silicon solar cell achieved through control of carrier recombination in nanostructures,” *Nat Nanotechnol*, vol. 7, no. 11, pp. 743–748, 2012, doi: 10.1038/nnano.2012.166.

[140] K. Chen, T. P. Pasanen, V. Vähänissi, and H. Savin, “Effect of MACE Parameters on Electrical and Optical Properties of ALD Passivated Black Silicon,” *IEEE J Photovolt*, vol. 9, no. 4, pp. 974–979, Jul. 2019, doi: 10.1109/JPHOTOV.2019.2917787.

[141] G. von Gastrow *et al.*, “Analysis of the Atomic Layer Deposited Al2O3 field-effect passivation in black silicon,” *Solar Energy Materials and Solar Cells*, vol. 142, pp. 29–33, Nov. 2015, doi: 10.1016/j.solmat.2015.05.027.

[142] T. Pasanen, V. Vähänissi, N. Theut, and H. Savin, “Surface passivation of black silicon phosphorus emitters with atomic layer deposited SiO2/Al2O3 stacks,” *Energy Procedia*, vol. 124, no. February 2018, pp. 307–312, 2017, doi: 10.1016/j.egypro.2017.09.304.

[143] X. Ye *et al.*, “18.45%-Efficient Multi-Crystalline Silicon Solar Cells with Novel Nanoscale Pseudo-Pyramid Texture,” *Adv Funct Mater*, vol. 24, no. 42, pp. 6708–6716, 2014, doi: 10.1002/adfm.201401589.

[144] P. Zhang *et al.*, “The influence of Ag-ion concentration on the performance of mc-Si silicon solar cells textured by metal assisted chemical etching (MACE) method,” *Solar Energy Materials and Solar Cells*, vol. 200, no. May, p. 109983, 2019, doi: 10.1016/j.solmat.2019.109983.

[145] W. Z. Shen *et al.*, “Large-area MACE Si nano-inverted-pyramids for PERC solar cell application,” vol. 188, no. March, pp. 300–304, 2019, doi: 10.1016/j.solener.2019.06.015.

[146] X. Li *et al.*, “High-efficiency multi-crystalline black silicon solar cells achieved by additive assisted Ag-MACE,” *Solar Energy*, vol. 195, no. November 2019, pp. 176–184, 2020, doi: 10.1016/j.solener.2019.11.045.

[147] I. Cesar *et al.*, “Excellent rear side passivation on multi-crystalline silicon solar cells with 20 nm uncapped Al2O3 layer: Industrialization of ALD for solar cell applications,” *Conference Record of the IEEE Photovoltaic Specialists Conference*, pp. 44–49, 2010, doi: 10.1109/PVSC.2010.5614176.

[148] B. Veith *et al.*, “Comparison of ICP-AlOx and ALD-Al2O3 layers for the rear surface passivation of c-Si solar cells,” *Energy Procedia*, vol. 27, pp. 379–384, 2012, doi: 10.1016/j.egypro.2012.07.080.

[149] Z. Zhao, Y. Kong, Z. Zhang, G. Huang, and Y. Mei, “Atomic layer-deposited nanostructures and their applications in energy storage and sensing,” *J Mater Res*, vol. 35, no. 7, pp. 701–719, 2020, doi: 10.1557/jmr.2019.329.

[150] T. E. Scheul, E. Khorani, T. Rahman, and S. A. Boden, “Characterization of atomic layer deposited alumina thin films on black silicon textures using helium ion microscopy,” *AIP Conf Proc*, vol. 2147, no. August, 2019, doi: 10.1063/1.5123858.

[151] Z. G. Huang *et al.*, “One-step-MACE nano/microstructures for high-efficient large-size multicrystalline Si solar cells,” *Solar Energy Materials and Solar Cells*, vol. 143, no. October 2018, pp. 302–310, 2015, doi: 10.1016/j.solmat.2015.07.017.

[152] T. Rahman *et al.*, “Passivation of all-angle black surfaces for silicon solar cells,” *Solar Energy Materials and Solar Cells*, vol. 160, pp. 444–453, Feb. 2017, doi: 10.1016/j.solmat.2016.10.044.

[153] A. Abdulkadir, A. A. Aziz, and M. Z. Pakhuruddin, “Impact of micro-texturization on hybrid micro/nano-textured surface for enhanced broadband light absorption in crystalline silicon for application in photovoltaics,” *Mater Sci Semicond Process*, vol. 105, no. September 2019, p. 104728, 2020, doi: 10.1016/j.mssp.2019.104728.

[154] J. Y. Li, C. H. Hung, and C. Y. Chen, “Hybrid black silicon solar cells textured with the interplay of copper-induced galvanic displacement,” *Sci Rep*, vol. 7, no. 1, pp. 1–10, 2017, doi: 10.1038/s41598-017-17516-6.

[155] Y. Jiang *et al.*, “Hybrid process for texturization of diamond wire sawn multicrystalline silicon solar cell,” *Physica Status Solidi - Rapid Research Letters*, vol. 10, no. 12, pp. 870–873, 2016, doi: 10.1002/pssr.201600318.

[156] A. Srivastava, D. Sharma, S. Laxmi, J. S. Tawale, P. Pathi, and S. K. Srivastava, “Excellent omnidirectional light trapping properties of inverted micro-pyramid structured silicon by copper catalyzed chemical etching,” *Opt Mater (Amst)*, vol. 131, no. May, p. 112677, 2022, doi: 10.1016/j.optmat.2022.112677.

[157] X. Wu, Y. Tan, H. Wu, J. Li, M. Cai, and P. Li, “Structural modification of diamond-wire-cut multicrystalline Si by Cu-catalyzed chemical etching for surface structuring,” *Thin Solid Films*, vol. 750, no. April 2021, p. 139199, 2022, doi: 10.1016/j.tsf.2022.139199.

[158] S. Kubendhiran, G. Sison, H. P. Hsu, and C. W. Lan, “Copper Assisted Inverted Pyramids Texturization of Monocrystalline Silicon in a Nitrogen Bubbling Bath for Highly Efficient Light Trapping,” *Silicon*, vol. 13, no. 9, pp. 3121–3129, 2021, doi: 10.1007/s12633-020-00650-8.

[159] H. Zheng, M. Han, P. Zheng, L. Zheng, H. Qin, and L. Deng, “Porous silicon templates prepared by Cu-assisted chemical etching,” *Mater Lett*, vol. 118, pp. 146–149, 2014, doi: 10.1016/j.matlet.2013.12.093.

[160] G. Sheng *et al.*, “Controllable nano-texturing of diamond wire sawing polysilicon wafers through low-cost copper catalyzed chemical etching,” *Mater Lett*, vol. 221, pp. 85–88, 2018, doi: 10.1016/j.matlet.2018.03.092.

[161] J. Zha *et al.*, “Constructing submicron textures on mc-Si solar cells via copper-catalyzed chemical etching,” *Appl Phys Lett*, vol. 110, no. 9, 2017, doi: 10.1063/1.4977191.

[162] P. Wang *et al.*, “18.88%-efficient multi-crystalline silicon solar cells by combining Cu-catalyzed chemical etching and post-treatment process,” *Solar Energy*, vol. 169, no. April, pp. 153–158, 2018, doi: 10.1016/j.solener.2018.04.049.

[163] K. Gao *et al.*, “Enhanced etching rate of black silicon by Cu/Ni Co-assisted chemical etching process,” *Mater Sci Semicond Process*, vol. 88, no. August, pp. 250–255, 2018, doi: 10.1016/j.mssp.2018.08.023.

[164] H. Jansen, H. Gardeniers, M. De Boer, M. Elwenspoek, and J. Fluitman, “A survey on the reactive ion etching of silicon in microtechnology,” *Journal of Micromechanics and Microengineering*, vol. 6, no. 1, pp. 14–28, 1996, doi: 10.1088/0960-1317/6/1/002.

[165] R. Hsiao and J. Carr, “Si/SiO2 etching in high density SF6/CHF3/O2 plasma,” *Materials Science and Engineering B*, vol. 52, no. 1, pp. 63–77, 1998, doi: 10.1016/S0921-5107(97)00217-1.

[166] M. Steglich, T. Käsebier, M. Zilk, T. Pertsch, E. B. Kley, and A. Tünnermann, “The structural and optical properties of black silicon by inductively coupled plasma reactive ion etching,” *J Appl Phys*, vol. 116, no. 17, Nov. 2014, doi: 10.1063/1.4900996.

[167] K. M. Park, M. B. Lee, and S. Y. Choi, “Investigation of surface features for 17.2% efficiency multi-crystalline silicon solar cells,” *Solar Energy Materials and Solar Cells*, vol. 132, pp. 356–362, 2015, doi: 10.1016/j.solmat.2014.07.023.

[168] J. Jin, H. Shen, P. Zheng, K. S. Chan, X. Zhang, and H. Jin, "> 20.5% Diamond Wire Sawn Multicrystalline Silicon Solar Cells With Maskless Inverted Pyramid Like Texturing," *IEEE J Photovolt*, vol. 7, no. 5, pp. 1264–1269, 2017.

[169] S. Wang *et al.*, "Effect of surface structure on electrical performance of industrial diamond wire sawing multicrystalline Si solar cells," *International Journal of Photoenergy*, vol. 2018, pp. 1–5, 2018, doi: 10.1155/2018/7947015.

[170] I. T. S. Heikkinen, P. Repo, V. Vähänissi, T. Pasanen, V. Malinen, and H. Savin, "Efficient surface passivation of black silicon using spatial atomic layer deposition," in *Energy Procedia*, 2017, vol. 124, pp. 282–287. doi: 10.1016/j.egypro.2017.09.300.

[171] H. Kohata and Y. Saito, "Maskless texturization of phosphorus-diffused layers for crystalline Si solar cells by plasmaless dry etching with chlorine trifluoride gas," *Solar Energy Materials and Solar Cells*, vol. 94, no. 12, pp. 2124–2128, 2010, doi: 10.1016/j.solmat.2010.06.040.

[172] B. Kafle *et al.*, "On the formation of black silicon features by plasma-less etching of silicon in molecular fluorine gas," *Nanomaterials*, vol. 10, no. 11, pp. 1–16, 2020, doi: 10.3390/nano10112214.

[173] B. Kafle, J. Seiffe, M. Hofmann, L. Clochard, E. Duffy, and J. Rentsch, "Nanostructuring of c-Si surface by F2-based atmospheric pressure dry texturing process," *Physica Status Solidi (A) Applications and Materials Science*, vol. 212, no. 2, pp. 307–311, 2015, doi: 10.1002/pssa.201431372.

[174] B. Kafle *et al.*, "Atmospheric pressure dry texturing enabling 20% conversion efficiency on multicrystalline silicon PERC solar cells," *AIP Conf Proc*, vol. 1999, no. August, 2018, doi: 10.1063/1.5049293.

[175] B. Kafle *et al.*, "Atmospheric Pressure Dry Etching of Polysilicon Layers for Highly Reverse Bias-Stable TOPCon Solar Cells," *Solar RRL*, vol. 6, no. 5, 2022, doi: 10.1002/solr.202100481.

[176] C. Amri, R. Ouertani, A. Hamdi, and H. Ezzaouia, "Effect of Silver-Assisted Chemical Vapor Etching on morphological properties and silicon solar cell performance," *Mater*

Sci Semicond Process, vol. 63, no. September 2016, pp. 176–183, 2017, doi: 10.1016/j.mssp.2017.02.019.

[177] M. ben Rabha, M. Saadoun, M. F. Boujmil, B. Bessaïs, H. Ezzaouia, and R. Bennaceur, “Application of the chemical vapor-etching in polycrystalline silicon solar cells,” *Appl Surf Sci*, vol. 252, no. 2, pp. 488–493, 2005, doi: 10.1016/j.apsusc.2005.01.028.

[178] M. Ju *et al.*, “A new vapor texturing method for multicrystalline silicon solar cell applications,” *Mater Sci Eng B Solid State Mater Adv Technol*, vol. 153, no. 1–3, pp. 66–69, 2008, doi: 10.1016/j.mseb.2008.10.030.

[179] M. Ju *et al.*, “Novel vapor texturing method for EFG silicon solar cell applications,” *Solar Energy Materials and Solar Cells*, vol. 107, pp. 366–372, 2012, doi: 10.1016/j.solmat.2012.07.015.

[180] B. R. Mohamed, H. Anouar, and B. Brahim, “Improvement of multicrystalline silicon solar cell performance via chemical vapor etching method-based porous silicon nanostructures,” *Solar Energy*, vol. 86, no. 5, pp. 1411–1415, 2012, doi: 10.1016/j.solener.2012.01.031.

[181] Z. Xiao, G. Geng, X. Wei, Z. Yue, and L. Zhou, “On the mechanism of the vapor etching of diamond wire sawn multi-crystalline silicon wafers for texturing,” *Mater Sci Semicond Process*, vol. 53, pp. 8–12, 2016, doi: 10.1016/j.mssp.2016.05.017.

[182] Z. Xiao, G. Geng, X. Wei, Z. Yue, and L. Zhou, “On the mechanism of the vapor etching of diamond wire sawn multi-crystalline silicon wafers for texturing,” *Mater Sci Semicond Process*, vol. 53, pp. 8–12, 2016, doi: 10.1016/j.mssp.2016.05.017.

[183] M. Cohen, “Novel Photon Capture Methods for Multicrystalline Silicon Solar Cells,” The University of Oxford, 2017.

[184] Labsphere, “Technical Guide: Integrating Sphere Theory and Applications,” 2017.

[185] Film-Sense, “Instrument Performance,” *Applications*. https://film-sense.com/film-sense-applications/#instrument (accessed Jun. 08, 2022).

[186] Film Sense, “FS-1 ™ Ellipsometer Manual,” 2015.

[187] K. M. Krishnan, “Scanning Electron Microscopy,” in *Principles of Materials Characterization and Metrology*, Oxford University Press, 2021, pp. 693–744. doi: 10.1093/oso/9780198830252.003.0010.

[188] O. C. Wells, “Scanning Electron Microscopy,” in *Encyclopedia of Materials: Science and Technology*, no. 1, K. H. J. Buschow, R. W. Cahn, M. C. Flemings, B. Ilschner, E. J. Kramer, S. Mahajan, and P. Veyssière, Eds. Elsevier, 2001, pp. 8265–8269. doi: 10.1016/B978-0-323-49778-7.00001-1.

[189] B. J. Griffin, “A comparison of conventional Everhart-Thornley style and in-lens secondary electron detectors-a further variable in scanning electron microscopy,” *Scanning*, vol. 33, no. 3, pp. 162–173, 2011, doi: 10.1002/sca.20255.

[190] ThermoFisher Scientific, “Energy and Line Widths of Available Anode Materials,” *XPS X-Ray Sources*. https://www.thermofisher.com/uk/en/home/materials-science/learning-center/surface-analysis/x-ray-generation.html (accessed Jun. 08, 2022).

[191] ThermoFisher Scientific, “X-ray Monochromator,” *XPS X-Ray Sources*. https://www.thermofisher.com/uk/en/home/materials-science/learning-center/surface-analysis/x-ray-generation.html (accessed Jun. 08, 2022).

[192] D. K. Schroder, *MATERIAL AND DEVICE SEMICONDUCTOR MATERIAL AND DEVICE*, 3rd ed. Phoenix, Arizona: John Wiley and Sons Ltd, 2006.

[193] R. A. Sinton and A. Cuevas, “Contactless determination of current-voltage characteristics and minority-carrier lifetimes in semiconductors from quasi-steady-state photoconductance data,” *Appl Phys Lett*, vol. 69, no. 17, pp. 2510–2512, Oct. 1996, doi: 10.1063/1.117723.

[194] H. Nagel, C. Berge, and A. G. Aberle, “Generalized analysis of quasi-steady-state and quasi-transient measurements of carrier lifetimes in semiconductors,” *J Appl Phys*, vol. 86, no. 11, pp. 6218–6221, 1999, doi: 10.1063/1.371633.

[195] SunLab, “SunLab - Model Sherescan 2.0 - High Resolution (Selective) Emitter Sheet Resistance Mapping.” https://www.energy-xprt.com/products/sunlab-model-

sherescan-20-high-resolution-selective-emitter-sheet-resistance-mapping-177078 (accessed Jun. 09, 2022).

[196] C. K. Fink, K. Nakamura, S. Ichimura, and S. J. Jenkins, “Silicon oxidation by ozone,” *Journal of Physics Condensed Matter*, vol. 21, no. 18, 2009, doi: 10.1088/0953-8984/21/18/183001.

[197] DuPont ™, “Viton ® Fluoroelastomer: Superior Sealing Performance in a Wide Variety of Aggressive Applications,” 2010.

[198] ERIKS, “Viton Material Properties,” *Rubber Technology Info*. https://rubbertechnology.info/en/rubber-products/seals/viton-seal-properties/viton-material-properties/ (accessed Jun. 21, 2022).

[199] Humphrey, “Viton vs. Buna: Which Seal for Your Applications,” *Humphre Products News*. https://www.humphrey-products.com/news/viton-vs-buna-which-seal-for-your-applications (accessed Jun. 21, 2022).

[200] MatWeb, “Thermal Properties for Thermoset Fluoroelastomer,” *Material Property Data*. https://www.matweb.com/search/datasheet.aspx?matguid=867df8088a9743dfa0ca99f4879c3c5a&ckck=1 (accessed Jun. 21, 2022).

[201] The Plastics Shop, “Thermal Stability of PTFE,” *PTFE Technical Information*. https://www.theplasticshop.co.uk/ptfe-technical-information.html (accessed Jun. 21, 2022).

[202] Applied Plastics Technology, “Teflon PTFE Information & Properties,” *Teflon PTFE*. https://www.ptfeparts.com/teflon-ptfe/ (accessed Jun. 21, 2022).

[203] Engineering & Design Plastics Ltd, “PTFE Properties,” *PTFE*. https://www.edplastics.co.uk/PTFE.htm (accessed Jun. 21, 2022).

[204] M. Morita, T. Ohmi, E. Hasegawa, M. Kawakami, and M. Ohwada, “Growth of native oxide on a silicon surface,” *J Appl Phys*, vol. 68, no. 3, pp. 1272–1281, 1990, doi: 10.1063/1.347181.

[205] S. I. Raider, R. Flitsch, and M. J. Palmer, “Oxide Growth on Etched Silicon in Air at Room Temperature,” *J Electrochem Soc*, vol. 122, no. 3, pp. 413–418, 1975, doi: 10.1149/1.2134225.

[206] C. Bohling and W. Sigmund, “Self-Limitation of Native Oxides Explained,” *Silicon*, vol. 8, no. 3, pp. 339–343, 2016, doi: 10.1007/s12633-015-9366-8.

[207] D. S. Jensen *et al.*, “ Silicon (100)/SiO 2 by XPS ,” *Surface Science Spectra*, vol. 20, no. 1, pp. 36–42, 2013, doi: 10.1116/11.20121101.

[208] D. S. Jensen *et al.*, “Multi-instrument characterization of the surfaces and materials in microfabricated, carbon nanotube-templated thin layer chromatography plates. An analogy to ‘The Blind Men and the Elephant,’” *Surface and Interface Analysis*, vol. 45, no. 8, pp. 1273–1282, 2013, doi: 10.1002/sia.5268.

[209] V. Gorodokin and D. Zemlyanov, “Metallic Contamination in Silicon Processing,” in *23rd IEEE Convention of Electrical and Electronics Engineers in Israel*, 2004, pp. 1–62. doi: 10.1002/9783527611805.ch1.

[210] D. Romero, J. M. Fernández Romero, and J. J. Laserna, “Distribution of metal impurities in silicon wafers using imaging-mode multi-elemental laser-induced breakdown spectrometry,” *J Anal At Spectrom*, vol. 14, no. 2, pp. 199–204, 1999, doi: 10.1039/a807362g.

[211] C. Hu and S. N. Superlattices, “Reports on Progress in Physics Related content The physics of SiO 2 layers,” 1990.

[212] S. R. Hofstein, “Stabilization of MOS devices,” *Solid State Electronics*, vol. 10, no. 7, pp. 657–670, 1967, doi: 10.1016/0038-1101(67)90096-2.

[213] M. A. Alam, D. Das, M. H. Azarian, B. Sood, and M. G. Pecht, “Influence of molding compound on leakage current in MOS transistors,” *IEEE Trans Compon Packaging Manuf Technol*, vol. 1, no. 7, pp. 1054–1063, 2011, doi: 10.1109/TCPMT.2011.2115240.

[214] K. P. Sreejith, A. K. Sharma, S. Behera, A. Kottantharayil, and P. K. Basu, “A low cost additive-free acid texturing process for large area commercial diamond-wire-

sawn multicrystalline silicon solar cells," *Solar Energy*, vol. 205, no. April, pp. 263–274, 2020, doi: 10.1016/j.solener.2020.05.018.

[215] F. Cao *et al.*, "Next-generation multi-crystalline silicon solar cells: Diamond-wire sawing, nano-texture and high efficiency," *Solar Energy Materials and Solar Cells*, vol. 141, pp. 132–138, Jul. 2015, doi: 10.1016/j.solmat.2015.05.030.

[216] C. M. Aldao and J. H. Weaver, "Halogen etching of Si via atomic-scale processes," *Prog Surf Sci*, vol. 68, no. 4–6, pp. 189–230, 2001, doi: 10.1016/S0079-6816(01)00047-8.

[217] G. W. Gale, H. Cui, and K. A. Reinhardt, *Aqueous Cleaning and Surface Conditioning Processes*. Elsevier Inc., 2018. doi: 10.1016/B978-0-323-51084-4.00004-6.

[218] N.-T. Nguyen, *Micromixers*, Second Edi. William Andrew Publishing, 2012. doi: 10.1016/b978-1-4377-3520-8.00004-8.

[219] A. S. H. Makhlouf, *Current and advanced coating technologies for industrial applications*. Woodhead Publishing Limited, 2011. doi: 10.1533/9780857094902.1.3.

[220] R. Smith, C. Peters, and H. Inomata, *Introduction to Supercritical Fluids: A Spreadsheet-based Approach*, vol. 4. Elsevier, 2013. doi: 10.1016/B978-0-444-52215-3.00004-0.

[221] L. L. Balassa, G. O. Fanger, and O. B. Wurzburg, "Microencapsulation in the food industry," *C R C Critical Reviews in Food Technology*, vol. 2, no. 2, pp. 245–265, 1971, doi: 10.1080/10408397109527123.

[222] J. Broadhead, S. K. Edmond Rouan, and C. T. Rhodes, "The spray drying of pharmaceuticals," *Drug Dev Ind Pharm*, vol. 18, no. 11–12, pp. 1169–1206, 1992, doi: 10.3109/03639049209046327.

[223] R. P. Patel, M. P. Patel, and A. M. Suthar, "Spray Drying Technology: An Overview," *Indian J Sci Technol*, vol. 2, no. 10, pp. 44–47, 2009.

[224] L. Qian, S. Song, and X. Li, "A new spray approach to produce uniform ultrafine coatings," *J Nanotechnol*, vol. 2018, pp. 1–9, 2018, doi: 10.1155/2018/8978541.

[225] B. v. Derjaguin and L. D. Landau, “Theory of the Stability of Strongly Charged Lyophobic Sols and of the Adhesion of Strongly Charged Particles in Solutions of Electrolytes,” *Acta Physicochimica U.R.S.S.*, vol. 14, pp. 633–662, 1941.

[226] E. J. W. Verwey and J. T. G. Overbeek, *Theory of the stability of lyophobic colloids: The interaction of sol particles having an electric double layer*. Amsterdam: Elsevier, 1948. doi: 10.1021/j150453a001.

[227] S. J. Park and M. K. Seo, *Intermolecular Force*, vol. 18. 2011. doi: 10.1016/B978-0-12-375049-5.00001-3.

[228] R. López-Esparza, M. A. Balderas Altamirano, E. Pérez, and A. Gama Goicochea, “Importance of molecular interactions in colloidal dispersions,” *Advances in Condensed Matter Physics*, vol. 2015, 2015, doi: 10.1155/2015/683716.

[229] W. D. Kingery, *Introduction to ceramics*. New York: Wiley, 1960.

[230] T. W. Healy, “Stability of Aqueous Silica Sols,” in *The Colloid Chemistry of Silica*, H. E. Bergna, Ed. Parkville: American Chemical Society, 1994, pp. 147–159. doi: 10.1201/9781420028706-24.

[231] M. Kobayashi, F. Juillerat, P. Galletto, P. Bowen, and M. Borkovec, “Aggregation and charging of colloidal silica particles: Effect of particle size,” *Langmuir*, vol. 21, no. 13, pp. 5761–5769, 2005, doi: 10.1021/la046829z.

[232] G. Vigil, Z. Xu, S. Steinberg, and J. Israelachvili, “Interactions of Silica Surfaces,” *J Colloid Interface Sci*, vol. 165, pp. 367–385, 1994.

[233] J. Israelachvili and W. Hakan, “Role of hydration and water structure in biological and colloidal interactions,” *Nature*, vol. 379, no. 18, pp. 219–225, 1996.

[234] N. V. Churaev, I. P. Sergeeva, V. D. Sobolev, and B. V. Derjaguin, “Examination of the surface of quartz capillaries by electrokinetic methods,” *J Colloid Interface Sci*, vol. 84, no. 2, pp. 451–460, 1981, doi: 10.1016/0021-9797(81)90236-8.

[235] S. A. Boden and D. M. Bagnall, “Tunable reflection minima of nanostructured antireflective surfaces,” *Appl Phys Lett*, vol. 93, no. 13, pp. 2008–2010, 2008, doi: 10.1063/1.2993231.

[236] S. J. Wilson and M. C. Hutley, “The optical properties of ‘moth eye’ antireflection surfaces,” *Opt Acta (Lond)*, vol. 29, no. 7, pp. 993–1009, 1982, doi: 10.1080/713820946.

[237] P. B. Clapham and M. C. Hutley, “Reduction of Lens Reflexion by the ‘Moth Eye’ Principle,” *Nature*, vol. 244, pp. 281–282, 1973.

[238] R. B. Stephens and G. D. Cody, “Optical Reflectance and Transmission of a Textured Surface,” *Thin Solid Films*, vol. 45, pp. 19–29, 1977.

[239] H. M. Branz, V. E. Yost, S. Ward, K. M. Jones, B. To, and P. Stradins, “Nanostructured black silicon and the optical reflectance of graded-density surfaces,” *Appl Phys Lett*, vol. 94, no. 23, pp. 88–91, 2009, doi: 10.1063/1.3152244.

[240] J. W. Leem, Y. M. Song, Y. T. Lee, and J. S. Yu, “Effect of etching parameters on antireflection properties of Si subwavelength grating structures for solar cell applications,” *Appl Phys B*, vol. 100, no. 4, pp. 891–896, 2010, doi: 10.1007/s00340-010-4128-1.

[241] S. A. Boden and D. M. Bagnall, “Optimization of moth-eye antireflection schemes for silicon solar cells,” *Progress in Photovoltaics: Research and Applications*, vol. 18, no. 3, pp. 195–203, 2010, doi: 10.1002/pip.951.

[242] T. H. Fung *et al.*, “Improved emitter performance of RIE black silicon through the application of in-situ oxidation during POCl3 diffusion,” *Solar Energy Materials and Solar Cells*, vol. 210, no. March, Jun. 2020, doi: 10.1016/j.solmat.2020.110480.

[243] M. Morita, T. Ohmi, E. Hasegawa, M. Kawakami, and M. Ohwada, “Growth of native oxide on a silicon surface,” *J Appl Phys*, vol. 68, no. 3, pp. 1272–1281, 1990, doi: 10.1063/1.347181.

[244] B. E. Deal, “The Oxidation of Silicon in Dry Oxygen, Wet Oxygen, and Steam,” *J. Electrochem. Soc.*, vol. 110, no. 6, pp. 527–533, 1963.

[245] B. E. Deal and A. S. Grove, “General Relationship for the Thermal Oxidation of Silicon,” *J Appl Phys*, vol. 36, no. 12, p. 3778, 1965, doi: 10.1063/1.1713945.

[246] S. I. Raider, R. Flitsch, and M. J. Palmer, “Oxide Growth on Etched Silicon in Air at Room Temperature,” *J Electrochem Soc*, vol. 122, no. 3, pp. 413–418, 1975, doi: 10.1149/1.2134225.

[247] R. C. Spiker and L. Andrews, “Matrix reactions of alkali metal atoms with ozone: Infrared spectra of the alkali metal ozonide molecules,” *J Chem Phys*, vol. 59, no. 4, pp. 1851–1862, 1973, doi: 10.1063/1.1680270.

[248] H. I. Starnberg, P. Soukiassian, and Z. Hurych, “Alkali-metal-promoted oxidation of the Si(100)2 X I surface: Coverage dependence and nonlocality,” *Phys Rev B*, vol. 39, no. 17, pp. 12775–12782, 1989.

[249] P. Soukiassian, T. M. Gentle, M. H. Bakshi, and Z. Hurych, “SiO2-Si interface formation by catalytic oxidation using alkali metals and removal of the catalyst species,” *J Appl Phys*, vol. 60, no. 12, pp. 4339–4341, 1986, doi: 10.1063/1.337485.

[250] E. M. Oellig, E. G. Michel, M. C. Asensio, and R. Miranda, “Ultrathin gate oxides formed by catalytic oxidation of silicon,” *Appl Phys Lett*, vol. 50, no. 23, pp. 1660–1662, 1987, doi: 10.1063/1.97760.

[251] A. J. Muscat, A. Rjeb, and D. Roy, “Oxidation of Si(111) 7 x 7 using alkali metal atoms: evidence for local promotion mechanisms,” *Surface Science Letters*, vol. 302, pp. 256–262, 1994.

[252] E. G. Michel, J. E. Ortega, E. M. Oellig, M. C. Asensio, J. Ferron, and R. Miranda, “Early stages of the alkali-metal-promoted oxidation of silicon,” *Phys Rev B*, vol. 38, no. 18, pp. 399–406, 1988.

[253] M. C. Asensio, E. G. Michel, E. M. Oellig, and R. Miranda, “Mechanism of alkali-promoted oxidation of silicon,” *Appl Phys Lett*, vol. 51, no. 21, pp. 1714–1716, 1987, doi: 10.1063/1.98553.

[254] B. Hellsing, “Electronic mechanism for alkali-metal-promoted oxidation of semiconductors,” *Phys Rev B*, vol. 40, no. 6, pp. 3856–3861, 1989.

[255] K. R. Williams, K. Gupta, and M. Wasilik, “Etch Rates for Micromachining Processing — Part II,” *Journal of Microelectromechanical Systems*, vol. 12, no. 6, pp. 761–778, 2003.

[256] C. R. Helms and B. E. Deal, “Mechanisms of the HF / H2O vapor phase etching of SiO2,” *Journal of Vacuum Science & Technology A: Vacuum, Surfaces, and Films*, vol. 10, no. 4, pp. 806–811, 1991.

[257] Britannica, “Deliquesecence.” https://www.britannica.com/science/deliquescence (accessed Apr. 13, 2022).

[258] “Water - Saturation Pressure vs. Temperature,” *Engineering ToolBox*, 2004. https://www.engineeringtoolbox.com/water-vapor-saturation-pressure-d_599.html (accessed Apr. 13, 2022).

[259] S. Ohe, *Computer Aided Data Book of Vapor Pressure*. Tokyo: Japan: Data Book Publishing Company, 1976.

[260] G. Boishin and L. Surnev, “Potassium adsorption and coadsorption with oxygen on a Si(111) surface,” *Surf Sci*, vol. 273, no. 3, pp. 301–310, 1992, doi: 10.1016/0039-6028(92)90068-H.

[261] W. Li, J. J. Klemeš, Q. Wang, and M. Zeng, “Energy Storage of Low Potential Heat using Lithium Hydroxide Based Sorbent for Domestic Heat Supply,” *J Clean Prod*, vol. 285, 2021, doi: 10.1016/j.jclepro.2020.124907.

[262] A. Kumar, M. Park, J. Y. Huh, H. M. Lee, and K. S. Kim, “Hydration phenomena of sodium and potassium hydroxides by water molecules,” *Journal of Physical Chemistry A*, vol. 110, no. 45, pp. 12484–12493, 2006, doi: 10.1021/jp063726b.

[263] M. L. Williams, “CRC Handbook of Chemistry and Physics, 76th edition,” *Occup Environ Med*, vol. 53, no. 7, pp. 504–504, 1996, doi: 10.1136/oem.53.7.504.

[264] N. Yamada, O. N. Kim, T. Tokimitsu, Y. Nakai, and H. Masuda, “Optimization of anti-reflection moth-eye structures for use in crystalline silicon solar cells,” *Progress in Photovoltaics: Research and Applications*, vol. 19, no. 2, pp. 134–140, 2011, doi: 10.1002/pip.994.

[265] ThermoFisher Scientific, “An overview of the damage caused to samples by electron beams,” *Electron Beam Damage in Scanning Electron Microscopes*. https://www.thermofisher.com/uk/en/home/materials-science/learning-center/applications/sample-degradation-scanning-electron-microscope-sem.html (accessed Sep. 02, 2022).

[266] I. Zubel, “Silicon anisotropic etching in alkaline solutions III: on the possibility of spatial structures forming in the course of Si(100) anisotropic etching in KOH and KOH + IPA solutions,” *Sens Actuators A Phys*, vol. 84, no. 1, pp. 116–125, 2000, doi: 10.1016/S0924-4247(99)00347-7.

[267] B. Kafle *et al.*, “On the emitter formation in nanotextured silicon solar cells to achieve improved electrical performances,” *Solar Energy Materials and Solar Cells*, vol. 152, pp. 94–102, 2016, doi: 10.1016/j.solmat.2016.03.031.

[268] G. Scardera *et al.*, “On the Enhanced Phosphorus Doping of Nanotextured Black Silicon,” *IEEE J Photovolt*, vol. 11, no. 2, pp. 298–305, 2021, doi: 10.1109/JPHOTOV.2020.3047420.

[269] R. Satpathy and V. Pamuru, “Making of crystalline silicon solar cells,” in *Solar PV Power: Design, Manufacturing and Applications from Sand to Systems*, San Diego: Elsevier Science & Technology, 2020, pp. 71–134. doi: 10.1016/B978-0-12-817626-9.00004-6.

[270] J. Oh, H. C. Yuan, and H. M. Branz, “An 18.2%-efficient black-silicon solar cell achieved through control of carrier recombination in nanostructures,” *Nat Nanotechnol*, vol. 7, no. 11, pp. 743–748, 2012, doi: 10.1038/nnano.2012.166.

[271] T. Pasanen, V. Vähänissi, N. Theut, and H. Savin, “Surface passivation of black silicon phosphorus emitters with atomic layer deposited SiO2/Al2O3 stacks,” *Energy Procedia*, vol. 124, no. February 2018, pp. 307–312, 2017, doi: 10.1016/j.egypro.2017.09.304.

[272] S. Werner, S. Mourad, W. Hasan, and A. Wolf, “Structure and composition of phosphosilicate glass systems formed by POCl3 diffusion,” *Energy Procedia*, vol. 124, pp. 455–463, 2017, doi: 10.1016/j.egypro.2017.09.280.

[273] R. W. Johnson, A. Hultqvist, and S. F. Bent, “A brief review of atomic layer deposition: From fundamentals to applications,” *Materials Today*, vol. 17, no. 5, pp. 236–246, 2014, doi: 10.1016/j.mattod.2014.04.026.